# The University of Nottingham

UNITED KINGDOM · CHINA · MALAYSIA

# Numerical Simulations of Geotechnical Engineering Problems Considering the Principal Stress Rotation

By

**Zhe Wang**

B.Eng.

*Thesis submitted to the University of Nottingham for*

*the degree of Doctor of Philosophy*

2016

# Abstract

Soil behaviors are quite complex under dynamic loadings, such as wave loading, earthquake loading, etc, but they share common characteristics that the soil is subjected to considerable principal stress rotations (PSR). PSR can generate plastic deformation even without a change of principal stress magnitudes. Continuous PSR can also generate excess pore water pressures and cumulative shear strains in undrained condition. Therefore, the PSR from the dynamic loadings can accelerate undrained soil liquefaction because it can cause cumulative plastic volumetric deformations. Ignoring PSR induced deformation may lead to unsafe design. It is therefore important to understand the soil behaviors under cyclic loadings with the PSR and take account of this PSR impact in the numerical simulations of corresponding geotechnical problems.

Although researchers have recognized the importance of the PSR in real geotechnical problems under diverse loading conditions and conducted extensive experimental studies, there are limited considerations of the PSR impact on numerical simulations of boundary value problems. Moreover, most of the constitutive models widely-used in the numerical investigations at present cannot simulate this PSR behavior properly. Therefore, a new kinematic hardening soil model (PSR model) developed on the basis of a well-established model with bounding surface concept is used to simulate the PSR behavior in this research. It can take account of the PSR impact by treating the stress rate generating the PSR independently.

To investigate the impacts of PSR in numerical simulations of geotechnical problems, the PSR model is implemented into both the single element and finite element analysis of a series of geotechnical problems by a constitutive model subroutine written in Fortran. In this subroutine, an explicit substepping integration algorithm with automatic error controls is used to perform the constitutive formulations. The imposed strain increment can be automatically divided and the sizes of the sub-increments are also automatically determined based on the prescribed error tolerance in this numerical integration scheme. The single element analyses include the simulations of the triaxial and hollow cylinder tests with monotonic, rotational and torsional loading paths, while the finite element analyses consist of the simulations of the centrifuge experimental tests under wave loadings and earthquake loadings. The predicted results by using the soil model with and without considering the PSR impact, as well as the experimental results will be compared.

From these single element and finite element analyses, it is evident that the rotational, torsional and dynamic loadings such as wave and earthquake loadings can produce the PSR and non-coaxiality in the soil. The comparisons between the predicted results from the modified PSR model, the original model, and the laboratory results from these experimental tests all show that although the original model can reflect some non-coaxiality, it can produce very limited build-up of pore water pressure and cumulative shear strain under cyclic loading path. However, due to consideration of the PSR impact, the modified PSR model can generate higher pore water pressure and shear strain than the original model, thus bringing the soil to the liquefaction and agrees better with the experimental results. Therefore, it is important to consider the PSR effect in the simulation of geotechnical problems such as wave-seabed interactions and

the earthquake induced liquefactions, and the PSR model presented in this research has a great ability and plays an important role in these numerical simulations.

# Acknowledgements

First and foremost, I would like to thank my supervisor—Dr. Yunming Yang for his valuable instructions, guidance and supervision throughout this research. Dr. Yang is also the person who gave me the opportunity to take this research program and introduced this topic to me.

Besides, I would like to thank my second supervisor—Professor Hai-Sui Yu for his profound knowledge and continuing pursuit of geotechnical engineering which have been and always will be inspiring me.

Special and sincere thanks are extended to all the staff and technicians in the Faculty of Science and Engineering and the Graduate School for their assistance and help during these challenging years, in particular Mr. Che, Mr. Li, and Mr. Shi for providing guidance on the laboratory tests, which help me better understand the soil behaviors.

I would like to thank all my friends in the Graduate School for their friendship and making my research experience so special, rewarding and wonderful.

Last but not least, I wish to thank all my family members and friends for their care and support during these tough years. I will surely continue pursuing my career with your endless love.

# List of Contents

## Chapter 5 The Finite Element Simulation of Wave-Seabed

## Chapter 6 The Finite Element Simulation of

# List of Tables

# List of Figures

# List of Notations

$B = (\sigma_2 - \sigma_3)/(\sigma_1 - \sigma_3)$: Parameter that measurers the relative magnitude of the intermediate principal stress

$C_u = D_{60}/D_{10}$:　　　Uniformity coefficient

$D_r$:　　　　　　Relative density

$D_{50}$:　　　　　Mean grain size

$D_{10}$:　　　　　Effective grain size

$e$ :　　　　　　Void ratio

$e_0$:　　　　　　Void ratio at $p_c = 0$

$e_c$:　　　　　　Critical void ratio

$e_{con}$:　　　　　Void ratio after consolidation

$e_{max}$:　　　　　Maximum void ratio

$e_{min}$:　　　　　Minimum void ratio

$G_S$ :　　　　　Specific gravity

$u_0$:　　　　　　The amplitude of the fluid pressure fluctuation imposed on the soil surface ($z=0$)

$\kappa = 2\pi/L$:　　　Wave number

$w = 2\pi/T$:　　　Angular frequency

$\chi_0 = \kappa u_0/Y'$:　　Cyclic stress ratio

$\chi_{cr}$:　　　　　Critical cyclic stress ratio

$Y'$ :　　　　　Saturated unit weight of soil

$K_D$:　　　　　Permeability

$L$:　　　　　　Wave length

$T$:　　　　　　Wave period

$p_c$:　　　　　　Confining pressure at critical state

$p_{at}$:  Atmospheric pressure

$R_{an}$:  Error tolerance of the forces in ABAQUS

$C_{an}$:  Error tolerance of the displacements in ABAQUS

$p = (\sigma_1+\sigma_2+\sigma_3)/3$ :  Mean total stress

$p' = (\sigma'_1+\sigma'_2+\sigma'_3)/3$:  Mean effective stress

$q$:  Deviatoric stress

$\sigma_1$, $\sigma_2$ and $\sigma_3$:  Major, intermediate and minor total principal stresses

$\sigma'_1$, $\sigma'_2$ and $\sigma'_3$:  Major, intermediate and minor effective principal stresses

$\varepsilon_q$ :  Deviatoric strain

$\varepsilon_1$, $\varepsilon_2$ and $\varepsilon_3$ :  Major, intermediate and minor principal strains

$\varepsilon_v = \varepsilon_1+ \varepsilon_2+ \varepsilon_3$:  Volumetric strain

$\sigma_z$, $\sigma_\theta$, $\sigma_r$:  Axial, circumferential and radial stress in hollow cylinder tests

$\tau_{\theta z}$, $\tau_{z\theta}$:  Shear stress in hollow cylinder tests

$\varepsilon_{\theta z}$, $\varepsilon_{z\theta}$:  Shear strain in hollow cylinder tests

$\sigma_x$, $\sigma_y$, $\sigma_z$:  Normal stresses in the finite element simulation

$\sigma_{xy}$, $\sigma_{yz}$, $\sigma_{xz}$:  Shear stresses in the finite element simulations

$\xi$:  Degree of non-coaxiality

$\Psi$:  State parameter

$\Phi$:  Angle between the principal stress and principal plastic strain rate

# Chapter 1 Introduction

## 1.1 Background

Dynamic loadings such as wave loadings and earthquake loadings can generate considerable principal stress rotation (PSR) in the soil. In 1983, Ishihara & Towhata first proposed that the PSR can cause the plastic deformation and non-coaxiality even without a change of principal stress magnitudes. Continuous PSR can also generate excess pore water pressure and cumulative shear strain in undrained condition. Similar phenomenon is also found by Ishihara & Yamazaki (1984), Bhatia et al. (1985), Miura et al. (1986), Gutierrez et al. (1991), etc. Therefore, the cumulative plastic volumetric deformations caused by the PSR from the dynamic loadings can accelerate undrained soil liquefaction. Ignoring this PSR induced deformation may lead to unsafe design.

Researchers have been carrying extensive work to investigate and model the soil behaviors under the PSR in experimental, theoretical, and numerical fields, and have greatly promoted the understanding and modeling of this research topic. For example, from the experimental perspective, the early simple shear tests and hollow cylinder tests revealed the relationship between the non-coaxiality and the fabric anisotropy (Roscoe et al., 1967). Then a series of centrifuge and 1 $g$ wave tests on seabed with sand have been carried out by different researchers to investigate the wave-seabed interactions (Nago & Maeno, 1987; Zen et al, 1990; Sassa & Sekiguchi, 1999). Sassa & Sekiguchi (1999) found that in their tests, the soil behaviors were largely affected by the

PSR under the progressive wave loading. Besides, researchers have also been paying enormous efforts to investigate the soil behaviors under the earthquake loadings. One of the most famous projects was the VELACS project (Verification of Liquefaction Analysis using Centrifuge Studies), which includes a variety of centrifuge tests among several universities in America (Arulanandan & Scott, 1993). In this project, 12 sets of different centrifuge models are subjected to various base motions to investigate the soil liquefaction under earthquake loadings and acquire data for the validation of different analysis tools including the numerical modeling.

Apart from the experimental tests, researchers also utilize a variety of soil models to simulate the soil behaviors with the PSR under both static and dynamic loadings, such as the multi-mechanism model, microplane model, hypoplasticity model, double shearing types of models, yield vertex theory model, etc (Rudnicki & Rice, 1975; Dafalias, 1986; Kolymbas, 1991; Fang, 2003; Yu & Yuan, 2005; Chang & Sture, 2006; Tejchman & Wu, 2009). However, the results of the numerical simulations are largely affected by the soil models used. Although there are a few models considering the PSR effect, most of them have not been seriously implemented into the finite element analysis of boundary value problems. For the wave-seabed interaction, one of the best known studies was the finite element simulation conducted by Sassa & Sekiguchi in 2001. They presented a cyclic plasticity constitutive model and implemented it to the finite element analysis of seabed liquefactions under both progressive and standing waves. However, in 2013, Jeng stated that Sassa's model had several limitations in the simulation of this kind of problem, such as the lack of consideration of viscosity, the assumption of infinite bed, etc. Furthermore, the simulation results from this cyclic plasticity model seem to be

very sensitive to the model parameters, which restricts its application. For the earthquake loading, although several researchers have implemented their soil models into the numerical simulations of the VELACS project subsequently (Andrianopoulos et al., 2010; Sadeghian & Namin, 2013; Pak et al., 2014), there are few of them taking account of the PSR effect.

In conclusion, the PSR effect plays an important role in the soil behaviors in many geotechnical problems such as the wave-seabed interactions and the earthquake induced liquefactions. It is essential to consider the PSR impact in these numerical simulations as the PSR can lead to plastic deformations and the soil liquefaction under these loading conditions. Although researchers have been paying efforts to investigate the soil behaviors under the PSR, there are few of them considering the PSR impact in numerical simulations of boundary value problems. Therefore, this research aims to simulate the geotechnical problems using a newly-developed PSR model which can take account of the PSR impact, thus testing its ability in the simulations of a variety of experimental tests and the significance of the PSR impact in the simulation of boundary value problems.

## 1.2 Aims and Objectives of the Research

The lack of the numerical simulations investigating the PSR effects and the proper soil model considering the PSR impact lead to this research. The aim of this investigation is to numerically test the ability of the PSR model and examine the significance of the PSR impact by implementing this model into the numerical simulations of boundary value problems. Therefore, the numerical simulations of a series of triaxial and hollow cylinder tests and

experimental centrifuge tests under wave loadings and earthquake loadings are carried out to investigate the PSR behaviors under these loading conditions. In these numerical simulations, the predicted results from the soil models with and without the PSR, as well as the experimental results will be compared.

The aims of the research can be divided as follows:

- To implement the original base model and the modified PSR model into both the single element and finite element simulations. The PSR model is modified based on a kinematic hardening model with bounding surface and critical state concept by treating the stress rate generating the PSR independently. It also employs the back-stress ratio as the hardening parameter and state parameter to represent sand with different confining stresses and void ratios.

- To study the significance of the PSR impact and validate the PSR model in the single element numerical simulations of a series of experimental tests.

- To investigate the significance of the PSR impact, validate the PSR model, and investigate the wave-induced liquefaction in the wave-seabed interactions using the finite element method.

- To study the significance of the PSR impact and the earthquake-induced liquefaction in the boundary value problem under the earthquake loadings, and also test the ability of the PSR model by the finite element simulation.

  To achieve these aims, the specific objectives pursued are as follows:

- To carry out a literature review on the theoretical, experimental and

numerical studies of soil behaviors under the PSR impact as well as the liquefaction in undrained soil under dynamic loadings.

- To develop a constitutive model subroutine with the numerical integration scheme for the PSR model and modify the finite element computer programs to enable the incorporation of the PSR model into the numerical simulations of boundary value problems.

- To implement the modified PSR model and the original base model into the numerical analysis with the single element computer programs. Experimental tests include a series of triaxial tests and hollow cylinder tests for both the Leighton Buzzard sand (Fraction B & E) and Nevada sand are simulated and comparisons are made between the predicted results and the experimental results.

- To calibrate the model parameters of the soils which will be used in the finite element analyzes by the single element simulations.

- To implement the modified PSR model and the original base model into the numerical analysis of boundary value problems using the finite element computer programs. The centrifuge wave tests for Leighton Buzzard sand (Fraction E) under both the progressive waves and the standing waves with different intensities and the centrifuge test for Nevada sand under the earthquake loadings are simulated.

## 1.3 Outline of the Thesis

This thesis consists of seven chapters, including this introductory section

(**Chapter 1**).

**Chapter 2** presents a general introduction on the soil behaviors related to the PSR effects, including the definition of the principal stress rotation and non-coaxiality, as well as the experimental evidence for them. Then the previous numerical studies and soil models considering the PSR and non-coaxiality are listed, together with their main findings and conclusions. The experimental tests simulated in this research are also reviewed. Furthermore, this section gives an introduction of the soil liquefaction which can be induced by the PSR effect as well as the criteria of liquefaction used in this research.

**Chapter 3** introduces the soils used in the simulations—Leighton Buzzard sand (Fraction B & E) and Nevada sand, as well as the experimental tests simulated. These tests include the triaxial tests, hollow cylinder tests, centrifuge wave tank tests, and centrifuge tests under the earthquake loading. Then this chapter summarizes the numerical simulation tools used in this research, including the Fortran program for the single element simulations, as well as the finite element method, explicit integration scheme, the PSR model subroutine, the finite element Fortran program and the commercial software for the simulations of boundary value problems.

**Chapter 4** introduces the original base model and the development of the new model considering the PSR impact (PSR model). Then the single element simulations for a series of experimental tests for both the Leighton Buzzard sand and the Nevada sand are presented. The PSR effect is investigated by the comparisons between the simulation results from the soil model with and without the PSR. Parameters for these two types of sand used in the following

finite element simulations are also calibrated in this chapter.

**Chapter 5** presents the predicted results of the centrifuge wave tests from both the original model and the modified PSR model and compare them with the experimental results. The performance of the PSR model in the wave-seabed interactions is validated by these comparisons. The PSR effect under the progressive wave loadings and the standing wave loadings as well as the wave-induced liquefaction is also discussed in this section.

**Chapter 6** focuses on the numerical simulation of the experimental centrifuge test under the earthquake loading. The predicted results from two models and the experimental results are compared, thus investigating the PSR effect and validate the modified PSR model in such a loading condition. Furthermore, the earthquake-induced liquefaction is discussed in this chapter as well.

**Chapter 7** summarizes the main findings and conclusions obtained from the previous chapters. Future suggestions and limitations of this research are also discussed in this chapter.

# Chapter 2 Literature Review

## 2.1 Introduction

The literature review first introduces the soil behaviors under the principal stress rotation, including the definition of the PSR and non-coaxiality, the previous experimental investigations on this topic, and the associate experimental evidences supporting the PSR effects.

Secondly, the numerical studies including the discrete element and finite element studies as well as the development of the soil models considering the PSR effects and soil non-coaxiality are briefly reviewed. The main findings and conclusions of these investigations are also listed.

Thirdly, the experimental tests simulated in the single element and finite element analyzes are introduced. The backgrounds of the investigations on the wave-seabed interaction and earthquake-induced liquefaction are also introduced.

This section finally introduces the soil behavior of liquefaction in undrained conditions together with the liquefaction criteria adopted in this research. The liquefaction behavior is examined in the following numerical simulations and is largely affected by the PSR.

## 2.2 Principal Stress Rotations and Non-coaxiality

### 2.2.1 Definition of the PSR and non-coaxiality

The loading conditions in the real geotechnical problems often cause the rotation of principal stresses. Plastic deformations can be induced in the soil when the principal stress directions are changing even without a change of principal stress magnitude. Furthermore, PSR can lead to the soil non-coaxiality, which means the non-coincidence between directions of the principal strain increment and directions of the principal stress. Numerical analysis carried out by Yang and Yu (2006) demonstrates that it is essential to take account of the PSR impact of a granular soil in geotechnical problems. They proposed that the PSR might be involved in both static and dynamic loadings and neglecting the deformations caused by the PSR can lead to unsafe designs. The importance of considering the PSR impact in the design of geotechnical structures has also been verified in a more secure project from Yu and Yuan (2005). In addition, special attentions should be paid to the PSR under dynamic loadings, such as wave and earthquake loadings because they can cause cumulative plastic volumetric deformations, thus leading to the liquefactions in undrained soils.

The PSR and non-coaxial behaviors are often associated with the anisotropic behavior of granular material. An anisotropic specimen is presented in Figure 2-1. In Figure 2-1(a), when the loading direction and the bedding plane are not normal to each other, the axis of principal stresses and axis of principal strain increments are coaxial even if the anisotropy is included in the specimen fabric. However, if the loading direction is not normal to the bedding plane as shown

in Figure 2-1(b), the axis of principal strain increments will deviate from the axis of principal stresses, thus inducing the non-coaxiality.



(a)                                    (b)
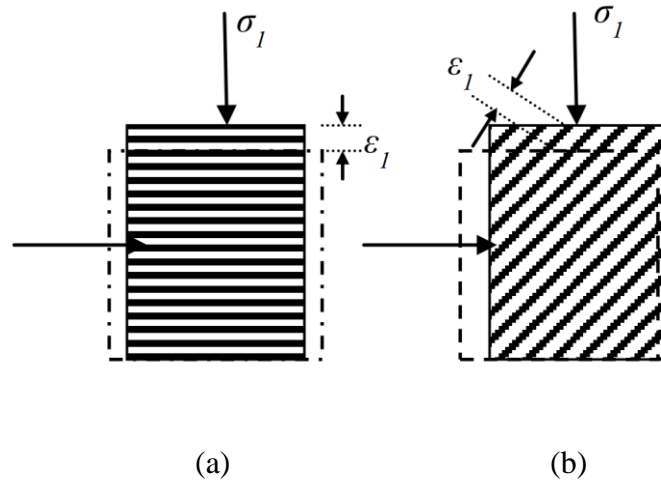
**Figure 2-1. The relationship between the anisotropy and non-coaxiality (Cai, 2010).**

## 2.2.2 Previous experimental studies on the PSR and non-coaxiality

During last 5 decades, numerous experimental studies have revealed the PSR and the non-coaxial behavior of the soil. For example, Roscoe et al. (1967) carried out an early simple shear test and proposed that the principal stress directions were not coincident with the principal strain rate directions before the peak shear stress was reached. The experimental results from Roscoe (1970) in Figure 2-2 also show the non-coaxial rotation of the principal stress and the principal strain increment, especially during the early stage of the shearing. Then the directions tend to be coincident as the shear strain increases. The non-coaxiality was also observed in the micro-mechanical study of a

photoelastic disc assembly to simulate the two-dimensional granular material from Drescher & Jong (1972).
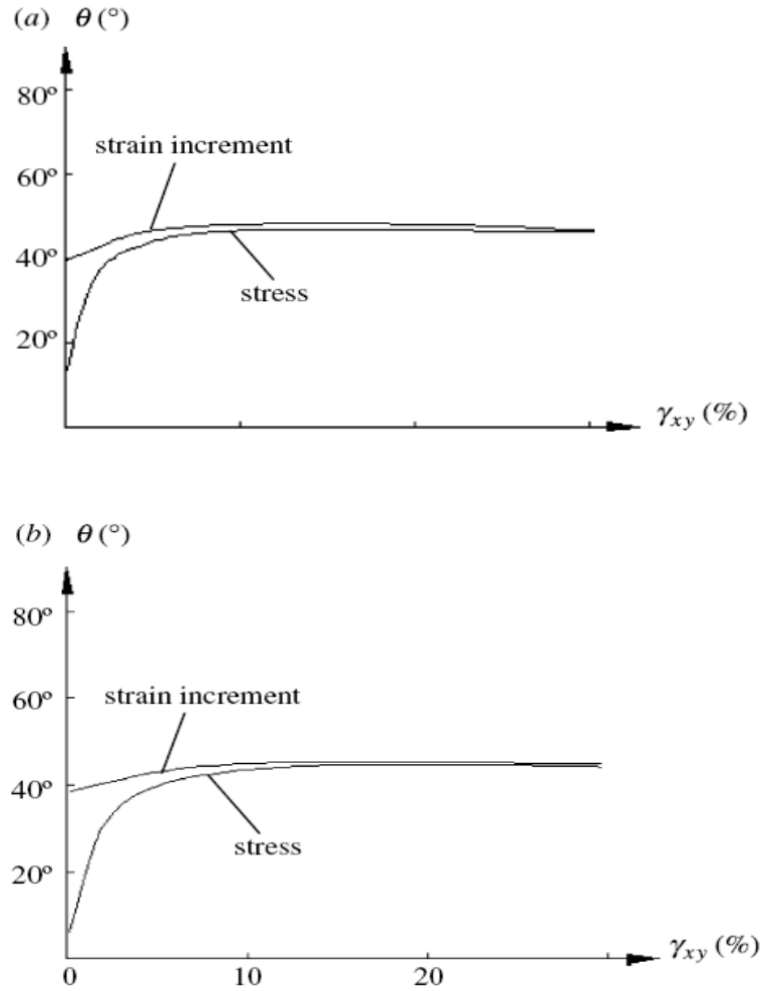


**Figure 2-2. Principal stress and strain increment rotations against shear strain during simple shear tests. (a) $\sigma_y$=135 kPa; (b) $\sigma_y$ =396 kPa (Roscoe, 1970).**

The non-coincidence of the directions of the principal stress and principal strain increment was also observed by Wong & Arthur (1985) using the Directional Shear Cell (DSC). In these tests, samples were subjected to a

two-stage loading under drained conditions in an initially isotropic plane. Figure 2-3 presents the relationships between the measured degree of non-coaxiality $\xi$ and the stress ratio with different reloading directions. The experimental results show an obvious non-coaxiality when the samples were reloaded with the directions of the principal stress $\Phi$ equals to 40° and 70° to the directions of pre-loading. However, the sand behaves almost coaxial when $\Phi = 0°$ or $\Phi = 90°$. Furthermore, the results again show that the non-coaxiality gradually becomes smaller with the increasing stress ratios and the coaxial behavior was achieved when the stress state was close to the failure. In 1986, they conducted another tests for both dense and loose sands during cyclic rotation of principal stresses using the directional shear cell apparatus. These studies showed that the difference between the principal stress and the principal strain incremental directions could be more than 30° in sand during continuous rotation of the principal stress.
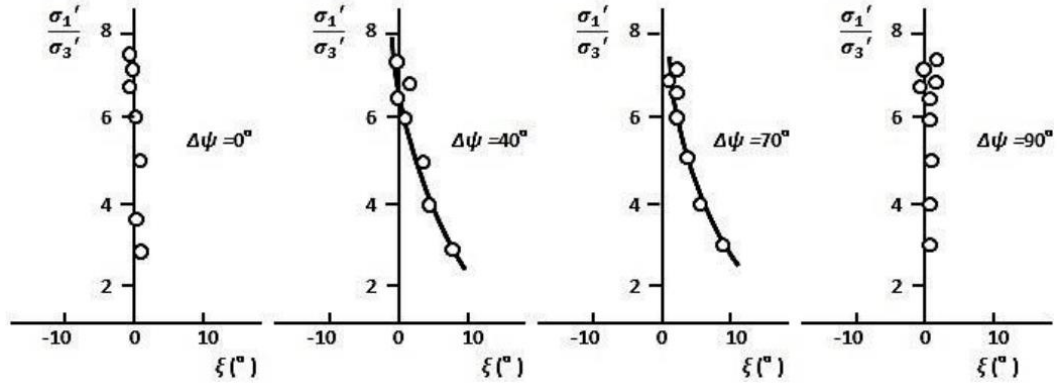


**Figure 2-3. Non-coaxiality measured in the directional shear test (Wong & Arthur, 1985).**

Ibraim et al. (2010) carried out a series of strain controlled tests for a two dimensional analogue granular material. The laboratory apparatus used in these tests allows the rotation of principal directions and the full control of plane deformations. The strain path was controlled by the imposed dilation angle and the direction of principal strain increment. The response of the difference between the directions of principal stresses and stain increments against the strain is presented in Figure 2-4. The direction of principal strain increment $\xi$ and the imposed dilation angle $v$ of the tests are indicated in the test names. For instance, A-T42 (9.6c) is a test with the direction of principal strain increment $\xi$ = 42° and the imposed dilation angle $v$ = 9.6 °. The letter $d$ and $c$ represents the dilation and compression respectively. It can be observed from Figure 2-4 that the degree of non-coaxiality between the directions of the principal stress and the strain rate gradually reduces as the shear strain continues increasing. Once again, coaxiality was almost achieved as the stress approaches the asymptotic state. Moreover, the results show that the rate of the rotations of principal stress axes increases with the inclination angle of the principal strain increment to the vertical direction.
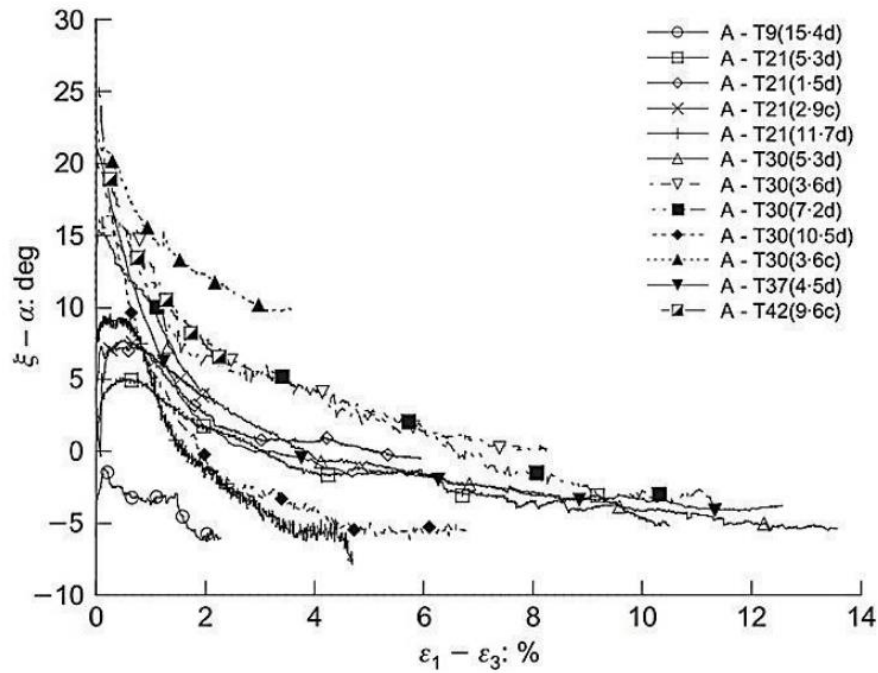
**Figure 2-4. Difference between the direction of the major principal stress and the direction of the major principal strain increment, with the fixed direction of principal axes (Ibraim et al., 2010).**

More recently, the PSR and the non-coaxial behavior are also reported in tests from the hollow cylinder apparatus, which allows the pure rotations of the principal stress (Ishihara & Towhata, 1983; Symes et al., 1982, 1984, 1988; Miura et al., 1986; Pradel et al., 1990; Gutierrez et al., 1991, 1993; Gutierrez & Ishihara, 2000; Lade et al., 2009).

Before the hollow cylinder apparatus was formally introduced by Hight et al. (1983), Symes et al. (1982) had firstly introduced their investigation on the effects of stress rotation and intermediate principal stress using this equipment. Drained tests were performed using Ham River sand with the constant effective confining stress of 600 kPa and back pressure of 400 kPa. The study was

divided into the monotonic loading tests ($\alpha = 45°$, $67.5°$ and $90°$, and $b = 0.5$), and the tests of continuous principal stress rotation ($b = 0.5$, $q = 110$ kPa, and $\alpha$ rotated from $0°$ towards $90°$). In the results from the monotonic loading tests shown in Figure 2-5(a), they found that the degrees of the principal stress were smaller than degrees of the principal strain increment. In the pure rotational tests shown in Figure 2-5(b), the non-coaxial soil behavior was observed and the deviation between the directions of the principal stress and principal strain rate reduced as the principal stress rotated from $0°$ towards $90°$.
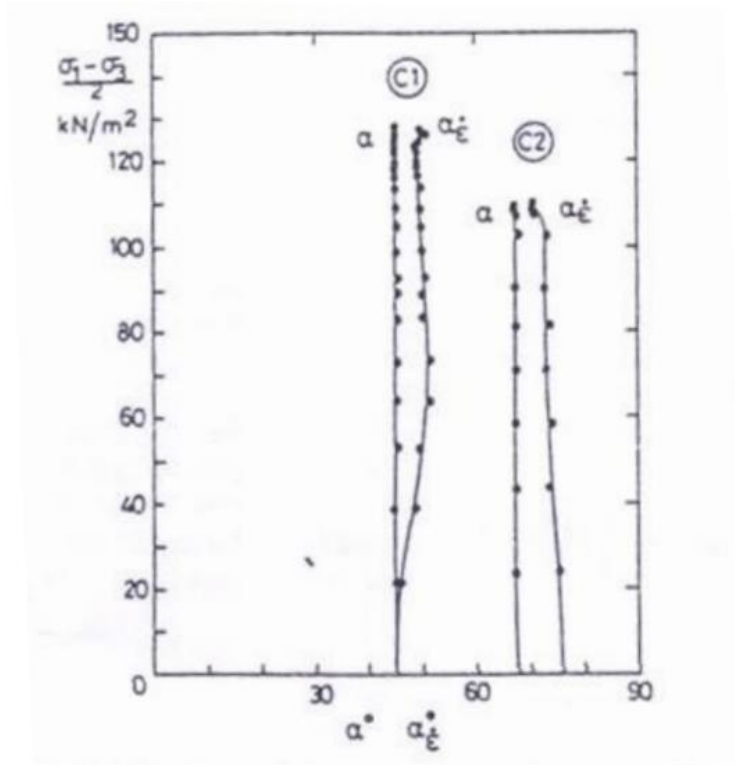


(a)   monotonic loading tests with $\alpha=45°$ and with $\alpha=67.5°$.

15
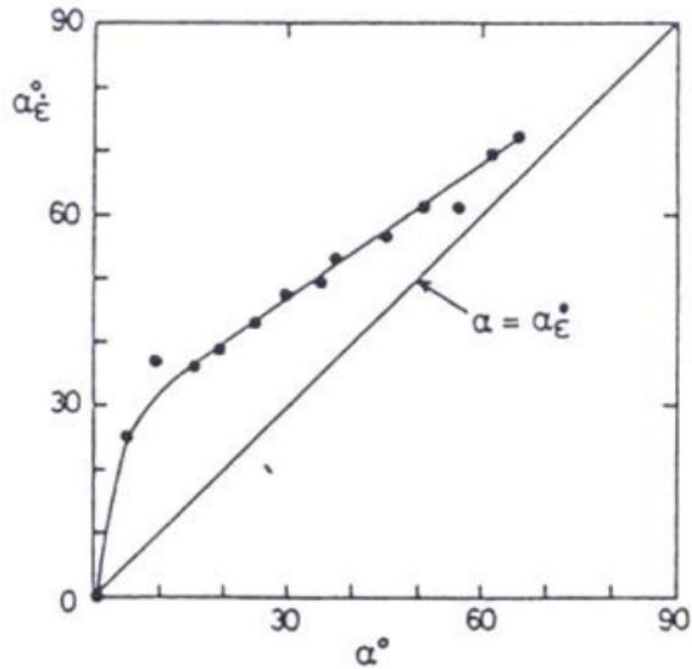
(b)    pure rotation of principal stress with constant $q$ of 110kPa

**Figure 2-5. Results of drained tests: (a) monotonic loading tests with $\alpha$=45°**
**and 67.5°; (b) pure rotation of $\alpha$ at constant $q$=110 kPa (Symes et al.,**
**1982).**

Then Symes et al. (1984) investigated the effects of the PSR as well as the
anisotropy using the medium-loose Ham River sand again. They carried out a
series of undrained tests using the hollow cylinder apparatus with the
dimensions of 254 mm/203 mm/254 mm. Three tests with the fixed direction
of the major principal stress $\alpha$ of 0°, 24.5° and 45°were performed in total. The
mean normal pressure $p$ and the value of $b$ are maintained at 600 kPa and 0.5
respectively, with gradually increased deviator pressure $q$ until failure. When
the direction of the major principal stress equals to 0° and coincides with the
axis of the symmetry of the specimen, the directions of principal stress and

strain increment was coaxial. When $\alpha = 24.5°$ and $\alpha = 45°$, directions of the principal stress and principal strain increment were not coaxial, as shown in Figure 2-6. It can be seen that the maximum degree of non-coaxiality reaches as much as 20 degrees, and this non-coaxiality reduces as the stress approaches the failure state.
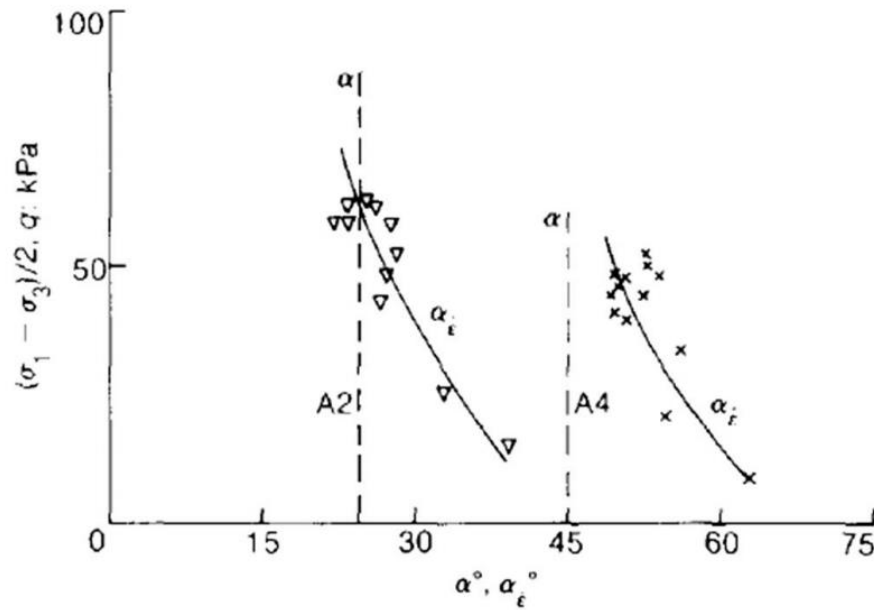


**Figure 2-6. Directions of principal strain increment in tests with $\alpha = 24.5°$ and $\alpha = 45°$ for undrained tests (Symes et al., 1984).**

The authors also conducted another investigation focusing on the effects of the PSR using drained saturated medium-loose sand (Symes et al., 1988). The same stress paths from their previous work in 1984 were applied to the specimen. Similar to the results from undrained tests, the results in Figure 2-7 also show the non-coaxiality between the directions of principal stresses and principal strain increments, and coaxiality was again observed when the

direction of major principal stress $\alpha = 0°$. For test with $\alpha = 24.5°$, the directions of principal stress and principal strain rate were coaxial at some point of the early stage. Generally, the degree of non-coaxiality still decreased with the increasing $q$ for the other two tests, and the largest deviation was still obtained about 20° at the beginning of test with $\alpha = 45°$.
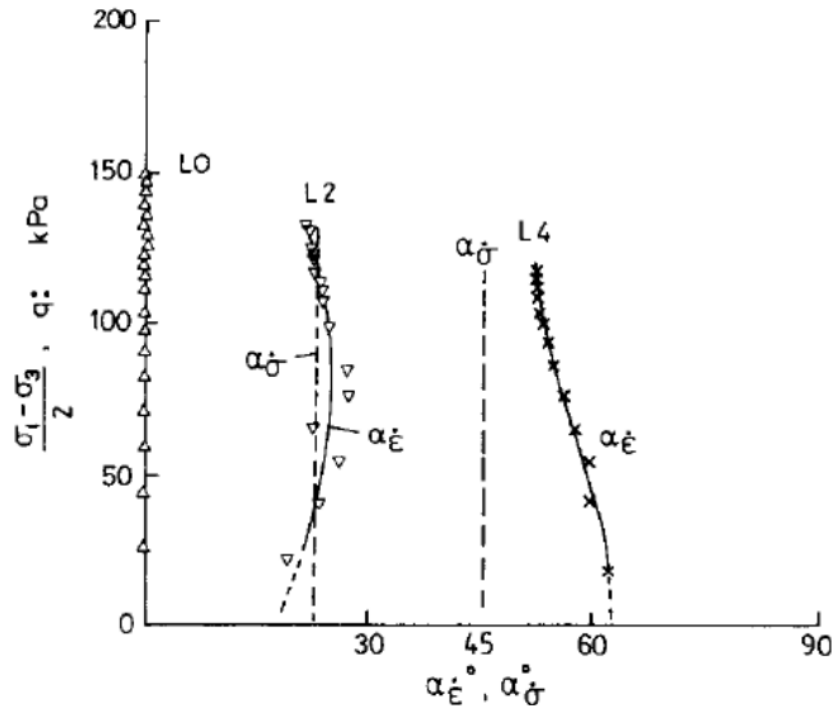


**Figure 2-7. Principal strain increment directions in tests with $\alpha$=24.5° and 45° for drained tests (Symes et al., 1988).**

Researchers from Japan have also paid enormous efforts to investigate the PSR behavior of granular materials using the hollow cylinder apparatus for a long time. Early in 1983, Ishihara & Towhata published the experimental results of the sand response under the cyclic rotation of principal stress directions. A hollow cylindrical specimen prepared using Toyoura sand with dimensions of

60 mm×100 mm×104 mm was subjected to the cyclic torsion. The result of strain increment vectors imposed on the stress space is presented in Figure 2-8. It can be seen that directions of strain increments did not coincide with the directions of current principal stresses or the stress increments. The deviation was large at the beginning of the cyclic rotation and reduced in the last stage.
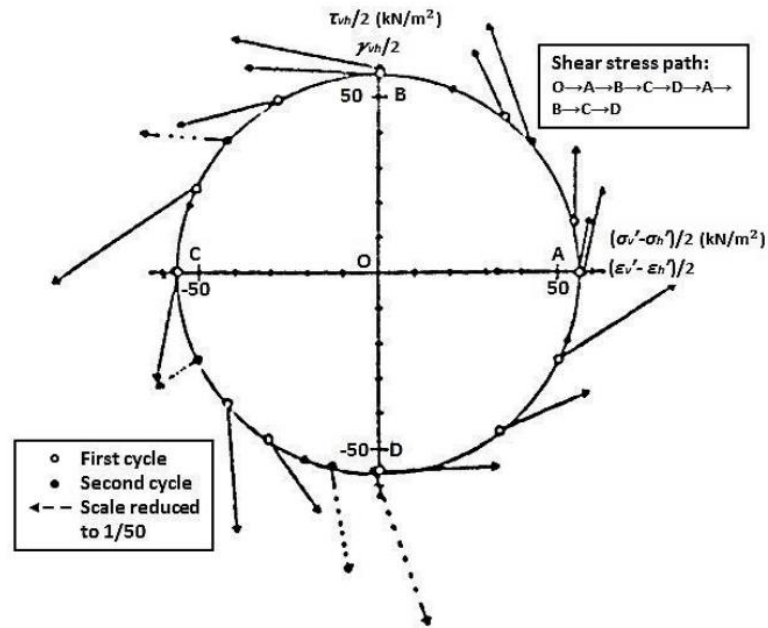


**Figure 2-8. Plot of strain increment vectors imposed on the stress space (Ishihara & Towhata, 1983).**

Miura et al. (1986) carried out a series of drained tests on dense Toyoura sand with an average relative density of 82% using the hollow cylinder apparatus to investigate the sand behavior under principal stress rotations. More general loadings involving the rotations of principal stress were applied to the specimens with the dimensions of 60 mm × 100 mm × 200 mm, prepared using the multiple sieving pluviation method.

The value of the effective confining pressure $p'$ and the intermediate principal stress ratio $b$ remained constant at 98 kPa and 0.5 respectively throughout the tests. Two types of drained loading paths were applied to the specimen in total. The first one was the monotonic shear test called the F test (Figure 2-9(a)). Monotonic loadings were applied with a fixed major principal stress direction $\alpha$ at 0°, 15°, 30°, 45°, 60°, 75° and 90° respect to the bedding plane. The second type is the pure PSR path called R test (Figure 2-9(b)), in which principal stresses rotated clockwise without changes of amplitudes. The R tests were performed at two different stress ratios and the major principal stress started to rotate at different initial angles. In the R1 test, the stress ratio of $(\sigma_1-\sigma_3)/(\sigma_1+\sigma_3)$ equals to 0.5 and started at an angle of 0°. In the R2 test, this stress ratio was held at 0.6 and started at an angle of 90°. Figure 2-10(a) plots the strain increment vectors from the F test. It can be seen that the directions of principal strain increment is slightly different from the directions of current principal stress. The maximum deviation of 7° was achieved towards the direction of $\alpha=45°$. When the shear stress equals to 0 (F 0° and F 180°), the directions of principal strain increments coincide with the principal stresses, which agrees with the results from Symes et al. (1984). Figure 2-10(b) and Figure 2-10(c) presents the directions of strain increments of the R test. The non-coaxial behavior can be clearly seen in these figures, and the larger the strains, the smaller the deviation between principal stress directions and principal strain incremental directions. Miura et al. (1986) concluded that in the R test, the directions of strain increments were between the directions of major principal stresses and principal stress increments.
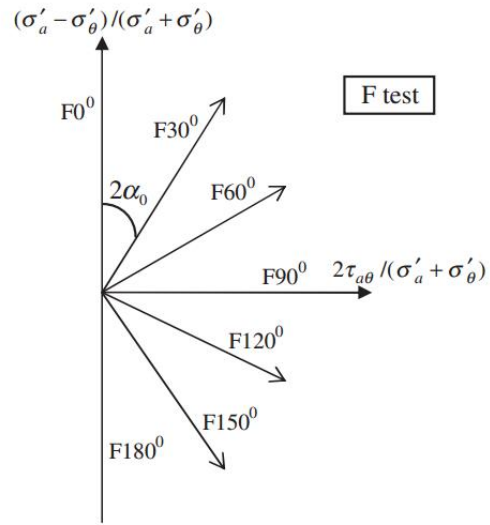
(a) Stress path of the monotonic loading (F tests)
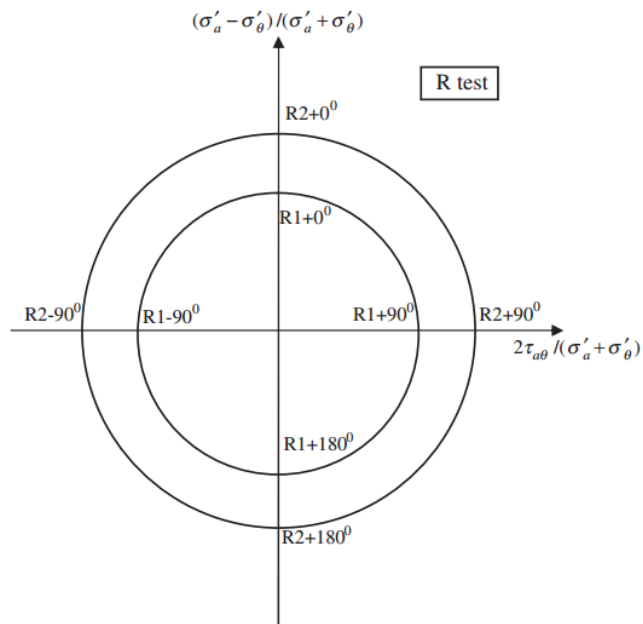


(b) Stress path of the pure principal stress rotational loading (R tests)

**Figure 2-9. Plot of the stress paths of F tests and R tests (Yang & Yu, 2013).**
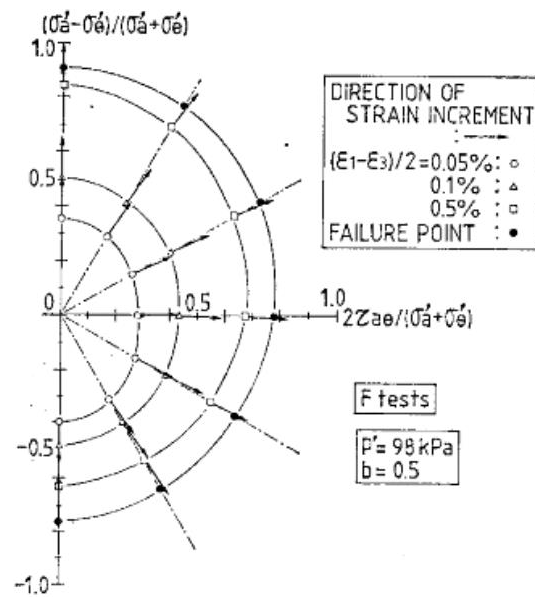
(a) Strain increment vectors under the monotonic loadings
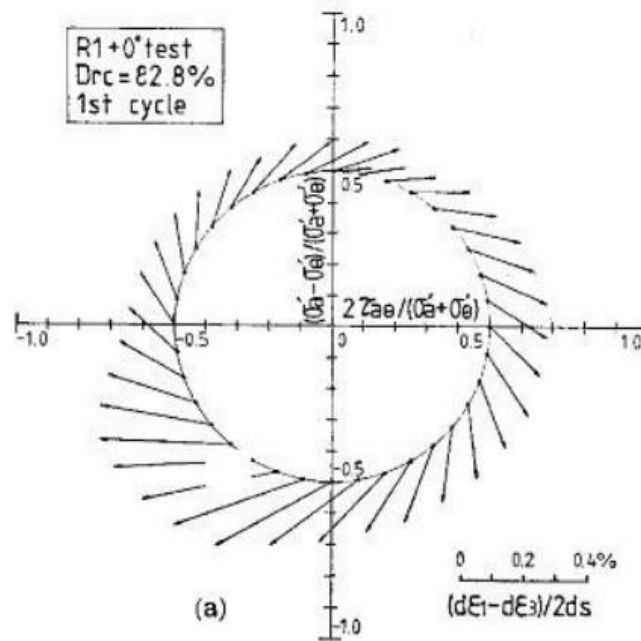


(b) Strain increment vectors under the principal stress rotations (R1+0°)
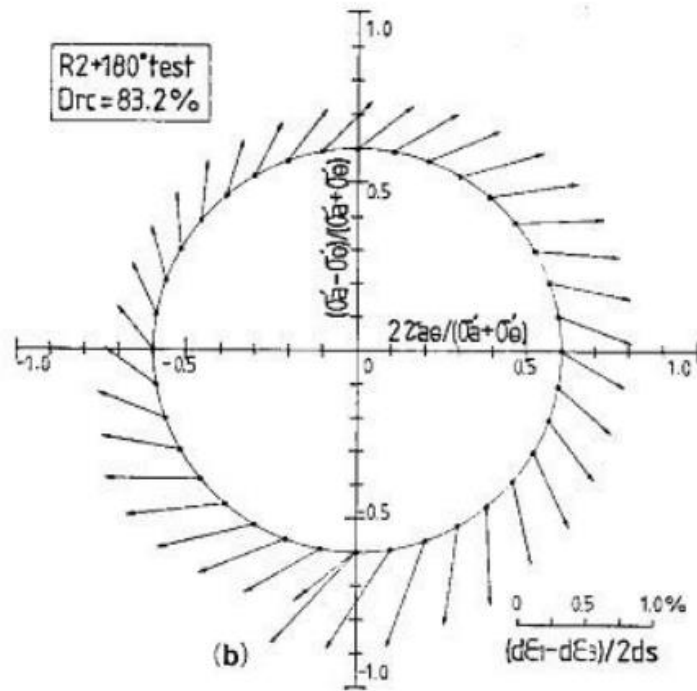
(c) Strain increment vectors under the principal stress rotations (R2+180°)

**Figure 2-10. Plot of the non-coincidence between principal strain increment directions and principal stress directions (Miura et al., 1986).**

Pradel et al. (1990) used the improved hollow cylinder apparatus to investigate the plastic flow of granular materials. This apparatus allows the independent control of the axial force, torque, inner cell pressure and outer cell pressure. The specimens of dense Toyoura sand with a relative density of $D_r = 70\%$ were subjected to the shear stress path firstly, and then the cyclic loading and unloading were applied with the small stress increments. They concluded from the results that the directions of principal plastic strain increment were highly related to the stress increment.

After that, Gutierrez et al. (1991, 1993) carried out a series of work to study the soil behavior under the PSR. In 1991, a plastic potential theory was proposed by them according to the experimental results from the hollow cylinder tests, which established the dependency of the plastic strain increment direction on the stress increment direction. Therefore, in this theory, the plastic flow of sand was represented based on the directions of the stress increment. Gutierrez et al. (1991) also carried out another experimental study in the same year to examine the non-coaxiality between the directions of principal stress and principal plastic strain increment. Specimens with the geometry of 100 mm in outer diameter, 60 mm in inner diameter, and 104 mm in height were subjected to three different stress paths including the monotonic loading tests at different fixed principal stress directions, pure rotation of principal stress directions at constant mobilized angles of friction of $\Phi = 20, 25, 30, 35, 40$ and $45°$, and combined loading paths involving simultaneous increase in shear stress and rotation of principal stress direction. Figure 2-11 shows the plastic strain increment vectors of the sand during these three tests. Generally, non-coaxial behavior can be seen in results from all the tests. In the result from the monotonic loading test shown in Figure 2-11(a), the plastic strain increment directions were deviated from the radial stress paths especially at low shear stress level, and these deviations reduced and may be neglected as the specimen approached the failure surface. The result also shows that the plastic strain increment takes much larger proportion in the total strain increment than the elastic strain increment. Figures 2-11(b) and 2-11(c) show the experimental results from the pure rotation loading and the combined loading tests. Compared to the monotonic loading test, the deviations between the principal stress direction and the principal plastic strain increment direction were more significant. The degree of non-coaxiality of plastic principal strain increment

directions and principal stress directions also reduced at higher shear stress levels.

Gutierrez et al. (1993) proposed an elastoplastic constitutive model to simulate the behavior of sand under the rotational shear on the basis of the experimental results from these three tests. Then, Gutierrez & Ishihara (2000) also published an analysis on the effects of non-coaxiality from the energy dissipation of sand according to the experimental results from the hollow cylindrical tests on sand conducted by Gutierrez et al. (1993).
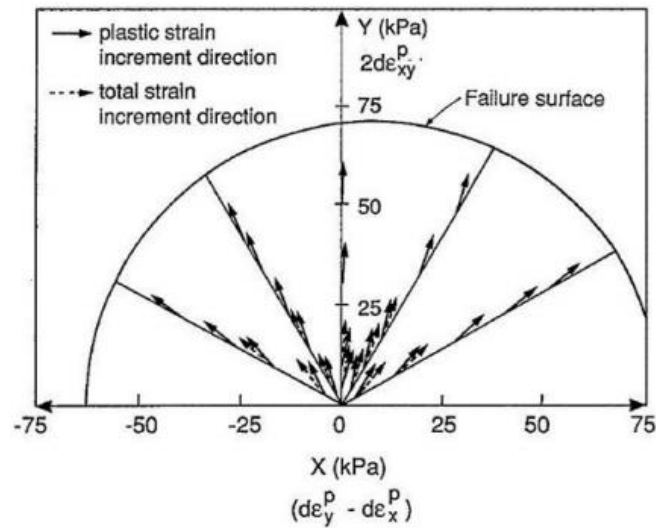


(a) Measured non-coaxiality in monotonic loading tests along different fixed principal stress directions.
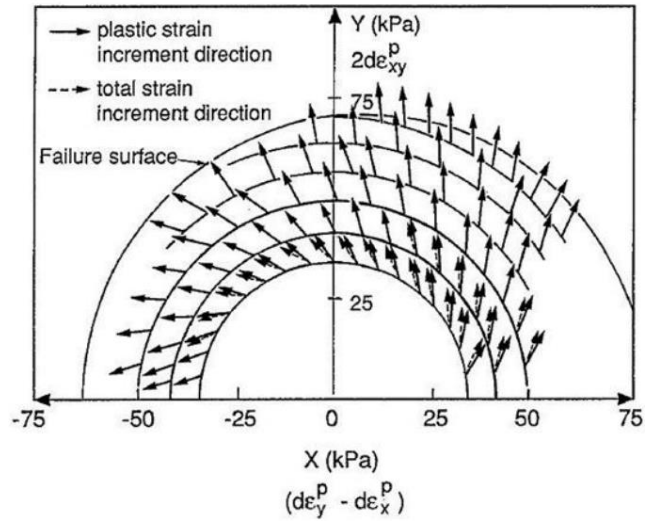
(b) Measured non-coaxiality in pure principal stress rotation tests at different levels of mobilized friction angle.
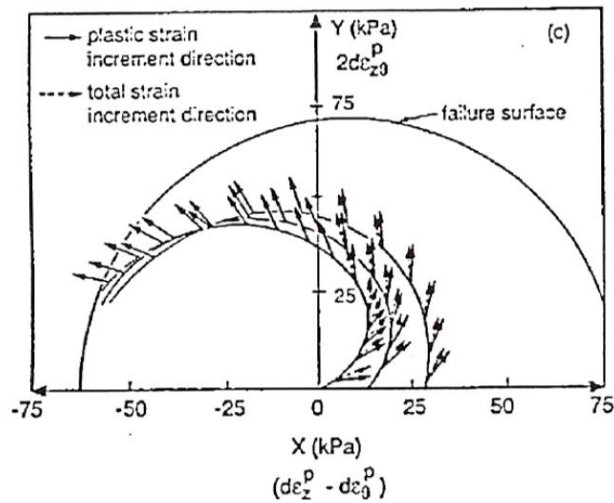


(c) Measured non-coaxiality in combined loading tests.

**Figure 2-11. Unit plastic strain increment vectors superimposed on the stress path for: (a) monotonic loading, (b) pure rotation and (c) combined loading (Gutierrez et al., 1991).**

Recently, Lade et al. (2009) carried out a series of tests using the hollow cylinder apparatus on the Santa Monica Beach sand specimen with the geometry of 22 cm × 18 cm × 40/25 cm. The directions of the principal stress and the principal strain increment are plotted in Figure 2-12. Similarly, Non-coaxiality was observed and the directions of principal stresses and principal strain increments were coincident at the failure state.
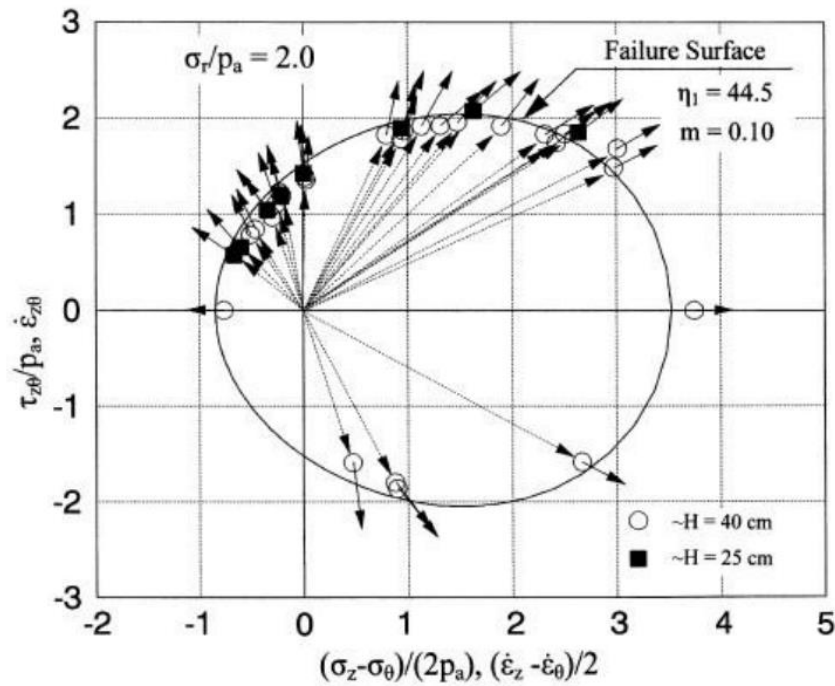


**Figure 2-12. Comparison of directions of principal stress with directions of principal plastic strain increments at failure during rotation of principal stresses in torsion shear tests on Santa Monica Beach sand (Lade et al., 2009).**

In conclusion, in these experimental tests including the simple shear test, directional shear test, hollow cylinder test, etc., various types of soil were subjected to the monotonic shearing at a fixed principal stress direction, the

pure principal stress rotation at constant deviatoric stress, or the combined loading paths. Researchers found that the deviation between the directions of principal stress and principal strain increment can be observed in the test results and this non-coaxiality decreases as the stress ratio increases and the specimen approaches the failure state. Moreover, the deviation between the principal stress direction and the principal strain incremental direction varies in the different tests and could be more than 30 degrees during the continuous rotation of the principal stress directions.

## 2.2.3 Previous numerical studies on the PSR and non-coaxiality

Apart from the experimental studies, researchers have been paying enormous efforts to numerically explore and model the non-coaxial and PSR behavior of soil. As the discrete element method (DEM) can be a useful tool to study the soil behavior, many investigations have been carried out using this method. For example, Thornton and Zhang (2006) investigated the shear banding and simple shear non-coaxial flow rules by a series of two dimensional numerical simulations. The simulation results of 5000 elastic spheres with seven different sizes using DEM are presented in Figure 2-13. They found from the results that the axis of principal stress and principal strain rate becomes coaxial as the specimens approaching the critical state, which agrees with the conclusion from Roscoe's research (Roscoe, 1970).
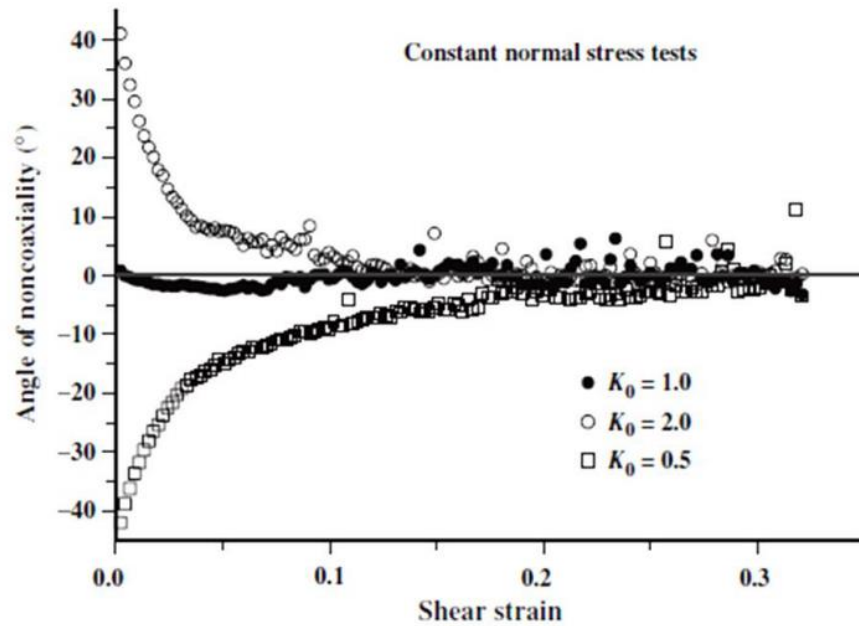
**Figure 2-13. Evolutions of the angle of non-coaxiality (Thornton & Zhang, 2006).**

Li and Yu (2009) carried out a two dimensional DEM simulation to model the anisotropy effect and the non-coaxial behavior of the granular material under the monotonic loading at fixed strain incremental directions. In their simulations, a specimen was prepared using a controlled deposition method to investigate the initial anisotropy generated during specimen preparation. Another specimen made of two equal sized clumps was first deposited and prepared by preloading the initial anisotropic specimen in the vertical direction and then unloading it to an isotropic stress state. The specimens were then sheared in a number of fixed principal strain incremental directions varying from vertical ($\alpha = 90°$) to horizontal ($\alpha = 0°$) at 15° intervals. Figure 2-14 presents the measured non-coaxiality of the directions of principal strain

increments and principal stresses versus the stress ratio for these two specimens. The experimental results of the first sample in Figure 2-14(a) show very limited deviations between the angles of principal stress directions and the principal strain increment directions. Because the greatest value observed was under 5°, the soil behavior could be approximately considered as coaxial in this case, which agrees well with the conclusions of Miura et al. (1986) and Gutierrez et al. (1991). In Figure 2-14(b), greater deviations between the directions of principal stress and principal strain increment were observed. This non-coaxiality was observed to be especially large when the loading direction was close to the normal direction of the preloading. However, the sand behaves almost coaxial when the reloading direction of major principal stress coincides with or perpendicular to the direction of previous loading. Moreover, this research also reveals that the deviation between directions of principal stress and principal strain increment reduces gradually as the shear strain and the stress ratio increases.
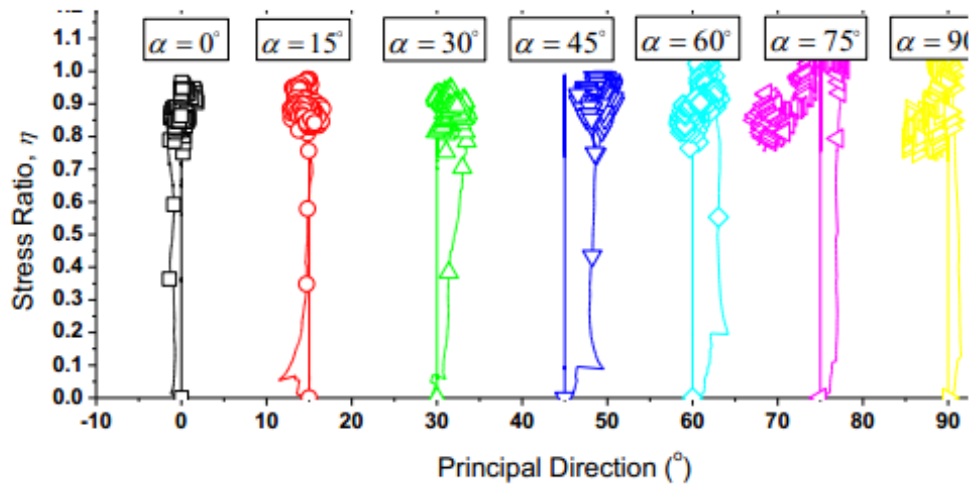


(a)    Initially anisotropic specimen
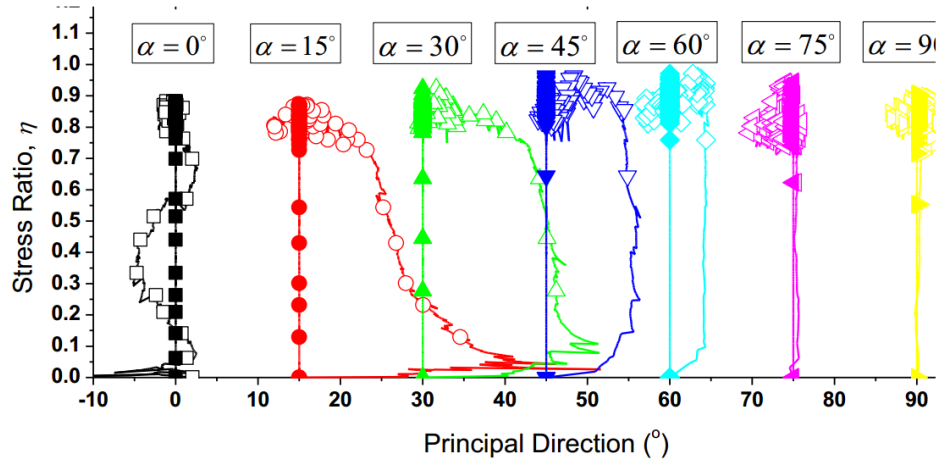
(b)    Preloaded specimens

**Figure 2-14. Measured stress and strain increment directions for: (a) initially anisotropic specimens; (b) preloaded specimens (Li & Yu, 2009).**

Li and Yu (2009) also carried out an analysis of the microscopic information characterized by principal directions of contact normal and contact force in the same year to investigate the underlying mechanisms of non-coaxiality. The results in Figure 2-15(a) show that the principal directions of contact force were almost coaxial with the loading direction throughout the loading stage. The principal directions of contact normal are presented in Figure 2-15(b). It can be seen from the figure that the principal directions of contact normal were coaxial with the direction of deposition when the tests started. Then generally the principal directions of contact normal gradually rotated and finally they were more or less coincident with the loading direction at large strain states except for the case with the loading directions $\alpha = 0°$ and 90°. For the test with the loading direction perpendicular to the preloading direction ($\alpha = 0°$), the direction of contact normal suddenly reached the coaxial state with the loading direction at the early stage of test. In the test with the loading direction parallel

to the pre-loading direction ($\alpha = 90°$), there was no deviation between the principal direction of contact normal and loading direction throughout the test. Oda et al. (1985) observed similar behaviors from their experimental research on two-dimensional assemblies of photoelastic rods. Therefore, Li and Yu (2009) concluded that as principal directions of contact force is almost coincident with the loading directions, non-coaxiality is mainly induced by the deviations between the principal directions of contact normal and the loading directions.
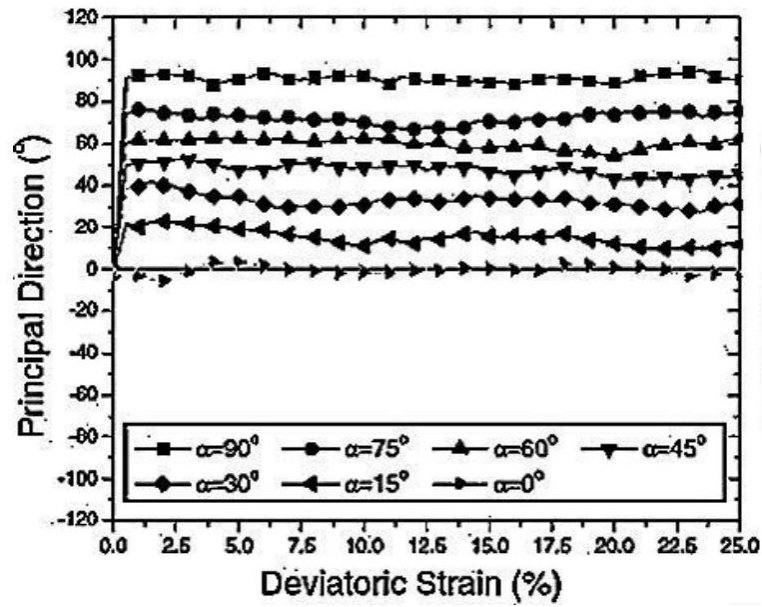


(a) Principal directions of contact force
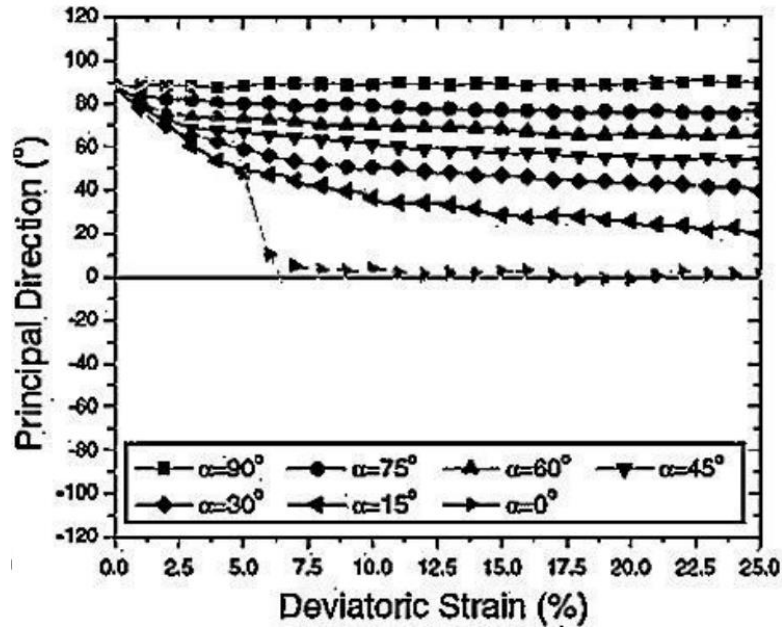
(b) Principal directions of contact normal

**Figure 2-15. Principal directions of: (a) contact force and (b) contact normal (Li & Yu, 2009).**

Apart from the DEM method, the finite element method (FEM) is also an effective tool to explore the soil behavior and has been widely used in many numerical studies for the PSR. For instance, Sassa & Sekiguchi (2001) carried out a series of numerical simulations including the finite element analysis of centrifuge wave tank tests. Three sets of stress paths for individual elements were firstly simulated to validate a constitutive soil model considering the PSR effect. The stress path and predicted results of the second set of simulation are presented in Figure 2-16. It can be seen from the figure that the undrained rotation of the principal axis can lead to the reduction of mean effective stress. The results from the third simulation with the undrained rotational shear stress also demonstrate that the contractive soil behavior along with the development

of shear strain can be induced by the PSR (Figure 2-17). Then this model was implemented into the finite element analysis of boundary value problems under the progressive wave and the standing wave loadings. They proposed the definition of cyclic stress ratio $\chi_0 = \kappa u_0/Y'$ to reflect the intensity of the wave loadings, where $\kappa$ is the wave number, $u_0$ *is the* amplitude of the fluid pressure fluctuation imposed on the soil surface and $Y'$ is the saturated unit weight of soil. They found that a greater build-up of the excess pore pressure $u$ can be observed under the progressive wave loading. Therefore, the soil bed was less resistant to the progressive wave than the standing wave due to the more significant PSR effect induced by the progressive wave (Figure 2-18). They also verified the value of critical cyclic stress ratio $\chi_{cr}$. This value represents the critical intensity of wave loadings above which liquefaction will occur in the centrifuge model test.
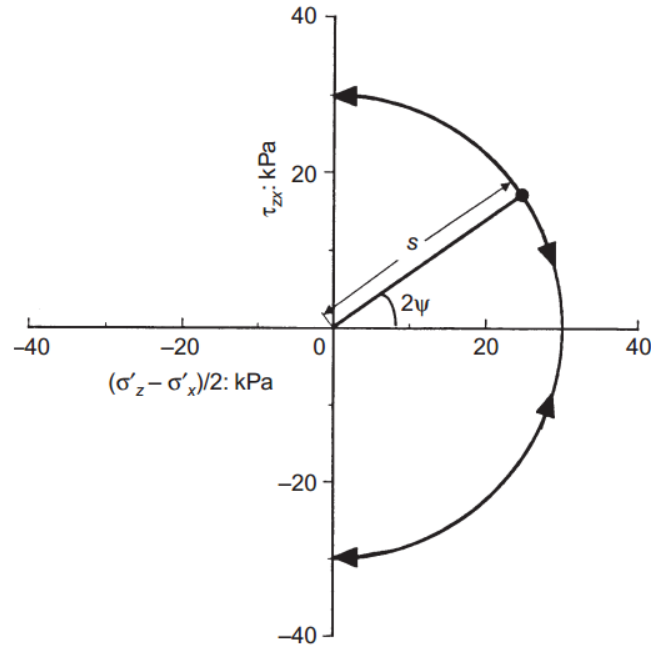


(a)
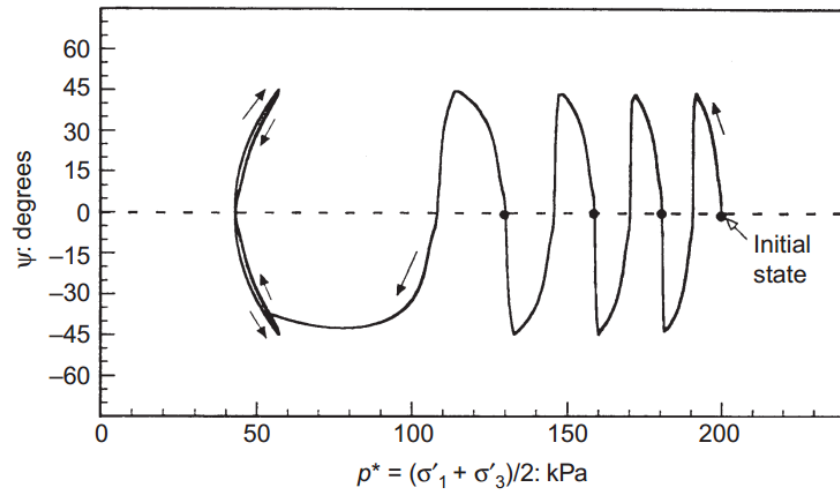
(b)

**Figure 2-16. The stress path of undrained cyclic rotation of principal stress axis (a) and the predicted decrease of the mean effective stress (b) from simulation 2 (Sassa & Sekiguchi, 2001).**
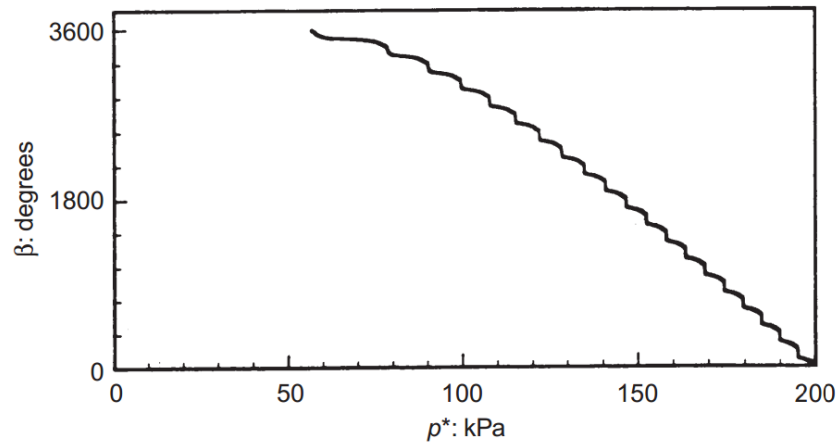


(a)
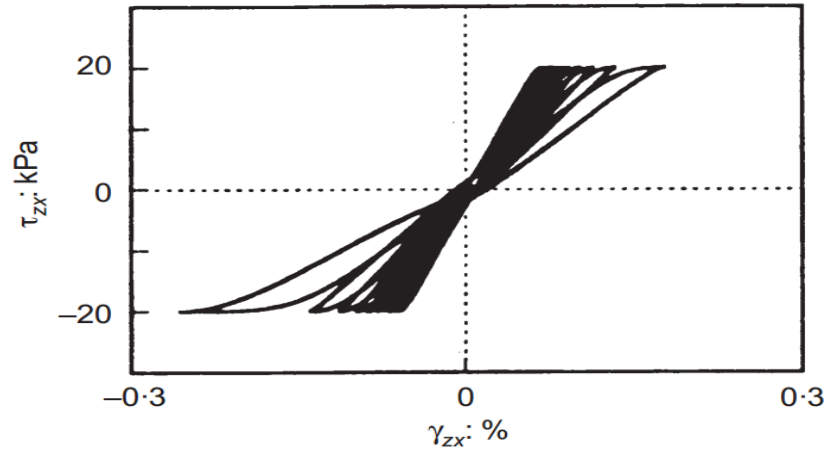
(b)

**Figure 2-17. Predicted soil responses for undrained rotational shear from simulation 3 (Sassa & Sekiguchi, 2001).**
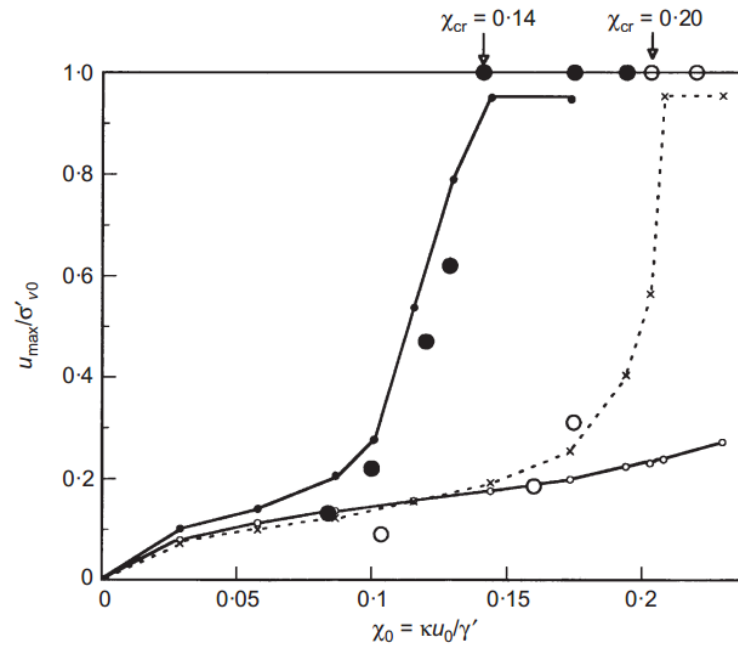


**Figure 2-18. Comparison of predicted and measured relationships of $u_{max}$ /$\sigma_{v0}$ to $\chi_0$ at shallow depth (Sassa & Sekiguchi, 2001).**

In order to implement the elastoplastic constitutive models in the FEM, it is essential to integrate the non-linear stress-strain responses over a given strain increment, thus obtaining the stresses at the end of a known displacement increment. Therefore, an effective numerical integration scheme is required to ensure the convergency and the efficiency of the numerical computations. Generally, there are two types of integration algorithms (Neto, 2008). The explicit integration scheme has been widely used to integrate the nonlinear stress-strain relationships, while the implicit integration scheme has also becoming increasingly popular recently. An explicit Euler scheme modified by Abbo (1997) to incorporate several refinements is used in this research. The comparative studies between the explicit and implicit integration schemes from Abbo (1997) show that this modified explicit algorithm provides the desirable error control and automatic sub-stepping, thus ensuring the efficiency and robustness during the finite element computations.

Numerical simulations of the non-coaxial and PSR behavior have also been attempted by the development of varies models with different theories. Non-coaxiality can be originally found in several pre-failure plasticity models for granular materials, such as hypoplastic models (Wang et al., 1990; Kolymbas, 1991) and multi-laminate models (Iai et al., 1992). Based on the conventional plasticity theory, Rudnicki and Rice (1975) also proposed the yield vertex theory to study the shear banding and strain localizations of granular materials. Besides the traditional plastic hardening modules simulating the stress increment orthogonal to the yield surface, they introduced a second hardening parameter to simulate the response of the stress increment directed tangentially to the yield surface (shown in Figure 2-19). Models developed based on the yield vertex theory shares a common feature that the

elastoplastic stiffness matrix is independent of stress increments, thus allowing the easy numerical implementations in the geotechnical problems. They concluded that the PSR and non-coaxiality plays an important role in shear band formations in sand.
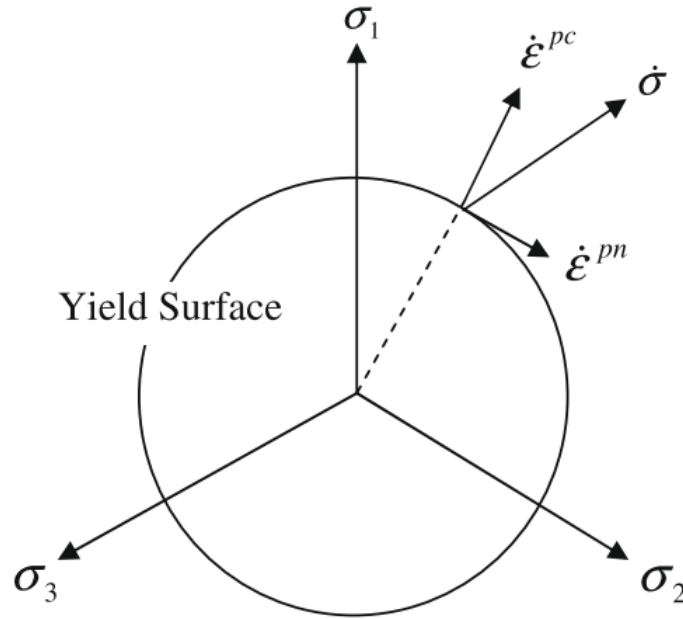


**Figure 2-19. Schematic illustration of coaxial and non-coaxial plastic strain rates on a yield surface in deviatoric plane (Yang & Yu, 2006).**

Non-coaxiality has also been a feature of a number of kinematic plasticity theories for granular materials. In 1958, Jong proposed the earliest kinematic models for granular material flow with graphical methods. These flow rules were based on the assumption of shear flow occurring along two surfaces where the available shear resistance had been exhausted. Then, Spencer (1964) developed the double shearing model using the same concept of double sliding but different rotation term from the model of Jong (1958). Mandel and Fernandez (1970) proposed a similar model and conducted further analysis for

the double sliding model to investigate the non-coaxiality between principal stress directions and principal strain increment directions.

In 1989, the formation of localized shear bands was simulated by using a non-coaxial cam-clay model developed by Yatomi et al. (1989). After that, several models were proposed based on the hypoplasticity theory (Wang et al., 1990; Kolymbas, 1991; Tejchman, 2009). In 1993, Gutierrez et al. proposed an elastoplastic kinematic hardening model based on experimental studies. It can consider the rotational loading and the volumetric strain induced by the PSR, thus simulating the PSR behaviors under cyclic loadings and the liquefactions of undrained sands. Moreover, in their model, the plastic principal strain increment direction was defined based on the effects of fabric anisotropy on non-coaxiality. However, its numerical implementations can be more complicated because its elastoplastic stiffness matrix is a function of the stress increment, thus leading to the nonlinear relationship between the stresses and strain increments.

Recently, more models were developed by researchers, such as the multi-mechanism model (Fang, 2003), extended platform model (Li &Dafalias, 2004), double shearing models (Yu & Yuan, 2005), microplane model (Chang &Sture, 2006), and so on. Nottingham Centre of Geomechanics (NCG) has also produced valuable work focusing on the PSR and non-coaxiality of granular materials. For example, Yu et al. (2005) and Yang and Yu (2006) employed the yield vertex non-coaxial theory by Rudnicki and Rice (1975) to explore the influences of the non-coaxial soil models on the stress-strain responses of soils. In their studies, the non-coaxial models was numerically integrated and implemented into the finite element software ABAQUS to

simulate the behaviors of shallow foundations under various initial conditions and loading conditions. Results from these simulations indicated that the coaxial models usually underestimate the soil deformations compared to the non-coaxial models when the soil is subjected to the PSR. Therefore, they argued that ignoring the PSR effects will under-predict deformations of the geotechnical structures for a given applied load, thus leading to an unsafe design in practice.

In 2013, Yang & Yu carried out a series of numerical simulations to explore the impact of PSR by using an elastoplastic model considering the PSR effect developed based on a kinematic hardening model with bounding surface concept. It includes the features of critical state concept, phase transformation line, back stress ratio and state parameter. This new model (PSR model) is also adopted in this research to investigate soil behaviors under the PSR and will be introduced in detail in Chapter 4. The basic concepts employed in this model are introduced here.

Critical state soil mechanics (Schofield & Wroth, 1968; Wood, 1990) provides the basic theoretical framework for this model. When the stress ratio $q/p$ equals the critical state stress ratio $M=q_c/p_c$, and simultaneously the void ratio $e$ equals the critical void ratio $e_c$, the soil is considered to deform continuously in shear with zero volumetric strain rate. The linear relationship between $e_c$ and $ln\ p_c$ is commonly used but in this research, the relation proposed by Li & Wang (1998) is adopted as follows:

$$e_c = e_0 - \lambda_c(p_c/p_{at})\ \ \xi \qquad\qquad (2.1)$$

where $e_0$ is the void ratio when $p_c=0$ , $\lambda_c$ and $\xi$ are constants. Then, the state

parameter $\Psi=e-e_c$ from Been & Jefferies (1985) is introduced to represent sands in different densities with one set of model constants. This model also adopts the phase transformation line to define the state when the soil transform from the contractive behavior to dilatant behavior (Ishihara et al., 1975). This concept is also known as the dilatancy stress ratio.

They firstly simulated stress-strain responses in the experimental drained tests of Toyoura sand under several typical loading conditions (Miura et al., 1986; Gutierrez et al., 1991). Stress paths of the F test and R test have been introduced in the last section. Figure 2-20 compares the test results and predicted results for the F tests. These simulations are intended to fit the average of the experimental results along different loading directions because the modified PSR model does not include the role of fabric change. It can be seen that the predicted results generally agree well with the test results and these monotonic loading tests are also simulated to calibrate the model parameters.
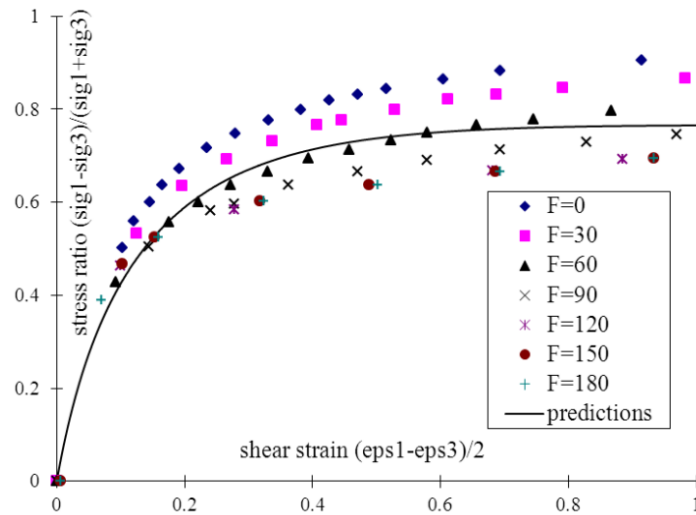


(a) Relationships between the stress ratio and the shear strain
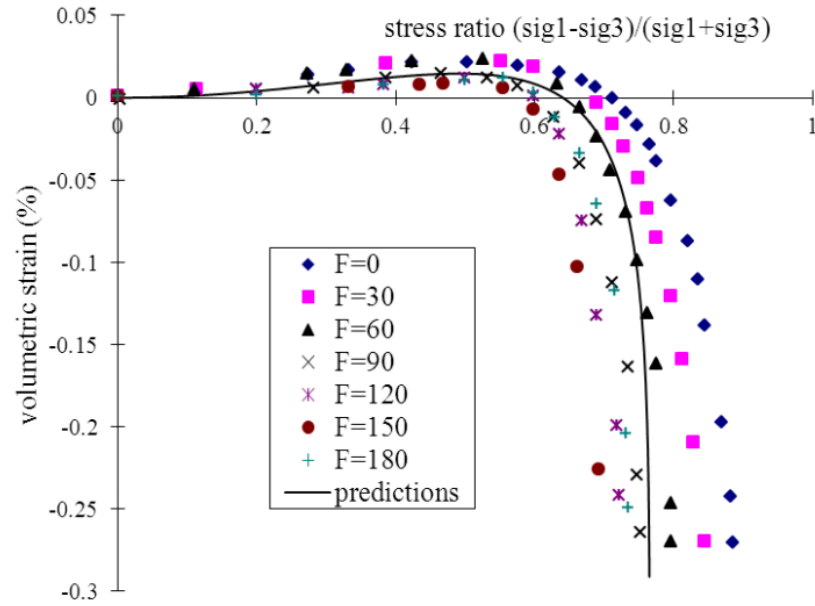
(b) Relationships between the volumetric strain and the stress ratio

**Figure 2-20. Comparisons between the test results and model predictions of the monotonic loadings in Miura et al. (1986) for Toyoura sand (F denotes the angle of loading) (Yang & Yu, 2013).**

Figure 2-21 and 2-22 show the evolutions of different strain components with rotational angles of principal stress from experimental results and numerical predictions for the PSR path R1 and R2. Figure 2-21 shows the reasonably good agreement between the test results and predictions from the original base model in the PSR path R1, except for the radial strain. However, in Figure 2-22, the discrepancy between the predicted and measured results from the original base model is much larger in R2 than in R1 especially for the shear strain and volumetric strain. The predicted results from the modified PSR model in these two figures indicate that the modified PSR model performed overall better than the original predictions, especially for the shear and volumetric strains.
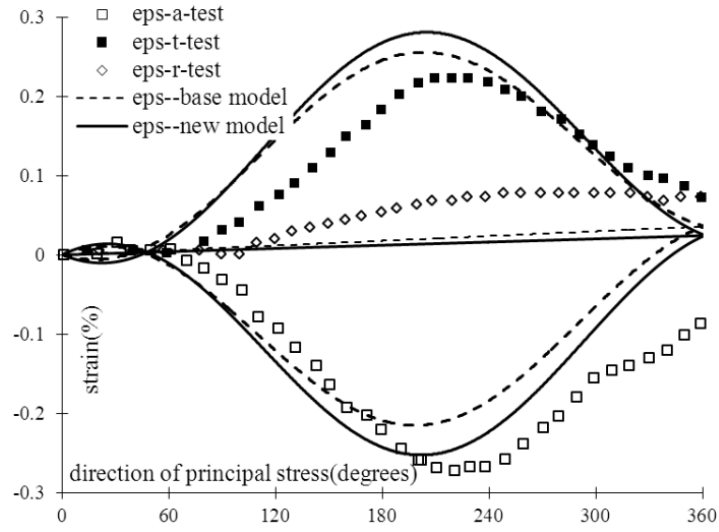
(a) Axial strain, circumferential strain and radial strain
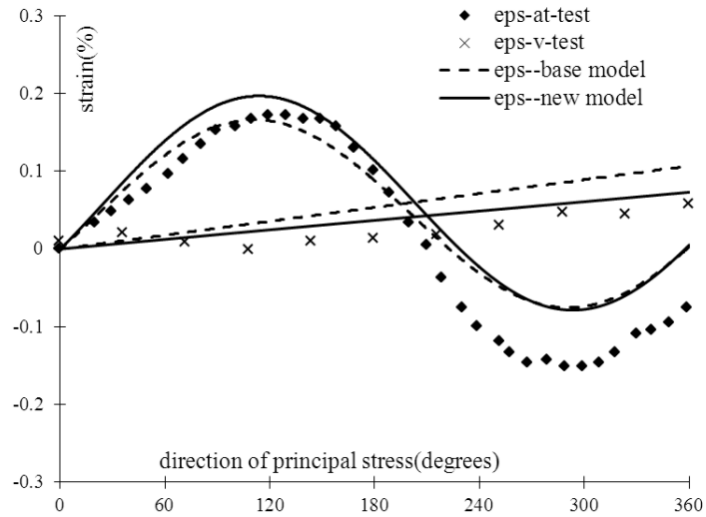


(b) Shear strain and volumetric strain.

**Figure 2-21. Test results and predictions of PSR loadings R1 in Miura et al (1986) with the original base model and the PSR model (eps-a: axial strain; eps-t: circumferential strain; eps-r: radial strain; eps-at: shear strain; eps-v: volumetric strain) (Yang & Yu, 2013).**
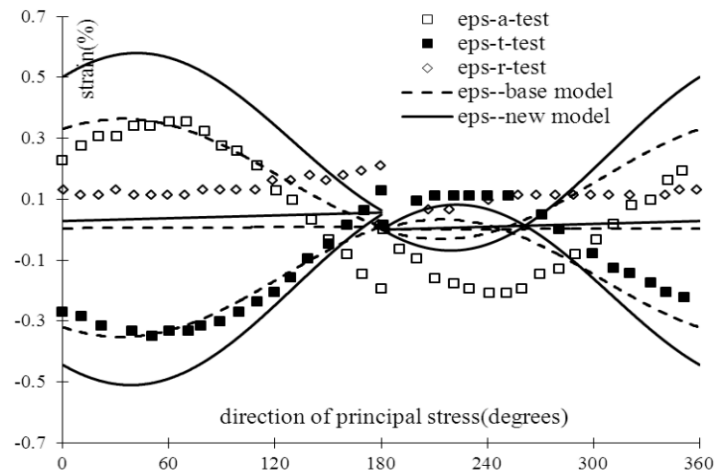
(a) Axial strain, circumferential strain and radial strain
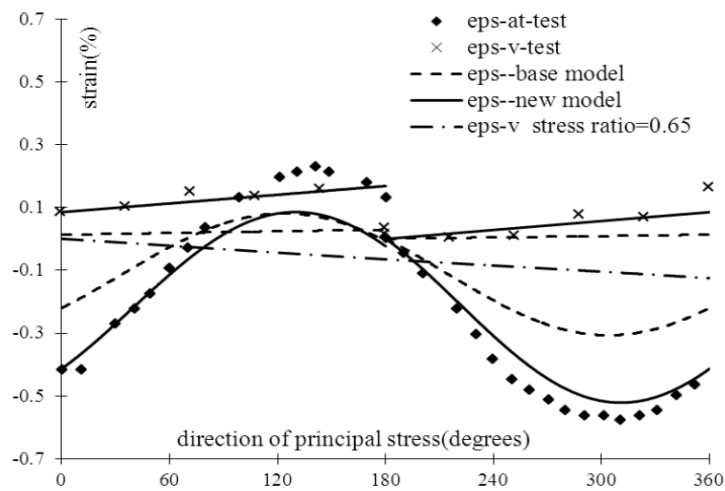


(b) Shear strain and volumetric strain.

**Figure 2-22. Test results and predictions of PSR loadings R2 in Miura et al (1986) and the volumetric strain for the additional stress ratio (0.65) with the original base model and the PSR model (eps-a: axial strain; eps-t: circumferential strain; eps-r: radial strain; eps-at: shear strain; eps-v: volumetric strain) (Yang & Yu, 2013).**

The authors also numerically studied the model performances with two PSRs along different directions by simulating the tests by Miura et al. (1986). In this test, $\sigma_x$ was increased to 196 kPa under the drained condition with the initial isotropic confining pressure of 98 kPa. The major cyclic shear stress $\tau_{xy}$ of the constant value of 10 kPa was then applied under undrained conditions. After one quarter of a cycle later than $\tau_{xy}$, $\tau_{xz}$ was applied with three different amplitudes of 0, 5 and 10 kPa, giving the ratio of shear amplitudes of 1:0, 2:1, 1:1, respectively. The predicted results of pore water pressures and axial strains from the modified PSR model and original model are shown in Figure 2-23. It can be seen from the figure that the modified PSR model generated much higher pore water pressures than the original model and resulted in the sudden increase of strains. Therefore, the liquefaction took place in all the cases by using the modified PSR model while the liquefaction didn't occur in the predictions by using the original model. This agrees with the observations before that the original model predicts a smaller plastic volumetric contraction (or even volumetric expansion) at a higher stress ratio under the PSR. They finally concluded that the PSR plays an important role in the soil behaviors and this PSR model is capable to reproduce the PSR induced soil behaviors. Furthermore, this simulation also reveals that multiple PSRs make soil reach liquefaction faster than one PSR.
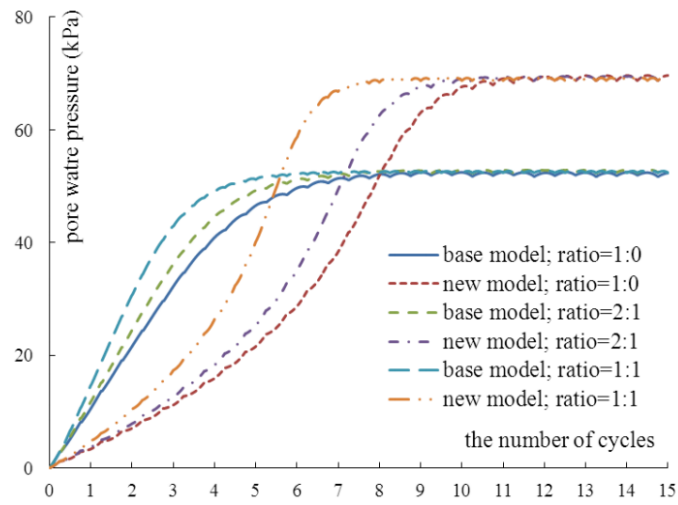
(a) Predicted results of pore water pressures
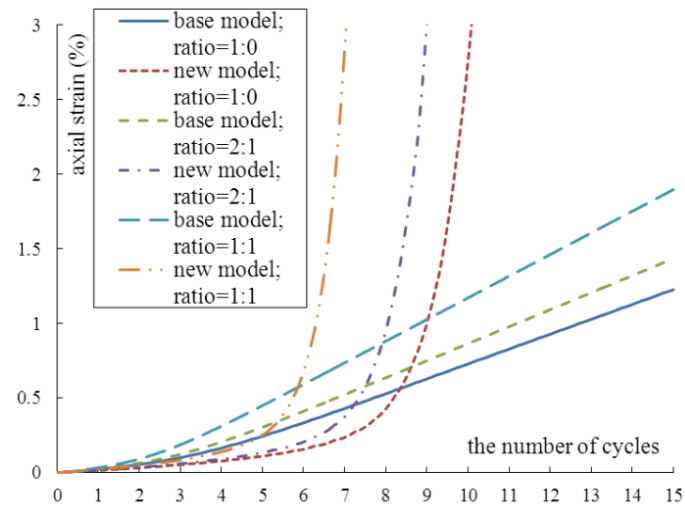


(b) Predicted results of axial strains

**Figure 2-23. Predicted pore water pressure and axial strain with different ratios of shear amplitudes in two PSRs from the original base model and PSR model (Yang & Yu, 2013).**

## 2.3 Experimental Tests and Problems Investigated in this Research

### 2.3.1 Experimental tests for single element simulations

Before the finite element simulations, the modified PSR model is first implemented into the single element simulations of 3 sets of experimental tests by using a single element computer program. The experimental tests simulated are introduced here.

Firstly, a series of monotonic loading tests with different loading directions ($\alpha$ = $0^o$ to $90^o$) and drained pure rotational shear tests with different stress ratios (Yang, 2013) are simulated. These tests were conducted in NCG at the University of Nottingham using the hollow cylinder test apparatus with Leighton Buzzard Sand (Fraction B). Details of the material and these tests can be found in Yang (2013).The stress paths of these test are illustrated in Figure 2-24 and Figure 2-25 in the space of $\sigma_{13}$ and $\sigma_1$-$\sigma_3$ (PSR space) because the pure rotation of principal stress can be presented clearly in this space.
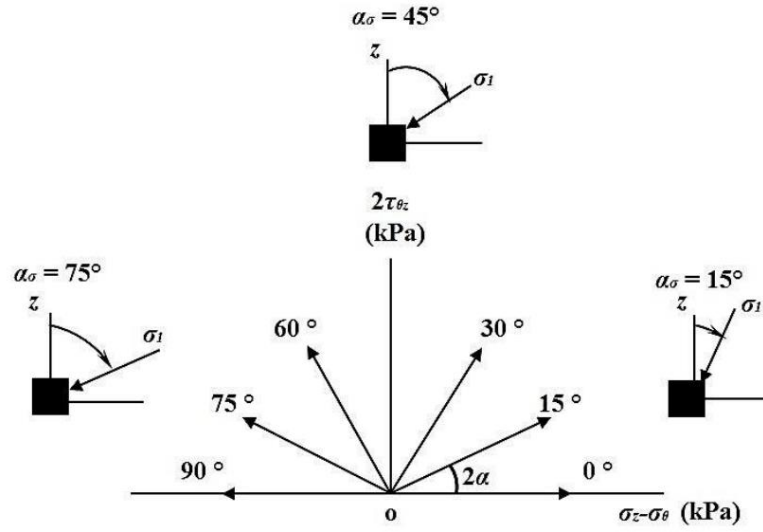
**Figure 2-24. Stress paths of monotonic loading in the PSR space (Yang, 2013).**
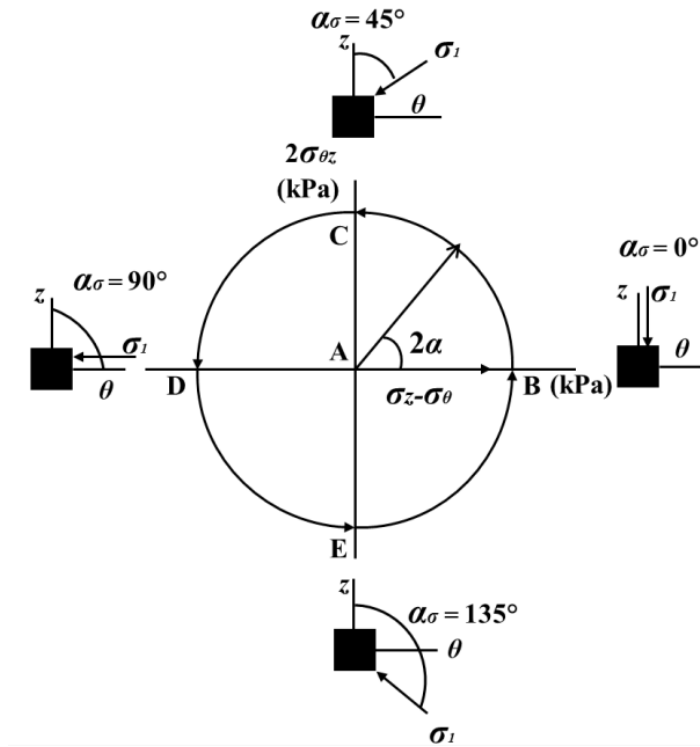


**Figure 2-25. Stress paths of pure rotational loading in the PSR space (Yang, 2013).**
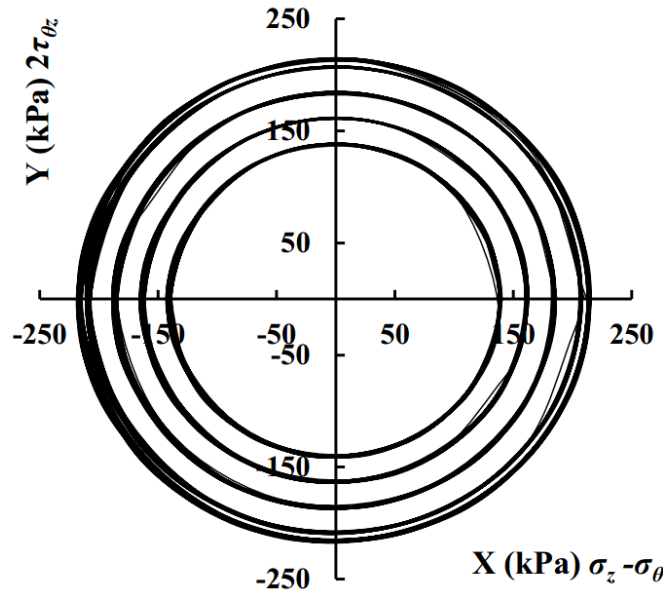
**Figure 2-26. Actual stress paths of pure rotational loading with different stress ratios in the PSR space (Yang, 2013).**

In these tests, specimens were firstly consolidated isotropically to an effective mean pressure $p'$ of 200 kPa. Then, the effective mean stress $p'$ and the intermediate principal stress parameter $b$ were maintained at 200 kPa and 0.5, respectively. In drained pure rotational tests, the major principal stress direction was rotated at a slow rate of 2 degree/min to ensure the full drainage.

Secondly, a series of drained triaxial tests using loose Leighton Buzzard sand (Fraction E) from Visone (2008) are simulated. After the isotropic compressions, the tests were conducted by increasing or decreasing the axial stress with constant effective confining stress $p'$ of 100 kPa and 200 kPa.

Thirdly, a series of triaxial, tosional and rotational tests for Nevada sand from Chen & Kutter (2009) are simulated. The stress paths of the undrained tosional and rotational tests are illustrated in Figure 2-27.
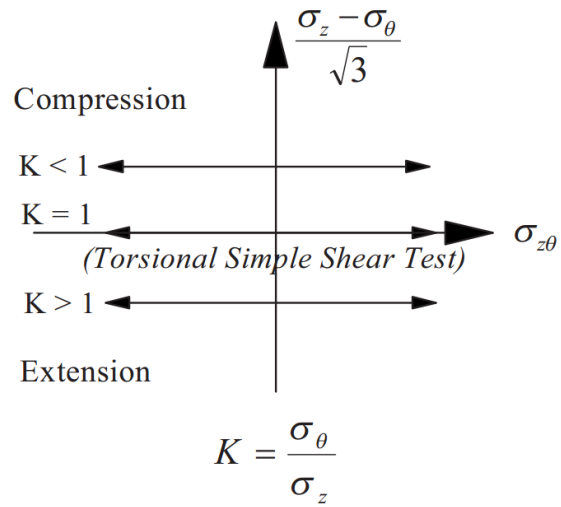
(a) Torsional shear tests
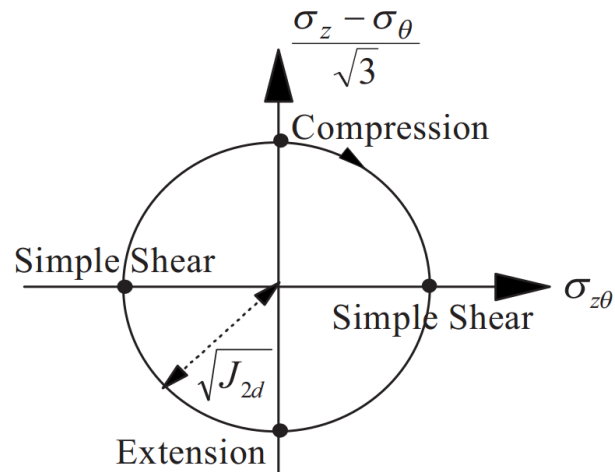


$$\sqrt{J_{2d}} = \sqrt{\frac{(\sigma_z - \sigma_\theta)^2 + 3\sigma_{z\theta}^2}{3}} = \text{constant}$$

(b) Rotational shear tests

**Figure 2-27. Stress paths of undrained torsional shear tests (a) and undrained rotational shear tests (b) (Chen & Kutter, 2009).**

The triaxial tests began with the isotropic initial condition. The mean confining pressure $p$ was held constant during the shearing step of all the triaxial and hollow cylinder tests. In the undrained torsional shear tests, the axial loading was applied on the isotropically consolidated sample until $K = \sigma_\theta/\sigma_z$ reached the desired value. The specimen was then subject to the cyclic shear stress. In the undrained rotational shear tests, the axial loading was also applied to the isotropically consolidated specimen before the rotational stress path in Figure 2-27 was performed.

## 2.3.2 The background and previous research works on wave-seabed interactions

Study of wave-seabed interaction is essential to offshore developments. There are a few characteristics on loading conditions on seabed soil, and one of them is that the soil is subjected to considerable PSR. In 1983, Ishihara & Towhata first proposed that the PSR can generate plastic deformations and the non-coaxiality even without a change of principal stress magnitudes. Continuous PSR can also generate excess pore water and cumulative shear strain in undrained condition. Similar phenomenon is also found by Ishihara & Yamazaki (1984), Bhatia et al. (1985), Miura et al. (1986), Gutierrez et al. (1991), etc. Therefore, the PSR induced by the wave loading can accelerate undrained soil liquefaction because it can cause cumulative plastic volumetric deformations. Due to the significance of the PSR in seabed soil, numerous experimental studies have been carried out. For instance, Nago & Maeno (1987) and Zen et al. (1990) investigated the behavior of cohesionless sediments subjected to oscillatory pore pressure with large scale model in 1g condition. Sassa & Sekiguchi (1999) also carried out a series of centrifuge wave tests on

seabed with fine-grained sand. They found that in the tests, the soil behaviors are largely affected by the PSR under the progressive wave loading. They also proposed the concept of critical cyclic stress ratio $\chi_{cr}$, below which the liquefaction will not occur.

Although researchers have recognized the importance of the PSR in seabed soil and conducted extensive experimental studies, there are few considerations of the PSR impact on numerical simulations of wave-seabed soil interactions. Only a few studies can be found in Dunn et al. (2006), Li & Jeng (2008). One of the best known researches in this topic was the finite element simulation conducted by Sassa & Sekiguchi (2001). They presented a cyclic plasticity constitutive model and implemented it to the finite element analysis of seabed liquefactions under both the progressive and standing waves. They compared the simulation results with the experimental data and found that the sand bed is less resistant to the liquefaction under progressive waves than standing waves due to the PSR impact. However, Jeng (2013) claims that Sassa's model has several limitations in the simulation of this kind of problem, such as the lack of consideration of viscosity and the assumption of infinite bed. One of them is that the simulation results from this cyclic plasticity model seem to be very sensitive to the model parameters, which restricts its application. Therefore, the significance of the PSR impact in numerical simulations of wave-seabed interactions will be examined by the numerical simulation of the centrifuge wave tank tests carried by Sassa & Sekiguchi (1999) using the modified PSR soil model, which can take into account the PSR effect.

### 2.3.3 The background and previous research works on earthquake-induced liquefactions

The soil behavior under the earthquake loading is a major research area in both numerical simulations and experimental tests in the field of geotechnical engineering. The loading conditions under earthquakes are quiet diverse and complex, but they share a common characteristic that the soil is subjected to considerable PSR. Continuous PSR induced by earthquake loadings can generate excess pore water pressure and cumulative shear strain in undrained condition, thus accelerating soil liquefaction. Ignoring PSR induced deformation may lead to unsafe earthquake design.

Numerous researches have been carried out to investigate the soil behavior under earthquake loadings. One of the most famous researches is the VELACS project (Verification of Liquefaction Analysis using Centrifuge Studies). It includes a variety of centrifuge tests and the corresponding numerical simulations among several universities in America (Arulanandan & Scott, 1993). However, in 1995, Arulanandan & Manzari claimed that the predicted results from these numerical simulations have great variations and errors which may be due to different soil models used by different researchers. They also stated that the predicted results were largely affected by the computer code and it seems that the program with fully coupled governing equations performs the best among all the results. Although several researchers have implemented their soil models into these numerical simulations subsequently (Andrianopoulos et al., 2010; Sadeghian & Namin, 2013; Pak et al., 2014), there are few of them considering the PSR effect. Therefore, this research aims to take into account the impacts of PSR in numerical simulations of the

centrifuge earthquake   tests — model No. 3 from the VELACS project — by using the modified PSR model and a fully coupled finite element program DYSAC2 (Muraleetharan et al., 1994).

## 2.4 Soil Behaviors of Liquefaction

### 2.4.1 Introduction

Last 20 years have witnessed the rapid development of marine structures, such as wind turbines, oil platforms, etc. The seabed foundations of these structures are vulnerable to the liquefaction due to excess pore water pressure (Ye et al., 2014). Several marine structure failures have been reported during these years, such as the quay wall failures in Turkey in 1999 and the port failures in Japan in 2003 (Sumer et al., 2007). Most of the structure collapses were resulted from the liquefaction of the seabed foundations, which can be induced from wave loadings and earthquake loadings. Liquefactions may occur in a short duration but cause catastrophic failures, financial losses, and deaths. Therefore, the study of the liquefaction behavior is important to the offshore foundation designs.

Soil liquefaction happens when the fluid saturated soil reduces its strength and stiffness to essentially zero under either monotonic or dynamic loadings and behaves like fluid. The reduction of effective stress under dynamic loadings can also lead to cyclic mobility, in which the soil will dilate and regain its strength as the shear strain increases. In this case the dynamic loadings can cause cumulative build-up of pore pressure and shear strains. These behaviors come from the mutual interaction of the soil components, particularly the soil

skeleton composed of grains and the pore fluid. When the soil is subjected to the dynamic loadings, the soil particles tend to rearrange to reach their optimal potential state in a dense manner, thereby leading to the compaction of the soil and the build-up of pore pressure, which consequently reduces the frictional forces between the soil particles and the bearing capacity of the whole seabed (Ehlers et al., 2013). Furthermore, the liquefaction mechanism consists of two types:   transient liquefaction and residual liquefaction, and both of them have been observed in laboratory and field tests. Transient liquefaction is caused by the phase lag of the wave-induced pore pressure and can only occur in the elastic seabed. Residual liquefaction, which is the main risk for the marine structure failures, can only occur in the elastoplastic seabed due to the build-up of pore pressure caused by the densification of soil under cyclic loadings (Ye et al., 2014). This research deals with the residual liquefaction caused by both the wave and earthquake loadings in an elastoplastic seabed as few investigations have addressed the residual liquefaction before.

However, liquefaction is difficult to investigate although it is important in the offshore foundation design. The laboratory tests such as the triaxial test, simple shear test, even the hollow cylinder test cannot properly simulate the loading paths causing liquefaction. The in-situ measurements are not practical while the centrifuge tests are expensive (Jefferies & Shuttle, 2011). Therefore, the numerical simulation has the potential to be the suitable method to investigate the liquefaction behavior and is utilized in this research.

## 2.4.2 Liquefaction criteria in the research

Identification of the occurrence of liquefaction is crucial to investigate this soil behavior. Basically, the liquefaction of the soil specimen in this research is judged by the criterion proposed by Sassa & Sekiguchi (1999). The definition and the theoretical reason for the liquefaction criterion are briefly introduced below.
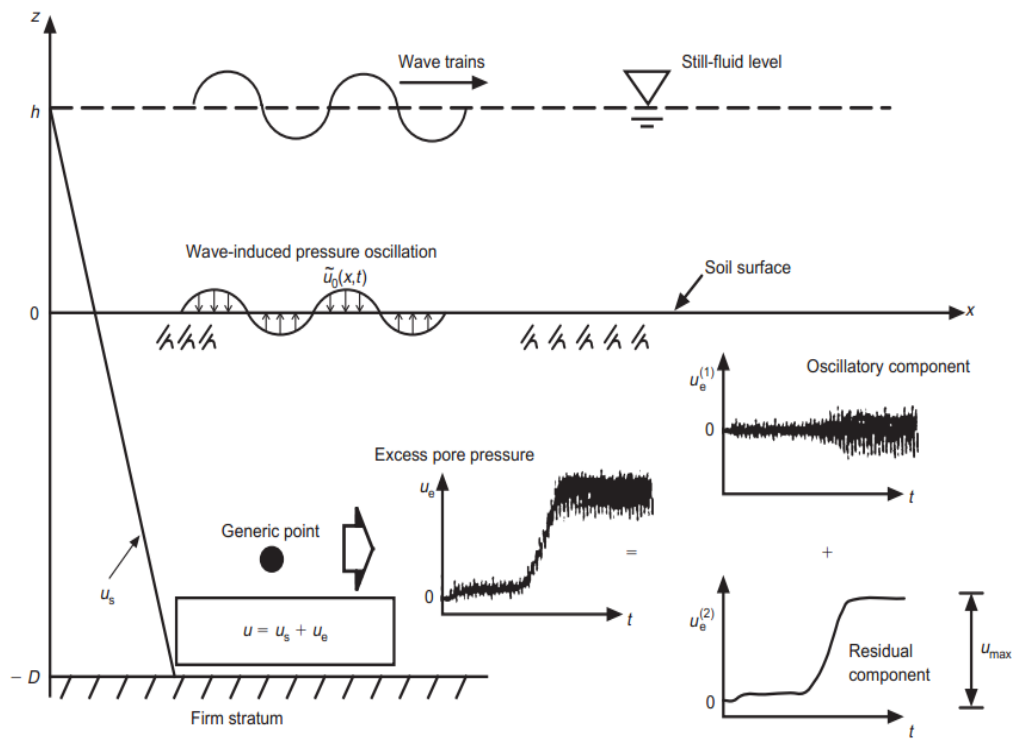


**Figure 2-28. Definitions of the pore water pressure components (Sassa & Sekiguchi, 1999).**

Figure 2-28 shows the fluid wave trains passing a soil bed and this passage of fluid waves can cause pressure oscillations at the fluid-soil interface. Therefore, the pore pressure $u$ at a generic point of the soil bed will vary with the time due

to the wave-induced pressure fluctuation and $u$ can be obtained from the equation that

$$u = u_e + u_s \tag{2.2}$$

where $u_e$ represents the wave-induced excess pore pressure at time $t$ at a generic point and $u_s$ stands for the hydrostatic pressure. Assume the excess pore water pressure is divided into two parts:

$$u_e = u_e^1 + u_e^2 \tag{2.3}$$

where $u_e^1$ is the oscillatory part and $u_e^2$ is the residual pore water pressure, which is determined by taking the average of the moving wave $u_e$ and stems from the contraction of the soil under cyclic plasticity. The average of $u_e^1$ over any wave cycle is defined to be zero. Unless specified, all pore water pressure presented in this thesis is the excess pore water pressure hereinafter.

Then let $\sigma_v$ denote the vertical effective stress at a given location. Liquefaction is considered to take place at a location that when the measured $u_e^2$ reaches the value of the initial vertical effective stress $\sigma_{v0}'$ because it follows that

$$\sigma_v' = \sigma_{v0}' + (d\sigma_v - u_e)$$

$$= \sigma_{v0}' + (d\sigma_v - u_e^1 - u_e^2) \tag{2.4}$$

where $d\sigma_v$ is the total vertical stress change induced by the wave at the same location. The occurrence of liquefaction is defined as the state where $\sigma_v' = 0$. Meanwhile, the horizontal effective stress $\sigma_h'$ is also assumed to be zero. Because the time averages of $d\sigma_v$ and $u_e^1$ over any wave cycle is considered to

be zero, from the mathematic manipulation it follows that when the liquefaction state is reached,

$$u_e^2 = \sigma_{v0}'$$ (2.5)

Therefore, in theory, the liquefaction is considered to take place when the measured residual pore water pressure $u_e^2$ has reached the value of the initial vertical effective stress $\sigma_{v0}'$ at a certain location.

However, the previous laboratory observations and numerical simulations for sand show that when the liquefaction occurs, $u_e^2$ usually does not reach the value of $\sigma_{v0}'$. For example, U.C. Berkeley performed several laboratory tests and found that liquefaction could still occur even when the residual pore water pressure is less than the downward initial vertical effective stress (Wu et al., 2003). Furthermore, in most of the numerical computations or the laboratory tests, sandy soil is a non-cohesive material and cannot withstand any tensile stress. So let $k$ denote the liquefaction coefficient and equation 2.5 becomes

$$u_e^2 = k * \sigma_{v0}'$$ (2.6)

where the value of $k$ may vary from 0.78 - 0.99 depending on the soil characteristics (Wu et al., 2004). Therefore, the occurrence of liquefaction is judged by comparing the value of the residual pore water pressure $u_e^2$ and the initial effective vertical stress $\sigma_{v0}'$ in this research. Moreover, liquefaction is also proved by some other criteria such as the reduction of effective confining pressure $p'$ and the dramatic increase of the shear strain, which also indicates the lower shear stiffness, and that the soil becomes less resistant to the shear stress. Although the liquefaction coefficient $k$ would be different in different

cases, in this research, liquefaction is considered to occur when *k* is equal to or larger than 0.9 or a dramatic increase of the shear strain (more than doubled) is observed.

## 2.5 Summary

This chapter has introduced the soil behaviors of the PSR and the non-coaxiality, and then has reviewed the previous experimental as well as the numerical investigations about this topic. The corresponding experimental evidences, numerical findings and the soil models used have been listed. The soil liquefaction and the liquefaction criteria used in this research have also been given.

Results from numerous experimental tests indicate that the non-coaxial behavior is often caused in the soil samples under various loading conditions including the PSR. The deviation between the directions of the principal stress and the principal strain increment can be observed especially during the early stage of the shearing. Then this non-coaxiality tends to reduce as the soil specimen approaches the critical state. Moreover, the difference between the principal stress direction and the principal strain incremental direction could be found more than 30 degrees during the continuous rotation of the principal stress directions.

Researchers have also paid great efforts to explore the PSR impact and non-coaxial behaviors by numerical methods. A variety of soil models associated with different theories have also been proposed during last decades. The simulation results also show that the non-coaxiality can be induced by the loading conditions with the PSR. Generally, the authors concluded that this

PSR can lead to the plastic deformations in the soil and it is essential to take account of the PSR behavior in geotechnical engineering simulations and designs.

The soil liquefaction has also been reviewed in this chapter because the foundations of the geotechnical structures are vulnerable to this phenomenon due to the excess pore water pressure. It may occur in a short time but cause catastrophic failures, financial losses, and deaths, hence is very important in the offshore foundation design. The liquefaction can be induced usually from the dynamic loadings such as wave loadings and earthquake loadings, which will be investigated in the following simulations. To judge the occurrence of the liquefaction, the criterion proposed by Sassa & Sekiguchi (1999) as well as other factors such as the effective confining pressure and the shear strain will be used in this research.

# Chapter 3 Methodology

## 3.1 Introduction

The PSR behavior will be investigated in the single element simulations and the finite element simulations of a series of experimental tests. This chapter introduces the soils, simulation procedures and the numerical tools involved in both the single element and finite element simulations. The properties of the three types of sand used in this research are introduced firstly, followed by a brief introduction of the single element simulations as well as the Fortran computer program used. Then this chapter describes the finite element simulations of boundary value problems. This section consists of an introduction of the finite element method, the commercial software — ABAQUS — used in the wave-seabed simulations and the DYSAC2 computer program used in the earthquake simulations. In order to apply the original model and modified PSR into the finite element simulations, it is essential to write the constitutive model subroutine with the numerical integration scheme. The subroutine representing the constitutive models written in Fortran and the explicit integration scheme adopted are introduced in this section as well. Finally, a summary is presented in the last section.

## 3.2 Soil Used in the Research

### 3.2.1 Introduction

In this research, the newly developed PSR model is adopted to simulate a series of experimental tests, in which three types of sand are used. Leighton Buzzard sand (Fraction B) is used in the simulations of hollow cylinder tests from Yang (2013) while Leighton Buzzard sand (Fraction E) is used in the simulations of the experimental tests from Visone (2008), as well as the centrifuge wave tests. Nevada sand No. 120 is used in the simulations of triaxial, tosional and rotational tests from Chen & Kutter (2009) and the centrifuge tests under the earthquake loading. These three types of sand are widely used in both the numerical and experimental investigations, therefore providing comparable data for this research (Arulmoli et al., 1992; Arulanandan, 1995; Sassa & Sekeguchi, 1999; 2001; Jeng, 2013; Sadeghian & Namin, 2013).

### 3.2.2 Soil properties

Leighton Buzzard sand is quarried in and around Bedfordshire, Leighton Buzzard in the east of England. It consists of sub-rounded particles and contains mainly quartz (Yang, 2013). The index properties of Leighton Buzzard sand (Fraction B & E) are listed in Table 3-1. Nevada No. 120 sand is uniform fine sand and its index properties are also summarized in Table 3-1 (Chen & Kutter, 2009).

**Table 3-1. Physical properties of Leighton Buzzard sand and Nevada sand (Chen & Kutter, 2009; Yang, 2013; Sassa & Sekiguchi, 1999).**

| Property | Leighton Buzzard sand (fraction B) | Leighton Buzzard sand (fraction E) | Nevada sand |
|---|---|---|---|
| Mean grain size $D_{50}$: mm | 0.62 | 0.15 | 0.17 |
| Uniformity coefficient $C_u$: $D_{60}/D_{10}$ | 1.56 | 1.58 | 2.0 |
| Specific gravity $G_s$ | 2.65 | 2.65 | 2.67 |
| Minimum void ratio $e_{min}$ | 0.52 | 0.64 | 0.511 |
| Maximum void ratio $e_{max}$ | 0.79 | 1.07 | 0.887 |

## 3.3 Single Element Simulations

### 3.3.1 Introduction

To assess the ability of the modified PSR model in simulating the soil behaviors, particularly the PSR behavior, a series of laboratory tests are simulated by a single element computer program. Firstly, a series of monotonic loading tests with different loading directions ($\alpha = 0^o$ to $90^o$) and drained pure rotational shear tests with different stress ratios (Yang, 2013) are simulated.

Leighton Buzzard sand (Fraction B) is used in these tests. Then, the triaxial tests with constant effective confining stress $p'$ from Visone (2008) are simulated with Leighton Buzzard sand (Fraction E). Finally, a series of triaxial, tosional and rotational tests for Nevada sand from Chen and Kutter (2009) are simulated. Furthermore, as the centrifuge wave tests and the centrifuge earthquake tests in the following chapters use the Leighton Buzzard sand (Fraction E) and Nevada sand respectively, the corresponding single element simulations for these two types of sand are also carried out to calibrate the model parameters which will be used in the following finite element simulations for the centrifuge tests under the wave and earthquake loadings. The comparison will be made between the predicted results from original model, the modified PSR model, and the experimental results.

## 3.3.2 The Fortran program

All the single element simulations are carried out with a computer program which applies to the single element stress-strain response analysis for the original model and the modified PSR model. This program is written in Fortran language, which is briefly introduced below.

Fortran is the first advanced computer programming language in the world. Although it has been used for more than 40 years, it is still very popular because of its similarity to the natural language, e.g. English, and math expressions. It always plays the important role in the computer programming, especially in scientific and engineering computation, thus suitable for the geotechnical project (Griffiths & Smith, 2003).

As the computer technology is developing rapidly, WINDOWS has gradually

replaced the DOS to become the new operating system. Therefore, Fortran77 and Intel Visual Fortran compiler, which is an application based on WINDOWS, are mainly utilized in this research.

## 3.4 Finite Element Simulations of Boundary Value Problems

### 3.4.1 Introduction and the finite element method

After the single element numerical simulations, two geotechnical boundary value problems—the experimental centrifuge wave test from Sassa & Sekiguchi (1999) and the centrifuge earthquake test No. 3 from the VELACS project (Verification of Liquefaction Analysis using Centrifuge Studies) (Arulanandan & Scott, 1993)—are simulated to further examine the performance of the modified PSR model. In these two simulations, the two models are implemented into two computer software using the finite element method which is introduced as follows. The predicted results by using the soil models with and without considering the PSR impact will be compared in these simulations as well.

Finite element method is one of the most widely used numerical methods in scientific researches and engineering analysis today. Because of its versatility and effectiveness, it attracts great attention in the engineering field. With the rapid development of computer science and technology, it has become an important part of computer aided engineering and numerical simulation (Griffiths & Smith, 2003).

The essence of finite element method lies in the following three aspects (Bathe, 1996):

- Split the computational domain representing a structure or a continuum into several elements, and connect them through the nodes in their borders.

- Represent the unknown field variables in the whole solution domain with the approximate function assumed in each element. The approximate functions in every element are then expressed by the values of the unknown field functions on each node and its corresponding interpolation function within the element, thus converting the original problem of solving the unknown field function with infinite degrees of freedom into a problem of solving the values of field functions on each node, which is a problem of limited degrees of freedom.

- Establish the algebraic equations or ordinary differential equations for solving basic unknown variables through the equivalent variational principle or weighted residual method to the mathematical model from the original problem. These equations are called finite element equations, and are expressed in the form of matrix. Then the solution of the problem can be obtained by solving these equations using numerical methods.

Due to the factors above, the finite element method has the following features:

- Adaptability for complex geometric configuration

- Applicability in various physical problems

- Reliability due to the establishment based on the strict theory

- Efficiency and suitability in computer calculation

## 3.4.2 ABAQUS in wave-seabed interactions

To investigate the soil behaviors under the wave loadings, the centrifuge wave tests from Sassa & Sekiguchi (1999) are simulated using the commercial finite element software – ABAQUS.

ABAQUS is one of the most powerful large scale finite element software in the world. It can be applied into a variety of projects, from simple linear elastic problems to complex nonlinear problems. Meanwhile, its effectiveness in the application of both engineering and science research is well verified. ABAQUS contains abundant element and material library, practical soil constitutive models, powerful interface module to simulate the soil and structure interaction, it can also calculate effective stress and pore pressure, model the filling or excavation, flexibly and accurately establish the initial stress state, thus has the a strong applicability in geotechnical engineering problems (Simulia, 2010).

Furthermore, it has various interfaces of subroutine such as the UMAT, thus providing a platform for secondary development. Applying the user defined material subroutine written in Fortran into ABAQUS, constitutive models developed by researchers can be utilized in the finite element modeling. Therefore, in this research, the original model and the modified PSR model are incorporated into ABAQUS by the UMAT subroutine to simulate the wave-seabed interactions.

In ABAQUS, Newton's method or quasi-Newton's algorithm are used to solve the non-linear equilibrium equations. ABAQUS adopts the exact Newton's

method when the user defined material subroutine is used. During the iteration for solving the non-linear equations, several parameters are used to control the error. For example, $R_{\alpha n}$ is the ratio of the largest residual force to the corresponding average force, and $C_{\alpha n}$ is the ratio of the largest displacement correction to the largest corresponding incremental displacement. The default force residual tolerance $R_{\alpha n}$ is 0.5% of the average force, while the default displacement correction tolerance $C_{\alpha n}$ is 1% of the incremental displacement. The error tolerances $R_{\alpha n}$ and $C_{\alpha n}$ can be modified larger than the default values by users to solve the non-linear problems difficult to converge (Yang & Yu, 2006).

To solve non-linear problems effectively, the size of the time increments is automatically adjusted in ABAQUS. If two consecutive increments take fewer than five iterations to achieve a converged solution, the solution is considered to be found relatively easily. In this case, ABAQUS automatically increases the size of the time increment by 50%. Conversely, for highly non-linear problems in which the converged solution is hard to obtained, ABAQUS will have to reduce the size of increment repeatedly. If the solution has not converged in fewer than 16 iterations or the solution appears to diverge, the current increment size will be abandoned by ABAQUS and the increment size is reset to the 25% of its previous value to start the iteration again. This process is repeated until the solution is converged. However, ABAQUS stops the analysis and reports the error massages if more than five attempts are required in reducing the time increment or the increment size becomes smaller than the minimum defined (Yang & Yu, 2010).

### 3.4.3 DYSAC2 program in earthquake-induced liquefactions

The soil characteristics including the PSR behavior are further investigated in the simulation of Model No. 3 from the VELACS centrifuge tests (Arulanandan & Scott, 1993). In this simulation, a finite element computer program DYSAC2 that can analyze the two dimensional dynamic geotechnical problems under plane strain conditions is utilized.

DYSAC2 was originally developed at University of California, Davis in 1988. During past years researchers have made several enhancements to DYSAC2 and presently it can solve the fully coupled dynamic governing equations of a two-phase saturated porous media (Muraleetharan et al., 1988). This program utilizes the four-node elements with reduced integration and the fluid bulk modulus terms. Each node has four variables of two soil skeletons and two fluid displacements. Both the vertical and horizontal base motions can be applied to the geotechnical structure. The spatially discrete governing equations of DYSAC2 are introduced as follows and details of formulations are available in Muraleethatan (1990) and Muraleetharan et al. (1994).

The equation for the mixed grain-fluid motion is given as:

$$\sigma + \rho g - (1 - \eta)\, \rho_s u - \eta \rho_f (u + w/\eta) = 0 \qquad (3.1)$$

The equation for the pore fluid motion is given by:

$$w = - k\, [h - \rho g + \rho\, (u + w/\eta)] \qquad (3.2)$$

The equation from the conservation of mass for the grain-fluid system can be written as:

$$\varepsilon = -w - [\eta/K_f + (1-\eta)/K_s]h + (1-\eta)\delta\sigma / 3K_s \qquad (3.3)$$

The combined bulk modulus $\Gamma$ of the solid grains and pore fluid can be defined as:

$$1/\Gamma = \eta/K_f + (1-\eta)/K_s \qquad (3.4)$$

The bulk modulus $K_f$ is of the order of $10^5 - 10^6$ kPa, while the bulk modulus $K_s$ is of the order of $10^{10} - 10^{20}$ kPa. Therefore, the last term of equation (3.3) can be neglected relative to other terms. With equation (3.4), equation (3.3) can be rewritten as:

$$\varepsilon = -w - h/\Gamma \qquad (3.5)$$

The effective stress for the soil is defined as:

$$\sigma = \sigma' - h\delta \qquad (3.6)$$

The stress-strain relationship is given as:

$$d\sigma = D \, d\varepsilon + d\sigma_0 \qquad (3.7)$$

The boundary conditions in this analysis indicates that at every point along the boundary of the soil mass,

$$T = \sigma n \qquad (3.8)$$

With the spatial discretization and mathematical formulations of these equations and substituting $w$ with the relationship $U = u + w/\eta$, the spatially discrete governing equations can be rewritten in matrix form as:

$$Ma \; + \; Cv \; + \; K_p d \; + \; p \; = \; f \tag{3.9}$$

where $a$, $v$ and $d$ are the vector of nodal accelerations, nodal velocities and nodal displacements respectively. The coefficient matrices $M$, $C$ and $K_p$ are mass matrix, damping matrix and pore fluid stiffness matrix, while $p$ is the internal force load vector and $f$ is the applied force load vector.

This program adopts a three parameter time integration scheme called the Hilber-Hughes-Taylor $\alpha$ method to integrate the spatially discrete finite element equations. Moreover, a predictor/multi-connector algorithm is also used to provide the quadratic accuracy and numerical damping characteristics (Hilber et al., 1977). The applicability of DYSAC2 has been demonstrated by numerous published examples, such as Muraleetharan and Arulanandan (1991), Arulanandan and Manzari (1992), Muraleetharan (1993), Muraleetharan et al. (1994; 1995), Arulanandan et al. (1997), etc. It has also been successful utilized in the design of Port of Los Angeles' Pier 400 together with other design methods (Wittkop, 1993; Muraleetharan et al., 1997).

The original DYSAC2 has only two constitutive models based on the bounding surface plasticity theory. To implement the modified PSR model into the analysis, the computer code needs to be rewritten. Fortunately, DYSAC2 is written in Fortran 77 with carefully selected variable names reflecting the quantities they represents and is quite modular, thus facilitating the incorporation of the modified PSR model as well as the VELACS centrifuge earthquake test. Moreover, a finite element mesh generation scheme together with a number of output files which can be easily post-processed is available in DYSAC2. However, it still took a great effort to modify the computer code in many locations to carry out the finite element analysis in this research.

# 3.5 Constitutive Model Subroutine and Explicit Integration Scheme

## 3.5.1 Introduction

The modified PSR model is implemented into the finite element problems by a constitutive model subroutine written in Fortran. In this subroutine, the constitutive formulations are performed using an explicit substepping integration algorithm with automatic error controls. According to this integration scheme, the strain increment passed down from the main program is divided into multiple sub-increments. Then the constitutive equations are integrated firstly using Euler scheme which is of the first order accuracy, followed by using the modified Euler scheme which is of the second order accuracy in each sub-increment. The error measurement of the numerical integrations is defined by taking the difference of the integration results of these two schemes. Once the integration error exceeds the error tolerance, the current sub-increment is re-subdivided according to the ratio of the local current error to the value of error tolerance. Furthermore, for a given sub-increment, the size of the next sub-increment is determined by the extrapolation of the current error compared with the error tolerance prescribed. Therefore, the imposed strain increment can be automatically divided based on the prescribed error tolerance in this scheme (Yang & Yu, 2006; 2010). The next sections will firstly present the numerical integration scheme adopted, followed by a introduction of the structure of the constitutive model subroutine.

## 3.5.2 The explicit integration scheme

To apply this integration scheme into the original and modified PSR model in the elasto-plastic regime, consider a time sub-increment $\Delta T_n$ and corresponding strain sub-increment $\Delta \varepsilon_n$. Given all the quantities at sub-step $n$-1, the quantities at sub-step $n$ are to be solved. The first step is to integrate the constitutive formulations using Euler scheme, given as:

$$\Delta \boldsymbol{\sigma}_1 = \mathbf{D}_{ep} \ (\boldsymbol{\sigma}_{n-1}, \ \mu_{n-1}) \ \Delta \varepsilon_n \tag{3.10}$$

$$\Delta \mu_1 = \Delta \lambda_1 \ (\boldsymbol{\sigma}_{n-1}, \ \mu_{n-1}, \ \Delta \varepsilon_n) \mathbf{B}(\boldsymbol{\sigma}_{n-1}) \tag{3.11}$$

where $\mu$ is the hardening parameter and $\lambda$ is the plastic strain rate multiplier. In the above and following equations, the subscript in vectors and tensors is left out for clear demonstration. The second step is to integrate the constitutive formulations using the modified Euler scheme, given as:

$$\Delta \boldsymbol{\sigma}_2 = \mathbf{D}_{ep} \ (\boldsymbol{\sigma}_{n-1} + \Delta \boldsymbol{\sigma}_1, \ \mu_{n-1} + \Delta \mu_1) \ \Delta \varepsilon_n \tag{3.12}$$

$$\Delta \mu_2 = \Delta \lambda_1 \ (\boldsymbol{\sigma}_{n-1} + \Delta \boldsymbol{\sigma}_1, \ \mu_{n-1} + \Delta \mu_1, \ \Delta \varepsilon_n) \mathbf{B} \ (\boldsymbol{\sigma}_{n-1} + \Delta \boldsymbol{\sigma}_1) \tag{3.13}$$

The value of $\boldsymbol{\sigma}_n$ and $\mu_n$ at the end of a time step are given as:

$$\boldsymbol{\sigma}_n = \boldsymbol{\sigma}_{n-1} + \Delta \boldsymbol{\sigma}_1 \tag{3.14}$$

$$\mu_n = \mu_{n-1} + \Delta \mu_1 \tag{3.15}$$

The final values of $\boldsymbol{\sigma}$ and $\mu$ at sub-step $n$ are expressed as:

$$\boldsymbol{\sigma}_{n'} = \boldsymbol{\sigma}_{n-1} + \frac{1}{2} \ (\Delta \boldsymbol{\sigma}_1 + \Delta \boldsymbol{\sigma}_2) \tag{3.16}$$

$$\boldsymbol{\mu}_{n'} = \mu_{n-1} + \frac{1}{2} (\Delta\mu_1 + \Delta\mu_2) \tag{3.17}$$

The local truncation error is determined based on $\Delta\boldsymbol{\sigma}_1$, $\Delta\boldsymbol{\sigma}_2$ and $\Delta\mu_1$, $\Delta\mu_2$, given as:

$$R_n = \max \left[ \frac{||\Delta\boldsymbol{\sigma}_1 - \Delta\boldsymbol{\sigma}_2||}{2||\boldsymbol{\sigma}_n||} , \frac{||\Delta\mu_1 - \Delta\mu_2||}{2\mu_n} \right] \tag{3.18}$$

If $R_n$ is larger than the error tolerance STOL, the current time sub-increment and corresponding strain sub-increment are extrapolated to smaller sizes according to the ratio of the $R_n$ to STOL, and the above computations are carried out again by using the reduced sub-increment. If $R_n$ is smaller than STOL, the computations move forward to next substep $n + 1$ and its sub-increment size is found based on $R_n$ and STOL, given as:

$$\Delta T_{n+1} = \sqrt{STOL/R_n} \; \Delta T_n \tag{3.19}$$

Moreover, for substep $n$, when $R_n$ exceeds STOL, the sub-increment $\Delta\boldsymbol{\varepsilon}_n$ is reduced by $q$, which is defined as:

$$q = \max \left\{ 0.9\sqrt{STOL/R_n} , 0.1 \right\} \tag{3.20}$$

When $R_n$ is less than STOL, the next sub-increment $\Delta\boldsymbol{\varepsilon}_{n+1}$ is increased by $q$, which is defined as:

$$q = \min \left\{ 0.9\sqrt{STOL/R_n} , 1.1 \right\} \tag{3.21}$$

When implementing this integration scheme, many additional details are to be considered, such as the transition from the elastic to plastic zones, the solution

for the negative plastic multiplier and the correction of stresses to yield surfaces, etc. The schemes for the yield surface intersection and the negative plastic multiplier are briefly introduced in the following sections. Further details can be found in Abbo (1997).

### 3.5.3 The yield surface intersection scheme

During the iteration of the elastoplastic analysis, the strain increments are determined by the nodal displacement increments using the relationship between the strain and displacement, which can be expressed as:

$$\Delta\boldsymbol{\varepsilon} = \mathbf{B}\Delta\mathbf{u} \qquad (3.22)$$

where $\Delta\boldsymbol{\varepsilon}$ is the vector of incremental strain, $\mathbf{B}$ is the strain-displacement matrix and $\Delta\mathbf{u}$ denotes the nodal incremental displacements. Then the corresponding elastic stress increment is calculated from the elastic stress-strain matrix $\mathbf{D}_e$ by using

$$\Delta\boldsymbol{\sigma}_e = \mathbf{D}_e\ \Delta\boldsymbol{\varepsilon} \qquad (3.23)$$

A change from elastic to plastic behavior caused by this increment occurs when $f(\boldsymbol{\sigma}_0, \mu_0) < 0$ and $f(\boldsymbol{\sigma}_0+\Delta\boldsymbol{\sigma}_e, \mu_0) = f(\boldsymbol{\sigma}_e, \mu_0) > 0$, hence depending on the initial stress $\boldsymbol{\sigma}_0$, the initial hardening parameter $\mu_0$, the yield function $f$, and the elastic stress $\boldsymbol{\sigma}_e = \boldsymbol{\sigma}_0+\Delta\boldsymbol{\sigma}_e$. Therefore, it essential to determine the fraction of $\Delta\boldsymbol{\sigma}_e$ belongs to the inner side of the yield surface. This judgment is needed many times during the iteration of an elastoplastic finite element analysis. A relatively efficient and accurate intersection scheme for this judgment is illustrated in Figure 3-1. In this scheme, an alternative approximation of the

yield condition $|f(\boldsymbol{\sigma}, \mu)| \leq$ FTOL is used to replace the exact yield condition of $f(\boldsymbol{\sigma}, \mu) = 0$, where FTOL is a small positive constant with the suitable value which are typically in the range of 10E-6 to 10E-9. From the finite precision arithmetic the yield condition above can be modified as:

$$f(\boldsymbol{\sigma}_0, \mu_0) < \text{- FTOL and } f(\boldsymbol{\sigma}_0, \mu_0) > + \text{FTOL} \qquad (3.24)$$

It is postulated that the stress increment intersects with the yield surface at $\boldsymbol{\sigma}_{\text{int}}$. Then to find the elastic portion of $\Delta\boldsymbol{\sigma}_{\text{e}}$ becomes to determine the scalar of $a$ in the nonlinear equation:

$$f(\boldsymbol{\sigma}_0 + a\Delta\boldsymbol{\sigma}_{\text{e}}, \mu_0) = f(\boldsymbol{\sigma}_{\text{int}}, \mu_0) = 0 \qquad (3.25)$$

In this equation, the unity value of $a$ means that the $\Delta\boldsymbol{\sigma}_{\text{e}}$ causes purely elastic strains, while the 0 value of $a$ indicates that the $\Delta\boldsymbol{\sigma}_{\text{e}}$ causes purely plastic strains. Therefore, the transition from the elastic to plastic occurs when the value of $a$ lies in the range of $0 < a < 1$, and elastic portion of the stress increment is given as $a\Delta\boldsymbol{\sigma}_{\text{e}}$. This single non-linear type of equation can be solved using the methods of secant, bisection, regula-falsi, modified regula-falsi, and Newton-Raphson method. In this research, the modified regula-falsi algorithm is used because it is unconditionally convergent and does not require calculating derivatives, thus usually converging in five iterations.
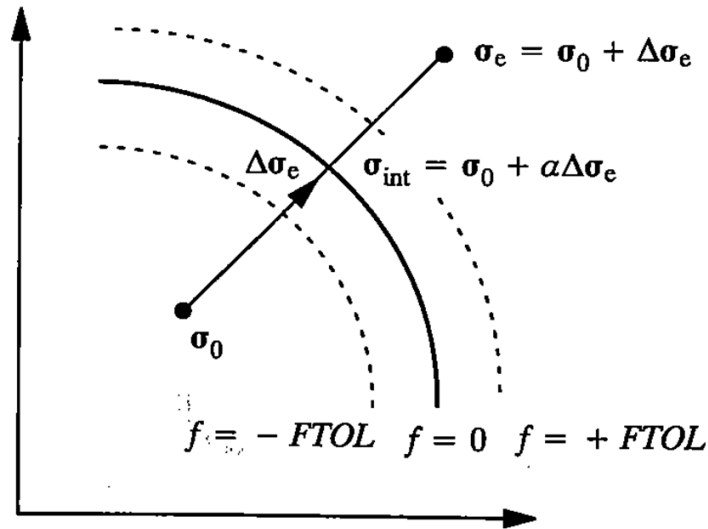
**Figure 3-1. Illustration of yield surface intersection: elastic to plastic transition (Abbo, 1997).**

## 3.5.4 Negative plastic multiplier

Apart from the situation in 3.5.3, a transition from the elastic to plastic may also occur when an elastic stress increment of the type shown in Figure 3-2 is applied to a stress state initially lying on the yield surface. In this case, the plastic multiplier is negative ($\Delta\lambda < 0$) and $f(\sigma_e, \mu_0) > +$ FTOL. The stress points with negative plastic multipliers can be found under monotonic loadings, especially when the trial stress increment $\Delta\sigma_e$ is very large. In this situation, the integration of the elastoplastic constitutive law is only required beyond the last intersection point because the fraction of the stress increment that lies inside the yield surface is elastic.
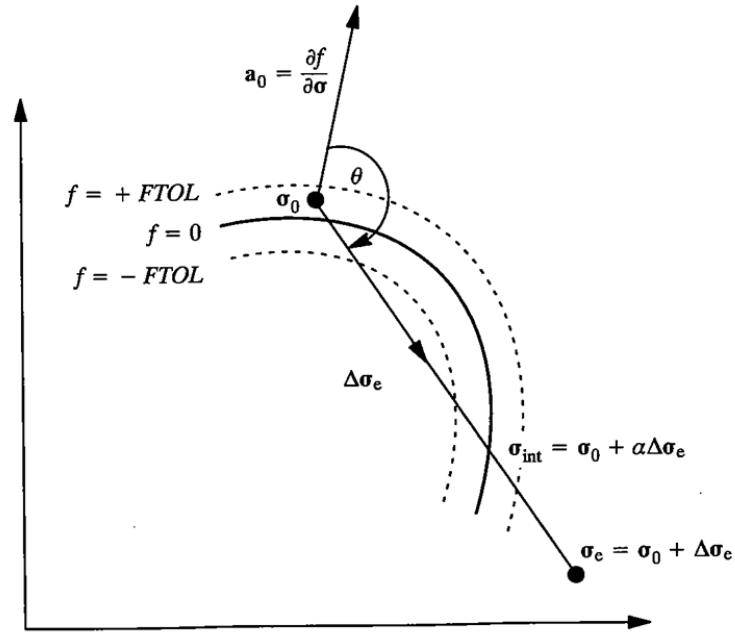
**Figure 3-2. Illustration of yield surface intersection: negative plastic**

**multiplier (Abbo, 1997).**

To detect the negative plastic multipliers, the cosine of the angle $\theta$ between $df/d\boldsymbol{\sigma}_0$ and $\Delta\boldsymbol{\sigma}_e$ is computed to check whether the $\cos\theta < $ LTOL, where LTOL is another tolerance. In this method, there is no need to calculate $\Delta\lambda$ explicitly, thus providing the efficiency. Finding the yield surface intersection for a negative plastic multiplier follows the same procedure introduced in the last section. However, it can be seen from Figure 3-2 that the use of the tolerance FTOL instead of the exact yield condition allows the stress points to lie just outside the yield surface. Therefore, the incremental stress path may cross the yield surface twice, thus making the situation more complex. To ensure the correct crossing using the modified regula-falsi algorithm, a different set of starting value of $a$ will be used. $a_0$ and $a_1$ must now satisfy the conditions of $f(\boldsymbol{\sigma}_0+a_0\Delta\boldsymbol{\sigma}_e, \mu) < -$ FTOL and $f(\boldsymbol{\sigma}_0+a_1\Delta\boldsymbol{\sigma}_e, \mu) > +$ FTOL, which make sure that $a_0$ and $a_1$ deal with the second intersection with yield surface. In this situation,

$a=1$ again means that the $\Delta\sigma_e$ causes purely elastic strains, while $a=0$ indicates that the $\Delta\sigma_e$ causes purely plastic strains. The value of $a$ still lies in the range of $0 <a< 1$.

To locate the suitable starting values of $a$, a strategy is used to break up the trial stress increment $\Delta\sigma_e$ into smaller sub-increments with the number of NSUB, which is usually set to ten. Each of these sub-increments is checked to see whether it crosses the yield surface. In the iteration, the stress increment and $a$ are divided by NSUB to obtain the sub-increments of $\Delta a = 1/\text{NSUB}$. Then each intervals determined by ($a_{n-1}$, $a_n$) is checked to see if the desired intersection occurs within it, where $a_n=a_{n-1} + n\Delta a$, $a_0=0$, and $n$ is from 1 to NSUB. The crossing with the yield surface occurs when $f(\sigma_0+a_{n-1}\Delta\sigma_e, \mu) < -$ FTOL and $f(\sigma_0+a_{n-1}\Delta\sigma_e, \mu) > +$ FTOL. A successful search with 4 sub-increments is geometrically illustrated in Figure 3-3. It can be seen that the required crossing with the yield surface lies between $a=0.75$ and $a=1$, which may be chosen as the suitable starting values for the modified regula-falsi method.
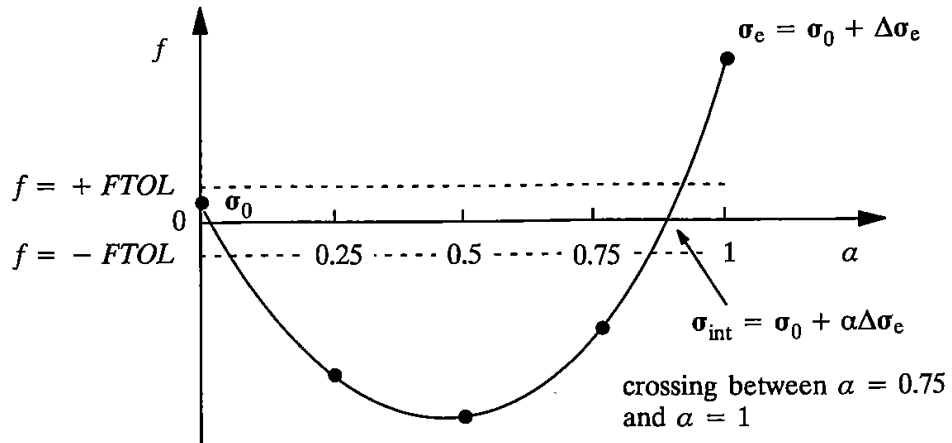


**Figure 3-3. Starting values for yield surface intersection: negative plastic multiplier (Abbo, 1997).**

### 3.5.5 The structure of PSR model subroutine

With the numerical integration scheme introduced above, the constitutive formulations of the original model and modified PSR model can be performed in the model subroutine. In the finite element simulations of this research, the model subroutine is implemented into two different finite element software, which have different interfaces as well. ABAQUS has the interface of UMAT subroutine for the incorporation of user developed model subroutines. However, DYSAC2 is not as powerful as ABAQUS. Although it is quite modular, it still does not have a specific interface for the user defined soil models. To implement the PSR model subroutine into DYSAC2, the whole code of this program needs to be modified in a number of lines. Therefore, the PSR model subroutines used in ABAQUS and DYSAC2 have different interfaces, format, and variables. However, they still share the similar structure of the main program, which will be presented as follows.

Subroutine of the PSR model
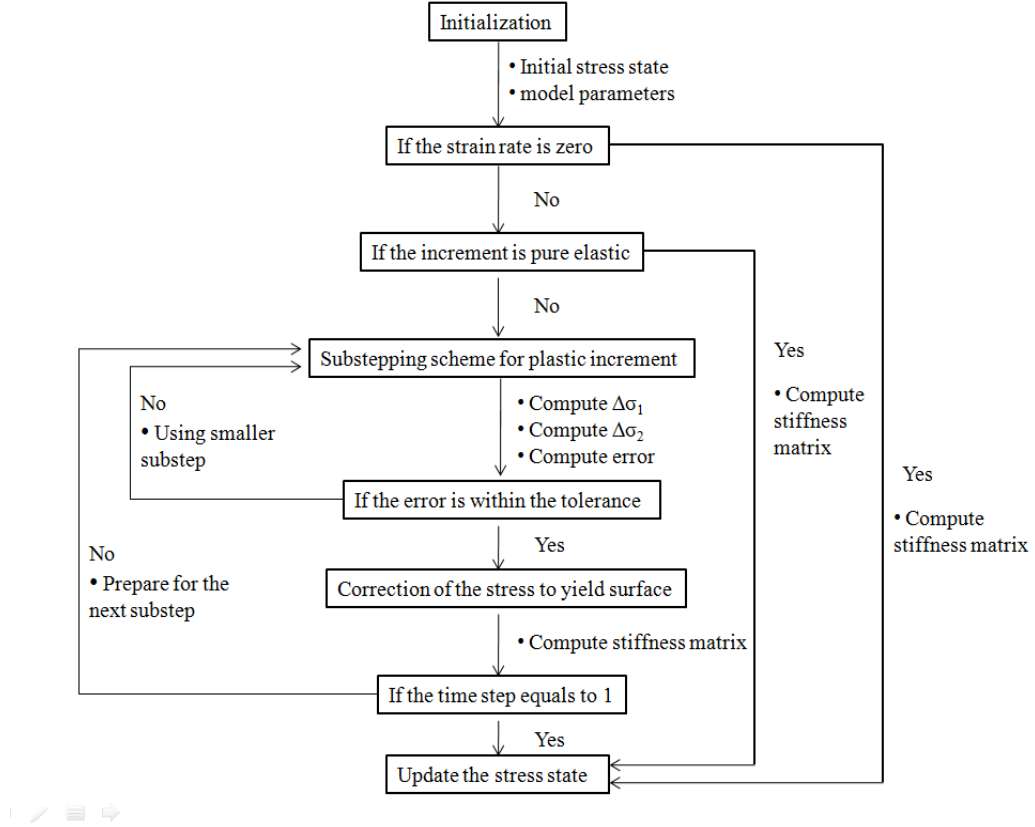


## 3.6 Summary

This chapter has introduced three types of soils—Leighton Buzzard sand (fraction B), Leighton Buzzard sand (Fraction E) and Nevada sand, which were used in the experimental tests simulated in this research. Physical properties of these sands including their index properties and particle shapes have been presented.

The numerical methods and processes used in the single element simulations have been described in detail. A series of experimental tests for the three types of sand specimen will be simulated to validate the modified PSR model and

investigate the PSR behavior. These numerical simulations are carried out by a single element computer program written in Fortran, which has also been introduced. The model parameters used in the finite element simulations will be also calibrated in these simulations.

This chapter has also listed the numerical tools used in the finite element simulations of the experimental centrifuge tests under the wave and earthquake loadings. To implement the modified PSR model into these boundary value problems, a constitutive model subroutine with the explicit substepping integration scheme and automatic error control has been written in Fortran. This scheme can automatically divide the imposed strain increment based on the prescribed error tolerance and determine the size of the next sub-increment by the extrapolation of the current error compared with the error tolerance prescribed. For the centrifuge wave tests, the commercial finite element software — ABAQUS — is used while the centrifuge earthquake tests use the finite element program called DYSAC2 which can analyze the two-dimensional dynamic geotechnical problems under plane strain conditions.

# Chapter 4 The PSR Model and Single Element Simulations

## 4.1 Introduction

The modified PSR model will be validated firstly by single element simulations of a series of experimental tests using three types of sand. The model parameters used in the following chapters of finite element simulations are calibrated in this chapter as the soils used in the single element simulations are also used in the finite element problems. This chapter starts with the introduction of a typical kinematic hardening model served as the original base model, followed by the development of the new model considering the PSR. Then it shows the single element simulation results for experimental tests for three different materials, including the hollow cylinder tests from Yang (2013) for Leighton Buzzard sand (Fraction B), triaxial tests from Visone (2008) for Leighton Buzzard sand (Fraction E) and triaxial, tosional and rotational tests from Chen & Kutter (2009) for Nevada sand No. 120. These simulation results are presented in three sections and the predicted results from the models with and without considering the PSR impact, as well as the experimental results will be compared.

## 4.2 The Original Base Model

A well-established soil model based on the classical plasticity with bounding surface concept and kinematic hardening is chosen as the base model. It

employs the back-stress ratio as the hardening parameter and the state parameter to represent influences of the different confining stresses and void ratios on sand behaviors. It also adopts the critical state concept and phase transformation line. However, it does not consider the PSR effect. This model will be briefly introduced here, and more details about this model can be found in Dafalias & Manzari (2004).

The yield function of the model is

$$f = [(\mathbf{s} - p\boldsymbol{\alpha}) : (\mathbf{s} - p\boldsymbol{\alpha})]^{1/2} - \sqrt{2/3}pm = 0 \tag{4.1}$$

where $\mathbf{s}$ is the deviatoric stress tensor and $p$ are the confining pressure. $\boldsymbol{\alpha}$ is the back-stress ratio tensor, which represents the center of yield surface in the stress ratio space (Figure 4-1) and serve as the hardening parameter. $m$ is the radius of yield surface, and $m$ is assumed to be a small constant, indicating no isotropic hardening. The normal to the yield surface is defined as:

$$\mathbf{l} = \frac{\partial f}{\partial \boldsymbol{\sigma}} = \mathbf{n} - \frac{1}{3}(\mathbf{n}:\mathbf{r})\ \mathbf{I}; \quad \mathbf{n} = \frac{\mathbf{r} - \boldsymbol{\alpha}}{\sqrt{2/3}m} \tag{4.2}$$

where $\mathbf{I}$ is the isotropic tensor and $\mathbf{n}$ represents the normal to the yield surface on the deviatoric plane. $\mathbf{r}$ represents the stress ratio and is equal to $\mathbf{s} / p$. The elastic shear strain rate $d\mathbf{e}^{e}$ and volumetric strain rate $d\varepsilon_{v}^{e}$ are

$$d\mathbf{e}^{e} = d\mathbf{s} / 2G \tag{4.3}$$

$$d\varepsilon_{v}^{e} = dp / K \tag{4.4}$$

where $G$ and $K$ are the elastic shear modules and bulk modules, respectively,

which are expressed as:

$$G = G_0\ p_{at}\ [(2.97 - e)^2\ /\ (1\ +\ e)]\ (p\ /\ p_{at})^{\ 1/2} \qquad (4.5)$$

$$K = 2(1\ +\ v)\ G\ /\ 3(1\ -\ 2v) \qquad (4.6)$$

where $G_0$ is a constant with the unit of MPa in this research, $p_{at}$ is the atmospheric pressure, $e$ is the void ratio, and $v$ is the Poisson's ratio.

The plastic strain rate $d\boldsymbol{\varepsilon}^p$ are defined as:

$$d\boldsymbol{\varepsilon}^p = \langle L \rangle\, \mathbf{R} \qquad (4.7)$$

$$L = \frac{1}{K_p} \left( \frac{\partial f}{\partial \boldsymbol{\sigma}} \right) : d\boldsymbol{\sigma} \qquad (4.8)$$

$$\mathbf{R} = \mathbf{n} + \frac{1}{3}\, D\, \mathbf{I} \qquad (4.9)$$

where $L$ represents the plastic multiplier (or loading index), and $\mathbf{R}$ is the normal to the potential surface, indicating the direction of the plastic strain rate. $K_p$ is the plastic modulus, and $D$ is the dilatancy ratio.
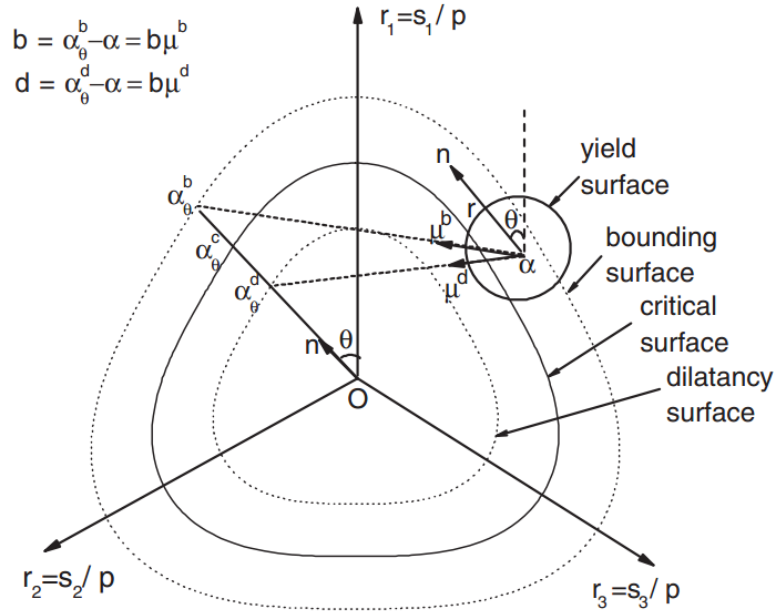
**Figure 4-1. Schematic illustration of the yield surface, critical, bounding, and dilatancy surfaces in the space of principal stresses (Manzari & Dafalias, 1997).**

The bounding surface plasticity allows the model to capture the features of reverse and cyclic loading response. In this bounding surface model, $K_p$ and $D$ are related to the distance of back-stress ratio $\boldsymbol{\alpha}$ from the bounding surface and dilatancy surface. Figure 4-1 shows these two surfaces as well as the critical state surface in the space of $\mathbf{s}/p$. The dilatancy surface and the critical state surface are extended from the phase transformation line and the critical state line, respectively. These principles apply to the full set of six stress variables, but only principal stresses are illustrated here for clarity. It can be seen that all these three surfaces are functions of the modified Lode angle $\theta$, which is defined as the angle between the deviatoric stress and the major principal stress in the deviatoric stress space of $\mathbf{s}/p$ and also schematically illustrated in Figure 4-1. A straight line is plotted from the origin of stress space with the direction $\mathbf{n}$,

which is the gradient of the yield surface. This line intersects with the critical state surface, bounding surface and dilatancy surface and gives the bounding back-stress ratio $\alpha_\theta^b$, dilatancy back-stress ratio $\alpha_\theta^d$ and critical back-stress ratio $\alpha_\theta^c$, respectively. They are defined as:

$$\boldsymbol{\alpha}_\theta^a = \sqrt{2/3}\, \alpha_\theta^a\, \mathbf{n}; \quad a = c,b,d; \quad \alpha_\theta^a = g(\theta,c)M\exp(\mp n^a\psi)-m \qquad (4.10)$$

$$g(\theta,c) = \frac{2c}{(1+c)-(1-c)\cos 3\theta}; \quad c = \frac{Q_e}{Q_c} \qquad (4.11)$$

From the equations above, the scalar $\alpha_\theta^a$ represents the size for different surfaces, and it is a function of the modified Lode angle and state parameter. If the current state is looser than its critical state with a positive state parameter, its bounding surface is inside the critical state surface, and its dilatancy surface is outside the critical state surface. It is the opposite if the current state is denser than its critical state with a negative state parameter. Its dependence on the modified Lode angle is reflected in the definition of $g(\theta,c)$, where $c$ is the ratio of a variable between the parameter of triaxial extension $Q_e$ and triaxial compression $Q_c$. In the equations above, the model parameters $n^b$ and $n^d$ are associated with the bounding and dilatancy back-stress ratios, respectively, and they are both positive. $M$ is the critical state stress ratio at the triaxial compression, and $m$ is the radius of the yield surface in the stress ratio space. The negative sign in the bracket is used for the bounding back-stress ratio, and the positive sign for the dilatancy one. The critical back-stress ratio is independent of state parameters, which makes $n^c$ zero. From the equations, the bounding and dilatancy surfaces vary according to the state parameter. When

the critical state is reached, the state parameter becomes zero and these two surfaces coincide with the critical state surface. $K_p$ and $D$ are given as:

$$K_p = \frac{2}{3} p \left[ G_0 h_0 (1 - c_h e) \left( \frac{p}{p_{at}} \right)^{-1/2} \right] \left[ \frac{|\mathbf{b} : \mathbf{n}|}{|(\boldsymbol{\alpha} - \boldsymbol{\alpha}_{in}) : \mathbf{n}|} \right] \tag{4.12}$$

$$h = \frac{b_0}{(\boldsymbol{\alpha} - \boldsymbol{\alpha}_{in}) : \mathbf{n}}; \quad b_0 = G_0 h_0 (1 - c_h e)(p / p_{ata})^{1/2} \tag{4.13}$$

$$D = A_d \mathbf{d} : \mathbf{n} \tag{4.14}$$

where $\mathbf{b}$ and $\mathbf{d}$ are the distances between the current back-stress ratio tensor and bounding and dilatancy back-stress ratio tensors, respectively. $h_0, c_h$ and $A_d$ are the model parameters. $\boldsymbol{\alpha}_{in}$ is the initial value of $\boldsymbol{\alpha}$ at the start of a new loading process and is updated when the denominator becomes negative. These equations indicate that $K_p$ and $D$ depend on the position of $\boldsymbol{\alpha}$ relative to $\boldsymbol{\alpha}_\theta^b$ and $\boldsymbol{\alpha}_\theta^d$, respectively, as well as the gradient $\mathbf{n}$. Finally, according to the consistency condition, the evolution of back-stress ratio or hardening parameter can be derived as:

$$d\boldsymbol{\alpha} = \langle L \rangle \mathbf{R}_\alpha = \langle L \rangle (2/3) h (\boldsymbol{\alpha}_\theta^b - \boldsymbol{\alpha}) \tag{4.15}$$

Where $\mathbf{R}_\alpha$ represents the direction of back-stress ratio evolutions. It can be approximated to coincide with the loading path as the radius of yield surface is very small.

## 4.3 The Development of the PSR Model Considering the Principal Stress Rotation

To consider the impact of the PSR, the original model was modified by Yang & Yu (2013) and the development of the new model is introduced below. Details of this modified PSR model can be found in Yang & Yu (2013).

In the modified PSR model, the plastic strain rate is split into the monotonic strain rate $d\boldsymbol{\varepsilon}_m^p$ and the PSR strain rate $d\boldsymbol{\varepsilon}_r^p$, where the subscript $m$ and $r$ represent the monotonic and PSR loading respectively, and it also applies to other quantities. It is postulated that this treatment of separation only applies to the derivation of plastic strain rates and the evolution of hardening parameter is not affected by this treatment. Therefore, according to the classical plasticity, the plastic strain rate can be expressed as:

$$d\boldsymbol{\varepsilon}_m^p = \langle L_m \rangle \mathbf{R}_m = \frac{1}{K_{pm}} (\frac{\partial f}{\partial \boldsymbol{\sigma}} d\boldsymbol{\sigma}_m) \mathbf{R}_m \tag{4.16}$$

$$d\boldsymbol{\varepsilon}_r^p = \langle L_r \rangle \mathbf{R}_r = \frac{1}{K_{pr}} (\frac{\partial f}{\partial \boldsymbol{\sigma}} d\boldsymbol{\sigma}_r) \mathbf{R}_r \tag{4.17}$$

It is assumed that $K_{pm} = K_p$ and $\mathbf{R}_m = \mathbf{R}$ (equation 4.8 & 4.9) because the original model is for non-PSR loading. The direction of the PSR strain rate $\mathbf{R}_r$ can be expressed as:

$$\mathbf{R}_r = \mathbf{n}_r + \frac{1}{3} D_r \mathbf{I} \tag{4.18}$$

where $\mathbf{n}_r$ is the direction of deviatoric plastic strain rate and can be

approximated as **n** for simplicity. Therefore, parameter $c_{nr}$ for the computation of $\mathbf{n}_r$ from their original development is omitted here. $D_r$ is the dilatancy ratio for the PSR loading rate, it can be derived from the postulate of the PSR dilatancy ratio of Gutierrez et al. (1991), which is expressed as:

$$D = \eta_c - c\frac{q}{p}$$

(4.19)

$$c = \cos(2\Phi)$$ (4.20)

where $\eta_c$ represents the critical state stress ratio and $q/p$ is the current stress ratio. $\Phi$ is the difference of angles between the principal stress and principal plastic strain rate, thus represents the non-coaxiality. This well-established theory is proposed on the basis of work and energy dissipation considering the non-coaxiality. $c$ will become unity, and the dilatancy ratio will be downgraded to Rowe's postulate in the case of coaxiality. These formulations can be rewritten as:

$$D = D_m + D_r = (\eta_c - \frac{q}{p}) + (1-c)\frac{q}{p}$$

(4.21)

The first term $D_m$ represents the contribution from the monotonic loading while the second term $D_r$ represents the contribution from the pure rotational loading. The formulation shows that the contribution of the second term is small when $q/p$ is close to the critical state stress ratio as the non-coaxiality is small. However, its contribution is also small when $q/p$ is close to zero although the non-coaxiality is large. Therefore, the largest contribution from the non-coaxiality to the dilatancy ratio occurs when the intermediate stress ratio is

reached. The assumption of small radius of yield surface indicates that $c = \cos(2\psi) = \alpha / \alpha_\theta^b$. Therefore, $D_r$ can be approximately defined as:

$$D_r = A_r(1 - \alpha/\alpha^b{}_\theta) \ \alpha \qquad (4.22)$$

where $A_r$ is a model parameter for the impact of PSR on the dilatancy ratio.

The plastic modulus $K_{pr}$ for the PSR loading rate is defined as:

$$K_{pr} = \frac{2}{3} p \left[ G_0 h_{0r} (1 - c_h e) \left( \frac{p}{p_{at}} \right)^{-1/2} \right] \left( \frac{|\mathbf{b} : \mathbf{n}|}{|(\boldsymbol{\alpha} - \boldsymbol{\alpha}_{in}) : \mathbf{n}|} \right)^{\xi_r} \qquad (4.23)$$

where $h_{0r}$ and $\xi_r$ are new model parameters. In order to make $K_{pr}$ more sensitive to the stress ration, $\xi_r$ is usually larger than unity as the single element numerical simulations at different stress ratios (Yang & Yu, 2013) indicate that the soil responses under the PSR loadings are more sensitive to stress ratios than the responses under the monotonic loadings.

At present, all new parameters for the modified PSR model have been introduced. Finally, to complete the model, the definition of the PSR loading rate $d\boldsymbol{\sigma}_r$ is required. To determine $d\boldsymbol{\sigma}_r$ in general stress space, it is first considered in the space with only $x$ and $y$ direction denoted as $\boldsymbol{\alpha}$. Let $d\boldsymbol{\sigma}_\mathbf{r}^\alpha$ represent $(d\sigma_{rx}^\alpha, d\sigma_{ry}^\alpha, d\sigma_{rxy}^\alpha)^T$, in the space of $\boldsymbol{\alpha}$ with only one PSR. Let $d\mathbf{t}_r^\alpha$ represent the vector $((d\sigma_{rx}^\alpha - d\sigma_{ry}^\alpha)/2, d\sigma_{rxy}^\alpha)^T$, and $\mathbf{t}^\alpha$ represent the vector $((\sigma_x - \sigma_y)/2, \sigma_{xy})^T$. To consider the PSR, the following conditions should be satisfied:

$$d\mathbf{t}_r^\alpha = d\mathbf{t}^\alpha - \frac{d\mathbf{t}^\alpha : \mathbf{t}^\alpha}{\mathbf{t}^\alpha : \mathbf{t}^\alpha} \mathbf{t}^\alpha \qquad (4.24)$$

$$d\sigma_{rx}^\alpha + d\sigma_{ry}^\alpha = 0 \qquad (4.25)$$
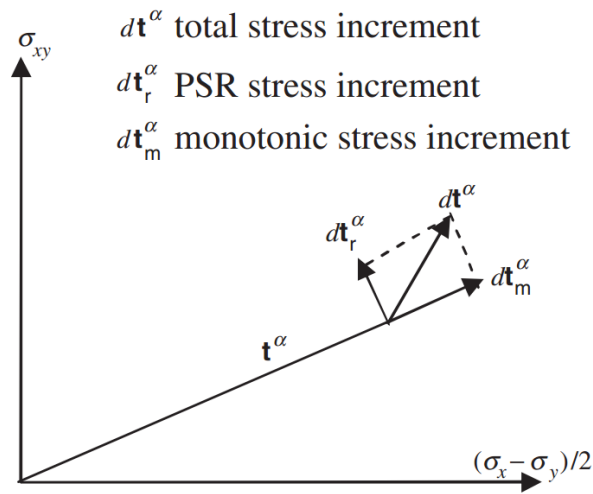


**Figure 4-2. Schematic illustration of the total, monotonic, and PSR stress increments in the space of $((\sigma_x\text{-}\sigma_y)/2, \sigma_{xy})$ (Yang & Yu, 2013).**

The meaning represented by equation (4.24) is schematically illustrated in Figure 4-2. Equations (4.24) and (4.25) can be re-arranged and expressed as $d\boldsymbol{\sigma}_r^\alpha = \mathbf{N}_r^\alpha d\boldsymbol{\sigma}$, and then in matrix form as:

$$\begin{pmatrix} d\sigma_{rx}^\alpha \\ d\sigma_{ry}^\alpha \\ d\sigma_{rxy}^\alpha \end{pmatrix} = \begin{bmatrix} \dfrac{1}{2} - \dfrac{(\sigma_x - \sigma_y)^2}{8t_J^\alpha} & -\dfrac{1}{2} + \dfrac{(\sigma_x - \sigma_y)^2}{8t_J^\alpha} & -\dfrac{(\sigma_x - \sigma_y)\sigma_{xy}}{2t_J^\alpha} \\[3mm] -\dfrac{1}{2} + \dfrac{(\sigma_x - \sigma_y)^2}{8t_J^\alpha} & \dfrac{1}{2} - \dfrac{(\sigma_x - \sigma_y)^2}{8t_J^\alpha} & \dfrac{(\sigma_x - \sigma_y)\sigma_{xy}}{2t_J^\alpha} \\[3mm] -\dfrac{(\sigma_x - \sigma_y)\sigma_{xy}}{4t_J^\alpha} & \dfrac{(\sigma_x - \sigma_y)\sigma_{xy}}{4t_J^\alpha} & 1 - \dfrac{\sigma_{xy}^2}{t_J^\alpha} \end{bmatrix} \begin{pmatrix} d\sigma_x \\ d\sigma_y \\ d\sigma_{xy} \end{pmatrix} \qquad (4.26)$$

where $t_J^\alpha = (\sigma_x - \sigma_y)^2/4 + \sigma_{xy}^2$. In this case, $d\boldsymbol{\sigma}$ contains only three stress variables $(d\sigma_x, d\sigma_y, d\sigma_{xy})$. Similarly, in the $\beta$ space $(y, z)$ and $\gamma$ space $(z, x)$, the PSR $d\boldsymbol{\sigma}_\mathbf{r}^\beta = (d\sigma_{ry}^\beta, d\sigma_{rz}^\beta, d\sigma_{ryz}^\beta)^T$ and $d\boldsymbol{\sigma}_\mathbf{r}^\gamma = (d\sigma_{rz}^\gamma, d\sigma_{rx}^\gamma, d\sigma_{rzx}^\gamma)^T$ can be defined as $d\boldsymbol{\sigma}_r^\beta = \mathbf{N}_r^\beta d\boldsymbol{\sigma}$ and $d\boldsymbol{\sigma}_r^\gamma = \mathbf{N}_r^\gamma d\boldsymbol{\sigma}$, respectively. They can also be expressed in the matrix form as:

$$
\begin{pmatrix} d\sigma_{ry}^\beta \\[2mm] d\sigma_{rz}^\beta \\[2mm] d\sigma_{ryz}^\beta \end{pmatrix} = \begin{bmatrix} \dfrac{1}{2} - \dfrac{(\sigma_y - \sigma_z)^2}{8t_J^\beta} & -\dfrac{1}{2} + \dfrac{(\sigma_y - \sigma_z)^2}{8t_J^\beta} & -\dfrac{(\sigma_y - \sigma_z)\sigma_{yz}}{2t_J^\beta} \\[4mm] -\dfrac{1}{2} + \dfrac{(\sigma_y - \sigma_z)^2}{8t_J^\beta} & \dfrac{1}{2} - \dfrac{(\sigma_y - \sigma_z)^2}{8t_J^\beta} & \dfrac{(\sigma_y - \sigma_z)\sigma_{yz}}{2t_J^\beta} \\[4mm] -\dfrac{(\sigma_y - \sigma_z)\sigma_{yz}}{4t_J^\beta} & \dfrac{(\sigma_y - \sigma_z)\sigma_{yz}}{4t_J^\beta} & 1 - \dfrac{\sigma_{yz}^2}{t_J^\beta} \end{bmatrix} \begin{pmatrix} d\sigma_y \\[2mm] d\sigma_z \\[2mm] d\sigma_{yz} \end{pmatrix}
$$
(4.27)

$$
\begin{pmatrix} d\sigma_{rz}^\gamma \\[2mm] d\sigma_{rx}^\gamma \\[2mm] d\sigma_{rzx}^\gamma \end{pmatrix} = \begin{bmatrix} \dfrac{1}{2} - \dfrac{(\sigma_z - \sigma_x)^2}{8t_J^\gamma} & -\dfrac{1}{2} + \dfrac{(\sigma_z - \sigma_x)^2}{8t_J^\gamma} & -\dfrac{(\sigma_z - \sigma_x)\sigma_{zx}}{2t_J^\gamma} \\[4mm] -\dfrac{1}{2} + \dfrac{(\sigma_z - \sigma_x)^2}{8t_J^\gamma} & \dfrac{1}{2} - \dfrac{(\sigma_z - \sigma_x)^2}{8t_J^\gamma} & \dfrac{(\sigma_z - \sigma_x)\sigma_{zx}}{2t_J^\gamma} \\[4mm] -\dfrac{(\sigma_z - \sigma_x)\sigma_{zx}}{4t_J^\gamma} & \dfrac{(\sigma_z - \sigma_x)\sigma_{zx}}{4t_J^\gamma} & 1 - \dfrac{\sigma_{zx}^2}{t_J^\gamma} \end{bmatrix} \begin{pmatrix} d\sigma_z \\[2mm] d\sigma_x \\[2mm] d\sigma_{zx} \end{pmatrix}
$$
(4.28)

where $t_J^\beta = (\sigma_y - \sigma_z)^2/4 + \sigma_{yz}^2$ and $t_J^\gamma = (\sigma_z - \sigma_x)^2/4 + \sigma_{zx}^2$. Combining $d\boldsymbol{\sigma}_\mathbf{r}^\alpha$, $d\boldsymbol{\sigma}_\mathbf{r}^\beta$ and $d\boldsymbol{\sigma}_\mathbf{r}^\gamma$, and letting $d\sigma_{rx} = d\sigma_{rx}^\alpha + d\sigma_{rx}^\gamma$, $d\sigma_{ry} = d\sigma_{ry}^\alpha + d\sigma_{ry}^\beta$ and $d\sigma_{rz} = d\sigma_{rz}^\beta + d\sigma_{rz}^\gamma$, $d\boldsymbol{\sigma}_r$ in the general stress space can be obtained as:

$$
d\boldsymbol{\sigma}_r = \mathbf{N}_r d\boldsymbol{\sigma}
$$
(4.29)

$\mathbf{N}_r$ can be expressed by $\mathbf{N}_r^\alpha$, $\mathbf{N}_r^\beta$ and $\mathbf{N}_r^\gamma$ in the matrix form as:

$$N_r = \begin{bmatrix} N_r^\alpha(1,1) + N_r^\gamma(2,2) & N_r^\alpha(1,2) & N_r^\gamma(2,1) & N_r^\alpha(1,3) & 0 & N_r^\gamma(2,3) \\ N_r^\alpha(2,1) & N_r^\alpha(2,2) + N_r^\beta(1,1) & N_r^\beta(1,2) & N_r^\alpha(2,3) & N_r^\beta(1,3) & 0 \\ N_r^\gamma(1,2) & N_r^\beta(2,1) & N_r^\beta(2,2) + N_r^y(1,1) & 0 & N_r^\beta(2,3) & N_r^\gamma(1,3) \\ N_r^\alpha(3,1) & N_r^\beta(3,2) & 0 & N_r^\alpha(3,3) & 0 & 0 \\ 0 & N_r^\beta(3,1) & N_r^\gamma(3,2) & 0 & N_r^\beta(3,3) & 0 \\ N_r^\gamma(3,2) & 0 & N_r^\gamma(3,1) & 0 & 0 & N_r^\gamma(3,3) \end{bmatrix}$$

(4.30)

The numbers in the bracket represent the element in the matrices of $\mathbf{N}_r^\alpha$, $\mathbf{N}_r^\beta$ and $\mathbf{N}_r^\gamma$ in the Equations 4.26 to 4.28. The PSR related equations derived so far are independent of stress increments and the number of PSRs.

With the formulations derived before, the elastoplastic stiffness can be obtained. The total stress increment can be defined as:

$$d\boldsymbol{\sigma} = \mathbf{E}(d\boldsymbol{\varepsilon} - d\boldsymbol{\varepsilon}^P) = \mathbf{E}(d\boldsymbol{\varepsilon} - d\boldsymbol{\varepsilon}_m^P - d\boldsymbol{\varepsilon}_r^P)$$

(4.31)

$$E_{ijkl} = K\delta_{ij}\delta_{kl} + G(\delta_{ik}\delta_{jl} + \delta_{il}\delta_{jk} - 2/3\delta_{ij}\delta_{kl})$$

(4.32)

where **E** is the elastic stiffness tensor. Substituting $d\boldsymbol{\varepsilon}_m^P$ and $d\boldsymbol{\varepsilon}_r^P$ from equations (4.16) and (4.17) into equation (4.31), it can be obtained that

$$d\boldsymbol{\sigma} = \mathbf{E}d\boldsymbol{\varepsilon} - \frac{1}{K_p}(\mathbf{E}\mathbf{R})(\mathbf{l}\,d\boldsymbol{\sigma}_m) - \frac{1}{K_{pr}}(\mathbf{E}\mathbf{R}_r)(\mathbf{l}\,d\boldsymbol{\sigma}_r)$$

(4.33)

Multiplying equation (4.33) with the normal to the yield surface **l**, it can be obtained that

$$\mathbf{l}\,d\boldsymbol{\sigma} = \mathbf{l}\,\mathbf{E}\,d\boldsymbol{\varepsilon} - \frac{1}{K_p}(\mathbf{l}\,\mathbf{E}\,\mathbf{R})(\mathbf{l}\,d\boldsymbol{\sigma}_m) - \frac{1}{K_{pr}}(\mathbf{l}\,\mathbf{E}\,\mathbf{R}_r)(\mathbf{l}\,d\boldsymbol{\sigma}_r) \tag{4.34}$$

Similarly, multiplying equation (4.31) with $\mathbf{N_r}$, and using the relationship

$$\mathbf{E}\,\mathbf{N_r} = 2G\,\mathbf{N_r} \tag{4.35}$$

it can be obtained that

$$\mathbf{N}_r\,d\boldsymbol{\sigma} = d\sigma_r = 2G(\mathbf{N_r}\,d\boldsymbol{\varepsilon}) - \frac{2G}{K_p}(\mathbf{N_r}\,\mathbf{R})(\mathbf{l}\,d\boldsymbol{\sigma}_m) - \frac{2G}{K_{pr}}(\mathbf{N_r}\,\mathbf{R}_r)(\mathbf{l}\,d\boldsymbol{\sigma}_r) \tag{4.36}$$

Multiplying equation (4.36) with $\mathbf{l}$, it can be obtained that

$$\mathbf{l}\,d\sigma_r = 2G(\mathbf{l}\,\mathbf{N}_r\,d\boldsymbol{\varepsilon}) - \frac{2G}{K_p}(\mathbf{l}\,\mathbf{N}_r\,\mathbf{R})(\mathbf{l}\,d\boldsymbol{\sigma}_m) - \frac{2G}{K_{pr}}(\mathbf{l}\,\mathbf{N}_r\,\mathbf{R}_r)(\mathbf{l}\,d\boldsymbol{\sigma}_r) \tag{4.37}$$

From equations (4.34) and (4.37), $\mathbf{l}\,d\boldsymbol{\sigma}_m$ and $\mathbf{l}\,d\sigma_r$ can be expressed as functions of $\mathbf{l}\,d\boldsymbol{\varepsilon}$. Therefore, the relationship between the stress and strain increments can be expressed as:

$$d\boldsymbol{\sigma} = \mathbf{E}^{ep}\,d\boldsymbol{\varepsilon} \tag{4.38}$$

$$\mathbf{E}^{ep} = \mathbf{E} - B_1\left[\frac{(\mathbf{E}\mathbf{R})(\mathbf{I}\mathbf{N}_r^*)}{K_{pr} + \mathbf{I}\mathbf{N}_r^*\mathbf{R}_r} - \frac{(\mathbf{E}\mathbf{R})(\mathbf{I}\mathbf{E})}{K_{pr} + \mathbf{I}\mathbf{E}\mathbf{R}_r}\right] - B_2\left[\frac{(\mathbf{E}\mathbf{R}_r)(\mathbf{I}\mathbf{N}_r^*)}{\mathbf{I}\mathbf{N}_r^*\mathbf{R}} - \frac{(\mathbf{E}\mathbf{R}_r)(\mathbf{I}\mathbf{E})}{K_p + \mathbf{I}\,\mathbf{E}\,\mathbf{R}}\right] \tag{4.39}$$

$$\mathbf{N}_r^* = 2G\,\mathbf{N}_r \tag{4.40}$$

$$B_1 = \left( \frac{\mathbf{IN}_r^* \mathbf{R}}{K_{pr} + \mathbf{IN}_r^* \mathbf{R}_r} - \frac{K_p + \mathbf{IER}}{K_{pr} + \mathbf{IER}_r} \right)^{-1}$$

$$(4.41)$$

$$B_2 = \left( \frac{K_{pr} + \mathbf{IN}_r^* \mathbf{R}_r}{\mathbf{IN}_r^* \mathbf{R}} - \frac{K_{pr} + \mathbf{IER}_r}{K_p + \mathbf{IER}} \right)^{-1}$$

$$(4.42)$$

Formulations above show that the stiffness tensor is independent of stress increments, and the stress and strain increments have a linear relationship, which indicates the easier numerical implementations in boundary value problems compared to the models whose stiffness tensor is the function of stress increments. In these equations, if $K_{pr}$ is set to be $K_p$ and $\mathbf{R}_r$ to be $\mathbf{R}$, they will be downgraded to the formulations in the classical plasticity.

## 4.4 The Calibrations and Single Element Simulations

### 4.4.1 Introduction and calibration

The PSR model developed above will be validated firstly by three single element simulations of a series of experimental tests. The model parameters are also calibrated by these simulations as the centrifuge tests simulated in the following chapters use the same materials as experimental tests in this chapter. This section starts with the single element simulation of the hollow cylinder tests from Yang (2013) for Leighton Buzzard sand (Fraction B). Then the triaxial tests from Visone (2008) for Leighton Buzzard sand (Fraction E) are simulated. Finally, the simulations of triaxial, tosional and rotational tests from Chen & Kutter (2009) for Nevada sand No. 120 is carried out. The predicted results from the models with and without considering the PSR effect, together with the experimental results will be compared. The specific notations in the

results presented in this chapter are introduced as follows. Basically, all stresses described in this thesis are effective stresses unless specified otherwise.

Effective confining stress:

$$p' = (\sigma_1' + \sigma_2' + \sigma_3')/3 \tag{4.43}$$

Deviatoric stress:

$$q = \{[(\sigma_1 - \sigma_2)^2 + (\sigma_2 - \sigma_3)^2 + (\sigma_1 - \sigma_3)^2]/2\}^{1/2} \tag{4.44}$$

Volumetric strain:

$$\varepsilon_v = (\varepsilon_1 + \varepsilon_2 + \varepsilon_3)/3 \tag{4.45}$$

Deviatoric strain:

$$\varepsilon_q = \{[(\varepsilon_1 - \varepsilon_2)^2 + (\varepsilon_2 - \varepsilon_3)^2 + (\varepsilon_1 - \varepsilon_3)^2]*2/9\}^{1/2} \tag{4.46}$$

All the model parameters are shown in Table 4-1 and divided into categories based on their functions. The calibration can be done from the results of triaxial tests. The elastic parameter $G_0$ is determined by the Equation 4.5 with $p_{at}$ equals 100 kPa in this research. The poisson's ratio $v$ is determined by the Equation 4.6. The critical state parameters $e_0$, $\lambda_c$ and $\xi$ are calculated from the plot of the relationship between $e_c$ and $p_c$ with Equation 2.1. $M$ can be determined from the experimental results of stress ratio-strain relationship at

the critical state. $c$ is calculated from the critical state stress ratios at triaxial compression and triaxial extension with Equation 4.11. The $m$ for the yield surface is often determined by $M/100$. Parameters $n^b$ and $n^d$ are determined from $n^b=\ln(M/M^b)/\Psi^b$ and $n^d=\ln(M/M^d)/\Psi^d$ proposed by Li & Dafalias (2000), where $\Psi^b$ and $M^b$ are values of $\Psi$ and $q/p$ at the peak stress ratio, and $\Psi^d$ and $M^d$ are those two values at the phase transform state. The parameters $h_0$, $c_h$ and $A_0$ can be found by trial and error. The calibration of $A_0$ can be started with fitting the curves of relationship between the volumetric strain and axial strain.

Three new model parameters related to the PSR are incorporated into the modified PSR model. They are $h_{0r}$ and $\xi_r$ for the plastic modulus, and $A_r$ for the flow rule. All of them are independent of the monotonic loading, and can be easily calibrated through the pure rotational loading paths at different stress ratio levels. As the shear strain is not influenced by the dilatancy ratio, $h_{0r}$ and $\xi_r$ can be obtained first by the curves of shear stress-strain relationship fitting the test results. $A_r$ can be obtained from the response between the other stress components and the volumetric strain.

## 4.4.2 The single element simulation of Leighton Buzzard sand (Fraction B)

A series of monotonic loading tests with different loading directions ($\alpha=0^{\circ}$ to $90^{\circ}$) and drained pure rotational shear tests with different stress ratios (Yang, 2013) are simulated using the original model and then the modified PSR model to test its ability in simulating the PSR and soil liquefaction. The model

parameters and initial conditions used in these simulations are listed in Table 4-1 and 4-2 respectively. Some critical test results are shown in Figures 4-3 and 4-4.

**Table 4-1. Soil parameters of Leighton Buzzard Sand (Fraction B).**

|  | Constant | Parameters | Value |
|---|---|---|---|
| Original model | Elasticity | $G_0$ | 275 |
|  |  | $v$ | 0.25 |
|  | Critical state | $M$ | 1.07 |
|  |  | $c$ | 0.77 |
|  |  | $\lambda_c$ | 0.017 |
|  |  | $e_0$ | 0.77 |
|  |  | $\xi$ | 0.7 |
|  | Yield surface | $m$ | 0.014 |
|  | Plastic modulus | $h_0$ | 2.5 |
|  |  | $c_h$ | 0.868 |
|  |  | $n^b$ | 0.7 |
|  | Dilatancy | $A_0$ | 0.7 |
|  |  | $n^d$ | 0.3 |
| Modified model | Plastic modulus | $h_{0r}$ | 2.27 |
|  |  | $\xi^r$ | 1.5 |
|  | Dilatancy | $A_r$ | 0.7 |

**Table 4-2.Initial conditions of Leighton Buzzard Sand (Fraction B) in the rotational shear tests.**

| Relative density after consolidation (%) | Voil ratio after consolidation $e_{con}$ | Stress ratio $q/p'$ | Principal stress parameter $b$ |
|---|---|---|---|
| 75.9 | 0.585 | 0.6 | 0.5 |
| 76.3 | 0.584 | 0.7 | 0.5 |
| 75.9 | 0.585 | 0.8 | 0.5 |
| 75.9 | 0.585 | 0.9 | 0.5 |
| 75.9 | 0.585 | 0.93 | 0.5 |
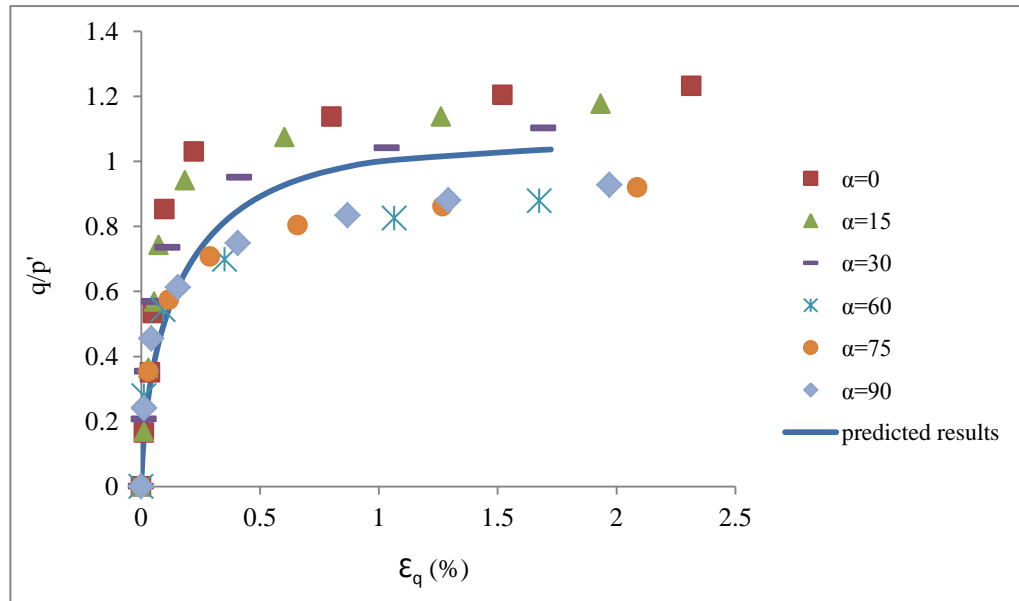


(a)
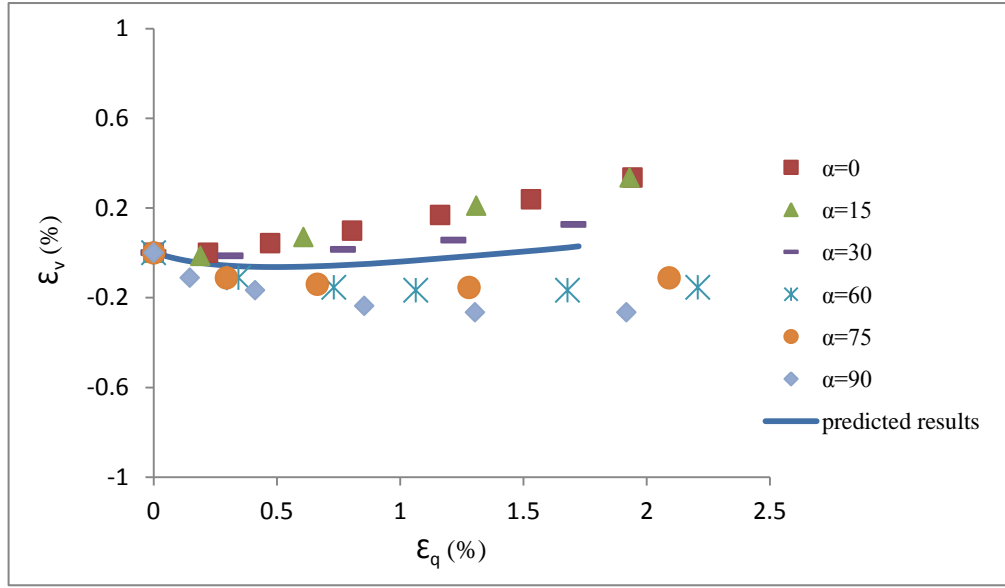
(b)

**Figure 4-3. Comparison of stress ratio-strain responses between the predicted results and laboratory results under the monotonic loading (dilation: positive).**

Figure 4-3 shows the comparison between the predicted results and the laboratory results under monotonic loadings. The original experimental tests consider the different loading angles to investigate the effect of fabric anisotropy of the sand. However, this model does not consider the fabric effect and cannot reflect the difference between the results under different loading angles. Therefore, the predicted results are intended to fit the average of the laboratory results. These results verify the ability of this model in simulating soil behaviors under the monotonic loading path.
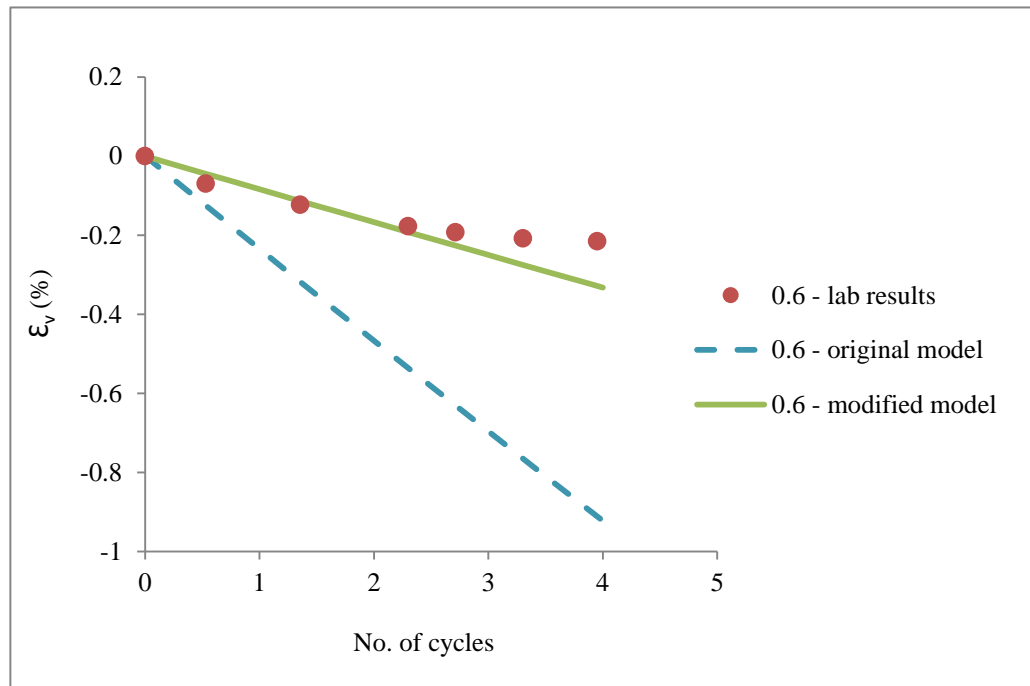
(a) stress ratio = 0.6.
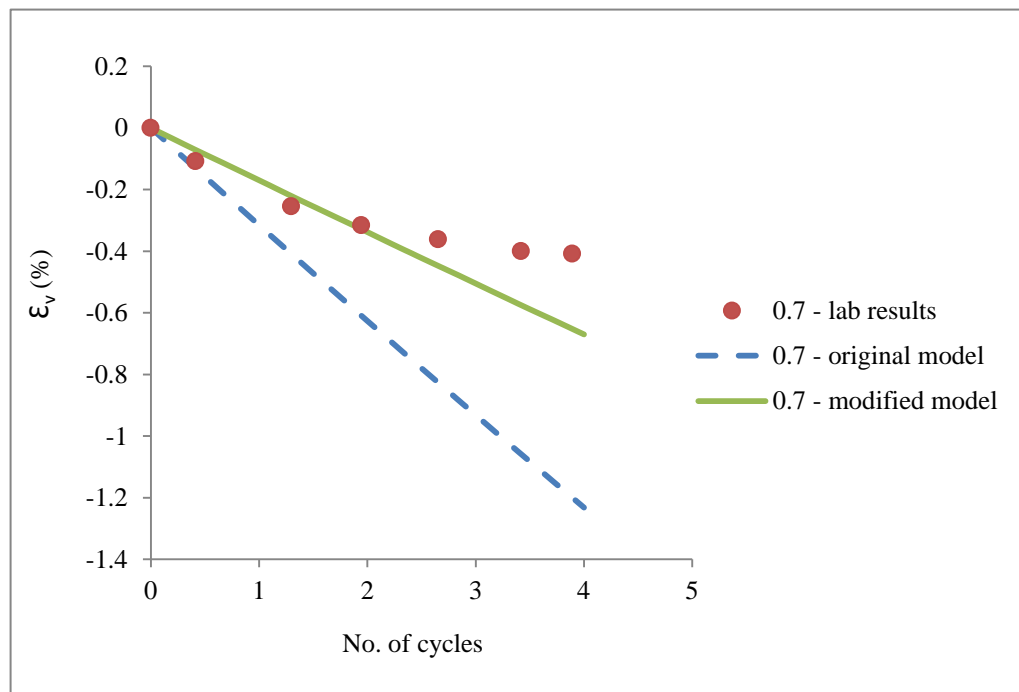


(b) stress ratio = 0.7.
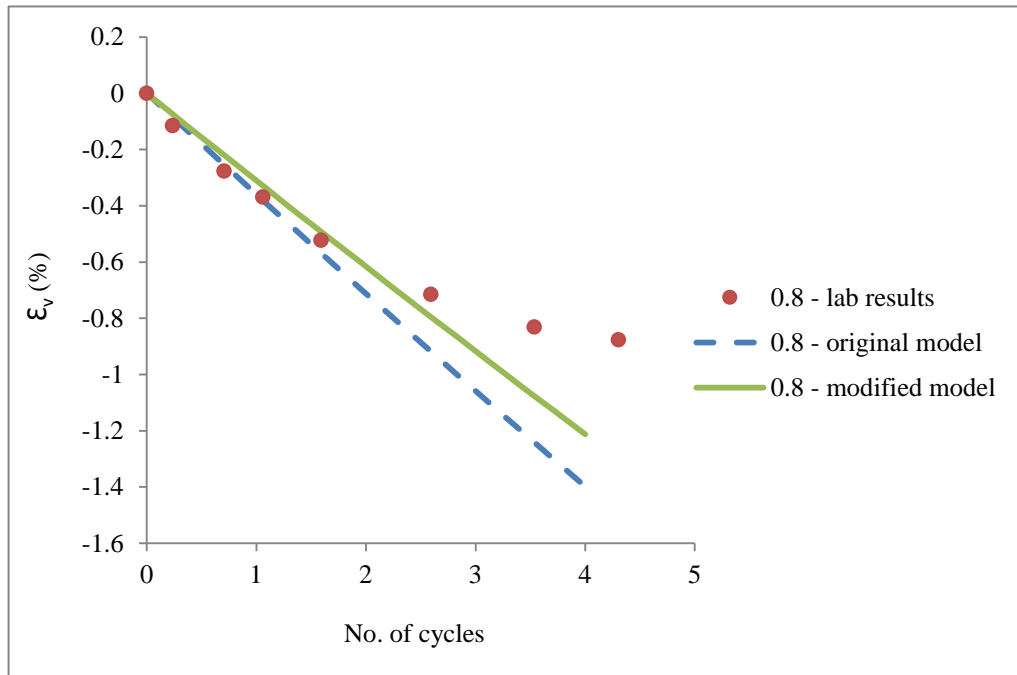
(c) stress ratio = 0.8.



(d) stress ratio = 0.9.

(e) stress ratio = 0.93.

**Figure 4-4. Comparison of volumetric strain developments between the predicted results and laboratory results under the drained pure rotational loading (dilation: positive).**
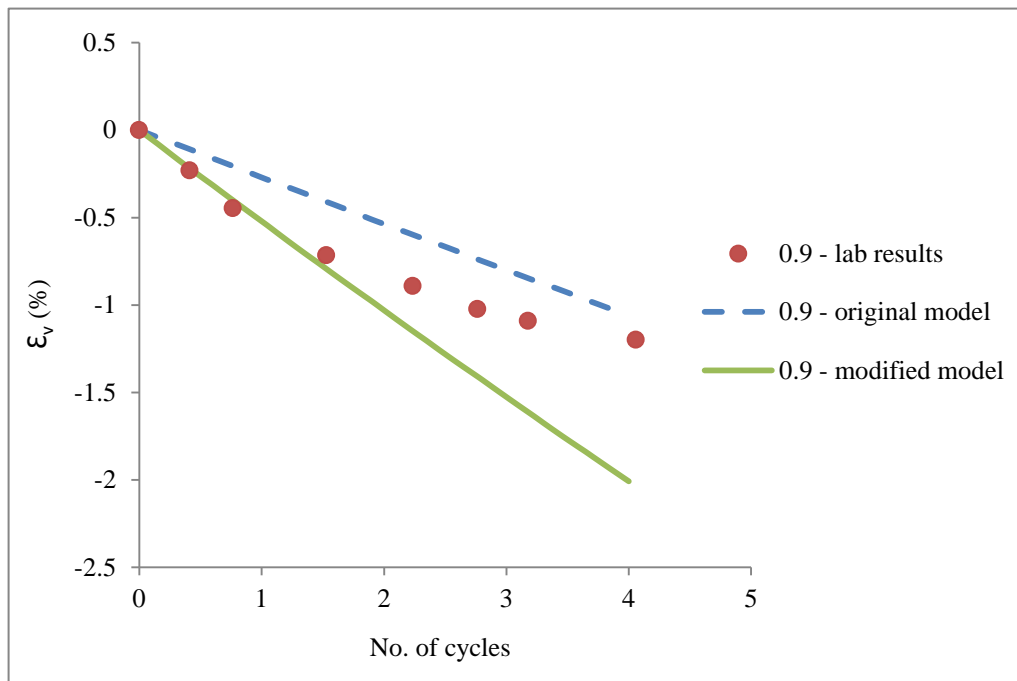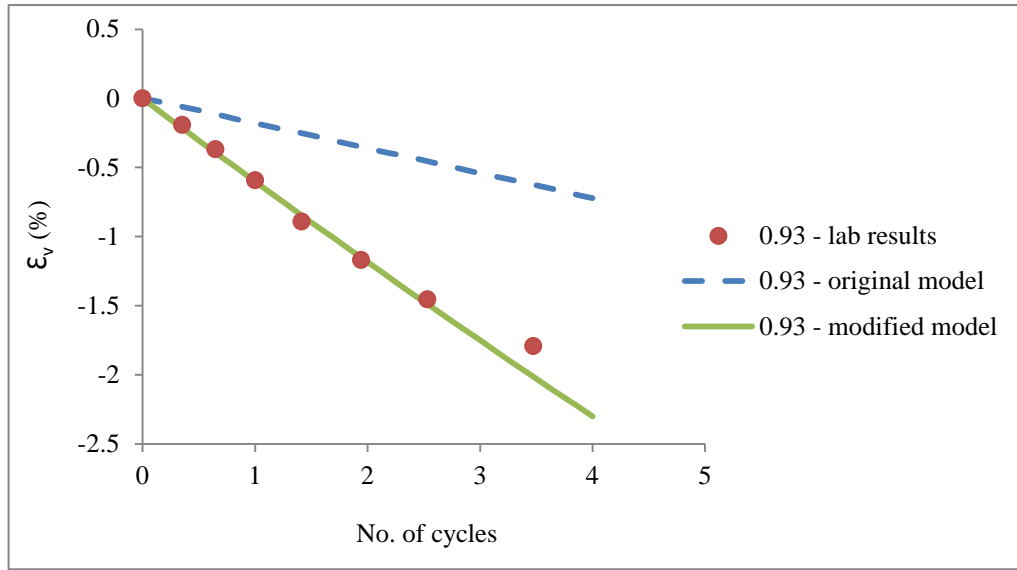
The predicted and experimental results of rotational shear loadings are shown in Figure 4-4. It can be seen that the original model underestimates the volumetric strain in the case of $q/p' = 0.93$ & 0.9, while it significantly overestimates the volumetric strain in the case of $q/p' = 0.8$, 0.7 & 0.6. This is mainly because the original model does not consider the PSR effect.

To better simulate this problem, the PSR model is developed based on the original model and used to simulate the same problem. In Figure 4-4, it can be observed that in the simulation of the same loading conditions, results from the modified PSR model show a significant difference compared to the original one. In the cases of $q/p'=0.6$, 0.7 & 0.8, the modified PSR model generate less volumetric strain, which agrees much better with the laboratory results. In the

case of $q/p'$=0.9, the original model underestimates the volumetric contraction, while the results from the modified PSR model only fit the laboratory results before the third cycle due to the large nonlinear effect as the principal stress continues to rotate. In the case of $q/p'$=0.93, which is close to the failure stress ratio, the results from the modified PSR model fit the laboratory results very well, while the original model still significantly underestimates the volumetric contraction. Generally, results from the modified PSR model fit better with the laboratory results than the original model. The experimental results also show a slight nonlinear trend while the responses of the predicted results are quite linear. This difference may be due to the fabric anisotropy which is beyond the scope of this study and not considered by the original and modified model in this research.

Therefore, the results from numerical simulations demonstrate that both the modified PSR model and the original model have the ability to simulate the monotonic loading conditions. However, the modified PSR model performs better than the original model under the rotational loading conditions with the PSR.

## 4.4.3 The calibration and the single element simulation of Leighton Buzzard sand (Fraction E)

Because the experimental centrifuge wave tests, numerically simulated in Chapter 5, use the loose Leighton Buzzard sand Fraction E (BS 100/170), the first 13 parameters in the original model are calibrated by using a series of triaxial tests with constant effective confining stress $p'$ from Visone (2008). All parameters including 3 PSR parameters which will be used in the finite element

simulations for the modified PSR model are listed in Table 4-3. The 3 PSR parameters are basically calibrated to better fit the experimental results from the centrifuge wave tank tests from Sassa & Sekiguchi (1999). Some typical results are shown in Figure 4-5. Compression is represented as positive sign.

**Table 4-3. Soil parameters of Leighton Buzzard Sand (Fraction E) used in the finite element analysis.**
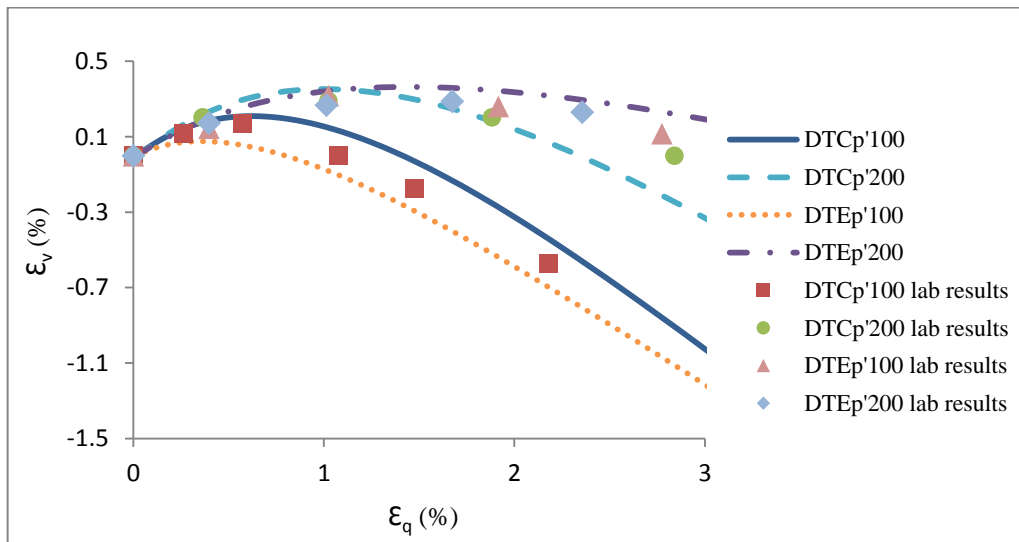
|  | Constant | Parameters | Value |
|---|---|---|---|
| Original model | Elasticity | $G_0$ | 100 |
|  |  | $v$ | 0.25 |
|  | Critical state | $M$ | 1.35 |
|  |  | $c$ | 0.712 |
|  |  | $\lambda_c$ | 0.15 |
|  |  | $e_0$ | 0.977 |
|  |  | $\xi$ | 0.203 |
|  | Yield surface | $m$ | 0.013 |
|  | Plastic modulus | $h_0$ | 10 |
|  |  | $c_h$ | 0.968 |
|  |  | $n^b$ | 0.3 |
|  | Dilatancy | $A_0$ | 1.0 |
|  |  | $n^d$ | 0.1 |
| Modified model | Plastic modulus | $h_{0r}$ | 3.3 |
|  |  | $\xi^r$ | 1.5 |
|  | Dilatancy | $A_r$ | 5.5 |
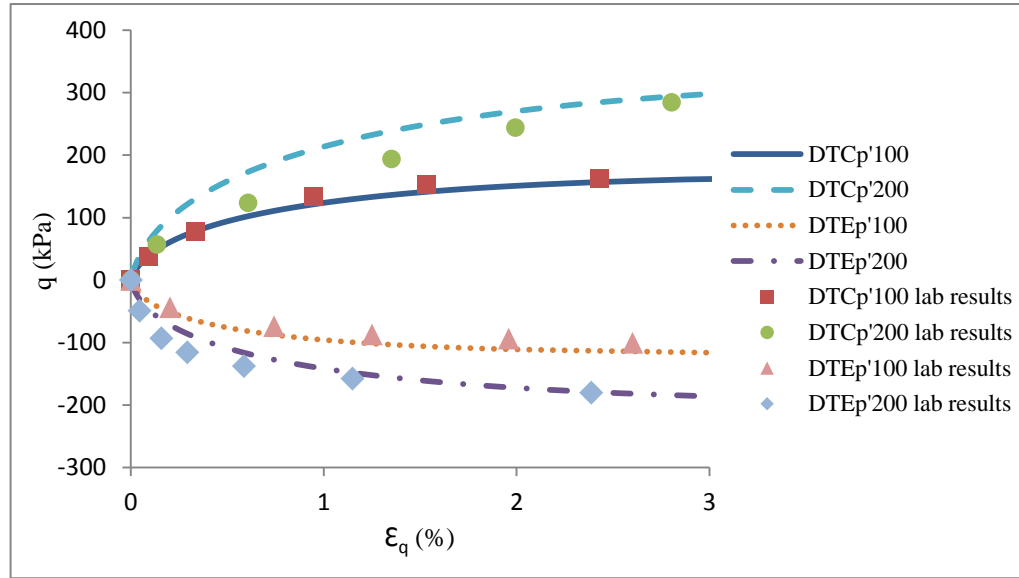
(a) Stress-strain responses



(b) Development of volumetric strain

**Figure 4-5. Predicted results and test results of Leighton Buzzard sand (Fraction E) from drained triaxial tests with constant *p'* (100 & 200 indicate the confining pressure, C stands for compression while E stands for extension).**

Figure 4-5 show that the predicted results generally fit the lab results very well. There is no difference between the simulation results from the original model and the modified PSR model because all the tests are subjected to the monotonic loadings which do not involve the PSR effect.

## 4.4.4 The calibration and the single element simulation of Nevada sand

The sand used in the centrifuge earthquake tests from VELACS project (Model No. 3) is the Nevada sand which has a specific gravity of 2.67 and the maximum and minimum void ratios of 0.887 and 0.511 respectively. All parameters used in the simulations of these centrifuge earthquake tests for the Nevada sand are calibrated by a series of triaxial, tosional and rotational tests for Nevada sand from Chen & Kutter (2009). The triaxial tests do not have the PSR effect because of their monotonic loading path, while the tosional and rotational tests have the PSR effect. These tests are also carried out to investigate the significance of the PSR and test the ability of the modified PSR model in simulating the PSR impact and soil liquefaction. All parameters are listed in Table 4-4. Some typical results are shown in Figures 4-6 to Figure 4-13.

**Table 4-4. Soil parameters of Nevada sand used in the finite element analysis.**

|  | Constant | Parameters | Value |
|---|---|---|---|
| Original model | Elasticity | $G_0$ | 150 |
|  |  | $v$ | 0.25 |
|  | Critical state | $M$ | 1.45 |
|  |  | $c$ | 0.712 |
|  |  | $\lambda_c$ | 0.005 |
|  |  | $e_0$ | 0.807 |
|  |  | $\xi$ | 0.5 |
|  | Yield surface | $m$ | 0.05 |
|  | Plastic modulus | $h_0$ | 5.5 |
|  |  | $c_h$ | 0.968 |
|  |  | $n^b$ | 0.55 |
|  | Dilatancy | $A_0$ | 0.6 |
|  |  | $n^d$ | 3.5 |
| Modified model | Plastic modulus | $h_{0r}$ | 0.9 |
|  |  | $\xi^r$ | 1.1 |
|  | Dilatancy | $A_r$ | 0.5 |

The initial conditions of the drained and undrained tests are summarized in Table 4-5. Figure 4-6 to Figure 4-9 show the predicted results along with the experimental results. It can be seen that both the predictions for the drained and

undrained tests generally fit the laboratory results very well. Therefore, this model has a good performance in reflecting soil behavior under drained monotonic loadings as well as the undrained monotonic loadings.

**Table 4-5. Test conditions for drained and undrained triaxial tests (Chen & Kutter, 2009).**

| Specimen | Relative density (%) | Back pressure (kPa) | B value (%) | Initial confining pressure (kPa) |
|----------|----------------------|---------------------|-------------|----------------------------------|
| N70D501 | 74 | 250 | 98.1 | 50 |
| N70D1001 | 72 | 250 | 98.6 | 100 |
| N70D100A | 76 | 200 | 100 | 100 |
| N70D100B | 82 | 200 | 98.3 | 100 |
| N70D100C | 85 | 200 | 99 | 100 |
| N70D2501 | 75 | 250 | 99.1 | 250 |
| N50U1 | 70 | 250 | 98.9 | 50 |
| N60U1002 | 63 | 250 | 96 | 100 |
| N60U2501 | 75 | 250 | 95.5 | 250 |
| N60U4002 | 66 | 250 | 97.3 | 400 |
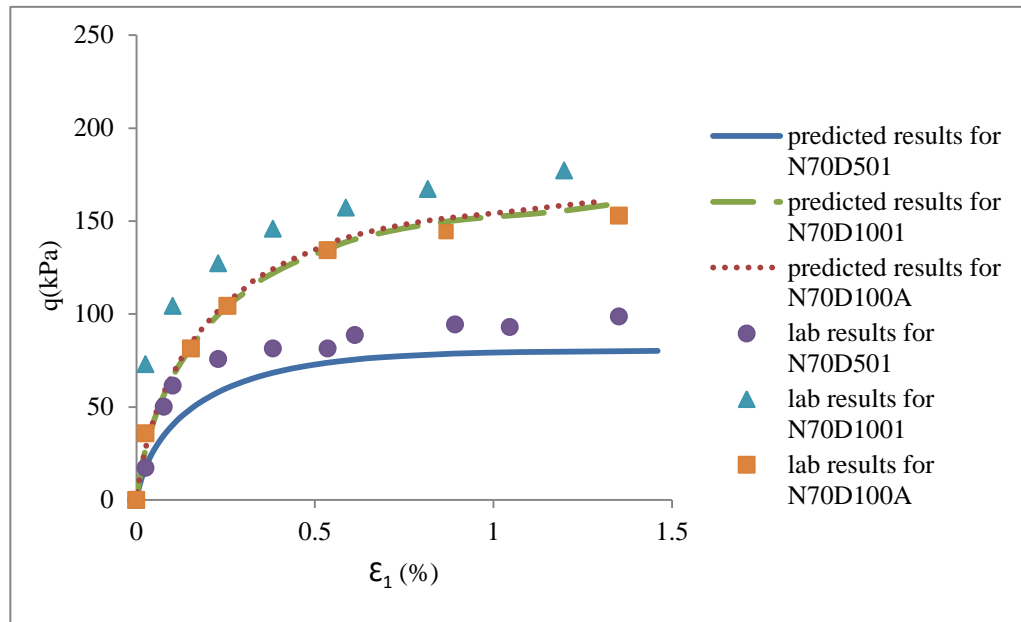
(a)
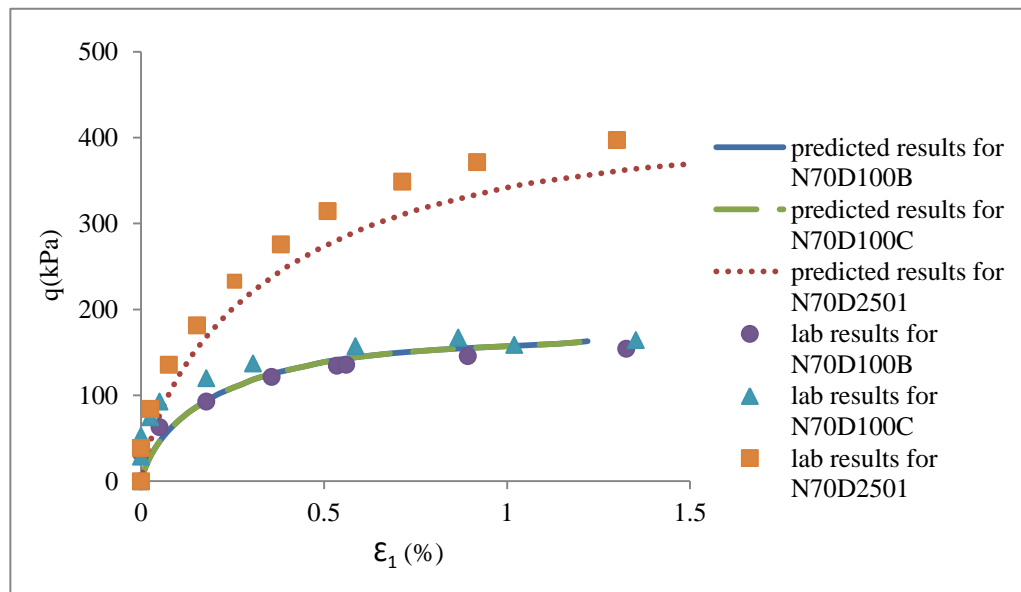


(b)

**Figure 4-6. Test results and model predictions of stress strain behaviors for the drained monotonic loadings.**

(a)



(b)

**Figure 4-7. Test results and model predictions of relationships between stress ratios and volumetric strains for the drained monotonic loadings.**
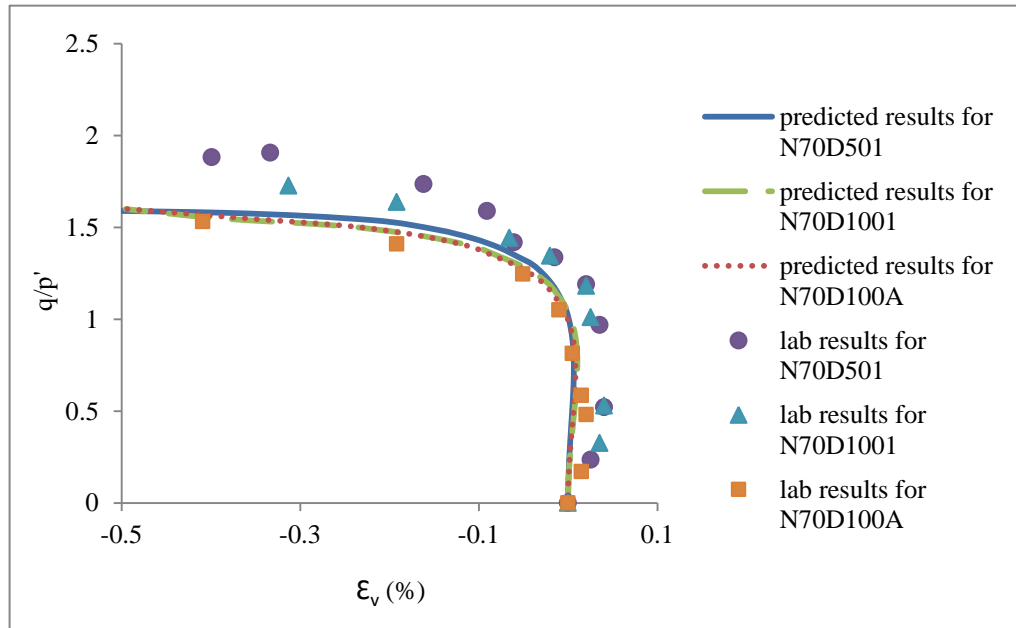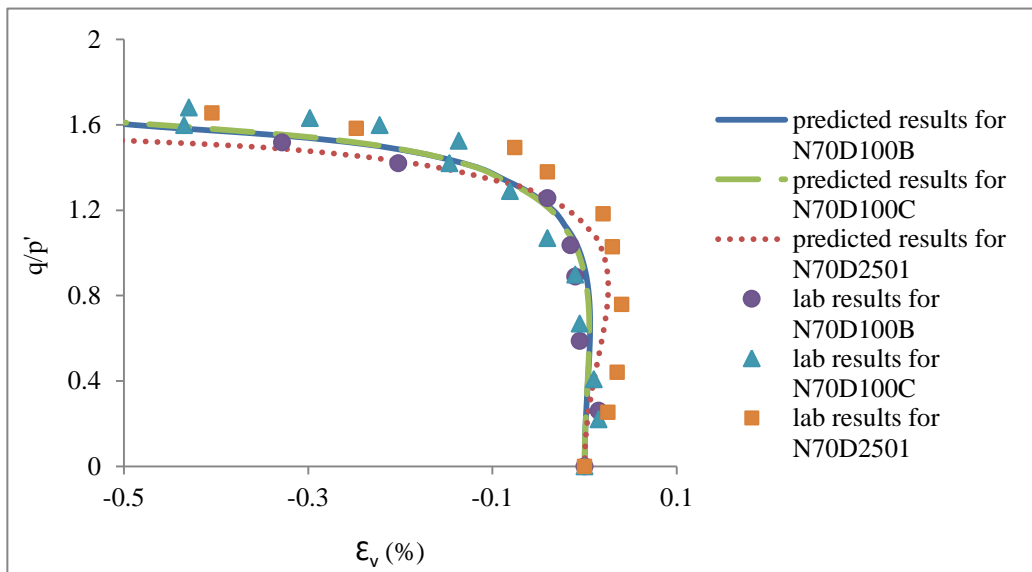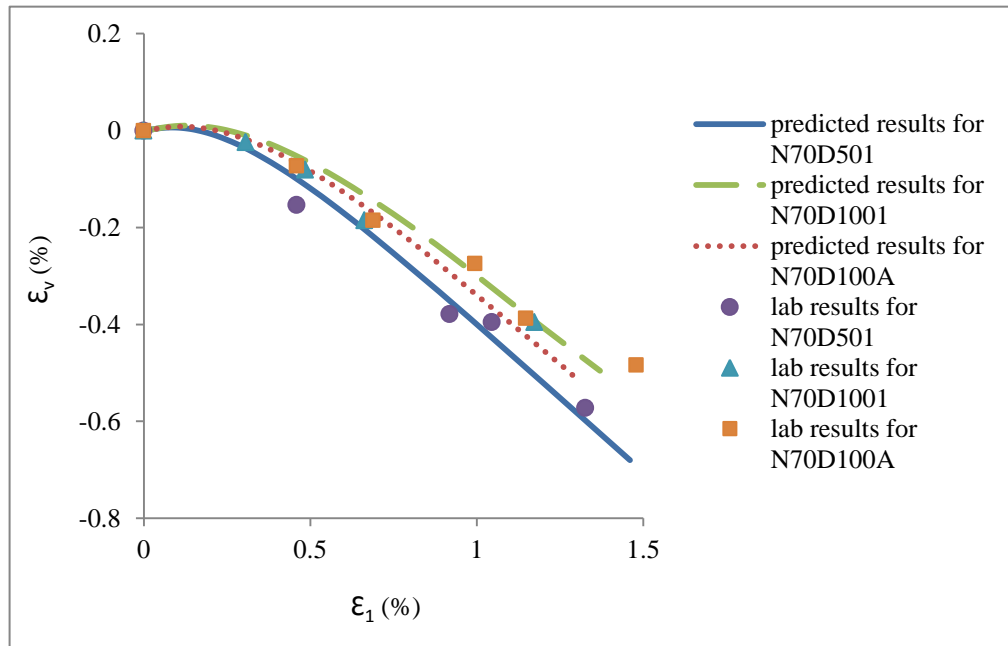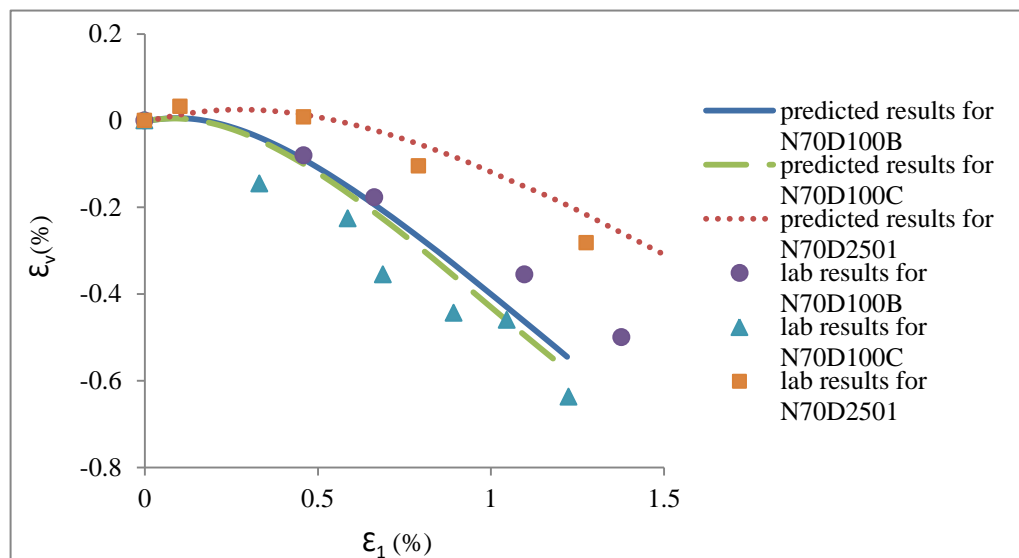
(a)



(b)

**Figure 4-8. Test results and model predictions of volumetric strain behaviors for the drained monotonic loadings.**
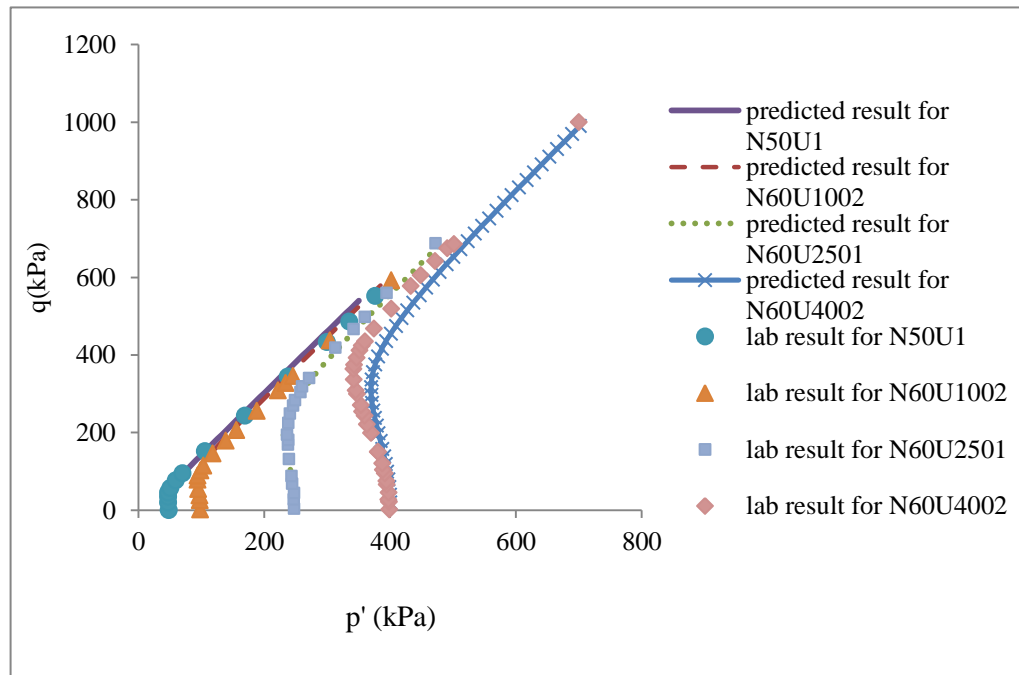
(a)
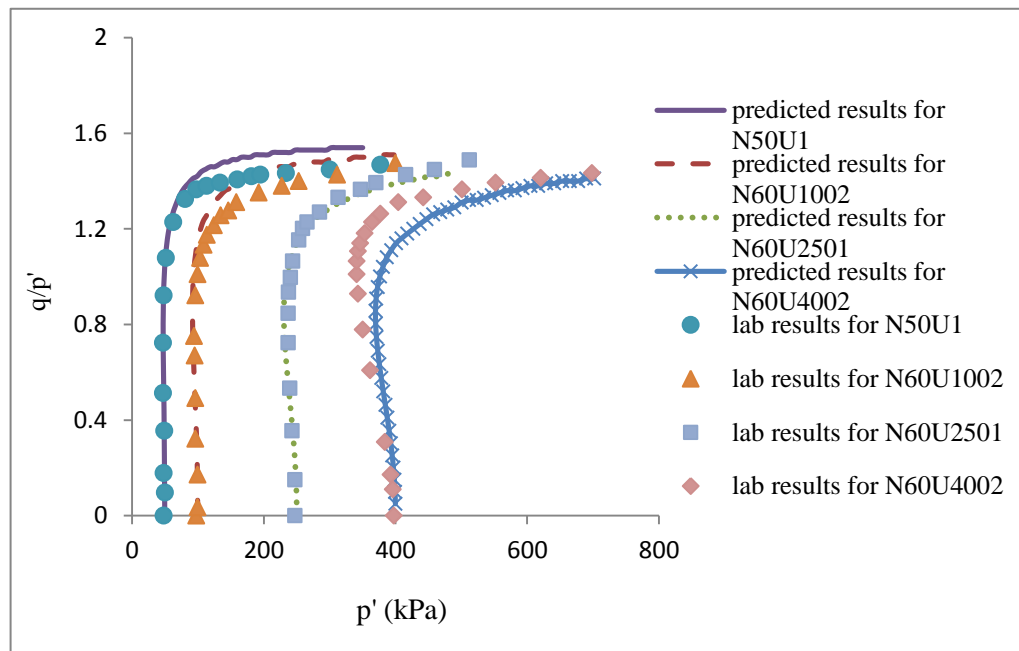


(b)
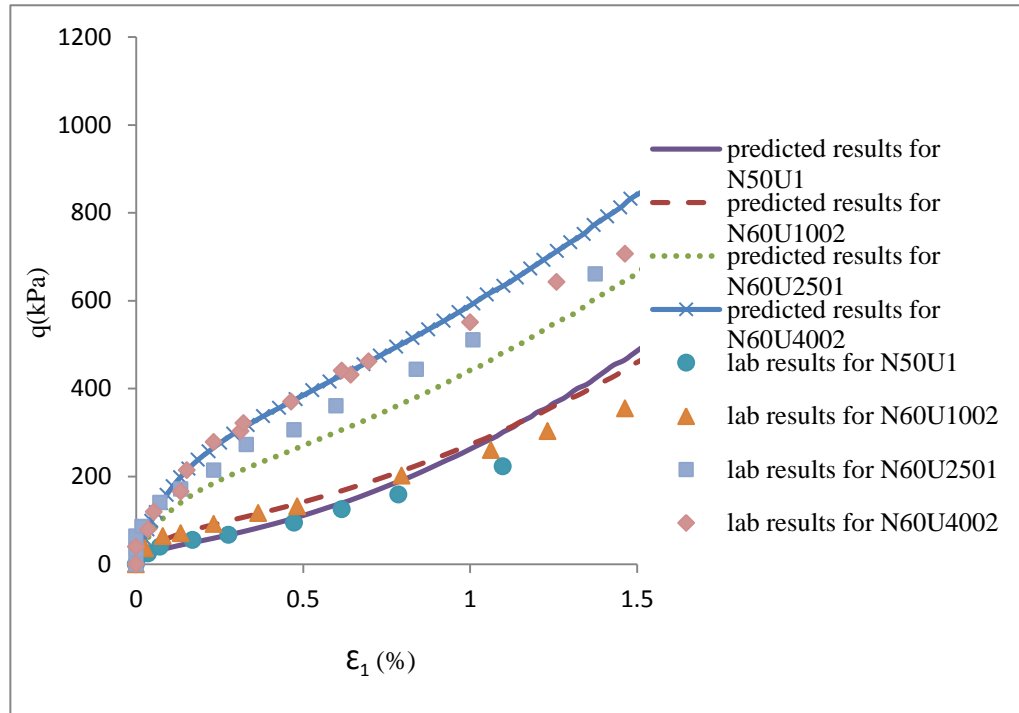
(c)

**Figure 4-9. Test results and model predictions for the undrained monotonic loadings.**

The initial conditions of the torsional shear tests are summarized in Table 4-6 and Figure 4-10 to Figure 4-12 show the results of them. The predicted results of Test NK10CU63 in Figure 4-10 show that both the original model and modified PSR model underestimate the reduction of the effective confining pressure $p'$ and the shear strain. This underestimation may also be resulted from the effect of fabric change. There is no difference between the predicted results from these two model because the principal stress does not rotate when $K(\sigma_\theta/\sigma_z) = 1.0$. However, results from the modified PSR model show significant differences compared to the original model in Tests NK73CU6 and NK138U51 in which the value of $K$ is not equal to 1.0 and the PSR effect is included.

In Figure 4-11, it can be seen from the results of the original model that the effective confining pressure $p'$ reduced about 75 kPa, then the $q$-$p'$ stress path shows the butterfly shape and $p'$ stops reducing. Meanwhile, as the shear stress continues to move repeatedly, no dramatic shear strain is observed, which is significantly different from the laboratory results because the original model does not consider the PSR. In the results from the modified PSR model, the effective confining pressure reduced from 200 kPa to 75 kPa, which is much lower than the minimum value from the original model (120 kPa). The modified PSR model also predicts greater value of $(\sigma_z\text{-}\sigma_\theta)/\sqrt{3}p'$ than the original model in Figure 4-11(b) because $\sigma_z\text{-}\sigma_\theta$ is held constant in the tests and the variation of this value is due to the variation of $p'$. In addition, a dramatic increasing of shear strain (more than doubled) can be seen in the last cycle in Figure 4-11(c), indicating the liquefaction of soil.

Figure 4-12 generally shows the similar trends. In Figure 4-12(a), both models overestimate the rate of the reduction of $p'$ in the first stage with the smaller value of the shear stress, while the $p'$ from the modified PSR model reduced almost 15 kPa more than the results from the original model and agrees much better with the lab results in the second stage of shearing. In Figure 4-12(c), the original model still significantly underestimates the shear strain while the modified PSR model overestimates the shear strain which may be due to the more complicated loading conditions of two stages with different shear stress magnitudes. Furthermore, it is difficult to accurately predict the shear strain after the liquefaction has taken place. Generally, although the modified PSR model still slightly underestimates the reduction of $p'$ and sometimes overestimates the shear strain, it brings the soil to the liquefaction as the shear strain is more than doubled at the later stage and performs much better than the

original model compared with the experimental results in the simulation of torsional shear tests.

**Table 4-6. Test conditions for torsioanl shear tests (Chen & Kutter, 2009).**

| Specimen | Relative density (%) | Back pressure (kPa) | B value (%) | Cell pressure (kPa) | K ($\sigma_\theta/\sigma_z$) | Testing cycles |
|---|---|---|---|---|---|---|
| NK73CU6-1 | 68 | 100 | 97 | 213 | 0.73 | 12.5 |
| NK73CU6-2 | 68 | 100 | 97 | 213 | 0.73 | 10 |
| NK10CU63 | 65 | 100 | 100 | 300 | 1.0 | 4 |
| NK138U51 | 71 | 200 | 99.2 | 400 | 1.38 | 4.75 |
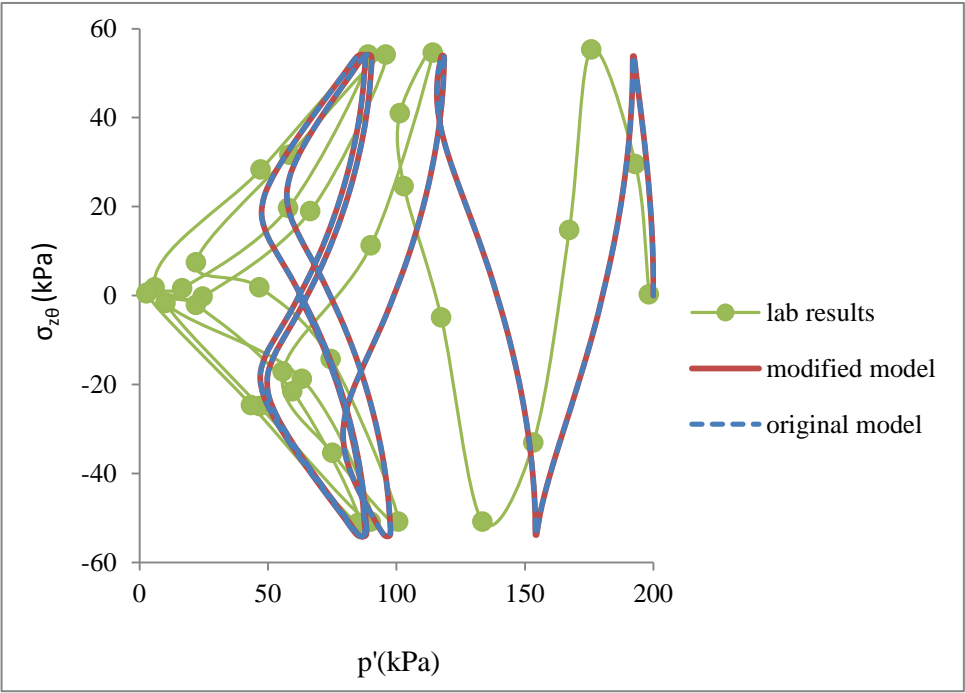


(a)
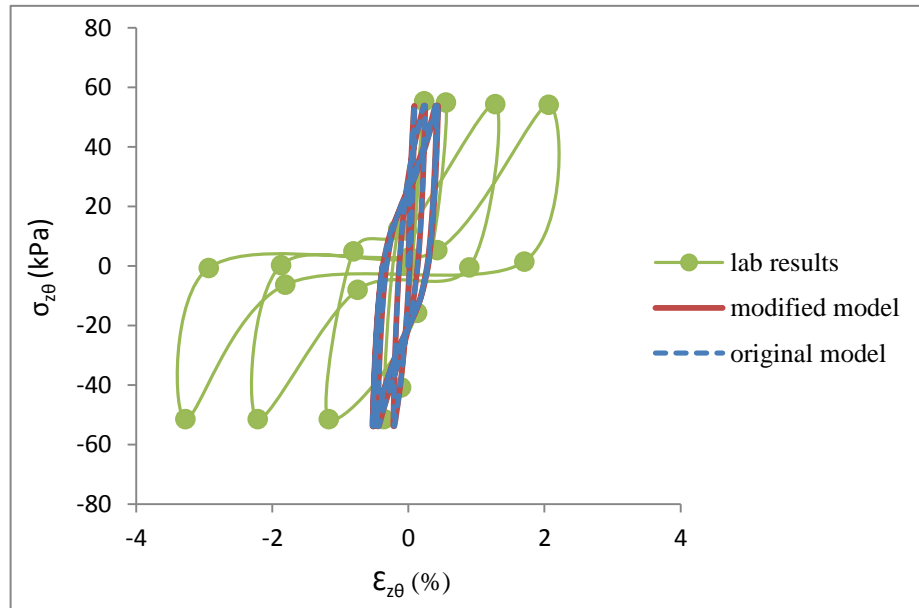
(b)

**Figure 4-10. Test results and model predictions for the Torsional Shear Test NK10CU63.**
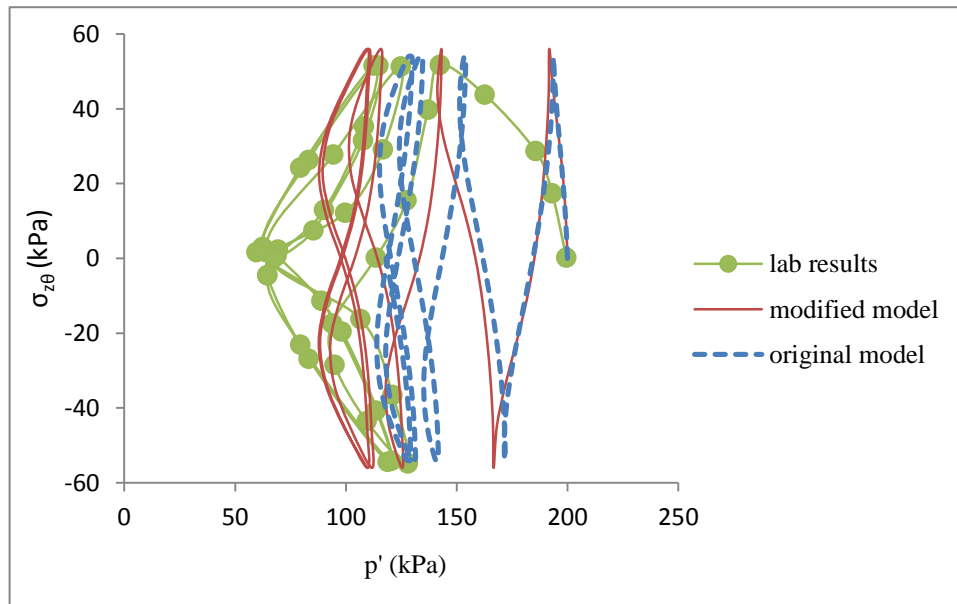


(a)
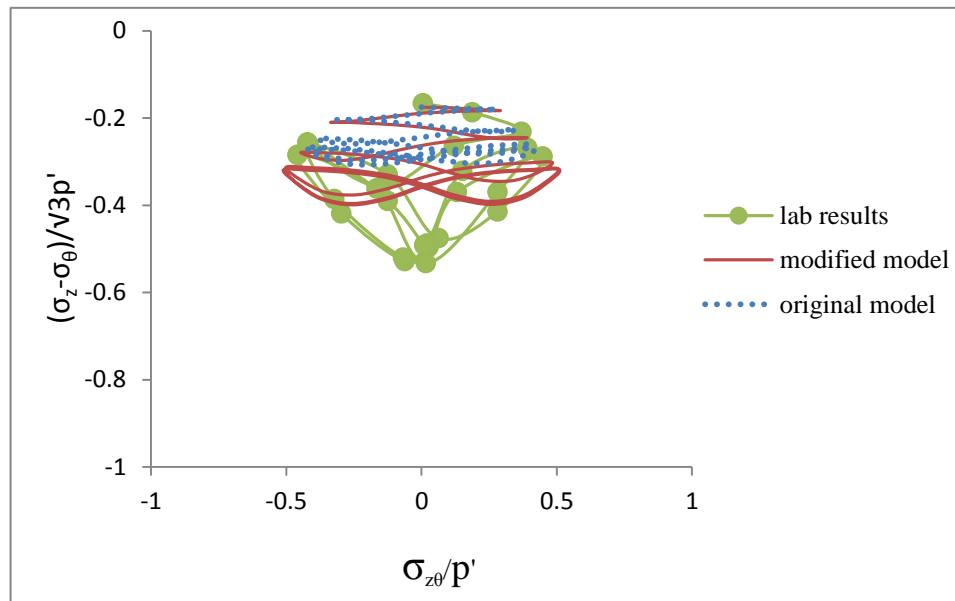
(b)
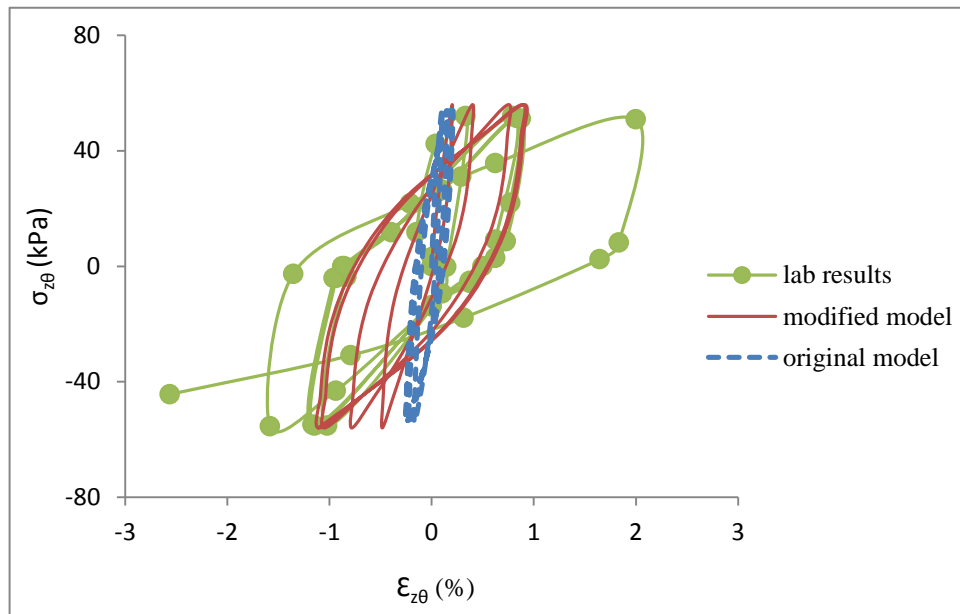


(c)

**Figure 4-11. Test results and model predictions for the Torsional Shear Test NK138U51.**

(a)
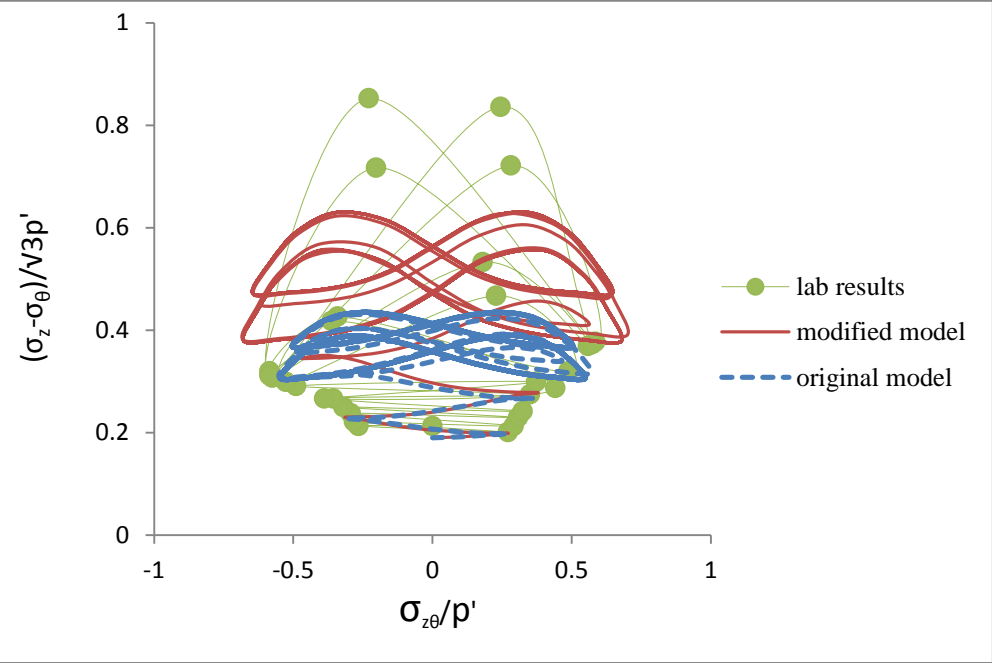


(b)
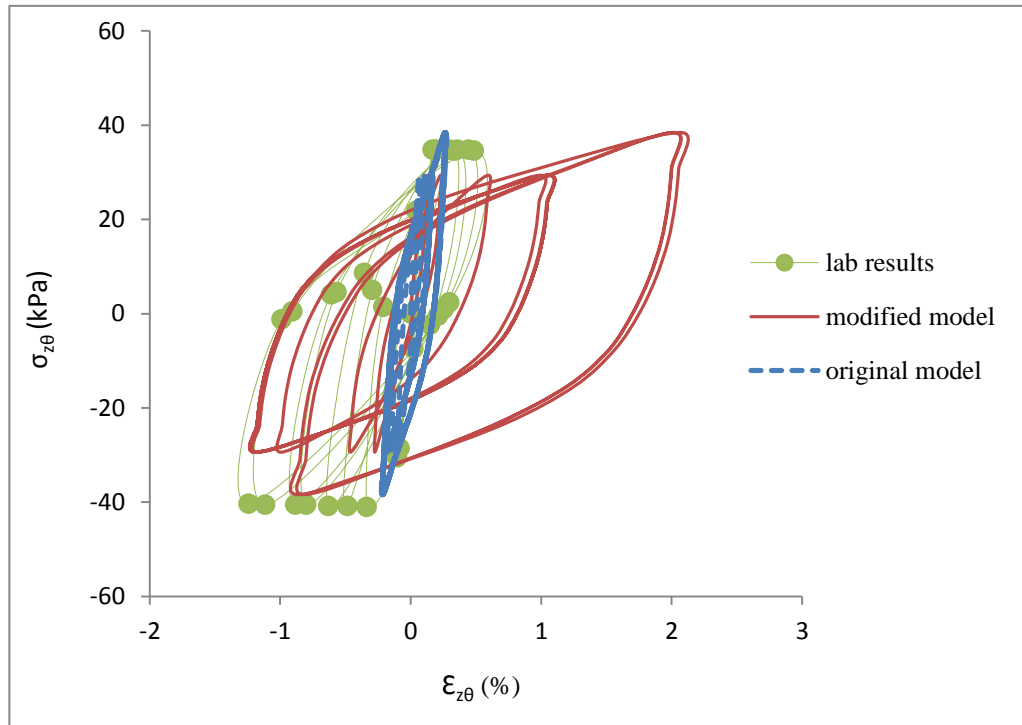
(c) Shear stress strain behaviors

**Figure 4-12. Test results and model predictions for the Torsional Shear Test NK73CU6.**

The test conditions for the rotational shear test NR40CU62 are listed in Table 4-7, and the simulation results and experimental results are shown in Figure 4-13. It can be seen from Figure 4-13(a) that the stress paths from these two models are exactly the same, while the soil responses are quite different. In the rest of figures, the predicted results from the original model show the limited effective confining pressure reduction and very small shear strain and deviatoric strain. Therefore, the original model can only predict limited reduction of p' and evolution of the shear strain of soil under undrained cyclic stress path including pure principal stress rotation, and is unable to bring the soil to liquefaction, because it does not consider the PSR effect completely.

However, in the predicted results from the modified PSR model, the effective confining pressure reduced 25 kPa more than the original model, and the maximum shear strain reached 3.5% with a dramatic increase in the last cycle, which agrees very well with the lab results and brings the soil to the liquefaction as well.

**Table 4-7. Test conditions for the rotational shear rest (Chen & Kutter, 2009).**

| Specimen | Relative density (%) | Back pressure (kPa) | B value (%) | Cell pressure (kPa) |
|----------|----------------------|---------------------|-------------|---------------------|
| NR40CU62 | 67 | 100 | 99 | 300 |
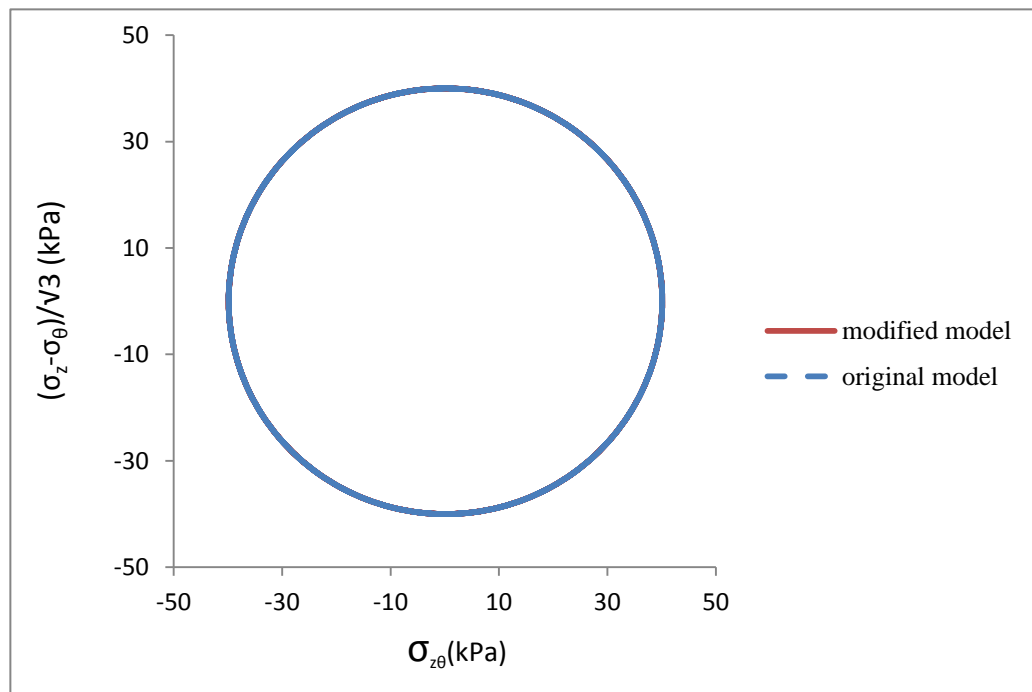


(a)
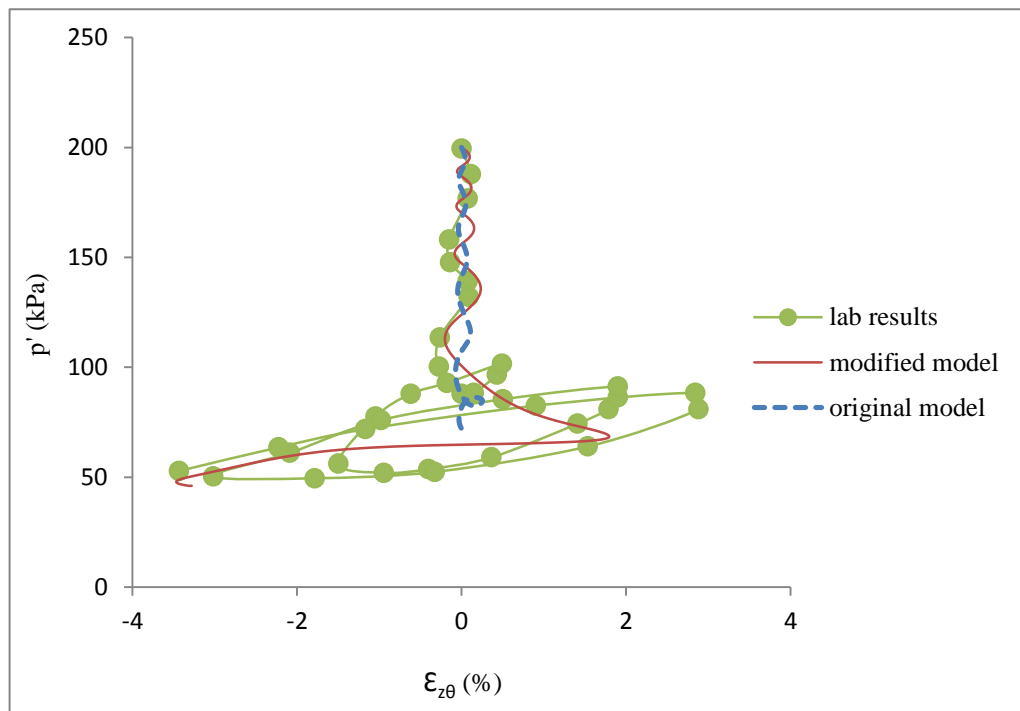
(b)
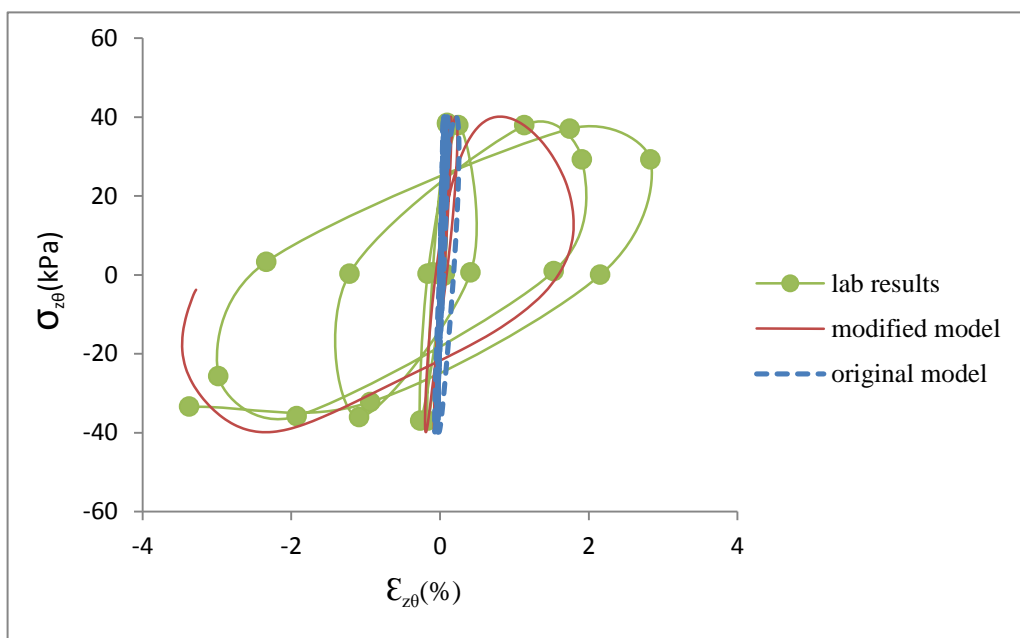


(c)
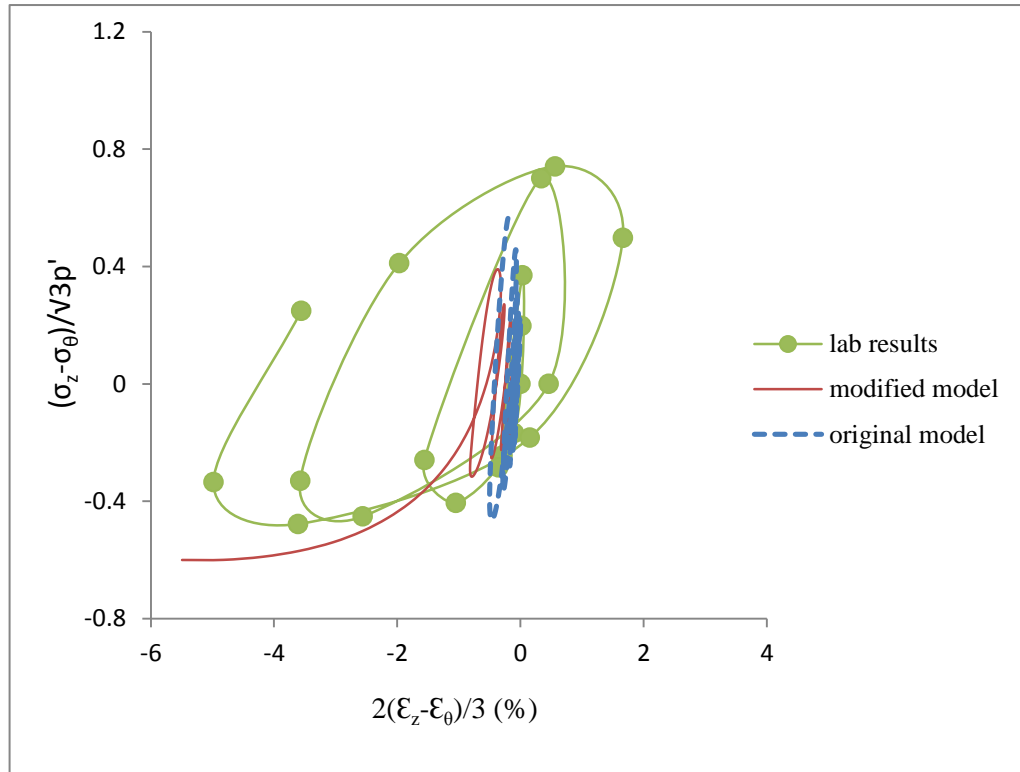
(d)

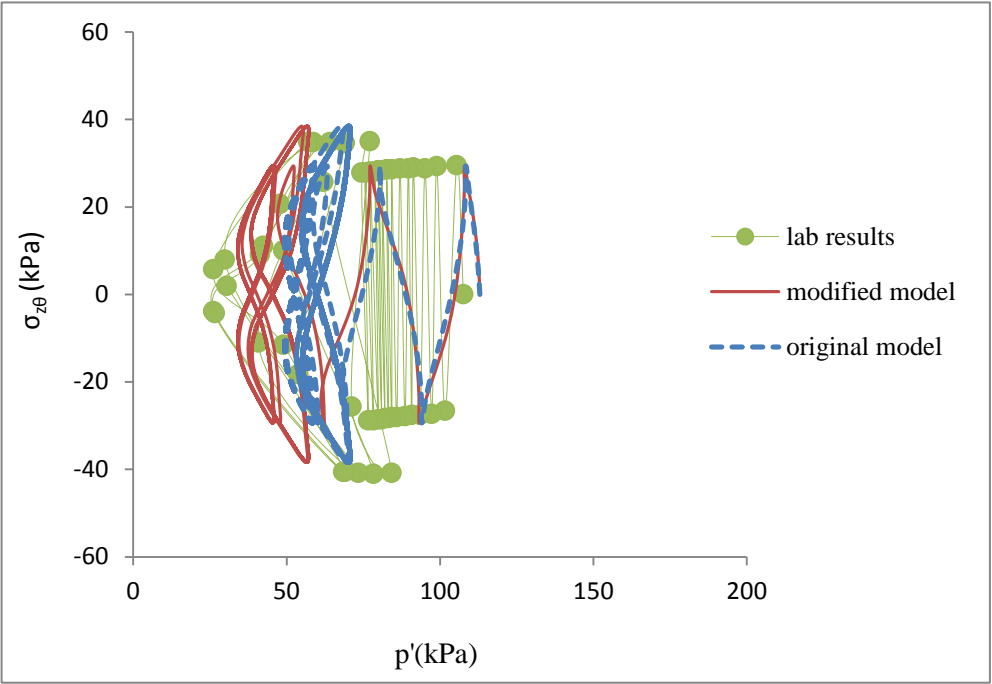**Figure 4-13. Test results and model predictions of the rotational shear test NR40CU62.**

In conclusion, the results from single element numerical simulations demonstrate that the modified PSR model has the ability to simulate the principal stress rotation and soil liquefaction, and agrees much better than the original model with the laboratory results under the same loading condition. Therefore, it is important to consider the PSR impact in the single element numerical simulations of these experimental tests. These results will be further verified by the finite element analysis in the following chapters.

## 4.5 Summary

This chapter has firstly introduced the original base model and the modified model considering the PSR impact. Then three single element simulations including the Hollow Cylinder tests from Yang (2013) for Leighton Buzzard sand (Fraction B), triaxial tests from Visone (2008) for Leighton Buzzard sand (Fraction E) and triaxial, tosional and rotational tests from Chen & Kutter (2009) for Nevada sand No. 120. have been presented to validate the model performance in simulating the PSR impact and calibrate the model parameters for these sands.

The original base model is developed based on the classical plasticity with bounding surface concept and kinematic hardening. The back-stress ratio and the state parameter are employed in this model to represent influences of the different confining stresses and void ratios on the sand behavior. Then, the new model is developed by treating the plastic strain rate induced from the PSR separately and without the modification on the evolution of the hardening parameter. The modified PSR model introduced three new PSR parameters which are independent of the monotonic loading, and can be easily calibrated through the pure rotational loading paths at different stress ratio levels. The stiffness tensor of the modified PSR model is independent of stress increments, and the stress and strain increments have a linear relationship, which indicates the easy numerical implementations in boundary value problems. Moreover, formulations in the modified PSR model will be downgraded to the original model when there is no PSR effect involved in the loading conditions.

In all the single element simulations, the predicted results from the models with

and without considering the PSR effect, as well as the experimental results have been compared to investigate the significance of PSR impact. Although diverse stress paths under both drained and undrained conditions have been simulated, the comparison generally show that the original model can only produce very limited $p'$ reduction and cumulative shear strain under cyclic loading paths, thus significantly underestimates the laboratory results and is unable to bring the soil to the liquefaction. However, in the same loading conditions, the modified PSR model generates much more reduction of $p'$ and shear strains, and agrees much better with the experimental results due to its complete ability in the simulation of the PSR impact. Furthermore, liquefactions can be observed in the predicted results from the modified PSR model, which agrees with the experimental sand behaviors. Both models are suitable for simulations of the monotonic loadings under drained and undrained conditions.

# Chapter 5 The Finite Element Simulation of Wave-Seabed Interactions

## 5.1 Introduction

The wave loading can generate considerable PSR in seabed soil. This chapter simulates the wave-seabed interactions using the finite element method. The impact of principal stress rotation (PSR) on the soil stress-strain responses in the simulations is considered by utilizing the modified PSR model. The focus of this chapter is on the investigation of PSR impacts. Both the original model and modified PSR model will be implemented into the finite element software to simulate experimental results by Sassa & Sekiguchi (1999). The predicted results by using the soil models with and without considering the PSR impact as well as the laboratory results from the centrifuge tests will be compared to explore the PSR impact in these boundary value problems. Both the progressive wave and standing wave loadings will be applied to the sand bed and the soil behaviors under these different wave loadings will be investigated.

## 5.2 Problem Definition

The centrifuge experimental study carried out by Sassa & Sekiguchi (1999) investigated the behaviors of sand bed under fluid wave trains. They found that the liquefaction has occurred in the sand specimen because of the build-up of residual pore pressures and the PSR effect plays an important role in this sand behavior. They also observed the different liquefaction resistance under the

progressive wave loading and the standing wave loading.

In these centrifuge tests with plane strain condition, a seabed with saturated sand is 100 mm deep and 200 mm wide (Figure 5-1). A steady-state acceleration of 50 $g$ is applied to the centrifuge. The sand is loose Leighton Buzzard sand 100/170. The soil specimen is subjected to both the progressive wave loading and the standing wave loading which has the wave length denoted by $L$ and wave period by $T$. These two types of wave loadings are defined by the pore pressure $u_0$ on the soil surface ($z=0$) as follows:

$$u = u_0 \sin(\kappa x - wt) \quad \text{(progressive wave)} \tag{5.1}$$

$$u = u_0 \cos(\kappa x) \sin(wt) \quad \text{(standing wave)} \tag{5.2}$$

where $u_0$ is the amplitude of the fluid pressure fluctuation imposed on the soil surface ($z=0$). $\kappa$ is the wave number and $w$ is the angular frequency of the waves, they are defined as:

$$\kappa = 2\pi/L \tag{5.3}$$

$$w = 2\pi/T \tag{5.4}$$
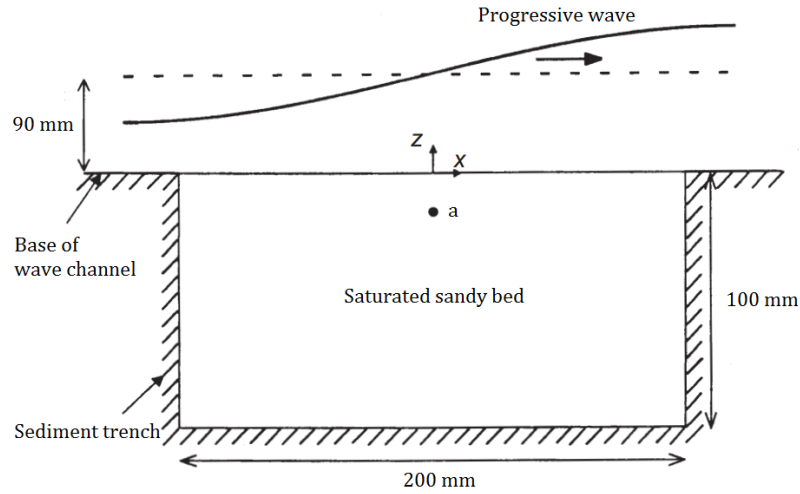
**Figure 5-1. Sand bed setup for the progressive wave loading.**

**Table 5-1. Cases analyzed for progressive wave loading.**

| Description | P1 | P2 | P3 | P4 | P5 | P6 | P7 | P8 |
|---|---|---|---|---|---|---|---|---|
| $u_0$ | 1.0 | 2.0 | 3.0 | 3.5 | 4.0 | 4.5 | 5.0 | 6.0 |
| $\chi_0 = \kappa u_0 / Y'$ | 0.03 | 0.06 | 0.09 | 0.10 | 0.12 | 0.13 | 0.14 | 0.17 |

For the progressive wave loading, 8 cases with different $u_0$ from 1 kPa to 6 kPa were simulated (Table 5-1). The intensity of the progressive wave is also represented by the cyclic stress ratio $\chi_0 = \kappa u_0 / Y'$ (Sassa & Sekiguchi, 2001), where the saturated unit weight of soil, $Y'$, was 425 kN/m$^3$, and $\kappa$ was 12.2m$^{-1}$. The standing wave loading is illustrated in Figure 5-2 and 10 cases with diverse cyclic stress ratios are also analyzed (Table 5-2). Antinode is set at the middle of the seabed width.

The problem is simulated by a finite element software—ABAQUS. The soil model and two types of waves are implemented by ABAQUS user subroutines

written in Fortran language. 55 quadrilateral elements (11 columns by 5 rows) with 4 nodes are used for the simulations. The bottom boundary is set to be fixed while the side boundaries are smooth vertically, and all of them are impermeable. The permeability $K_D$ used is 0.0015 m/s. All cases analyzed are assumed to be under $K_0$ condition before the wave loading is applied, and $K_0$ is set to be 0.52, which is in accordance with the simulation from Sassa & Sekiguchi (2001). 25 cycles of the wave loading are considered in total, with a time increment of 0.0024 suggested by Sassa & Sekiguchi (2001). Generally, the same setting is used in this simulation compared to the simulation from Sassa & Sekiguchi (2001). Furthermore, the numerical implementation of the modified PSR model is performed using an explicit substepping integration algorithm with automatic error controls. In this integration scheme, the imposed strain increment can be automatically divided based on the prescribed error tolerance and details can be found in Abbo (1997).
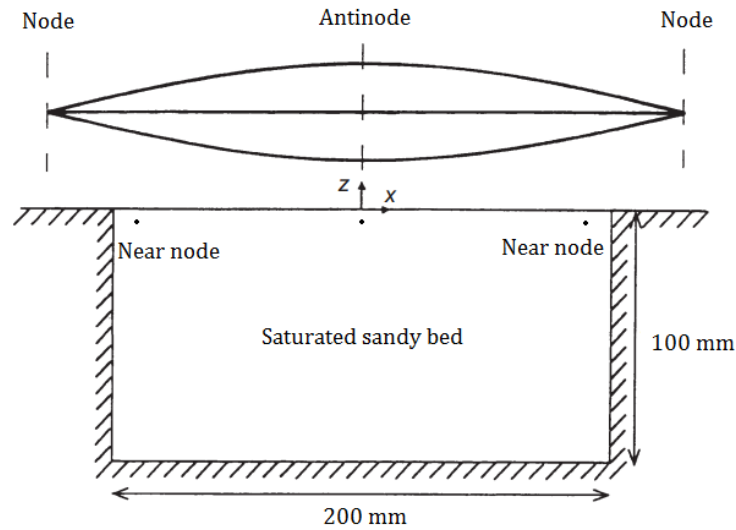


**Figure 5-2. Sand bed setup for the standing wave loading.**

**Table 5-2. Cases analyzed for standing wave loading.**

| Description | S1 | S2 | S3 | S4 | S5 | S6 | S7 | S8 | S9 | S10 |
|---|---|---|---|---|---|---|---|---|---|---|
| $u_0$ | 1.0 | 2.0 | 3.0 | 4.0 | 5.0 | 6.0 | 6.7 | 7.0 | 7.2 | 8.0 |
| $\chi_0 = \kappa u_0/Y'$ | 0.03 | 0.06 | 0.09 | 0.12 | 0.14 | 0.17 | 0.19 | 0.20 | 0.21 | 0.23 |

# 5.3 Predicted Results and Comparisons with the Experimental Data

## 5.3.1 The progressive wave

Case P8 with the cyclic stress ratio $\chi_0=0.17$ is studied first. The soil response in the centerline of the seabed width with the depth of 15 mm (point $a$ in Figure 5-1) is presented in Figure 5-3 to 5-7. Only 19 cycles are recorded in these figures because the modified PSR model has already brought the soil to liquefaction in the 19th cycle. Unless specified, all stresses described in this chapter are effective stresses unless specified otherwise. Different formulation of deviatoric stress $q$ presented as follows is used in this chapter and next chapter to consider the full six stress variables.

Effective confining stress:

$$p' = (\sigma_1' + \sigma_2' + \sigma_3')/3 \tag{5.6}$$

Deviatoric stress:

$$q = \{2*[(\sigma_x - \sigma_y)^2 + (\sigma_y - \sigma_z)^2 + (\sigma_x - \sigma_z)^2] + \sigma_{xy}^2 + \sigma_{yz}^2 + \sigma_{xz}^2\}^{1/2} \tag{5.7}$$

In Figure 5-3, a significant build-up of residual pore water pressure can be observed in results from both the original model and modified PSR model due to the plastic contractive behavior of sand under the cyclic loading. However, the modified PSR model produces a higher pore pressure in the whole process, and finally reaches a residual pore pressure of 6.0 kPa. This value is about 95% of $\sigma_{v0}$, indicating the occurrence of liquefaction. The original model has a maximum residual pore pressure of 4.9 kPa, which is lower than the results from the modified PSR model and experimental tests, and does not reach liquefaction because it is only about 76% of $\sigma_{v0}$. Generally, the modified PSR model agrees better with the laboratory results, especially the residual pore pressure at liquefaction. However, both two models overestimate the pore pressure during the early stage of the simulation.
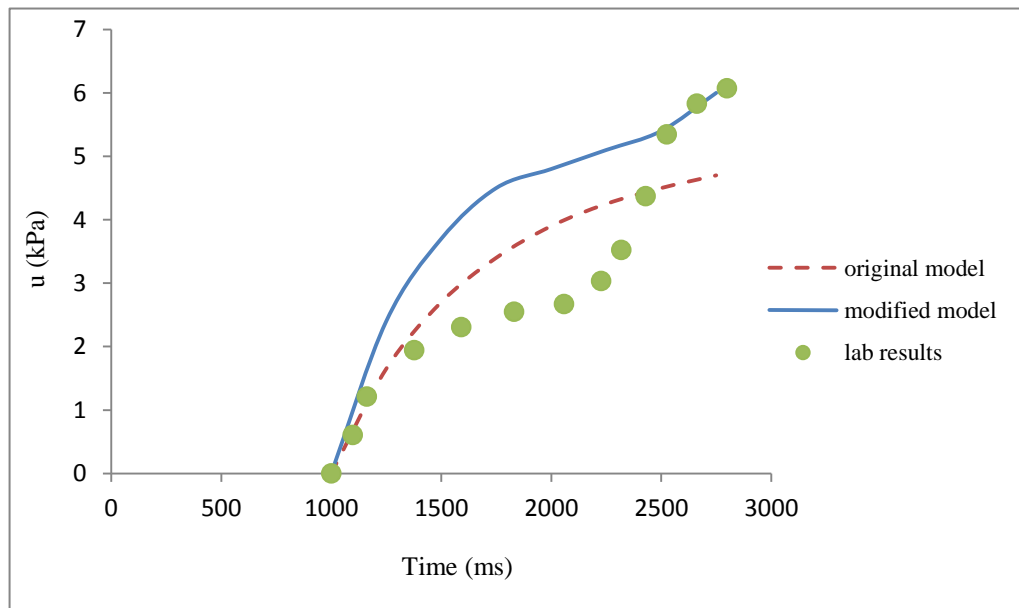


**Figure 5-3. Comparison of time history of excess pore water pressure between the simulations and laboratory tests in case P8.**

The same difference can be seen in the effective confining pressure $p'$ as well. In Figure 5-4, as the progressive wave repeatedly moving along the seabed surface, $p'$ continues to decrease in both the original and modified PSR model. But $p'$ from the modified PSR model decreases much more rapidly than the original model, and finally reaches a value very close to 0 as the residual pore pressure reaches the maximum value. In the original model, $p'$ reaches the lowest value of 0.75 kPa, and the average trend becomes flatter after 2 seconds. The $q$-$p'$ curve of the modified PSR model presented in Figure 5-5 also shows the decrease of $p'$. The test starts from point A and end at point B, where $q$ and $p'$ approaches the value of 0.
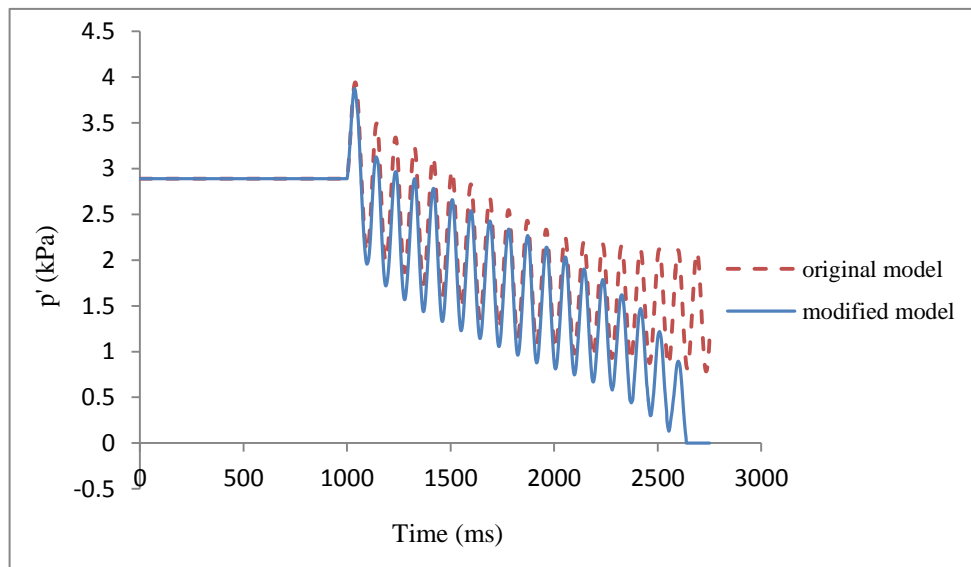


**Figure 5-4.Predicted reductions of effective confining pressure in case P8.**
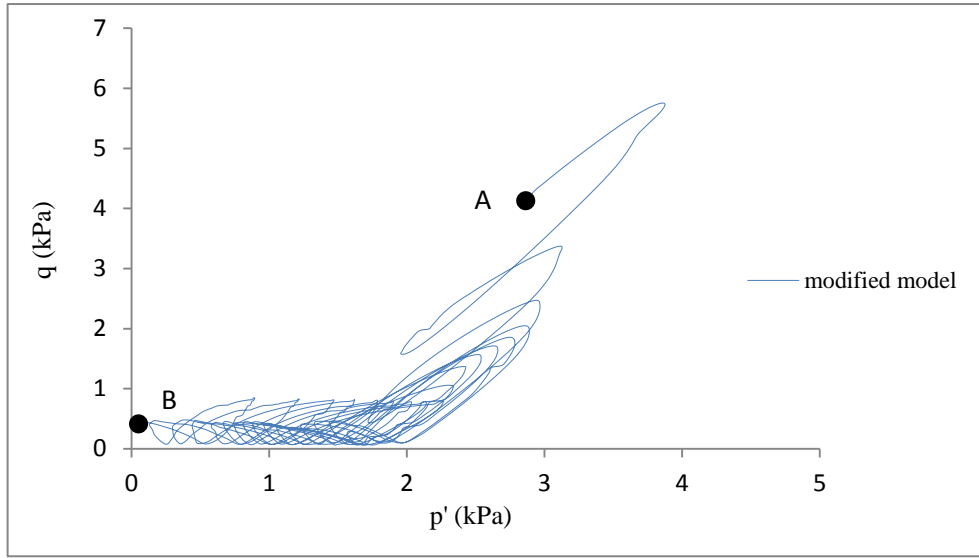
**Figure 5-5. Predicted stress paths from the modified model in case P8.**

The stress paths of the original model and modified PSR model in stress space of $\sigma_{xz}$ and $(\sigma_x-\sigma_z)/2$ are plotted separately in Figures 5-6(a) and 5-6(b) for clarity. They clearly show that the principal stress is continuously rotating under the progressive wave. In addition, as $(\sigma_x-\sigma_z)$ decreases, $\sigma_x$ tends to be equal to $\sigma_z$.
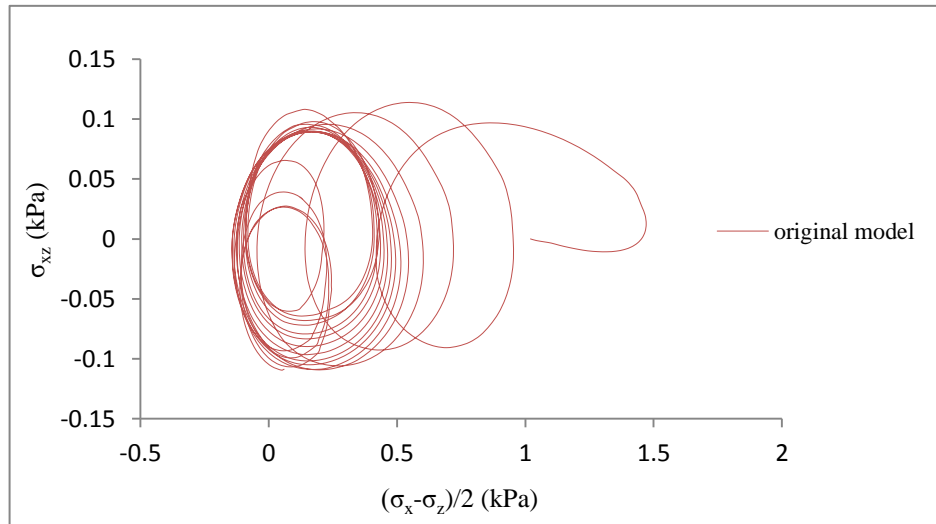


(a) the original model
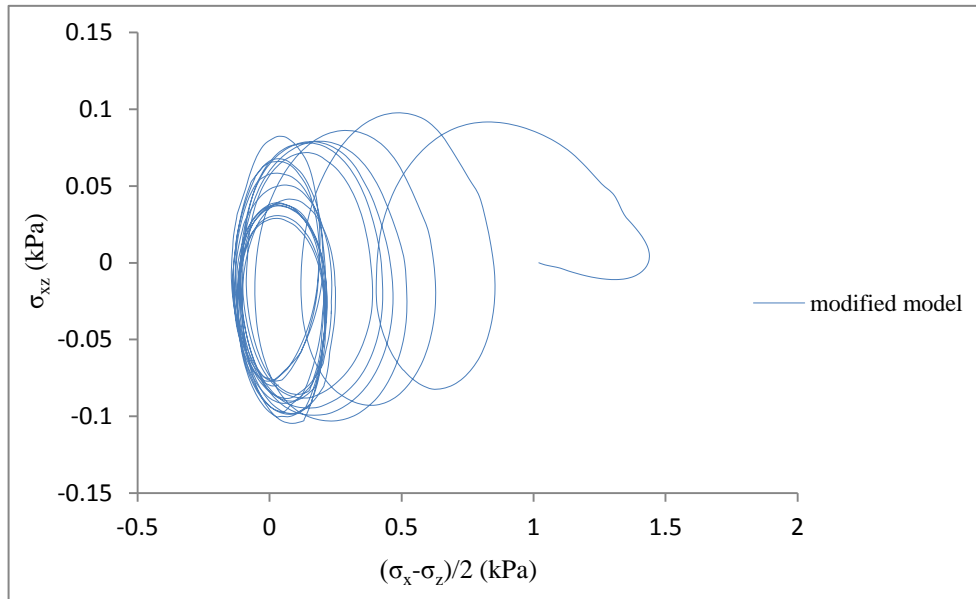
(b) the modified model

**Figure 5-6. Predicted stress paths in the PSR space in case P8.**

In total, 25 cycles are simulated for all 8 cases, and the overall results of excess pore pressure distribution along depth are shown in Figure 5-7 below. Generally, all results show a nonlinear behavior, especially for the cases with high cyclic stress ratio. The occurrence of liquefaction strongly depends on the cyclic stress ratio $\chi_0$, because the results give a general trend that the higher cyclic stress ratio can generate the higher pore pressure. Note that these results are recorded for the full 25 cycles, which is different from the results presented above for 19 cycles of case P8.

Results in these 8 cases show that along the depth, the modified PSR model usually generates much higher pore water pressure. In the shallow depth (-15

mm) of case P8 (Figure 5-7(b)), the modified PSR model brings the soil to liquefaction in $19^{th}$ cycle while the original model only achieves the maximum pore pressure of 5.7 kPa in $25^{th}$ cycle, which is close but still does not reach the 90% of $\sigma_{v0}$. In the case of P7, the modified PSR model achieves the liquefaction in the last cycle, while the original model only predicts the maximum pore pressure of 4.6 kPa, which is much lower than the modified PSR model even after full 25 cycles are performed. In the case of P6, liquefaction doesn't occur with both two models. The modified PSR model also predicts higher pore water pressures than the original model in cases of P3, P4 and P5.

However, this difference between the original model and modified PSR model becomes unapparent when the cyclic stress ratio is small. In the cases of P1 and P2, the results of the original model and modified PSR model are very similar, only slight difference around depth 15 mm in case P2 can be observed. This is because the PSR effects are decreasing while the amplitudes of imposed waves are reducing. Figure 5-7(a) shows a clear trend that generally, the higher cyclic stress ratio leads to the more obvious difference between the modified and original model, which means the larger PSR effects. In summary, among all 8 cases, liquefaction occurs only in case P7 and P8 with the modified PSR model, in which the excess pore water pressures are close to the $\sigma_{v0}$ above the depth of 20 mm. This agrees with Sassa & Sekiguchi (1999) that the cyclic stress ratio of 0.14 in case P7 is the critical value for liquefaction in this depth. The original model cannot predict this critical value of cyclic stress ratio because it significantly underestimates the pore pressure build-up.

(a)

σ'$_{v0}$ against depth line

original model

modified model
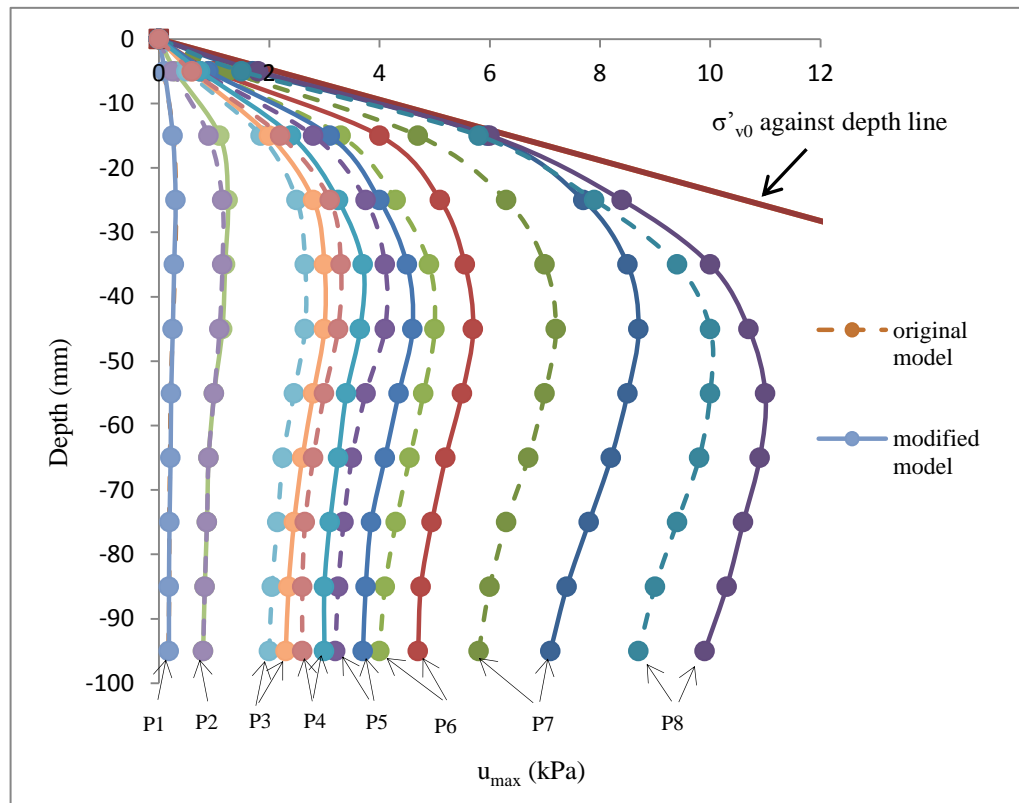
$u_{max}$ (kPa)
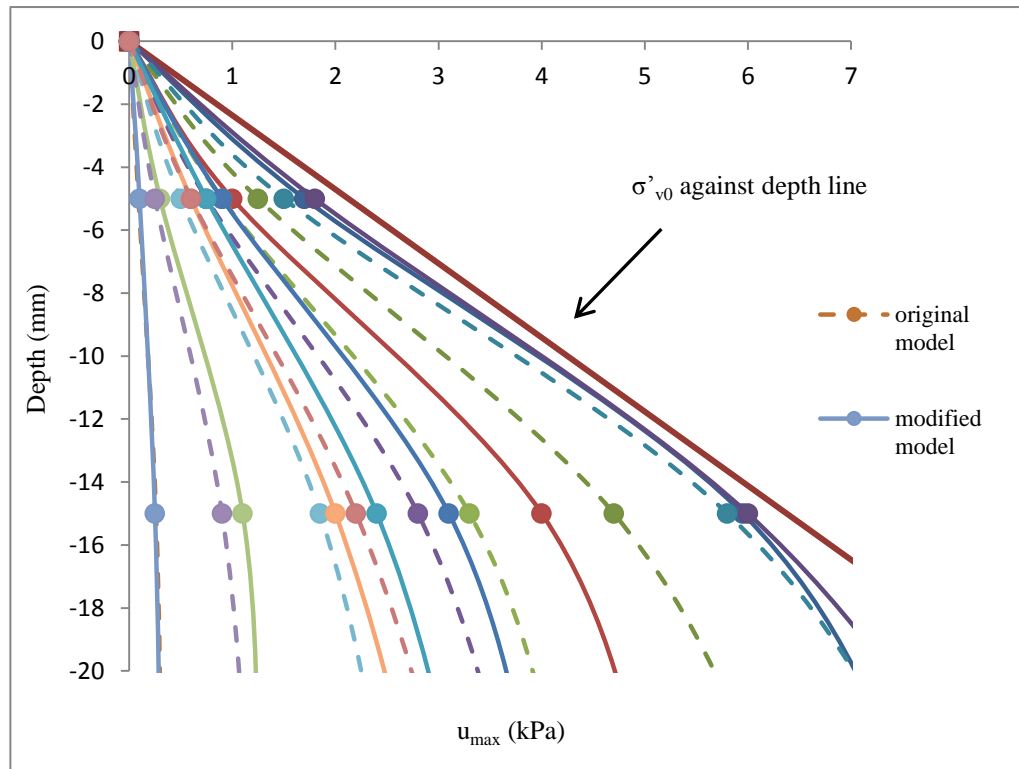
(b)

**Figure 5-7. Predicted $u_{max}$ with depth under progressive wave loadings. (a) results with full range of model depth. (b) detailed results above the depth of 20 mm.**

Figures 5-8 & 5-9 compare the results from the original and modified PSR model with the laboratory results in the shallow depth of 15 mm. The critical cyclic stress ratio for the occurrence of liquefaction can also be clearly seen here in the result from the modified PSR model. Moreover, comparison of values between the original and modified PSR model can still reflect that the PSR impact increases when the cyclic stress ratio becomes larger. Generally, the result of the modified PSR model agrees better with the laboratory results than the original model, especially in the range of high cyclic stress ratios. For

the cases of $\chi_0$ from 0.05 to 0.1, although the results from the original model are closer to the lab data, the differences between these two models are very small, which can be neglected. Figure 5-9 shows the reduction of $p'$ in the simulations by using these two models. Among all the data, $p'$ shows a strong nonlinear behavior and only reduces to zero in the cases of P7 and P8 with the modified PSR model, indicating the same trend in the excess pore water pressure discussed above.
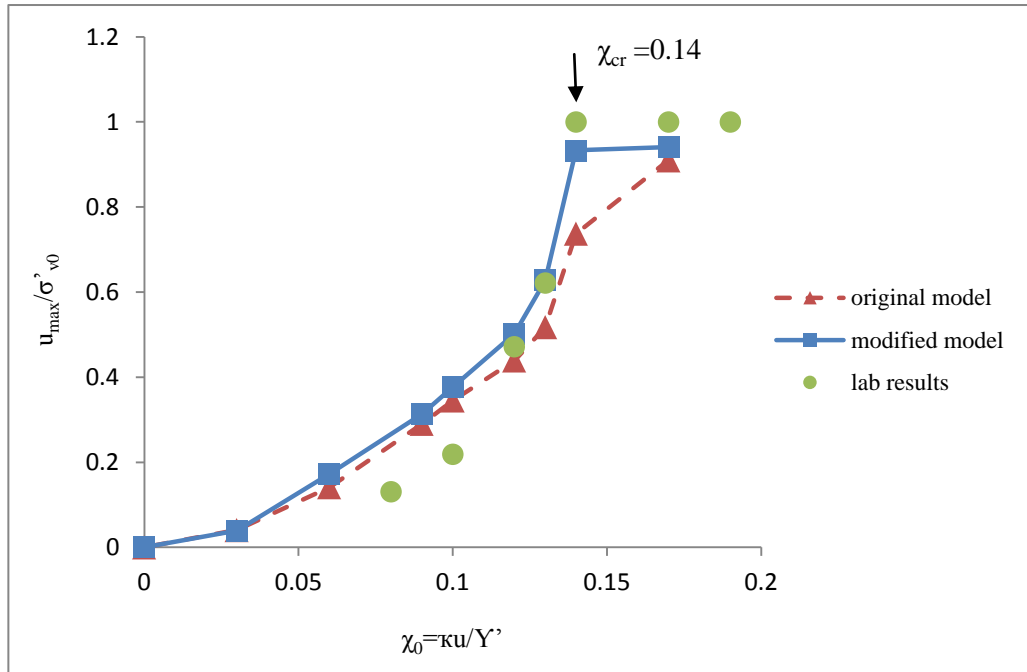


**Figure 5-8. Comparison of $u_{max}/\sigma'_{v0}$ with $\chi_0$ at the shallow soil depth (-15 mm) between the predicted results and laboratory results under the progressive wave loading.**
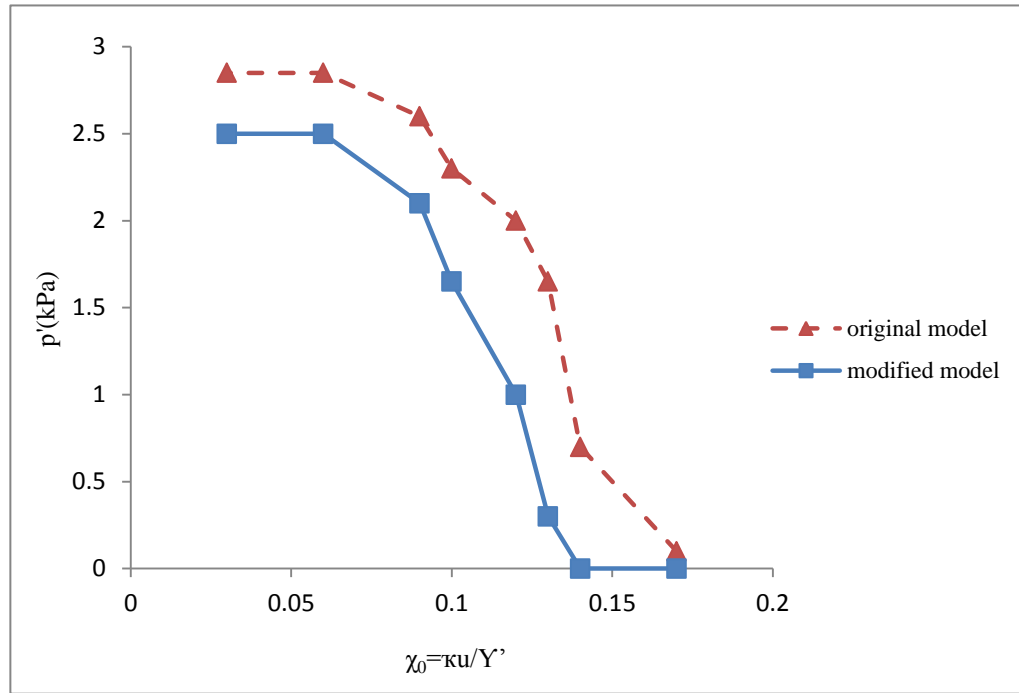
**Figure 5-9. Predicted *p'* with $\chi_0$ at the shallow soil depth (-15 mm) under the progressive wave loading.**

Figures 5-10 to 5-12 show the predicted pore water pressure contours at t=0.0024, 0.18 and 1.7 seconds in case P8. At the end of first time increment, a slight build-up of pore water pressure can be seen in Figure 5-10. At that time, there is no difference between the predicted results from the original model and modified PSR model because the wave intensity is very small. Figure 5-11 shows that at the start of shaking (t=0.18 seconds) an obvious build-up of pore water pressure can be seen at the top level of soil and generally decreases with the increasing depth. This trend is more obvious in the results from the modified PSR model with a larger liquefaction zone at the top level (pore water pressure ≥ 90% of initial effective vertical stress). The overall pore water pressures predicted from the modified PSR model are larger than the predicted results from the original model with a difference of more than 1 kPa. In Figure

5-12, the largest pore pressure zone progress downwards from the top level to the shallow depth (around 20 mm) at the time of 1.7 seconds. The overall predicted results from the modified PSR model are again larger than the results from the original model because of the consideration of PSR impact.
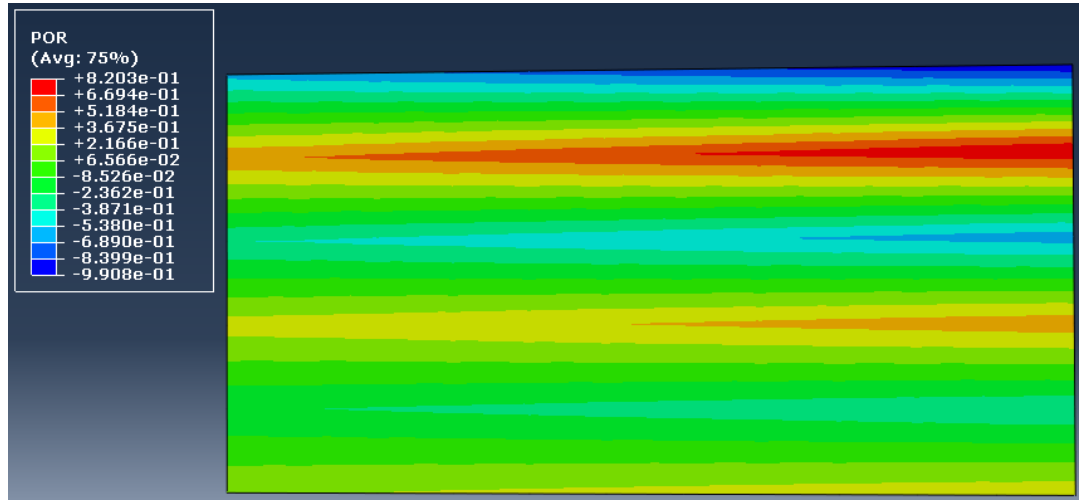


(a) The original model
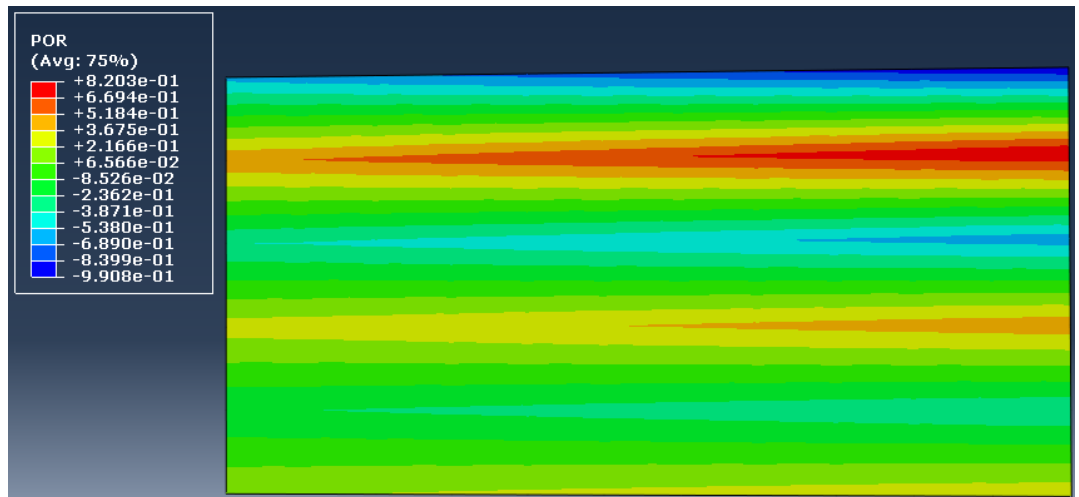


(b) The modified model

**Figure 5-10. Pore water pressure contours at t=0.0024 seconds in case P8.**
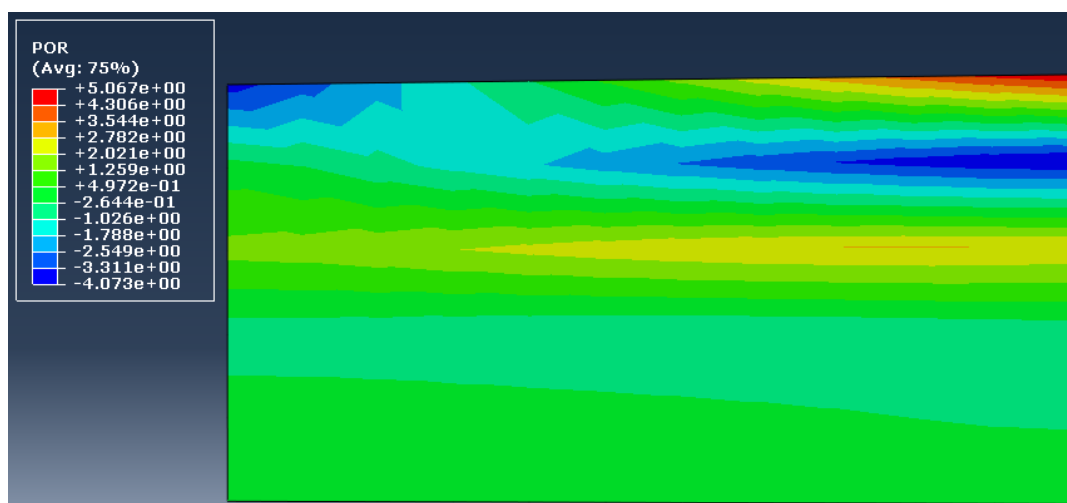
(a) The original model
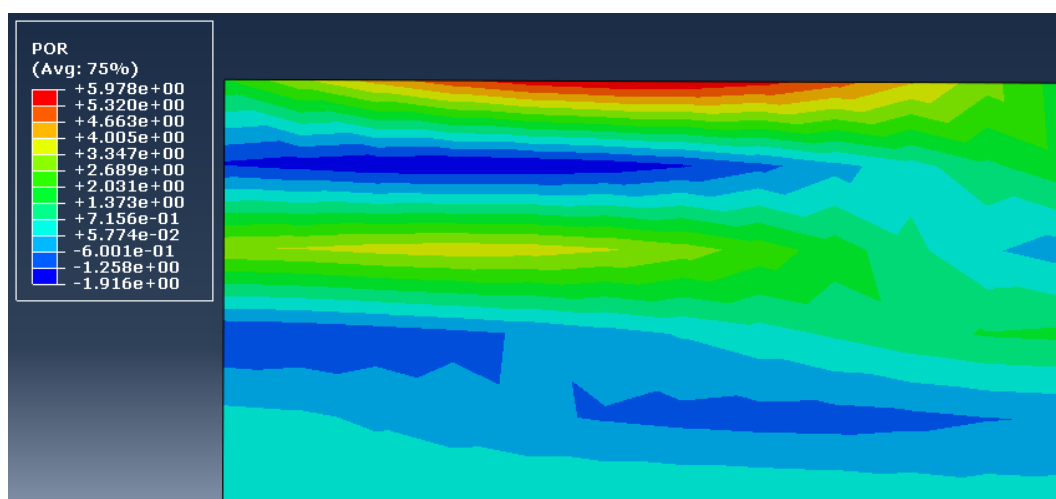


(b) The modified model

**Figure 5-11. Pore water pressure contours at t=0.18 seconds in case P8.**

(a) The original model
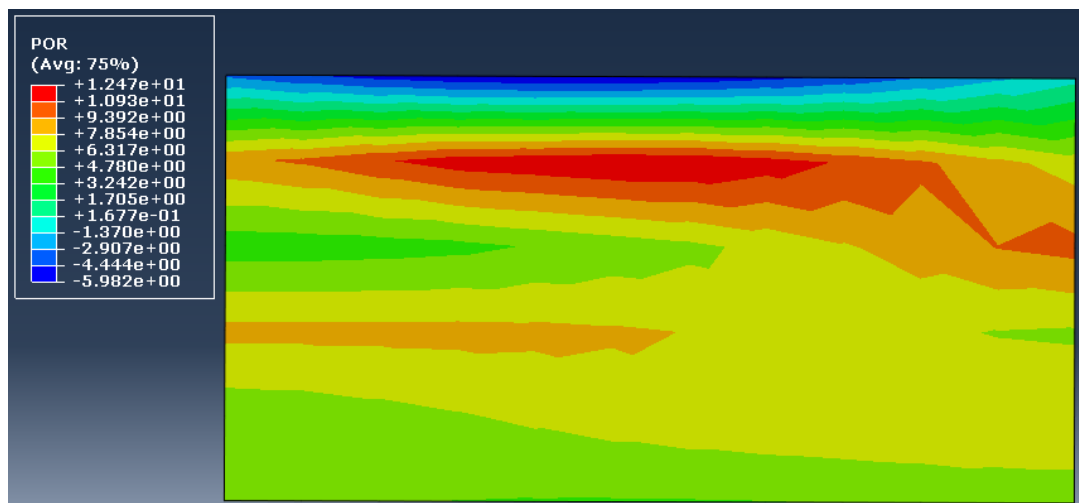


(b) The modified model

**Figure 5-12. Pore water pressure contours at t=1.7 seconds in case P8.**

## 5.3.2 The standing wave

The overall results from the two models of antinode and near node, which is set at the depth of 5 mm, 85 mm from the mid-width, are presented in Figure 5-13.

The results of near node are discussed firstly. Generally, results from the two models both show a nonlinear trend that the larger cyclic stress ratio can generate higher excess pore water pressure. The modified PSR model can still generate higher excess pore water pressure than the original model,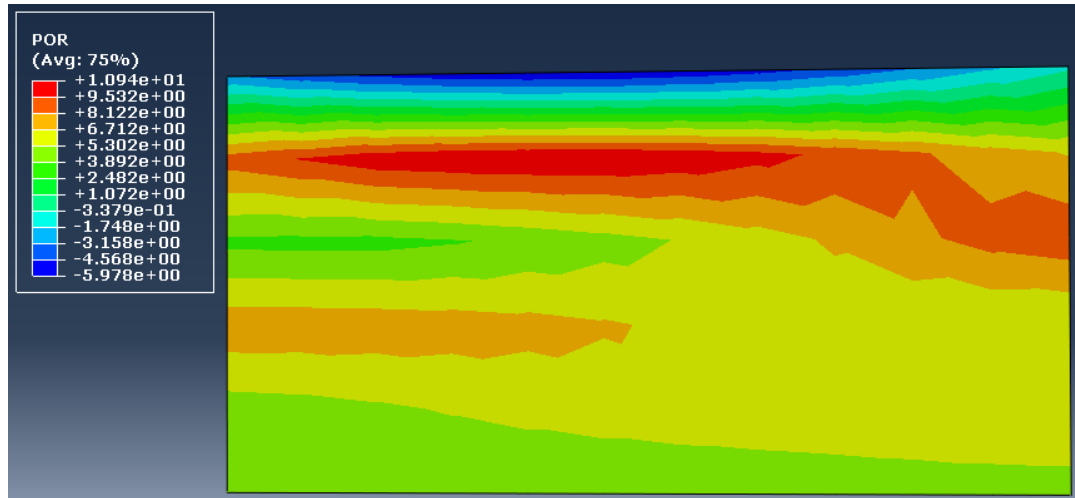 although liquefaction does not happen in both two models. It should be noted that the PSR impact still increases with the cyclic stress ratio, as the difference of pore water pressure between two models are becoming larger as the cyclic stress ratio increases, which is similar to the results from the progressive wave loading. The predicted results of positions near node cannot be verified due to the lack of laboratory results, but the general trend still show that more severe waves lead to larger PSR effects and the modified PSR model predicts larger build-up of pore pressure than the original model.

The general trend of results from the modified PSR model of antinode agrees well with the laboratory results and shows the same characters mentioned in results of the near node. It achieves the $u_{max}/\sigma_{v0}$ of 90% (the occurrence of liquefaction) at the cyclic stress ratio of 0.2, which is exactly the same wave intensity as the laboratory results. However, the predicted results from the original model nearly coincide with the results from the modified PSR model, which means that there is almost no difference between simulation results from these two models in this position. The stress path in the PSR space in Figure 5-14 shows that this is because the PSR can hardly be observed in this position. It can be seen that the maximum value of $(\sigma_x-\sigma_z)/2$ is nearly 30 times the maximum value of $\sigma_{xz}$, which means their magnitudes are not in the same order. This indicates that the cyclic loadings without the PSR play the main role now, thus leading to the limited effect of the modified PSR model at the antinode under the standing wave loading. Furthermore, this PSR effect laterally

increases from the antinode to the boundary of the soil bed. However, this is just one special position under a specific type of wave loading. As the progressive wave plays the main role in natural wave conditions, the overall different performances between the modified PSR model and original model show that it is still essential to consider the PSR impact in the simulation of most of the real wave loading conditions.
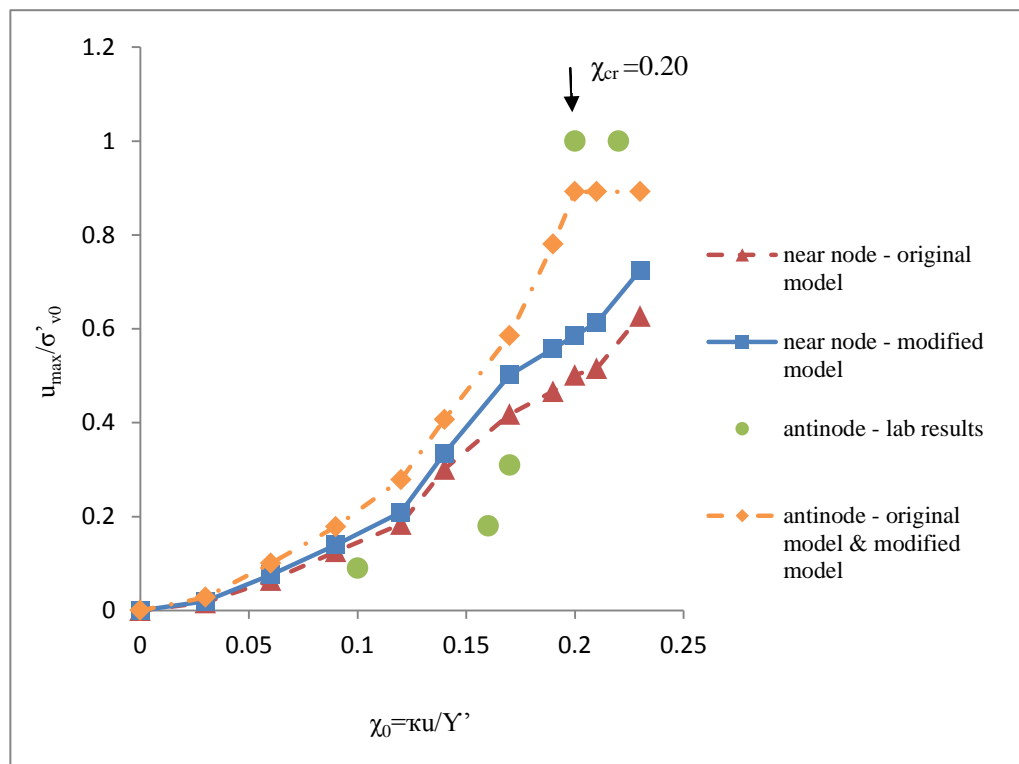


**Figure 5-13. Comparison of $u_{max}/\sigma'_{v0}$ with $\chi_0$ at the shallow soil depth (-5 mm) between the predicted results and laboratory results under the standing wave loading.**
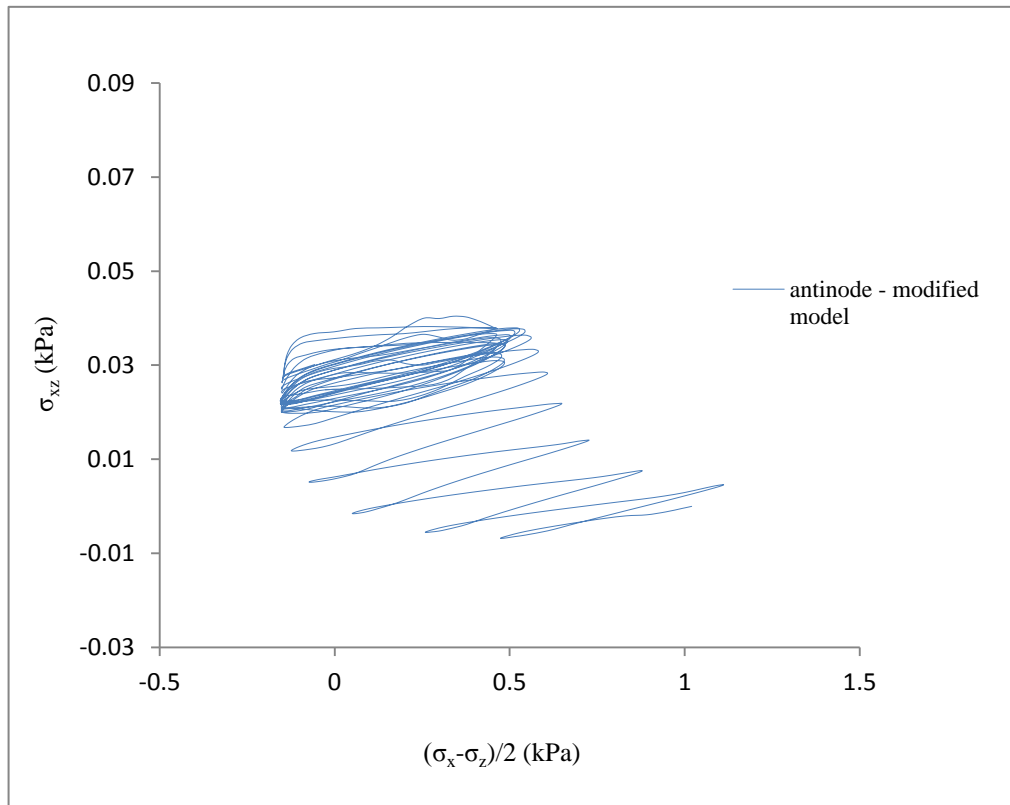
**Figure 5-14. Predicted stress paths in the PSR space from the modified model at the antinode under the standing wave loading.**

## 5.4 Summary

In this chapter, the wave-induced liquefaction of seabed has been simulated using the newly developed PSR model which can consider the principal stress rotation. Both the modified PSR model and the original model were implemented into the finite element simulations of wave-seabed interactions to test their abilities and comparisons are made between them and the experimental results. Although the original model can reflect some PSR effects

in the simulations of wave-seabed interactions, generally the modified PSR model performs better and agrees better with the lab results than the original model. The critical conclusions are summarized in detail as follows.

- It is evident that both the progressive wave and the standing wave loadings produce the PSR in problems of wave-seabed interactions. Therefore, simulation of the PSR is important in offshore foundation designs. This PSR effect increases with the severity of imposed wave loadings reflected by the cyclic stress ratio. The higher cyclic stress ratio leads to the more obvious difference between the modified PSR model and the original model.

- Generally, wave loadings with larger cyclic stress ratios can generate higher pore water pressures. The original model can only produce very limited $p'$ reduction and cumulative shear strain under wave loadings. The modified PSR model can generate higher excess pore water pressures and larger shear strains than the original model, thus bringing the soil to the liquefaction and agrees better with the laboratory results due to its complete ability in the simulation of the PSR impact. Therefore, ignoring the PSR impact can lead to the underestimation of pore pressure build-up and deformations. Moreover, the modified PSR model can also reflect the characteristics of critical cyclic stress ratio above which the liquefaction will occur.

- The standing wave produces less PSR effect than the progressive wave, and under the standing wave, the PSR effect laterally reduces from the boundary of the soil bed to the antinode, where nearly no PSR was observed. Therefore, the modified PSR model has limited effect in the

simulation at the antinode under the standing wave. However, this is just one very special case. As the natural wave loadings are much more random, it is important to consider the PSR effect in the simulation of wave-induced liquefactions. Therefore, the modified PSR model presented in this research has the ability to simulate the PSR impact and plays an important role in the numerical simulations of wave-seabed interactions.

# Chapter 6 The Finite Element Simulation of Earthquake-Induced Liquefactions

## 6.1 Introduction

Dynamic loadings such as earthquake loadings can generate considerable principal stress rotation (PSR) in the saturated sand. This PSR effect can generate excess pore water pressures and cumulative shear strains, thus causing liquefaction in undrained conditions. This chapter simulates a centrifuge model test under the earthquake loading using the fully coupled finite element method and the modified PSR model to investigate the impact of PSR. This modified model and the original base model will be implemented into the numerical simulation of a boundary condition problem — Centrifuge Model Test No. 3 from the VELACS project. The capability of this PSR soil model is also verified by comparisons of the predicted results between the modified PSR model, the original model and the laboratory results from the centrifuge tests.

## 6.2 Problem Definition

The centrifuge test of Model No. 3 in VELACS project is selected to assess the ability of the modified PSR model and investigate the significance of the PSR impact under earthquake loadings. This is a water saturated layer of sand

deposited in a laminar box of the depth of 220 mm (Figure 6-1). The model is divided vertically into two sand layers which have the relative density of 40% and 70% respectively. The laminar box is subjected to the base motion illustrated in Figure 6-2. The base shaking in the *y* direction was negligible and the base shakings in the *x* and *z* directions are major and minor shakings respectively.
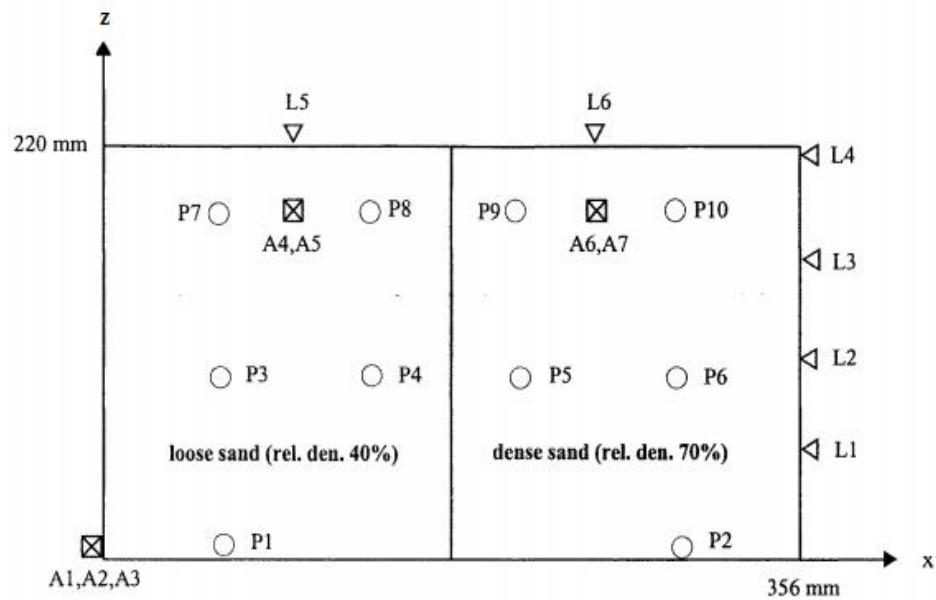


(a) Front view
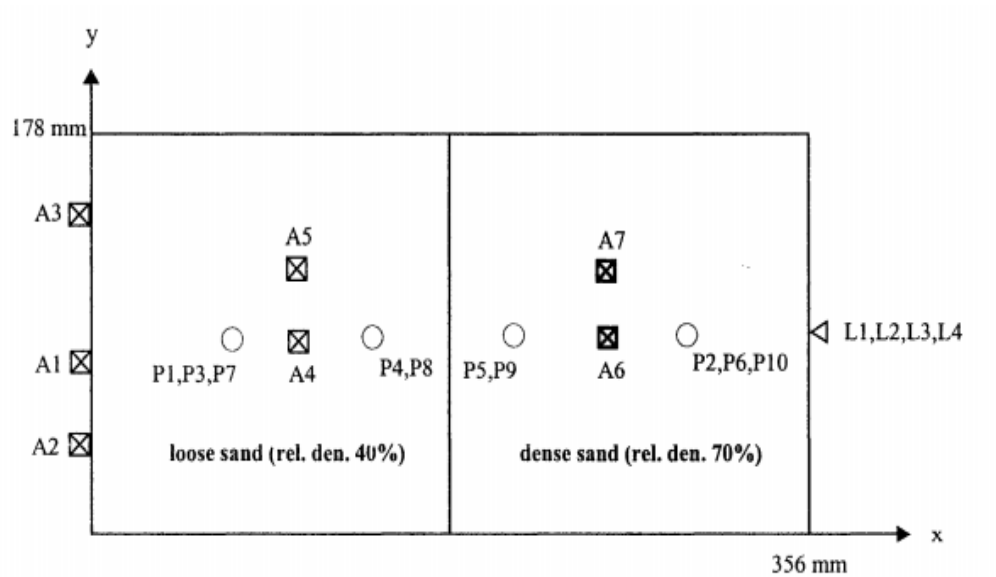
(b) Plan view

○   pore pressure transducer

⊠   horizontal & vertical accelerometer

◁   displacement transducer

**Figure 6-1. The configuration and the location of measuring instruments for the centrifuge model test (Yang, 2003).**

The input base motions and accelerations along the height of the soil sample were measured with 7 accelerometers. 10 pore pressure transducers were used to measure the pore pressures at the corresponding locations. The lateral deformations and settlements were measured by 6 displacement LVDT transducers. In total 23 transducers, illustrated in Figure 6-1, were used in this test.
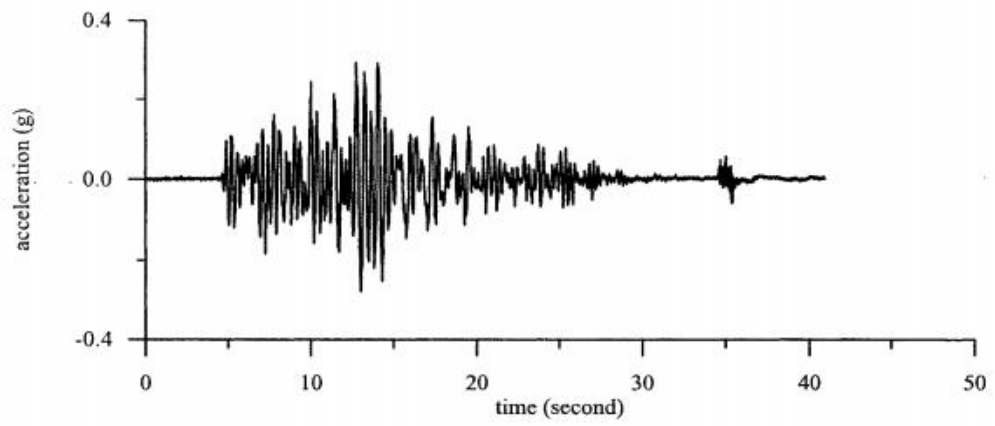
(a) Horizontal base motion
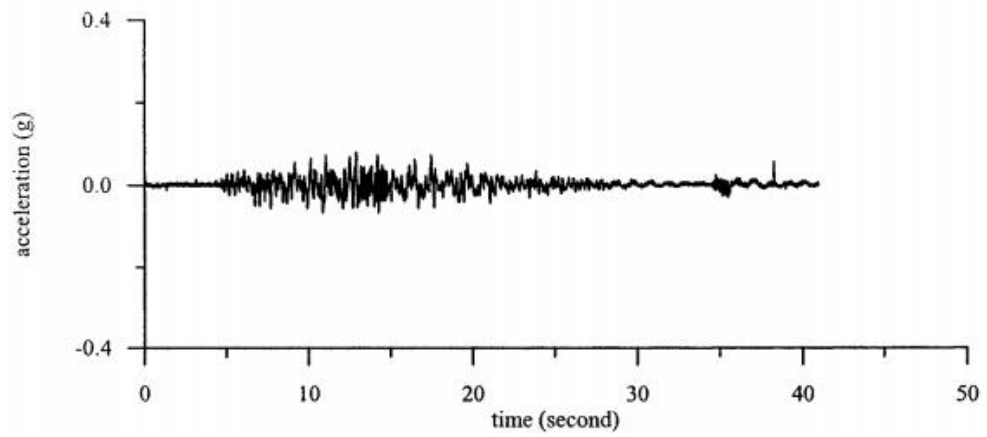


(b) Vertical base motion

**Figure 6-2.The input acceleration time history (Yang, 2003).**

To simulate the centrifuge test, the two dimensional finite element computer code DYSAC2 with the fully coupled analysis was used. This program adopts the finite element solution of the dynamic governing equations for a saturated porous media as well as a three parameter time integration scheme called the Hilber-Hughes-Taylor $\alpha$ method. A predictor/multi corrector algorithm is also used to provide the quadratic accuracy. More details of this computer program can be found in Chapter 3.

The problem is simulated in the model scale with the gravitational acceleration of 50 $g$. The whole box is divided into 162 elements (Figure 6-3). The mesh size is in accordance with numerical simulations for this centrifuge model carried by Yang (2003). No horizontal water flow is allowed on the side boundaries while no vertical water flow is allowed on the base, which is fixed to the ground. The adjacent nodes on the sides of the box are tied up with each other to simulate the behaviors of the soil sample in the laminar box. The permeability used in this simulation is $4.6E10^{-5}$ by taking the average value from Figure 6-4 to account for the different relative densities of the sand. The pore water pressure, stress, strain and the displacement are recorded for 30 seconds with a time increment of 0.0018 s, because after 30 s the liquefaction spreads over the majority of the model and the soil becomes very unstable.
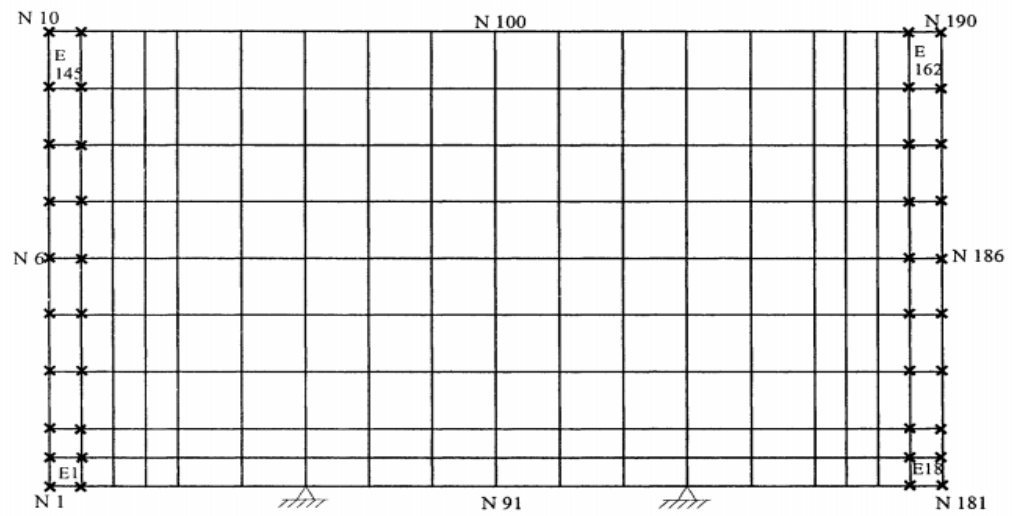
N: nodal point

E: element

x: tied up nodes for the simulation of laminar box

Base: fixed and no vertical water flow

Sides: no horizontal water flow

**Figure 6-3. Elements and boundary conditions of the finite element model**

**(Yang, 2003).**
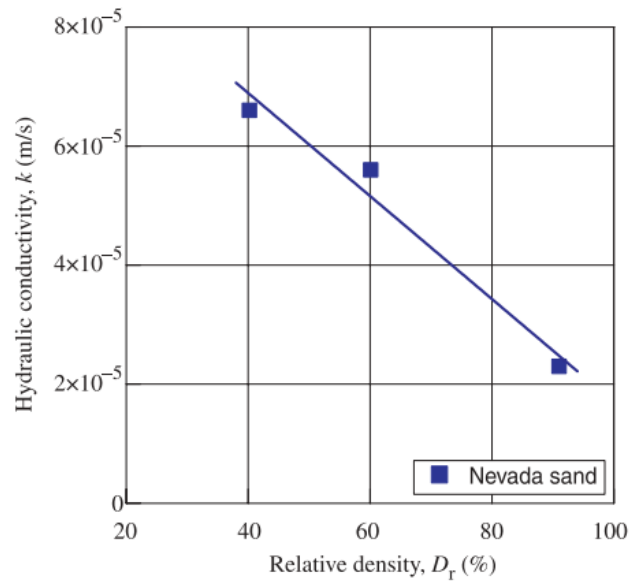
**Figure 6-4.The permeability of Nevada sand (Arulmoli et al. 1992).**

# 6.3 Predicted Results and Comparison with the Experimental Data

## 6.3.1 Pore water pressures

The induced excess pore water pressures (denoted by $u$) of typical locations of P1, P2, P3, P6, P7, P10 are presented in Figures 6-5. In the loose sand (P1, P3, P7), the results from the modified PSR model reach nearly the same peak value from the experimental data. The maximum pore water pressure in location P7 reaches 21 kPa, which exceeds the 90% of initial vertical stress (18.9 kPa). The predicted pore water pressures in locations P1 and P3 does not exceed the 90% of initial vertical stresses. This indicates that liquefaction only occurs in the top

level of the soil model, which agrees with the laboratory results. However, the original model does not bring the soil to liquefaction at all measured locations as the predicted results are lower than the 90% of initial vertical stresses and significantly underestimate the pore water pressures. For example, in location P1, the peak pore water pressure from the original model is 29 kPa, which is 16 kPa lower than the experimental value. Generally, the results from the modified PSR model agree better with the experimental data, although they slightly overestimate the pore water pressure in the early stage.

In the dense sand (P2, P6, P10), the modified PSR model slightly overestimates the pore water pressure during the full stage, while the original model overestimates the pore water pressure during the early stage and still underestimates the pore water pressure during the later stage. Liquefaction is still not reached in the results from the original model while the modified PSR model brings the soil to the liquefaction at the top level of soil sample (location P10).

Therefore, generally the modified PSR model performs better than the original model. The difference between the results of these two models comes from the large PSR effects induced by the earthquake loading in the sand. Accumulative excess pore water pressure is caused by the PSR impact which the original model does not consider.

It also can be seen that the loose sand liquefies faster than the dense sand. For example, in the results from the modified PSR model at the shallow depth (locations P7 and P10), the peak pore water pressure of 21 kPa is reached at the time of 20 s in the loose sand while the peak value of 20 kPa is reached at 30 s in the dense sand. However, the pore water pressures in the loose sand dissipate

faster after the peak value. This may be due to the movement of water from the loose sand to the dense sand and the soil behaviors are difficult to predict after liquefaction has taken place.
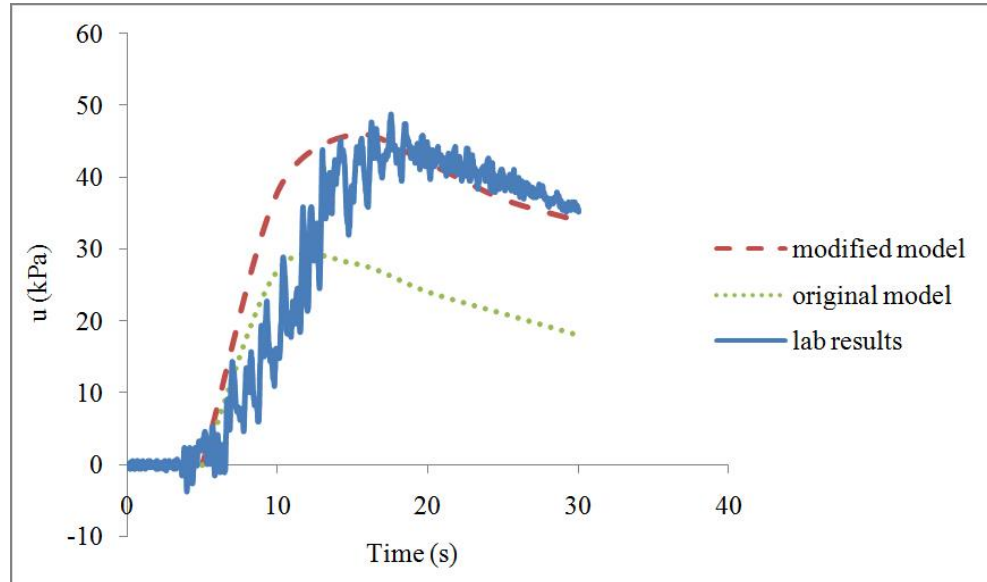


(a) Location P1.
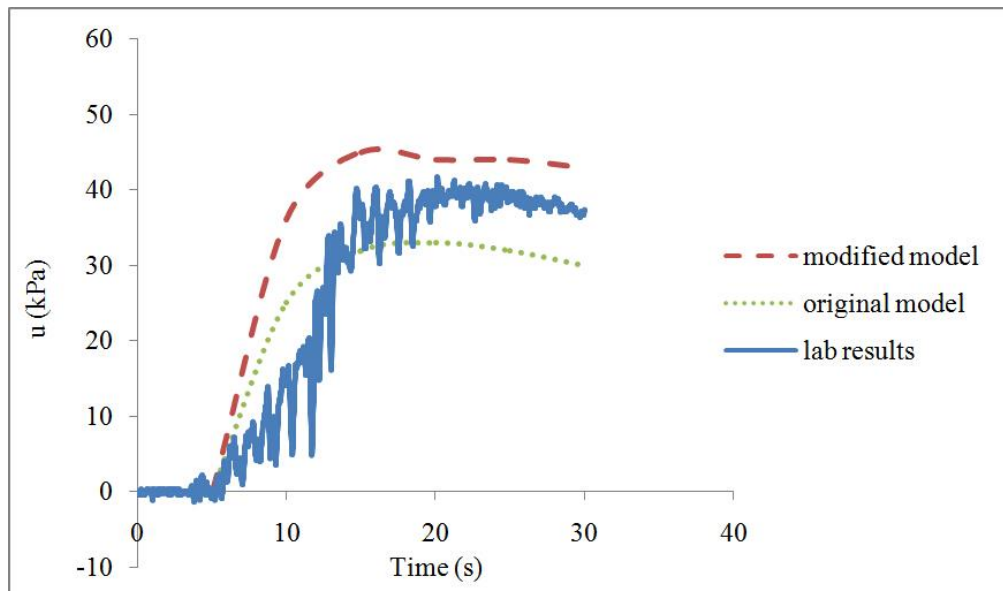


(b) Location P2.
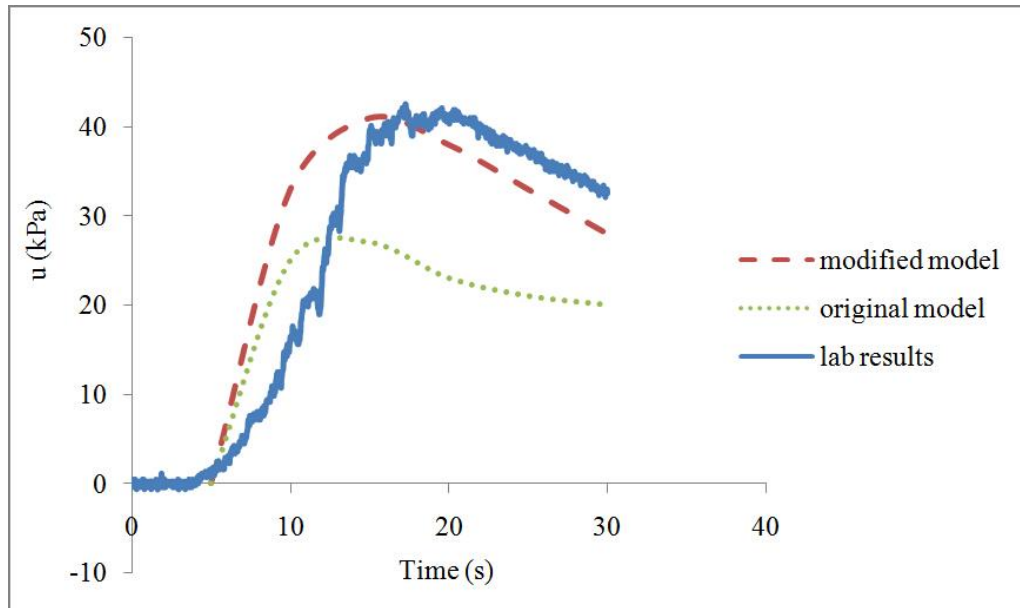
(c) Location P3.
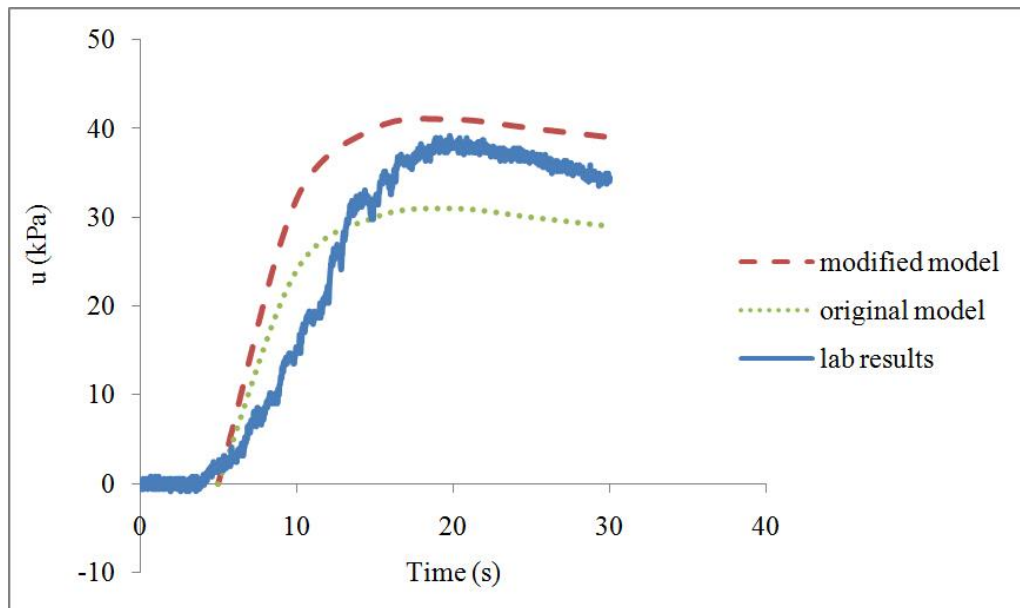


(d) Location P6.
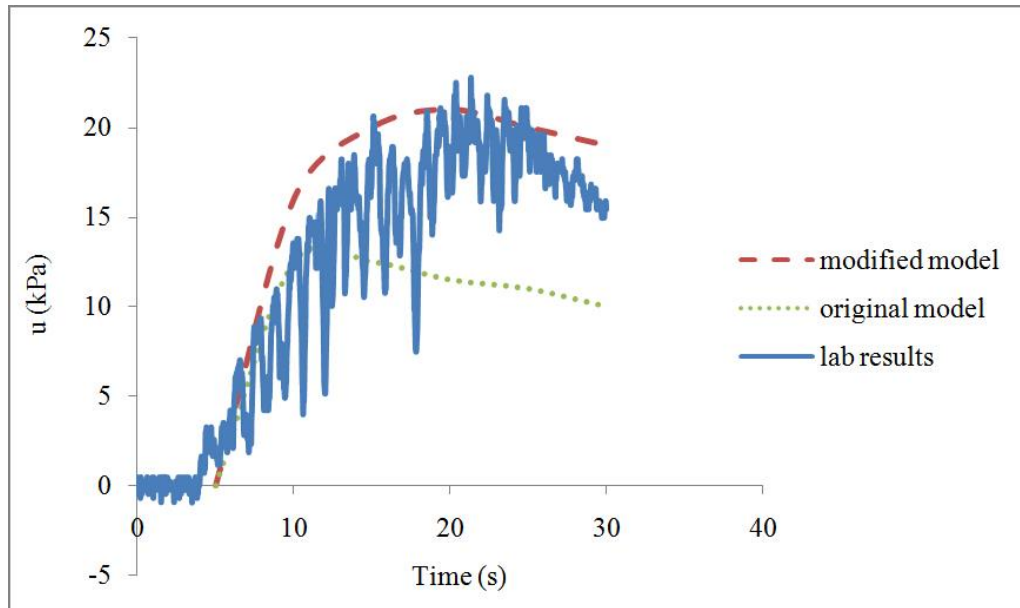
(e) Location P7.
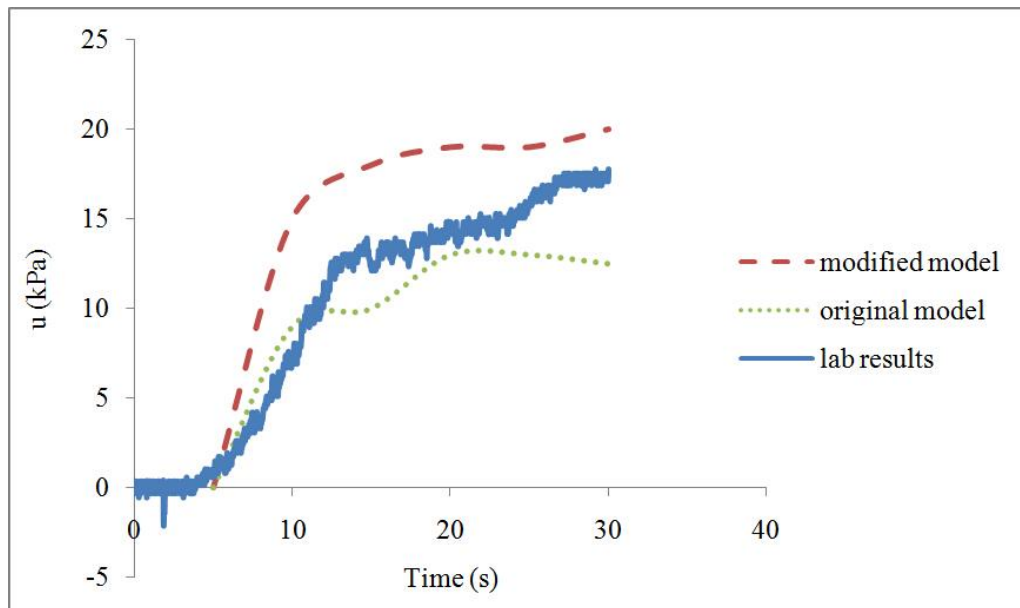


(f) Location P10

**Figure 6-5.Comparison of time history of excess pore water pressure between the predicted results and the experimental results.**

## 6.3.2 Stress paths

The PSR effects can be clearly seen in the stress space of $\sigma_{xz}$ and $(\sigma_x-\sigma_z)/2$. The stress paths in the PSR stress space of location P6 from both models are shown in Figures 6-6. It can be seen that although the stress paths are quite random, the principal stresses from the two models are both continuously rotating under the earthquake loading. Furthermore, as $(\sigma_x-\sigma_z)$ decreases, $\sigma_x$ tends to be equal to $\sigma_z$, which indicates the lower of the deviatoric stress and the shear strength of soil.

In Figures 6-7, the stress paths of location P6 from the two models start from point A and end at point B. They both show the decrease of the effective confining stress $p'$ and the butterfly shape in the final stages. It can be seen that the amplitudes of deviatoric stresses decrease as well. However, the modified PSR model brings the effective confining pressure $p'$ and the deviatoric stress $q$ to 0 even without the incorporation of fabric effects, while the original model only brings the $p'$ to the lowest value of 5 kPa. This indicates the lower shear strength of soil from the modified PSR model than that from the original model. This difference between the two models still comes from the accumulative plastic volumetric deformations caused by the PSR effect.
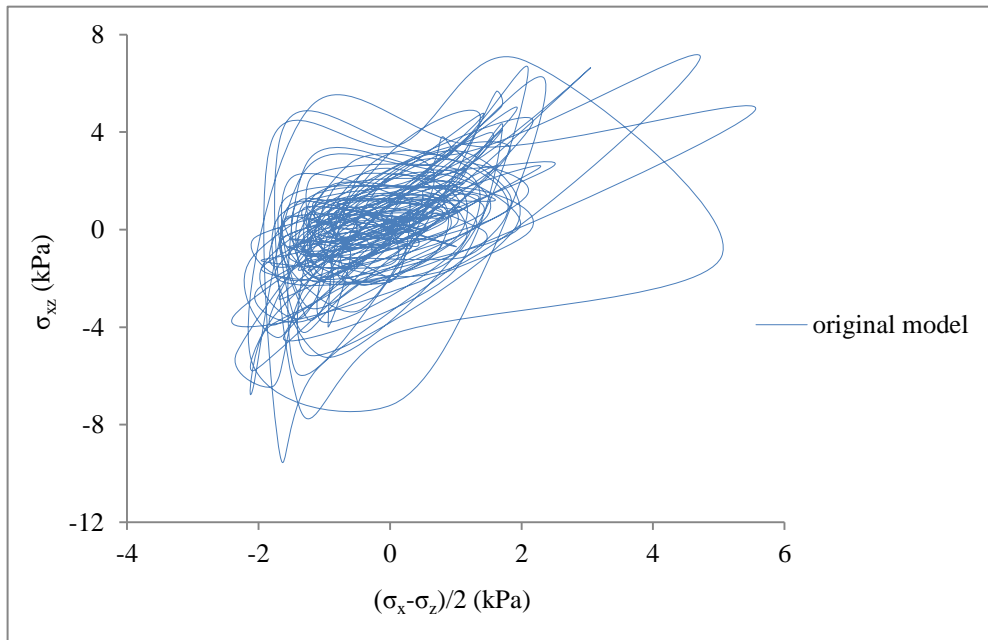
(a) The original model
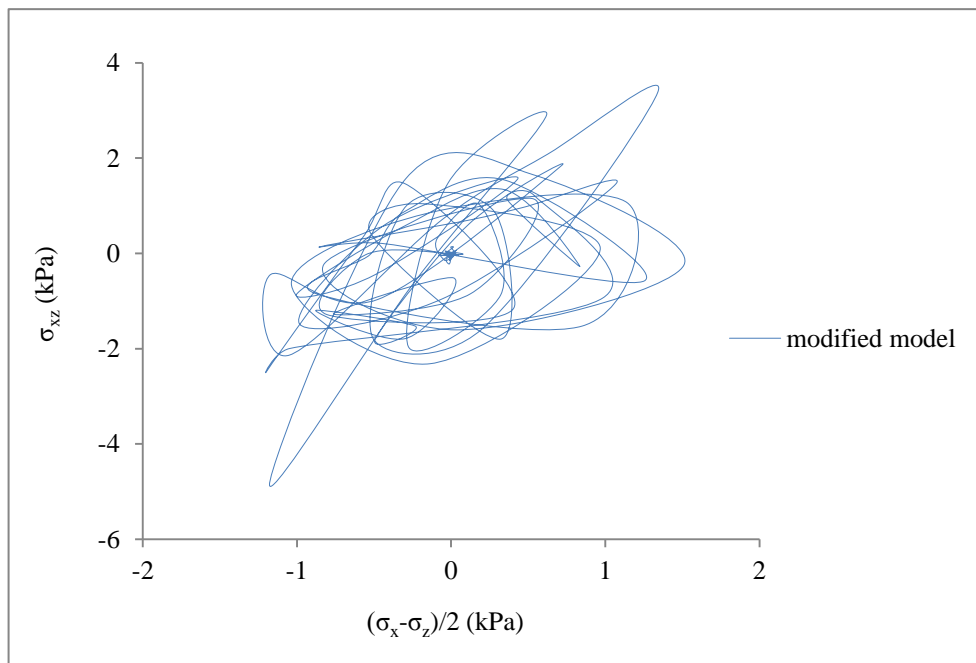


(b) The modified model

**Figure 6-6. Predicted stress paths in the PSR space in location P6.**
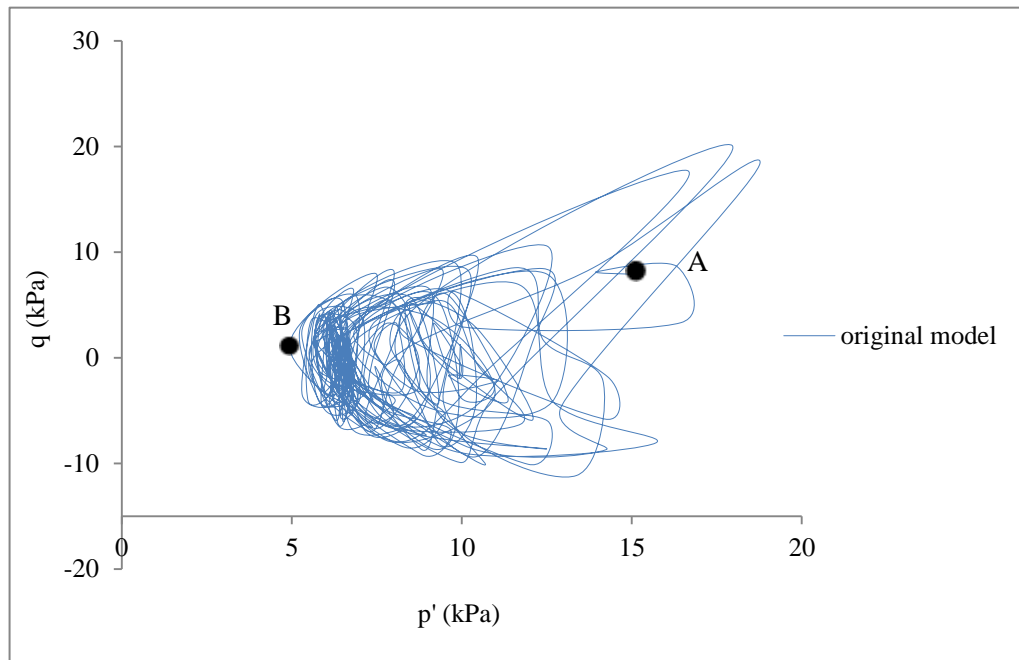
(a) The original model
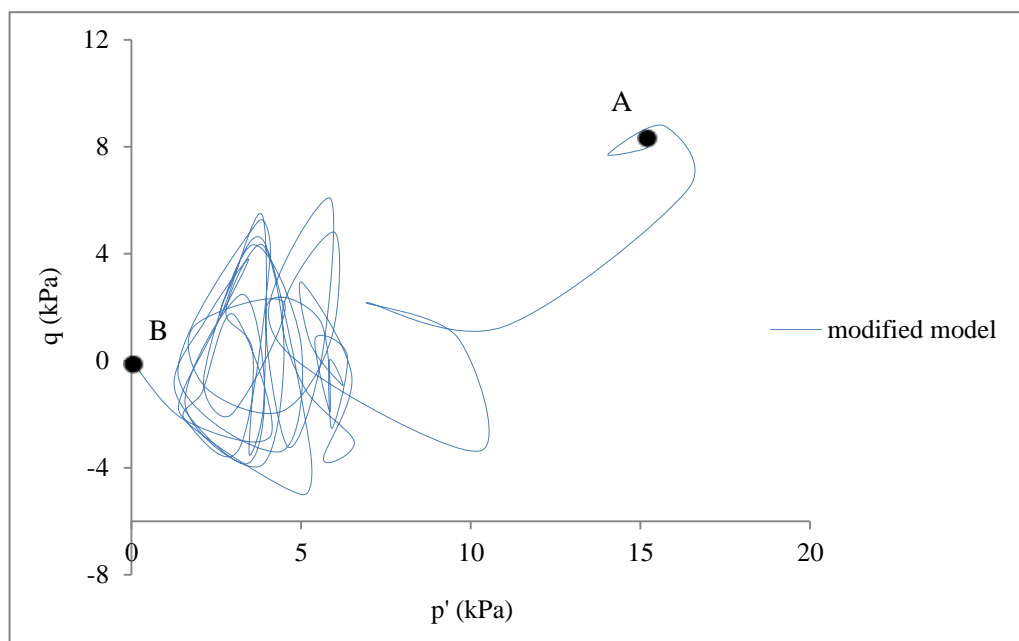


(b) The modified model

**Figure 6-7. Predicted stress paths in location P6.**

## 6.3.3 Time history of accelerations

The time history of the accelerations measured in the centrifuge tests and predicted from the two models in the numerical simulations are presented in Figure 6-8 to Figure 6-11. It can be seen that the predicted accelerations from the modified PSR model generally agree with the measured results in locations of all the 4 accelerometers. Only some slight overestimations of less than 0.05 g can be observed. However, in the predicted results from the original model, the discrepancy can be more than 0.25 g, such as accelerations in location A6. The predicted results from the modified PSR model agree better with the measured accelerations because of its consideration of the PSR impact, thus better reflecting the true behavior of the sand.
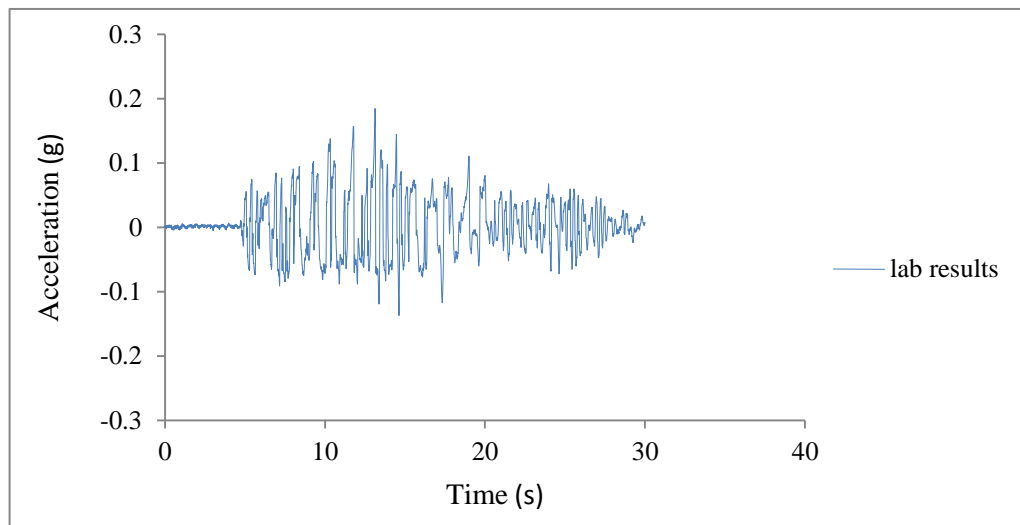


(a) Lab results
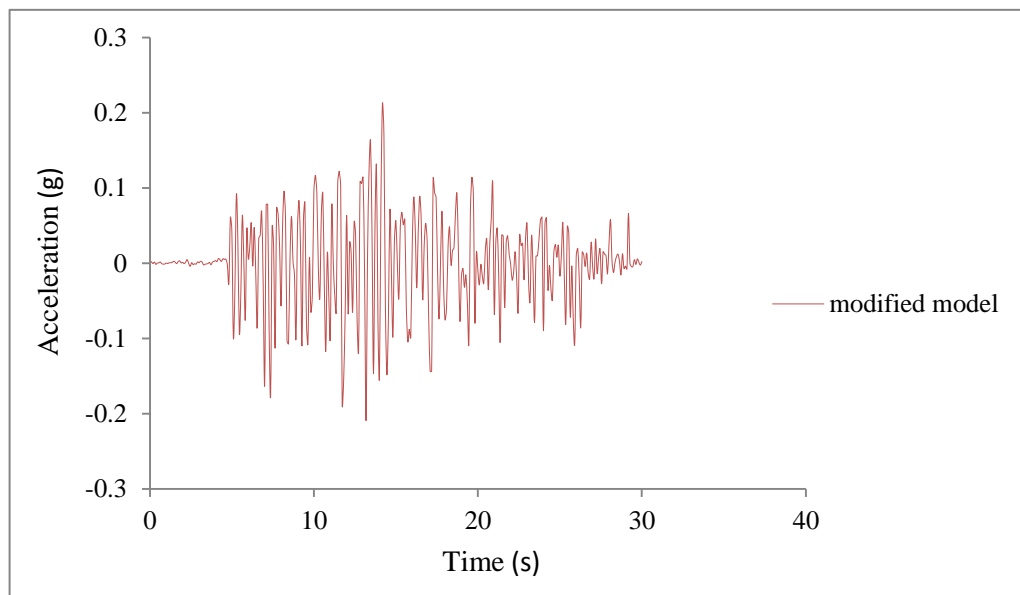
(b) Predicted results from the modified model
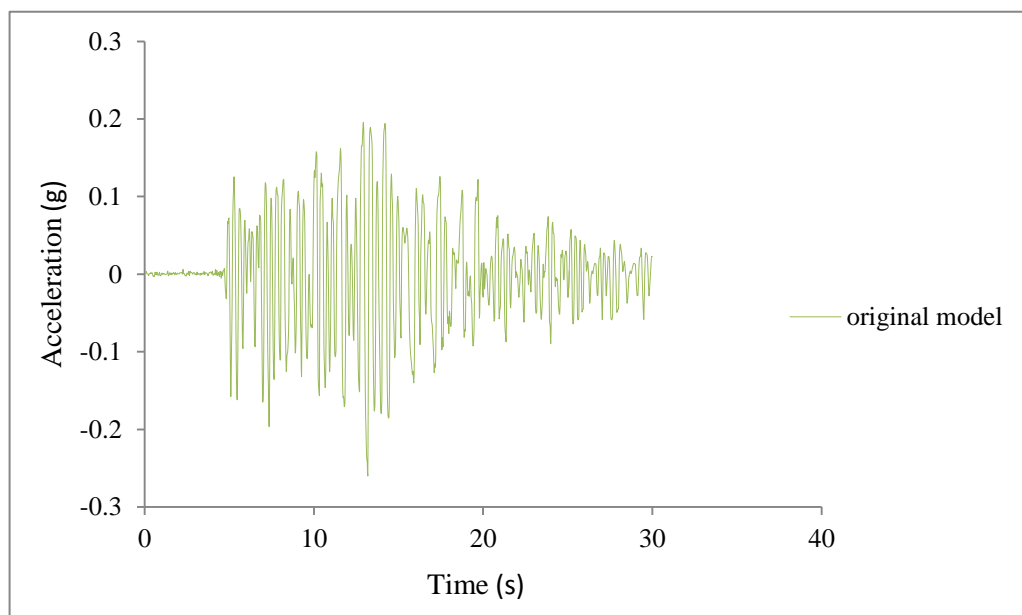


(c) Predicted results from the original model

**Figure 6-8. The measured and predicted acceleration from the modified model in location A4.**
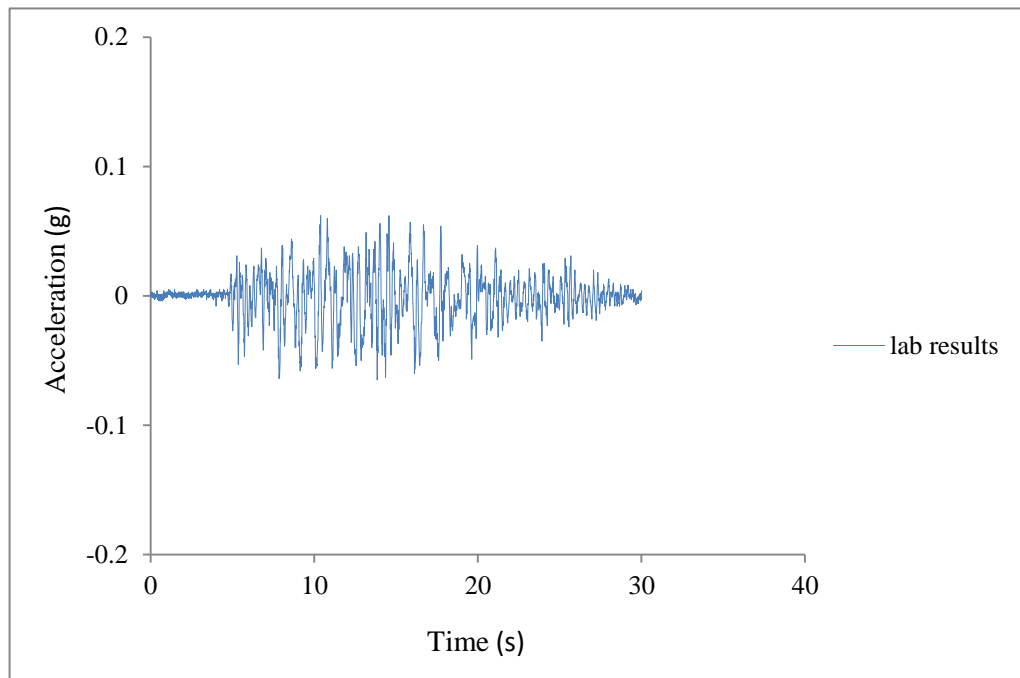
(a) Lab results
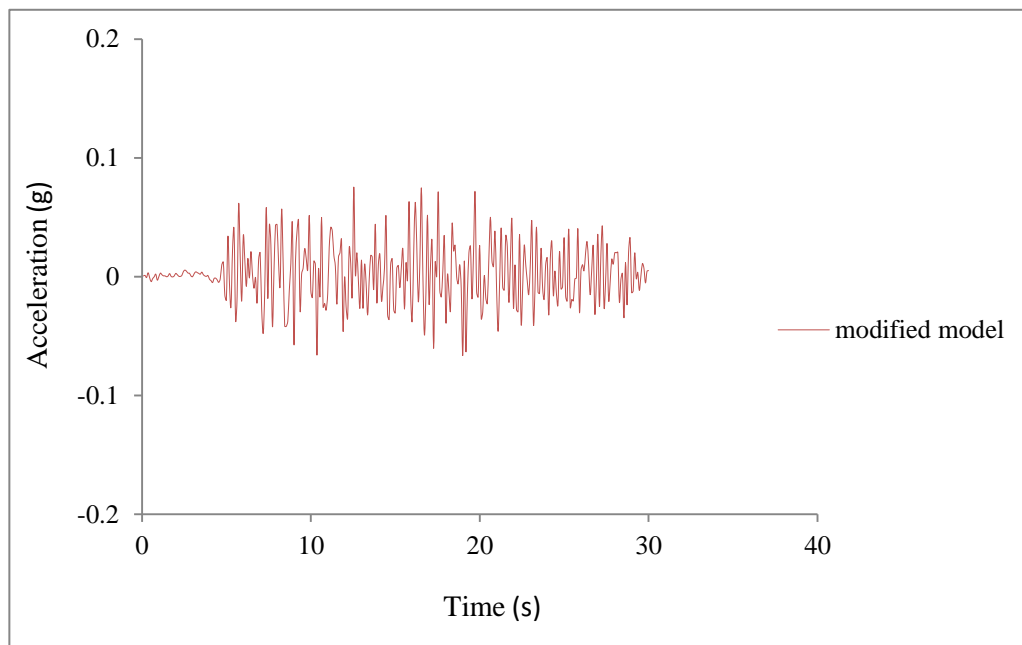


(b) Predicted results from the modified model
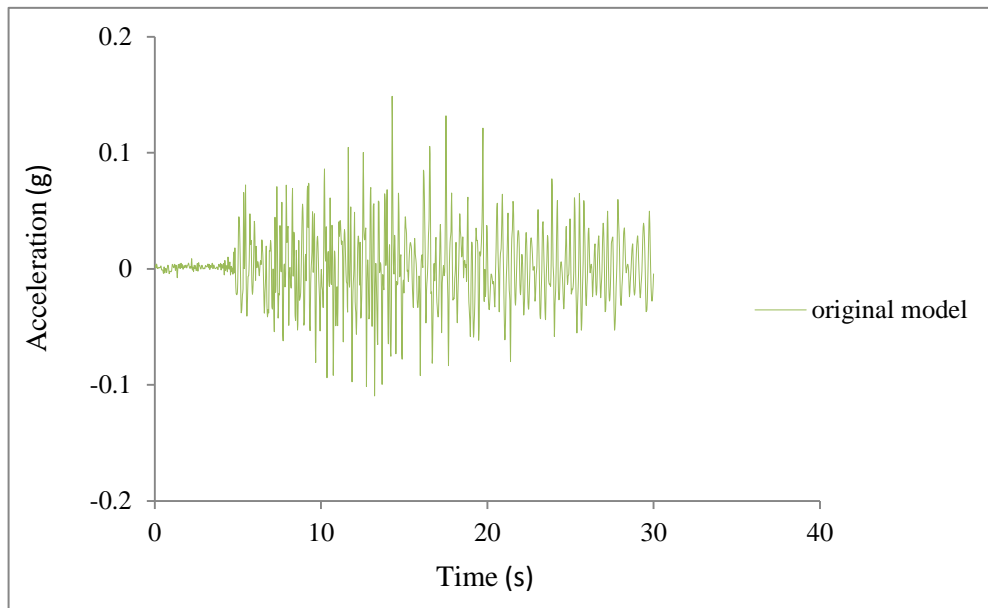
(c) Predicted results from the original model

**Figure 6-9. The measured and predicted acceleration from the modified model in location A5.**
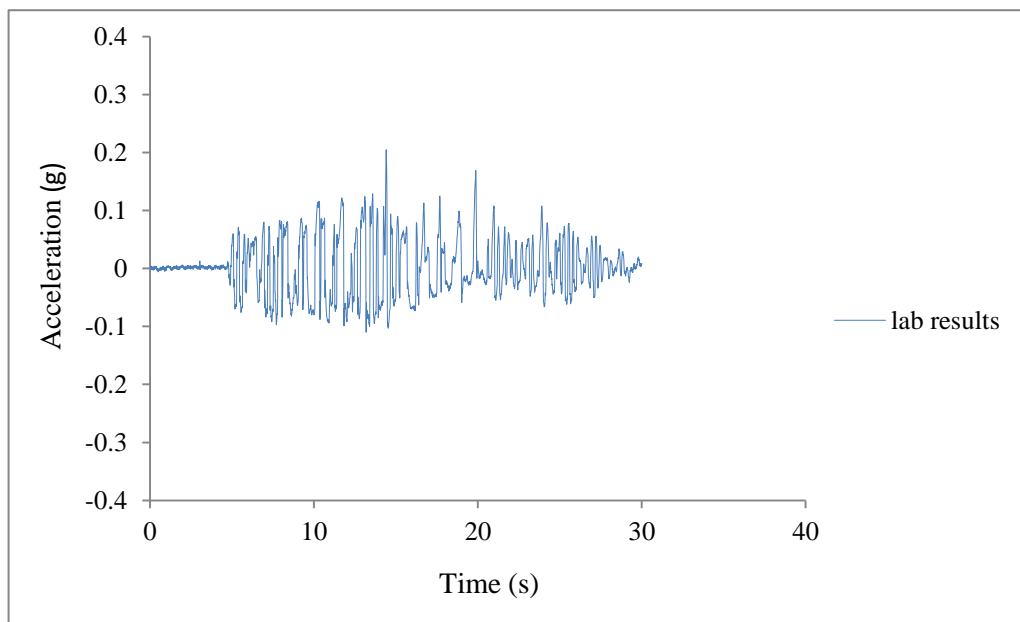


(a) Lab results
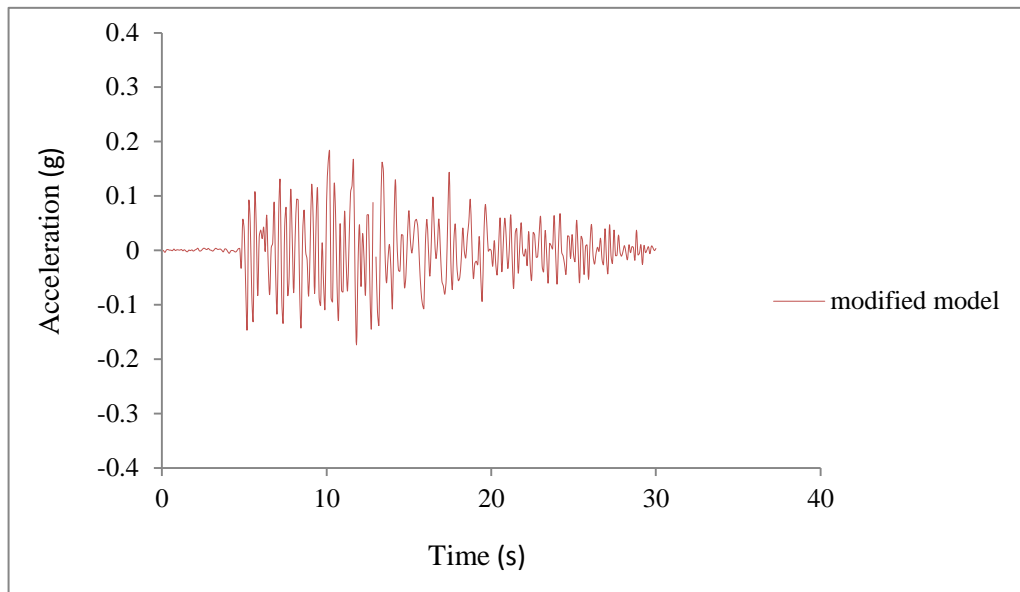
(b) Predicted results from the modified model
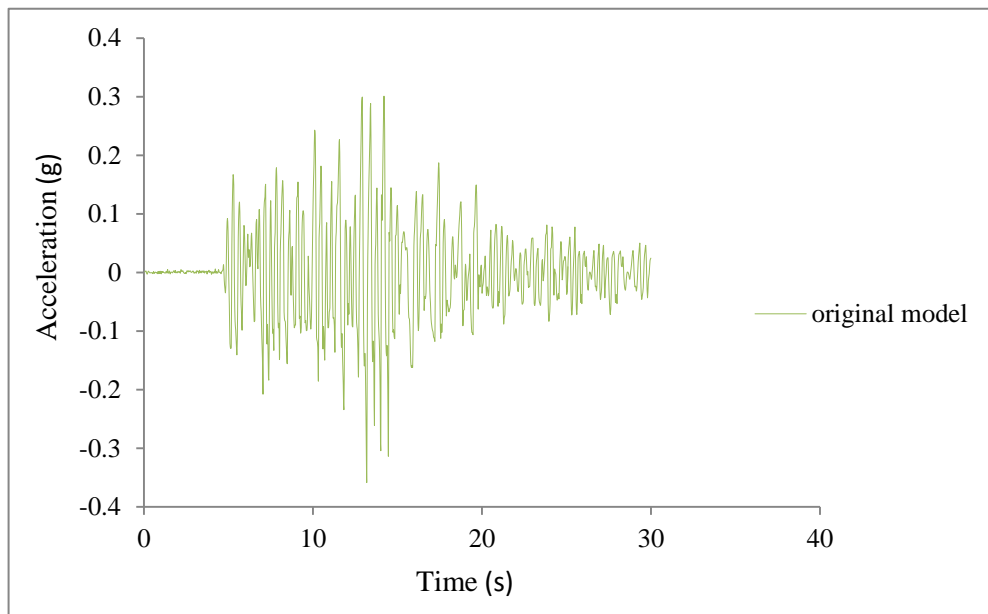


(c) Predicted results from the original model

**Figure 6-10. The measured and predicted acceleration from the modified model in location A6.**
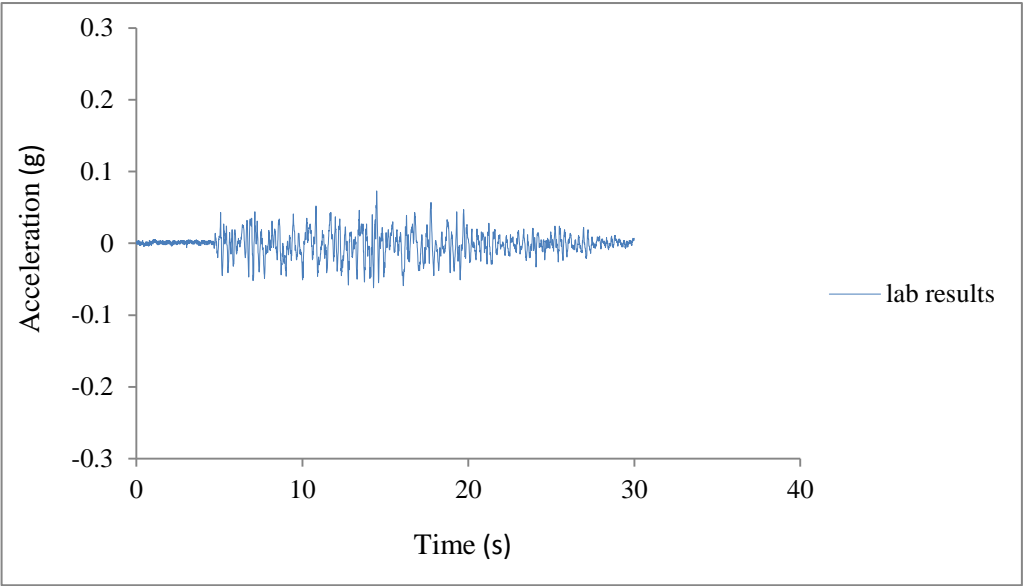
(a) Lab results
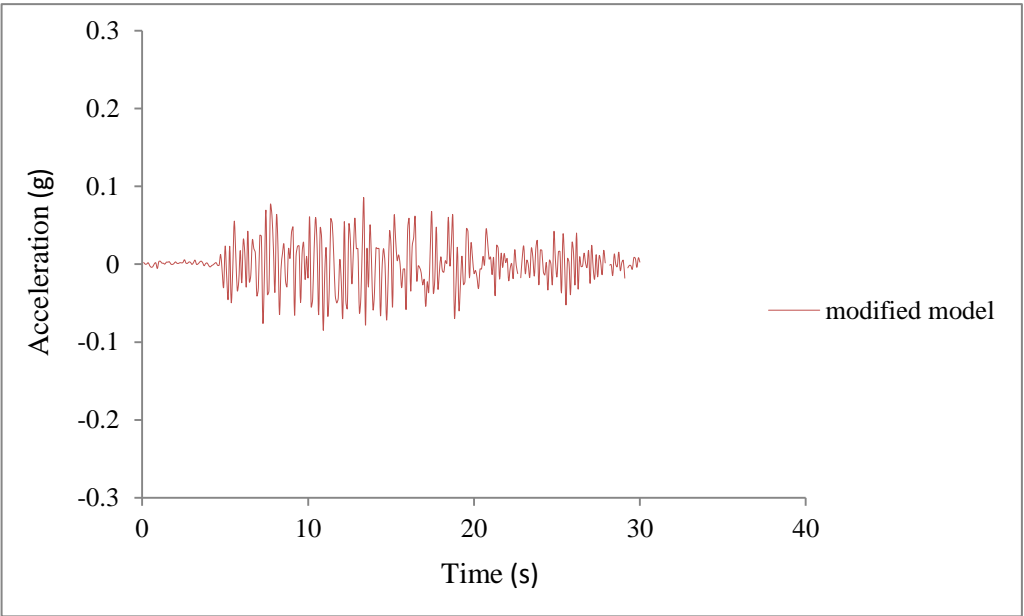


(b) Predicted results from the modified model
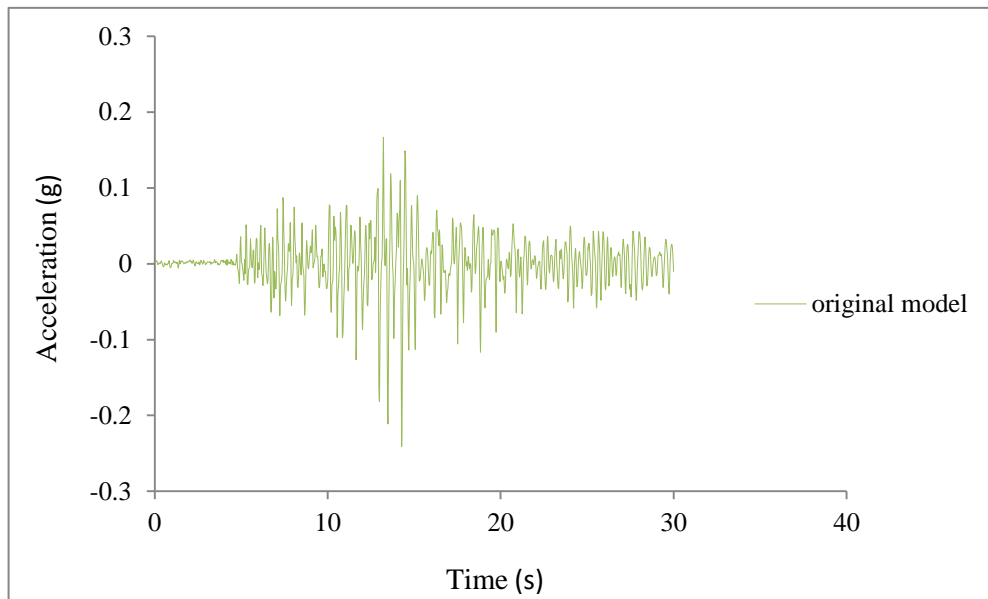
(c) Predicted results from the original model

**Figure 6-11. The measured and predicted acceleration from the modified model in location A7.**

## 6.3.4 Settlements and displacements

The settlements of typical locations L5 & L6 are shown in Figures 6-12. The results from the two models again show significant differences. Although the settlements all increase after the start of the shaking, the settlements from the original model reaches the maximum value of 2.8 mm and 4 mm in 30 seconds at locations L5 and L6 respectively, while the modified PSR model brings the maximum settlements to 85 mm and 125 mm respectively. The largest settlement from the modified PSR model reaches nearly 30 times the result from the original model, which indicates that the original model significantly

underestimates the settlement of the soil. However, the modified PSR model still underestimates the settlements compared with the experimental data. This may be due to the movement of the LVDT transducer and the assumption of the constant permeability. Numerous studies found that the permeability tends to increase as the liquefaction spreads during the earthquake loadings (Andrianopoulos et al., 2010; Fareet al., 2011; Shahiret al., 2012). Therefore, to simulate the settlements better, the changing $K_D$ is required in the future investigations.
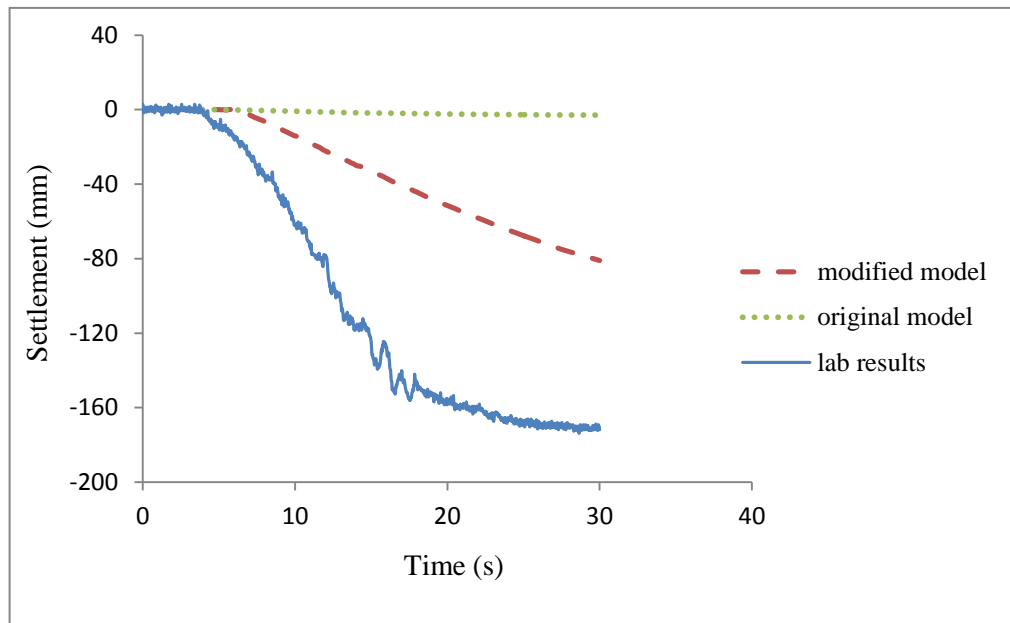


(a) Location L5
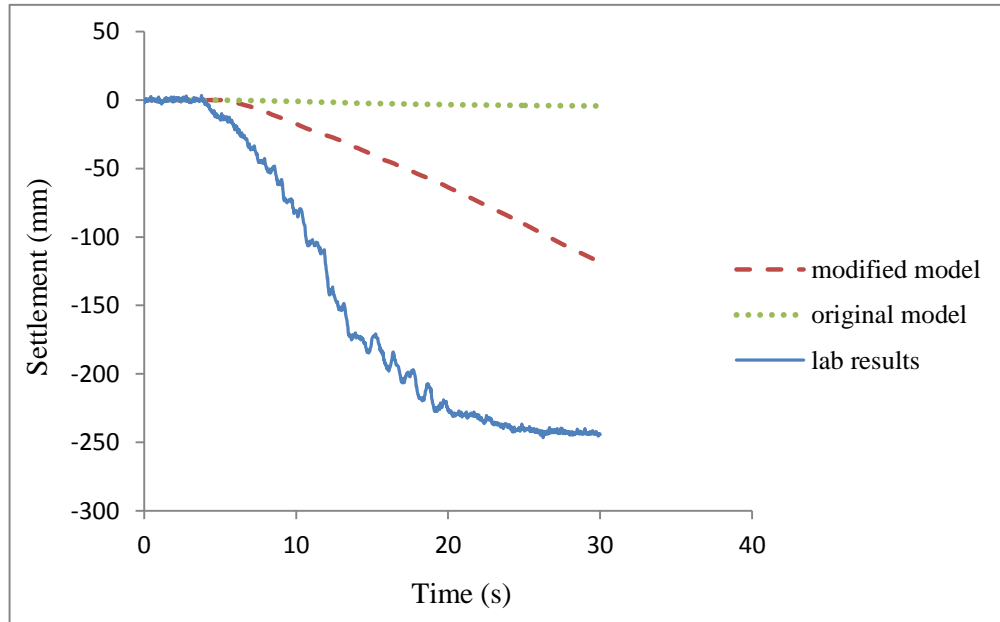
(b) Location L6

**Figure 6-12. Comparison of time history of settlement between the predicted results and the experimental results.**

The test results and predicted results of the lateral displacements are presented in Figure 6-13. It can be seen that the original model significantly underestimates the lateral displacements in locations of 4 LVDTs (L1, L2, L3 and L4). In the location of L4, the original model even produces the negative displacement while the measured displacement is positive. The comparisons show that the modified PSR model can produce larger lateral displacements than the original model, thus agreeing better with the experimental results. Generally, the predictions from the modified PSR model agree with the measured results in the locations of L1 and L2. However, it still underestimates the lateral displacements in the locations of L3 and L4. The reason for this may be consistent with the underestimation of the settlements measured at the locations of L5 and L6 described before as the locations of L3 and L4 are

relatively close to the locations of L5 and L6.
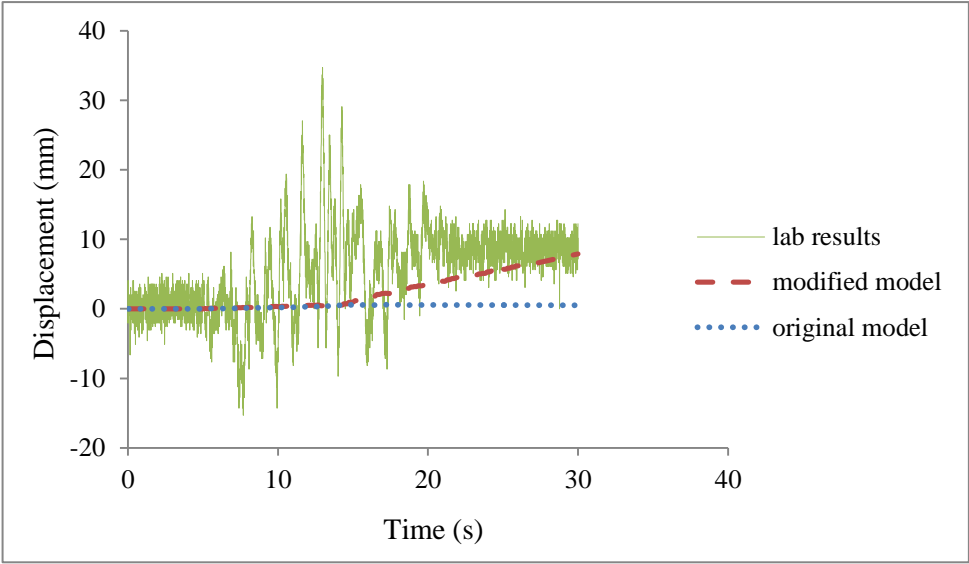


(a) L1
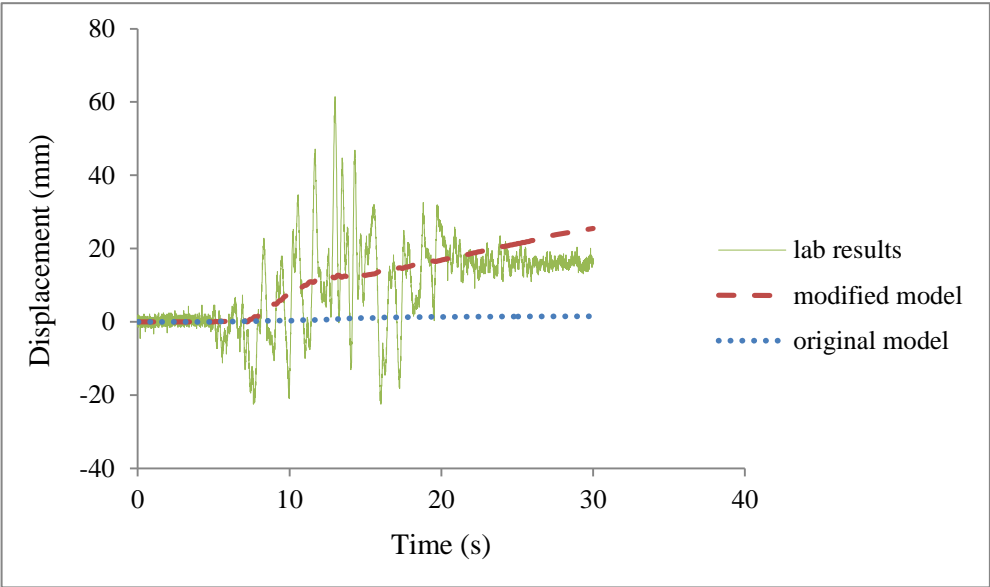


(b) L2
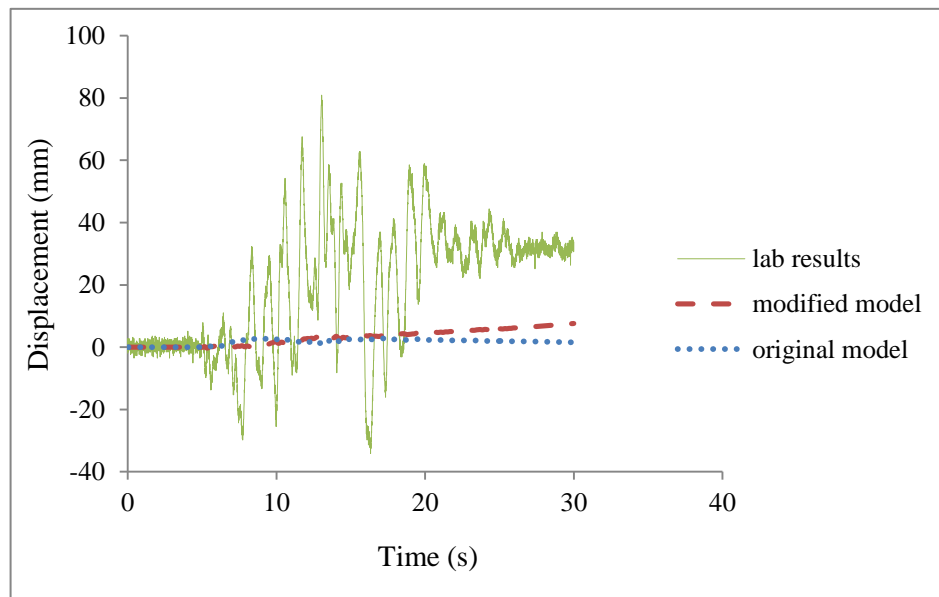
(c) L3
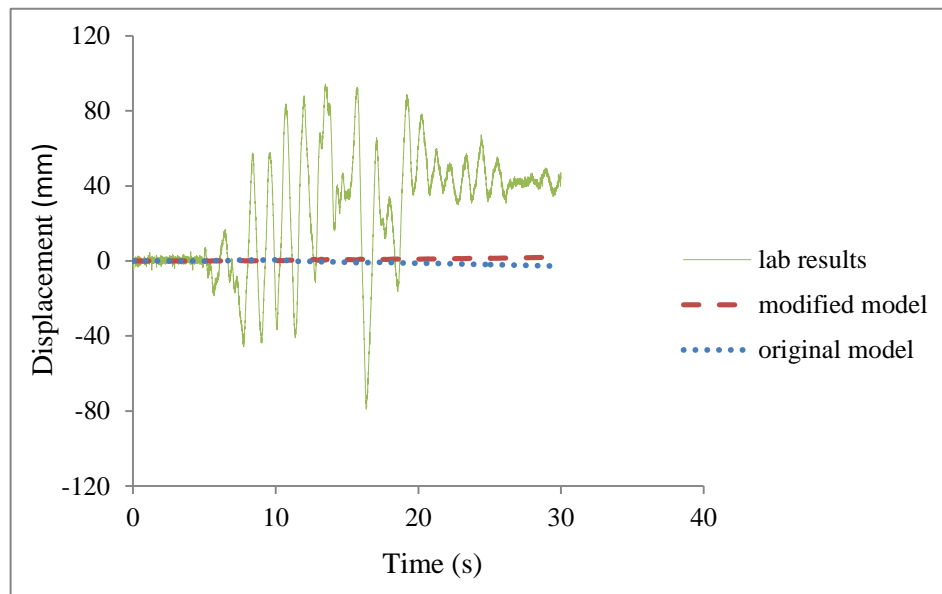


(d) L4

**Figure 6-13. Comparison of time history of lateral displacements between the predicted results and the experimental results.**

## 6.4 Summary

In this chapter, the earthquake-induced liquefaction of sand has been simulated using the newly developed PSR model which can consider the principal stress rotation. Both the modified PSR model and the original model were implemented into the finite element simulations of the centrifuge test under earthquake loadings to test their abilities and comparisons were made between the predicted results and the experimental results.

The original model significantly underestimates the pore water pressure build-up, the reduction of $p'$ and the cumulative shear strain. Liquefactions are not observed in the predicted stress path from the original model. However, the modified PSR model can generate higher excess pore water pressure than the original model and bring the soil to the liquefaction at the top level, which agrees with the laboratory results. The accelerations predicted agree well with the measured results. The comparisons show that the modified PSR model predicts much larger lateral displacements and settlements than the original model and performs better compared with the experimental results. However, the modified PSR model still underestimates the lateral displacements and settlements close to the surface, which may be due to the movement of the LVDT transducer and the assumption of the constant permeability. Generally, the predicted results from the modified PSR model agree better with the experimental results due to its complete ability in the simulation of the PSR.

It is evident that the earthquake loading can produce the PSR in the soil. Continuous rotation of principal stresses can be observed in simulation results from both the original model and the modified PSR model. As the natural

earthquake loadings are much more complex, it is therefore important to consider the PSR effects in the simulation of earthquake-induced liquefactions. In conclusion, the modified PSR model presented in this research has the ability to simulate the PSR effects and plays an important role in the numerical simulations of soil behaviors under earthquake loadings.

# Chapter 7 Summary and Conclusions

## 7.1 Summary

### 7.1.1 Background and reasons for the study of principal stress rotations

Principal stress rotations (PSR) occur in most of geotechnical problems under a variety of loading conditions. Plastic deformations and the non-coaxiality which means the non-coincidence between the principal strain increment directions and the principal stress directions can be caused by this PSR even without a change of principal stress magnitudes. Continuous PSR can also generate excess pore water pressure and cumulative shear strain in undrained conditions, especially under the dynamic loading. This PSR behavior can further accelerate undrained soil liquefaction because of the cumulative plastic volumetric deformations. Ignoring the PSR impacts may lead to unsafe design.

The PSR and non-coaxial behavior can be found in numerous experimental investigations. Roscoe et al. (1967) proposed that the principal stress directions were not coincident with the principal strain rate directions before the peak shear stress based on their findings from a simple shear test. The non-coaxiality was also observed in the directional shear cell tests from Wong & Arthur (1985) and micro-mechanical study of a photoelastic disc assembly to simulate the two-dimensional granular material from Drescher & Jong (1972). After that, the PSR impact and non-coaxiality were widely explored by researchers using

the hollow cylinder apparatus. Results from these experimental tests indicate that loading conditions involving the PSR can cause the non-coaxial behavior in the soil samples. This non-coaxiality can be observed especially during the early stage of the shearing. Then the difference between the directions of the principal stress and the principal strain increment tends to reduce as the soil specimen approaches the critical state. Moreover, the deviations between the principal stress directions and the principal strain incremental directions could be more than 30 degrees under the continuous PSR.

The investigation of the PSR and non-coaxial behaviors has been attempted by numerous numerical methods as well. The discrete element method (DEM) was widely used by researchers to study the non-coaxiality (Thornton & Zhang, 2006; Li & Yu, 2009), and similar conclusions from the experimental studies were proposed by them. A few researchers have also explored the significance of PSR using the finite element method (FEM) together with different numerical integration schemes (Abbo, 1997; Sassa & Sekiguchi, 2001). A variety of soil models based on different theories have been proposed during the last decades to simulate the PSR and non-coaxial impacts as well, such as double shearing model (Spencer, 1964), hypoplastic models (Wang et al., 1990; Kolymbas, 1991), multi-laminate models (Iai et al., 1992), yield vertex theory model (Rudnicki & Rice, 1975), etc. In 2013, Yang and Yu conducted a series of numerical simulations to investigate the impact of PSR by using an elastoplastic model considering the PSR effect (PSR model) developed based on a kinematic hardening model with bounding surface concept. This model is also used in this research to study the PSR impact under various loading conditions.

Generally, the experimental studies and numerical simulations all demonstrated that the PSR can lead to the plastic deformations and non-coaxiality in the soil and it is essential to take account of the PSR impact in geotechnical studies and designs. Therefore, this research aims to investigate the significance of PSR effect in geotechnical problems by numerical simulations of various experimental tests using the newly-developed PSR model which can take account of PSR impacts. The ability of this PSR model is also tested in the simulations of these experimental tests including the triaxial tests, simple shear tests, hollow cylinder tests, and centrifuge tests under wave loadings and earthquake loadings.

### 7.1.2 Liquefaction and its criteria

Liquefaction is a phenomenon in which the soil behaves like fluid due to the significant reduction of its strength and stiffness under various loading conditions. The change of the interaction between the soil skeleton composed of grains and the pore fluid leads to this phenomenon. When the soil is subjected to the cyclic loadings, the contraction of the soil and the build-up of pore pressure occur because of the rearrangement of the soil particles to reach an optimal potential state, which further causes the loss of the frictional force and bearing capacity of the soil. According to Ye et al. (2014), there are two mechanisms of the liquefaction—transient liquefaction and residual liquefaction. Transient liquefaction comes from the phase lag of the pore pressure in the elastic seabed. Residual liquefaction is caused by the compaction of elastoplastic seabed soil under dynamic loadings and is investigated in this research.

It is important to study the liquefaction because the offshore foundations are vulnerable to this soil behavior. Catastrophic failures of the structure have been reported to occur in a short time due to the soil liquefaction and caused further damages such as financial losses and deaths. Moreover, liquefaction can be induced under a variety of loading conditions such as wave loadings and earthquake loadings. However, it is difficult to study the liquefaction because of the limitations of the laboratory tests and in-situ measurements such as the inappropriate stress path and the high research price, etc. Therefore, the numerical simulations used in this research can be considered as a suitable method to explore the liquefaction behavior.

The criterion proposed by Sassa & Sekiguchi (1999) is adopted in this research to judge the occurrence of the liquefaction. In this theory, the excess pore water pressure $u_e$ is divided into the oscillatory part $u_e^1$ and the residual pore water pressure $u_e^2$, which is determined by taking the average of the moving wave and stems from the contraction of the soil under cyclic plasticity. Then the occurrence of the liquefaction is judged by calculating the ratio $k$ of the measured $u_e^2$ to the value of the initial vertical effective stress $\sigma_{v0}'$ at one location. The typical values for this ratio of liquefaction may vary from 0.78 - 0.99. Moreover, liquefaction is also considered by some other criteria such as the sudden increase of the shear strain and the reduction of effective confining pressure as they also indicates the lower shear stiffness of the soil.

### 7.1.3 Numerical implementations

In this research, a series of experimental tests for the Nevada sand and Leighton Buzzard sand (Fraction B & E) were numerically simulated using the

modified PSR model and original model to study the PSR impact. The simulation consists of two parts: the single element simulation and the finite element simulation.

In the single element simulations, these two models were incorporated into a single element computer program written in Fortran, which is the first advanced computer programming language in the world and especially suitable for scientific and engineering computations such as geotechnical problems (Griffiths & Smith, 2003). This program is performed with the Intel Visual Fortran compiler and capable for the single element stress-strain response analysis. The PSR model parameters are also calibrated in these single element simulations.

The finite element method was used to simulate the experimental centrifuge tests under the wave loading and the earthquake loading to further explore the PSR impact in the geotechnical boundary value problems. The simulation of centrifuge wave tests utilizes the commercial finite element software—ABAQUS, which is one of the most powerful large scale finite element software in the world. It contains abundant element and material library and can be used for nonlinear problems with the freedom of pore pressure. Furthermore, it has various interfaces of subroutines such as UMAT, which allows the implementation of the modified PSR model in this research. When the user defined material subroutine is used, ABAQUS uses the exact Newton's method to solve the non-linear equilibrium equations (Simulia, 2010). In the simulation of the centrifuge earthquake tests, another finite element computer program DYSAC2 which can analyze the two dimensional dynamic geotechnical problems under plane strain conditions is adopted. DYSAC2 can

solve the fully coupled dynamic governing equations of a two-phase saturated porous media using the four-node elements with the reduced integration and the fluid bulk modulus terms (Muraleetharan et al., 1988). This program adopts a three parameter time integration scheme called the Hilber-Hughes-Taylor $\alpha$ method to integrate the spatially discrete finite element equations, along with a predictor/multi-connector algorithm to provide the quadratic accuracy and numerical damping characteristics (Hilber et al., 1977). In this research, the computer code of DYSAC2 written in Fortran 77 has been modified to incorporate the modified PSR model and original model into the centrifuge earthquake test from the VELACS project.

The original model and modified PSR model were implemented into the finite element simulations by a constitutive model subroutine written in Fortran. This constitutive model subroutine adopted an explicit substepping integration algorithm with automatic error controls. In this integration scheme, the strain increment obtained from manipulations of the main program is divided into multiple sub-increments. The constitutive formulations are integrated firstly using Euler scheme of the first order accuracy, then using the modified Euler scheme of the second order accuracy in each sub-increment. The difference of the integration results from these two schemes gives the error measurement of the numerical integrations. The current sub-increment is re-subdivided based on the ratio of the local current error to the integration error tolerance if the error tolerance is exceeded. Furthermore, the imposed strain increment can be automatically divided based on the prescribed error tolerance because the size of the next sub-increment is also determined by the extrapolation of the current error compared with the error tolerance prescribed (Yang & Yu, 2006; 2010). When implementing this integration scheme, many additional details such as

the transition from the elastic to plastic zones, the solution for the negative plastic multiplier and the correction of stresses back to the yield surface were considered as well (Abbo, 1997).

## 7.2 Conclusions

This research has firstly simulated a series of experimental soil tests including the triaxial tests, simple shear tests and hollow cylinder tests using the single element computer program. Then the centrifuge wave tests and centrifuge earthquake tests have been numerically simulated using the finite element method. The critical conclusions are summarized in detail as follows.

### 7.2.1 Soil behaviors in the single element simulations

- Although the original model can reflect some PSR effects in the single element simulations under the PSR loadings, generally the modified PSR model performs better and agrees better with the experimental results than the original model. The original model can only produce very limited reduction of effective confining pressures and cumulative shear strains under cyclic loading paths, thus significantly underestimates the laboratory results and is unable to bring the specimen to the liquefactionin most of cases. However, the modified PSR model generates much more reduction of $p'$ and larger shear strains, and agrees much better with the experimental results due to its complete ability in the simulation of the PSR impact. Furthermore, the modified PSR model brings the soil to liquefaction, which agrees with the soil behaviors in the experimental results.

- It is evident that the predicted results from the modified PSR model only

show difference compared to the original model when the specimen is subjected to loading paths involving the PSR. There is no difference between the simulation results from these two models under monotonic loadings because the stress paths do not involve the PSR. The comparison from the simulations for all three types of sand all demonstrates that both two models have the great ability to simulate the monotonic loadings under drained and undrained conditions.

## 7.2.2 Soil behaviors in the finite element simulations under the wave loading

- It can be seen from the simulation results that the principal stress is continuously rotating under the progressive wave, and both the progressive wave and the standing wave loadings produce the PSR in the seabed. Therefore the consideration of the PSR impact is important in offshore foundation designs.

- Generally, the original model significantly underestimates the build-up of the excess pore water pressure, the reduction of the effective confining pressure and the cumulative shear strain under both the progressive waves and standing waves. However, the modified PSR model generates higher excess pore water pressure and the shear strain than the original model, thus bringing the soil to the liquefaction and agrees better with the laboratory results.

- Generally, more severe wave loadings can generate higher pore water pressures. The PSR impact also increases with the severity of imposed

wave loadings reflected by the cyclic stress ratio. The higher cyclic stress ratio leads to the more obvious difference between the modified PSR model and the original model, which means the larger PSR effects. Therefore, the modified model can bring the soil to liquefaction, thus reflecting the characteristics of critical cyclic stress ratio above which the liquefaction will occur.

- Although the standing wave produces less PSR effect than the progressive wave, the modified PSR model still performs better than the original model compared to the experimental results under the standing wave. Under the standing wave, the PSR effect laterally reduces from the boundary of the soil bed to the antinode, where nearly no PSR was observed. Therefore, the modified PSR model has limited effect in the simulation at the antinode under the standing wave. However, this is just one very special case and location. As the natural wave loadings are much more random, it is important to consider the PSR impact in the simulation of wave-seabed interactions. Therefore, the modified PSR model presented in this research has a great ability and plays an important role in the simulations of wave-induced liquefaction.

### 7.2.3 Soil behaviors in the finite element simulations under the earthquake loading

- It is evident that the earthquake loading can produce the PSR in the soil bed. Continuous rotation of principal stresses can be observed in simulation results from both the original model and the modified PSR model. Therefore, it is also important to consider the PSR impact in the

simulation of earthquake-induced liquefaction.

- The simulation results show that the original model significantly underestimates the pore water pressure build-up, the $p'$ reduction and the cumulative shear strain. Liquefaction cannot be observed in the predicted stress path from the original model. The modified PSR model can generate higher pore water pressures and shear strains than the original model, and bring the soil to the liquefaction which agrees well with the laboratory results. The accelerations predicted also agree well with the measured results from the experimental centrifuge test.

- The comparison of the lateral displacements and settlements show that both the modified PSR model and the original model underestimate these results. This may be due to the movement of the LVDT transducer and the assumption of the constant permeability. However, the modified PSR model still predicts much larger displacements and settlements than the original model and performs much better compared with the experimental results.

- Generally, the predicted results from the modified PSR model agree much better with the experimental results due to its ability in the simulation of the PSR impact. As the natural earthquake loadings are much more complex, it is therefore important to consider the PSR effects in earthquake designs. In conclusion, the modified PSR model presented in this research has a great ability and plays an important role in the simulations of the soil behaviors under earthquake loadings.

# 7.3 Recommendations for Future Research

The current study has compared the predicted results from numerical simulations of a series of experimental tests with the test results and provided the better understanding of the PSR effect and other soil behaviors related to the PSR. However, as a tool to find the solution to the real geotechnical problem, numerical simulations still have some limitations, such as the postulations, the simplifications made. In this process, important features are retained while less important features are omitted to achieve the result. Furthermore, numerical problems are often encountered in the computations. To achieve better simulation results, it is essential to consider the problem more completely. Therefore, some suggestions for the future work are discussed below.

## 7.3.1 The modified PSR model

- This study focuses on the impact of the PSR on the soil behaviors using the PSR model modified on the basis of a kinematic hardening model from Dafalias & Manzari (2004). Therefore, the fabric anisotropy and non-associativity in deviatoric space in their original model are not considered to facilitate the postulations used in this research. However, the soil behaviors from the fabric anisotropy have been widely observed in the experimental tests. The PSR and fabric effects are both important and they are often mutually interacted. Therefore, to achieve more accurate results for problems such as the experimental tests investigating the anisotropy, the corresponding features can be added into the model.

- It can be seen from the formulations of the original model and modified PSR model that the square root of the effective confining pressure *p'* is included. However, in the finite element simulation of boundary value problems, the singularity problem is likely to occur in the soil elements, especially at the surface of the soil bed. This problem may lead to the negative effective confining pressure, thus causing numerical problems such as computation errors and non-convergence in some elements during the iterations. Although these problems only happen in the late stage in a few integration points very close to the surface of soil beds and do not affect the computation of the whole soil bed, special cares such as the cutoff value of the effective confining pressure *p'* and very small increments are given to these elements in this research. These measures may cause a slight discrepancy of the simulation results and increase the computation costs. Therefore, it is recommended that the model can be further developed to avoid this problem by using the rounded tip on the yield surface or modifying the related formulations and theories for the cases when the effective confining pressure becomes negative.

## 7.3.2 Numerical implementations

- The simulation results from the centrifuge earthquake test in Chapter 6 show that both the original model and the modified PSR model underestimate the displacements and settlements under the earthquake loading. This may be due to the constant permeability used in the research. Studies demonstrate that the permeability tends to increase as the liquefaction spreads in the soil during the earthquake shakings (Andrianopoulos et al., 2010; Fareet al., 2011; Shahiret al., 2012).

Therefore, in order to obtain more accurate results for the displacements and settlements, the changing value of permeability is suggested to use in future numerical studies.

- The centrifuge earthquake tests are simulated in this research using the DYSAC2 program which is only available for finite element problems under the plane strain condition. To further investigate the soil behaviors under the PSR, it is essential to simulate more complex geotechnical problems under the 3-dimensional condition. Therefore, DYSAC2 program can be modified to consider the 3-D condition or implement the modified PSR model into other software which is capable for the earthquake analysis under the 3-D condition. Although the 3-D finite element model is used in the numerical simulation of centrifuge wave tests in Chapter 5, this model is fully constrained in the $z$ direction, hence simulating the plane strain condition as well. Further investigations considering more complex geotechnical problems under wave loadings such as the soil-structure interaction of the embankment, breakwater and wind turbine under the 3-D condition are suggested to be conducted.

- The single element simulations and conventional laboratory tests are useful to study the soil responses under the PSR. Several single element simulations under the PSR in one direction have been carried out in this research. However, it is important to investigate the soil behaviors under the PSR in two and three directions using the single element simulations because there are multiple PSRs (or shear stresses) in real world geotechnical engineering problems. Therefore, parallel studies including both the single element numerical simulation and experimental study under

multiple PSRs are highly recommended in future.

# References

Abbo, A. J. (1997), Finite Element Algorithms for Elastoplasticity and Consolidation, PhD Thesis, University of Newcastle, Australia.

Andrianopoulos, K. I., Papadimitriou, A. G. & Bouckovalas, G. D. (2010), Bounding Surface Plasticity Model for the Seismic Liquefaction Analysis of Geostructures, Soil Dynamics and Earthquake Engineering, 30, 895–911.

Arulanandan, K. & Manzari, M. T. (1992), Liquefaction Analysis of Stratified Soil Layers: A Verification of Coupled Stress-Flow Approach, Proceedings, Tenth World Conference on Earthquake Engineering, Madrid, Spain, 1349 – 1353.

Arulanandan, K. & Scott, F. R. (1993), Verification of Numerical Procedures for the Analysis of Soil Liquefaction Problems, Proceedings, International Conference on the Verification of Numerical Procedures for the Analysis of Soil Liquefaction Problems, California, USA.

Arulanandan, K., Manzari, M., Zeng, X., Fagan, M., Scott, R. F. & Tan, T. S. (1995), Significance of the VELACS Project to the Solution of Boundary Value Problems in Geotechnical Engineering, Proceedings, Third International Conference on Recent Advances in Geotechnical Earthquake Engineering and Soil Dynamics, 2, St. Louis, Missouri, 825 – 832.

Arulmoli, K., Muraleetharan, K. K., Hosain, M. M. & Fruth, L. S. (1992),

VELACS Laboratory Testing Program, Soil Data Report, Report to the National Science Foundation, Washington, D.C. by the Earth Technology Corporation, Irvine, Calif.

Bhatia, S. K., Schwab, J. & Ishibashi, I.(1985), Cyclic Simple Shear, Torsional Shear and Triaxial—A Comparative Study, Proceedings, Advanced in the Art of Testing Soils Under Cyclic Conditions, American Society of Civil Engineers, New York, 232 – 254.

Bathe, K. J. (1996), Finite Element Procedures, Prentice-Hall, Inc, New Jersey, USA.

Been, K. & Jefferies, M. G. (1985), A State Parameter for Sands, Geotechniques, 35(2), 99–112.

Cai, Y. Y. (2010), An Experimental Study of Non-Coaxial Soil Behavior Using Hollow Cylinder Testing, PhD thesis, the University of Nottingham, UK.

de Josselin de Jong, G. (1958), The Undefiniteness in Kinematics for Friction Materials, Proceeding, Conference on Earth Pressure Problem, Brussels, 1, 55–70.

Chang, K. T. & Sture, S. (2006), Microplane Modeling of Sand Behavior under Non-Proportional Loading, Computers and Geotechnics, 33, 177 –187.

Chen, Y. R. & Kutter, B.L. (2009), Contraction, Dilation, and Failure of Sand in Triaxial, Torsional, and Rotational Shear Tests, Journal of Engineering Mechanics, 135(10), 1155–1165.

Dunn, S. L., Vun, P. L. & Chan, A. H. C. (2006), Numerical Modeling of Wave-Induced Liquefaction Around Pipelines, American Society of Civil Engineers, Journal of Waterway, Port, Coastal, and Ocean Engineering, 132(4), 276–288.

Dafalias, Y. F. (1986), Bounding Surface Plasticity, I: Mathematical Foundation and Hypoplasticity, Journal of Engineering Mechanics, American Society of Civil Engineers, 112 (12), 1263 –1291.

Dafalias, Y. F. & Manzari, M. T. (2004), Simple Plasticity Sand Model Accounting for Fabric Change Effects, Journal of Engineering Mechanics, American Society of Civil Engineers, 130(6), 622 – 634.

Drescher, A. & de Josselin de Jong, G. (1972), Photoelastic Verification of a Mechanical Model for the Flow of a Granular Material, Journal of the Mechanics and Physics Solids, 20, 337–351.

Ehlers, W., Schenke, M. & Markert, B. (2013), Liquefaction Phenomena in Fluid-Saturated Soil Based on the Theory of Porous Media and the Framework of Elasto-Plasticity, ZAMM. Z. Angew. Math. Mech, 1 – 10.

Fang, H. L. (2003), A State-Dependent Multi-Mechanism Model for Sands, Geotechnique, 53(4), 407 –420.

Fare, O. G., Rahmani, A. & Pak, A. (2011), Numerical Simulation of Soil Settlement in Liquefiable Grounds, Pan-American Conference on Soil Mechanics and Geotechnical Engineering, Toronto, Canada.

Gutierrez, M., Ishihara, K. & Towhata, I. (1991), Flow Theory for Sand During Rotation of Principal Stress Direction, Soils and Foundations, 31(4), 121 – 132.

Gutierrez, M., Ishihara, K. & Towhata, I. (1993), Model for the Deformation of Sand During Rotation of Principal Stress Directions, Soils and Foundations, 33(3), 105 –117.

Gutierrez, M. & Ishihara, K. (2000), Non-coaxiality and Energy Dissipation in Granular Material, Soils and Foundations, 40, 49–59.

Griffiths, D. V. & Smith, I. M. (1998), Programming the Finite Element Method, John Wiley & Sons, Inc, UK.

Hilber, H. M., Hughes, T. J. R. & Taylor, R. L. (1977), Improved Numerical Dissipation for Time Integration Algorithms in Structural Dynamics, Earthquake Engineering and Structural Dynamics, 5, 283 – 292.

Hight, D. W., Gens, A. & Symes, M. J. (1983), The Development of a New Hollow Cylinder Apparatus for Investigating the Effects of Principal Rotation in Soils, Geotechnique, 33(4), 355–383.

Iai, S., Matsunaga, Y. & Kameoka, T. (1992), Strain Space Plasticity Model for Cyclic Mobility, Soils and Foundations, 32(2), 1–15.

Ibraim, E., Lanier, J., Muir Wood, D. & Viggiani, G. (2010), Strain Path Controlled Shear Tests on an Analogue Granular Material, Geotechnique, 60(7), 545–559.

Ishihara, K., Tatsuoka, F. & Yasuda, S. (1975), Undrained Deformation and Liquefaction of Sand under Cyclic Stresses, Soils and Foundations, 15(1), 29–44.

Ishihara, K. & Towhata, I. (1983), Sand Response to Cyclic Rotation of Principal Stress Directions as Induced by Wave Loads, Soils and Foundations, 23(4), 11 – 26.

Ishihara, K. & Yamazaki, A. (1984), Analysis of Wave-Induced Liquefaction in Seabed Deposits of Sand, Soils and Foundations, 24(3), 85 – 100.

Jeng, D. S. (2013), Porous Models for Wave-seabed Interactions, Shanghai JiaoTong University Press and Springer-Verlag Berlin Heidelberg, Shanghai.

Jefferies, M. & Shuttle, D. (2011), Understanding Liquefaction through Applied Mechanics, 5th International Conference on Earthquake Geotechnical Engineering January, 10-13, Santiago, Chile.

Kolymbas, D. (1991), An outline of plasticity, Archive of Applied Mechanics, 61, 143 –151.

Lade, P. V., Namb, J. & Hong, W. P. (2009), Interpretation of Strains in Torsion Shear Tests, Computers and Geotechnics, 36, 211–225.

Li, X. S. & Dafalias, Y. F. (2000), Dilatancy for Cohesionless Soils, Geotechnique, 50(4), 449 – 460.

Li, X. S. & Dafalias, Y. F. (2004), A Constitutive Framework for Anisotropic

Sand including Non-Proportional Loading, Geotechnique, 54(1), 41 –55.

Li, J. & Jeng, D. S. (2008), Response of a Porous Seabed around Breakwater Heads, Ocean Engineering, 35 (8-9), 864 – 886.

Li, X. S. & Wang, Y. (1998), Linear Representation of Steady-State Line for Sand, Journal of Geotechnical and Geoenvironmental Engineering 124(12), 1215 – 1217.

Li, X. & Yu, H. S. (2009), Influence of Loading Direction on the Behavior of Anisotropic Granular Materials, International Journal of Engineering Science, 47(11-12), 1284–1296.

Miura, K., Miura, S. & Toki, S. (1986), Deformation Behavior of Anisotropic Dense Sand under Principal Stress Axes Rotation, Soils and Foundations, 26(1), 36 – 52.

Manzari, M. T. & Dafalias, Y. F. (1997), A Critical State Two-Surface Plasticity Model for Sands, Geotechnique, 47(2), 255 – 272.

Mandel, G. & Fernandez, L. R. (1970), Fully Developed Plastic Shear Flow of Granular Materials, Geotechnique, 20(3), 277–307.

Muraleetharan, K. K., Mish, K. D., Yogachandran, C. & Arulanandan, K. (1988), DYSAC2 (Version 1.0), Dynamic Soil Analysis Code for 2-Dimensional Problems, Computer Code, Department of Civil Engineering, University of California, Davis, California.

Muraleetharan, K. K. (1990), Dynamic Behavior of Earth Dams, PhD Dissertation, University of California, Davis, California.

Muraleetharan, K. K. & Arulanandan, K. (1991), Dynamic Behavior of Earth Dams Containing Stratified Soils, Proceedings, International Conference, Centrifuge, A. A. Balkma, Rotterdam, Netherlands, 401 – 408.

Muraleetharan, K. K. (1993), Numerical Prediction for Model No. 1, Proceedings, International Conference on the Verification of Numerical Procedures for the Analysis of Soil Liquefaction Problems, A. A. Balkema, Rotterdam, Netherlands, 187 – 196.

Muraleetharan, K. K., Arulmoli, K., Jagannath, S. V., Wittkop, R. C. & Foxworthy, J. E. (1994), Validation of a Computer Code for the Analysis of Dike Retaining Structures, Proceedings, International Conference Centrifuge, A. A. Balkema, Rotterdam, Netherlands, 203 – 208.

Muraleetharan, K. K., Mish, K. D. & Arulanandan, K. (1994), A Fully Coupled Non-Linear Dynamic Analysis Procedure and Its Verification Using Centrifuge Test Results, International Journal for Numerical and Analytical Methods in Geomechanics, 18, 305 – 325.

Muraleetharan, K. K. (1995), VELACS Extension Project, Constitutive Model Calibration and Predictions, Technical Report, School of Civil Engineering and Environmental Science, University of Oklahoma, Norman, Oklahoma.

Muraleetharan, K. K., Arulmoli, K., Jagannath, S. V. & Thiessen, D. A. (1995), Performance of Port Facilities During the Northridge Earthquake, Proceedings, Third International conference on Recent Advances in Geotechnical Earthquake Engineering and Soil Dynamics, St. Louis, Mossouri, 3, 215 – 221.

Muraleetharan, K. K., Arulmoli, K., Jagannath, S. V., Wittkop, R. C. & Foxworthy, J. E. (1997), Use of Centrifuge and Numerical Modeling in the Design of Port of Los Angeles' Pier 400, Transportation Research Record, Transportation Research Board, National Research Council.

Muraleetharan, K. K., Mish, K. D., Yogachandran, C. & Arulanandan, K. (1997), User's Manual for DYSAC2 (Version 7.0), Dynamic Soil Analysis Code for 2-Dimensional Problems, Technical Report, School of Civil Engineering and Environmental Science, University of Oklahoma, Norman, Oklahoma.

Nago, H. & Maeno, S. (1987), Pore Pressure and Effective Stress in a Highly Saturated Sand Bed under Water Pressure Variation on its Surface, J. Natural Disaster Sci, 9(1), 23 – 35.

Neto, E. S., Peri ´c, D. & Owen, D. (2008), Computational Methods for Plasticity, Theory and Applications, John Wiley & Sons Ltd, United Kingdom, 137–262.

Oda, M., Nemat-Masser, S. & Konishi, J. (1985), Stress-Induced Anisotropy in Granular Masses, Soils and Foundations, 25(3), 85–97.

Pak, A., Seyfi, S. & Ghassemi, A. (2014), Numerical Investigation into the

Effects of Geometrical and Loading Parameters on Lateral Spreading Behavior of Liquefied Layer, Acta Geotechnica 9(6), 1059–1071.

Pradel, D., Ishihara, K. & Gutizrrez, M. (1990), Yielding and Flow of Sand Under Principal Stress Axes Rotation, Soils and Foundations, 30(1), 87–99.

Rudnicki, J. W.& Rice, J. R. (1975), Conditions for the Localization of Deformation in Pressure-Sensitive Dilatant Materials, Journal of Mechanics and Physics of Solids, 23, 371 –394.

Roscoe, K. H., Bassett, R. H. & Cole, E. R. L. (1967), Principal Axes Observed During Simple Shear of a Sand, 4th European Conference on Soil Mechanics and Foundation Engineering, Oslo, 231–237.

Roscoe, K. H. (1970), The Influence of Strains in Soil Mechanics, Geotechnique, 20, 129–170.

Sassa, S. & Sekiguchi, H. (1999), Wave-Induced Liquefaction of Beds of Sand in a Centrifuge, Geotechnique, 49 (5), 621 – 638.

Sassa, S. & Sekiguchi, H. (2001), Analysis of Wave-Induced Liquefaction of Sand Beds, Geotechnique, 51(2), 115 – 126.

Sadeghian, S. & Namin, L. N. (2013), Using State Parameter to Improve Numerical Prediction of a Generalized Plasticity Constitutive Model, Computers & Geosciences, 51, 255–268.

Schofield, A. N. & Wroth, C. P. (1968), Critical State Soil Mechanics,

McGraw-Hill, New York.

Spencer, A. J. M. (1964), A Theory of the Kinematics of Ideal Soils under Plane Strain Conditions, Journal of the Mechanics and Physics Solids, 12, 337–351.

Symes, M. J., Hight, D. W. & Gens, A. (1982), Investigation Anisotropy and the Effects of Principal Stress Rotation and of the Intermediate Principal Stress Using a Hollow Cylinder Apparatus, IUTAM Conference on deformation and failure of granular materials, Delft, 441–449.

Symes, M. J., Gens, A. & Hight, D.W. (1984), Undrained Anisotropy and Principal Stress Rotation in Saturated Sand, Geotechnique, 34(1), 11–27.

Symes, M. J., Gens, A., Hight, D. W. (1988), Drained Principal Stress Rotation in Saturated Sand, Geotechnique, 38(1), 59–81.

Shahir, H., Pak, A., Taiebat, M. & Jeremić, B. (2012), Evaluation of Variation of Permeability in Liquefiable Soil under Earthquake Loading, Computers and Geotechnics, 40, 74 – 88.

Simulia. (2010), ABAQUS/CAE user's manual, USA.

Sumer, B. M., Ansal, A., Cetin, K. O., Damgaard, J., Gunbak, A. R., Hansen, N. O., Sawicki, A., Synolakis, C. E., Yalciner, A. C., Yuksel, Y. & Zen, K. (2007), Earthquake-Induced Liquefaction Around Marine Structures, Journal of Waterway, Port, Coastal, and Ocean Engineering, 33, 55 –

82.

Tejchman, J. & Wu, W. (2009), Non-Coaxiality and Stress-Dilatancy Rule in
Granular Materials, FE Investigation within Micro-Polar Hypoplasticity,
International Journal for Numerical and Analytical Methods in
Geomechanics, 33, 117 –142.

Thornton, C. & Zhang, L. (2006), A Numerical Examination of Shear Banding
and Simple Shear Non-coaxial Flow Rule, Philosophical Magazine, 86,
3425–3452.

Visone, C. (2008), Performance-Based Approach in Seismic Design of
Embedded Retaining Walls, PhD thesis, University of Napoli Federico
II, Napoli, Italy, Annex A1 – A21.

Wang, Z. L., Dafalias, Y. F. & Shen, C. K. (1990), Bounding Surface
Hypoplasticity Model for Sand, Journal of Engineering Mechanics,
American Society of Civil Engineers, 116 (5), 983 –1001.

Wittkop, R. C. (1993), Applications of VELACS Philosophy to Port of Los
Angeles Pier 400 Project, Proceedings, International Conference on the
Verification of Numerical Procedures for the Analysis of Soil
Liquefaction Problems, A. A. Balkema, Rotterdam, Netherlands, 2,
1647 – 1655.

Wong, R. K. S. & Arthur, J. R. F. (1986), Sand Sheared by Stresses with
Cyclic Variations in Directions, Geotechnique, 36(2), 215–226.

Wood, D. M. (1990), Soil Behavior and Critical State Soil Mechanics,

Cambridge University Press, Cambridge, UK.

Yang, L. (2013), Experimental Study of Soil Anisotropy Using Hollow Cylinder Testing, PhD Thesis, University of Nottingham, UK.

Yang, Y. M. & Yu, H. S. (2006), Application of a Non-Coaxial Soil Model in Shallow Foundations, Geomechanics and Geoengineering, 1(2), 139 – 150.

Yang, Y. & Yu, H. S. (2006), A Non-Coaxial Critical State Soil Model and its Application to Simple Shear Simulations, International Journal for Numerical and Analytical Methods in Geomechanics, 30, 1369–1390.

Yang, Y. M. & Yu, H. S. (2006), Numerical Simulation of Simple Shear with Non-Coaxial Soil Models, International Journal for Numerical and Analytical Methods in Geomechanics, 30, 1 – 19.

Yang, Y. & Yu, H. S. (2010), Numerical Aspects of Non-Coaxial Model Implementations, Computers and Geotechnics, 37, 93–102.

Yang, Y. & Yu, H. S. (2013), A Kinematic Hardening Soil Model Considering the Principal Stress Rotation, International Journal for Numerical and Analytical Methods in Geomechanics, 37, 2106–2134.

Yang, Y. (2003) The Middle Surface Concept an its Application to Constitutive Modeling of Soils, PhD Thesis, University of Oklahoma, USA.

Yatomi, C., Yashima, A., Iizuka, A. & Sano, I. (1989), General Theory of Shear Bands Formation by a Non-coaxial Cam-Clay Model, Soils and Foundations, 29(3), 41–53.

Ye, J., Jeng, D., Ren, W. & Zhu, C. (2014), Numerical Simulation of the Wave-Induced Dynamic Response of Poro-Elastoplastic Seabed Foundations and a Composite Breakwater, Applied Mathematical Modeling.

Yu, H. S., Yang, Y. & Yuan, X. (2005), Application of Non-Coaxial Plasticity Models in Geotechnical Analysis, Proceedings, the16th International Conference on Soil Mechanics and Geotechnical Engineering, 2, Osaka, 993–996.

Yu, H. S. & Yuan, X. (2005), On a Class of Non-Coaxial Plasticity Models for Granular Soils, Proceedings of the Royal Society A – Mathematical Physical and Engineering Sciences, 462 (2067), 725 –748.

Zen, K., Yamazaki, H. & Sato, Y. (1990), Oscillatory Pore Pressure and Liquefaction in Seabed Induced by Ocean Waves, Soils and Foundations, 30(4), 147–161.